Annual Report 2004

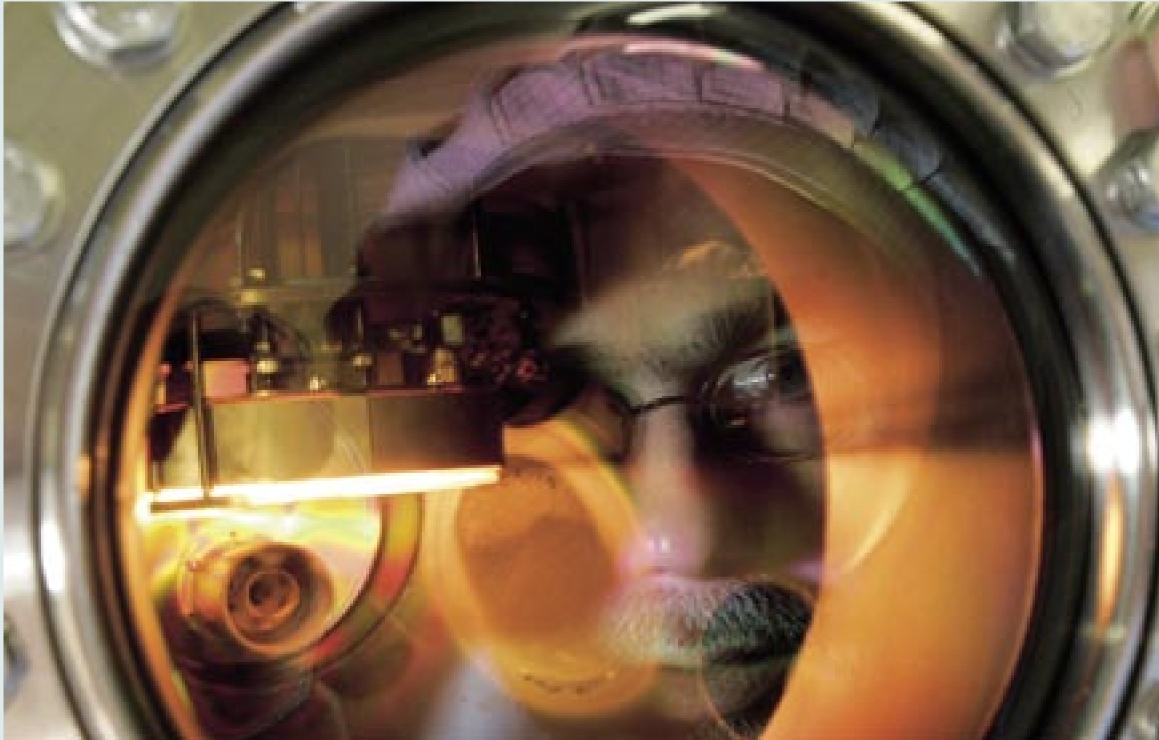

Center for Micro- and Nanotechnologies

Technical University
of Ilmenau

Front page:

Dr. Thomas Stauden in front of a Molecular
Beam Epitaxy (MBE)
Epitaxial growth of semiconductor materials
for optical and electrical devices.
Courtesy of Michael Reichel (ari)

Editorial Board:

Editor:
Principal of the TU Ilmenau,
Prof. Dr.-Ing. Peter Scharff

Editorial office:
ZMN, Dr. Herwig Döllefeld

Layout/press:
Klapproth and Koch, Weimar

Funding:
μ-Comp e. V.

Center for Micro- and Nanotechnologies

Preface

Engineering touches all aspects of civilization. Great works of humankind, from the construction of pyramids to the creation of the internet, are marvels of engineering. Engineering is an evolving discipline that reinvents itself to explore and create solutions to new problems. Fields such as molecular biotechnology and nanoscale sciences that did not exist in the recent past are now expected to produce dramatic breakthroughs. Progress in engineering is driven by the application of various fields of human understanding and is subject to episodes of rapid enlightenment introduced by advances in technology. Thus, while strategic planning is important for any organization, it is critical for an engineering college where its role is two-fold: leadership in creating revolutionary technological advances, and education of students who will have a significant positive impact on society. In order to achieve its mission and bring its vision to life, the Technical University Ilmenau has established the goal to be recognized as a premier research university in micro- and nanosystems including the following fields of expertise: advanced nano-materials, nanosciences, micro- and nanotechnologies, nanopositioning- and nanosensor arrays as well as nano- and picofluidic systems.

The *Center for Micro- and Nanotechnologies* (ZMN) provides an outstanding infrastructure well above of state of the art to enable engineering at very small length scales in order to produce important technologies that utilize materials with new and fundamentally different properties for basic, as well as applied research. Advances in engineering achieved at the ZMN have made it possible to fabricate structures at the molecular level using techniques derived from the microelectronics industry (top-down approach), or to grow them using new molecular fabrication techniques (bottom-up approach). It is possible to create microscopic structures with the desired dynamical response for use as sensors, switches, and devices the size of biological cells. One can imagine electronic devices the size of molecules that interact directly with biological systems. Such developments are expected to revolutionize many areas of society, economic development, and our personal lives.

Micro- and nanoscale research, as well as nanobiotechnology engage a broad range of expertise from different disciplines and relates to a number of facets of the Technical University Ilmenau. Ilmenau´s strength in Micro- and Nanosciences stems from pioneering efforts initiated in 1991 with the establishment of the submicron facility on campus. The University´s strength in engineering and more recently in micro-, as well as nanoscale science has grown and is highlighted by the Center for Micro- and Nanotechnologies and ongoing research activities including nanoscale systems, micro-electrical-mechanical-(bio) systems, picofluidics, nanoelectronics, and nanoactuation. These scientific achievements will be further strengthened by two junior research groups starting in 2005 with a budget of about 4 Mio. € focusing on topics like functionalized ceramics, biosensors, and microfluidics. Our scientific concept was introduced to visitors like nobel prize winner Prof. K. Klitzing, the president of the German Science Foundation Prof. Winnacker, the minister of economy in Thuringia Dr. Reinholz, and many colleagues which (and without any exception) strongly motivated us to continue our scientific approaches and to further focus on the chosen topics.

Our success was enabled by outstanding efforts and support of the Federal Ministries of Research and Economy, the German Science Foundation, the European Commission, as well as all members of the ZMN. I would like to take the opportunity to thank all my colleagues, the scientific staff, the technicians and our students for all their dedicated work and team spirit. I look forward to be part of a special team which is able to convert the challenges of today basic nanosciences into the all day applications of tomorrow.

Oliver Ambacher

Contents

Research Departments and Staff of the ZMN 5
- Materials Science 6
- Technology 8
- Design 13
- Devices 14
- Modules 15
- Systems 17
- Analytics 17

Infrastructure and Equipment 19
- inside clean room 19
- outside clean room 23

Finances 25

Scientific Activities
- Materials Science 26
- Technology 42
- Design 70
- Devices 72
- Modules 84
- Systems 92
- Analytics 98

Publications and Conference Contributions
- Materials Science 114
- Technology 115
- Design 118
- Devices 119
- Modules 119
- Systems 120
- Analytics 120

Theses 122

Invited Talks, Colloquia, and Workshops 124

Scientific Projects 126

Research Departments and Staff of the ZMN

Administration

Faculty and Staff:

Oliver Ambacher
director
phone: -3402

Theodor Doll
director, former
phone: 06131-990-100

Heiko Thust
deputy director
phone: -2605

Herwig Döllefeld
central services
phone: -3400

Gabriele Barthel
financial management
phone: -3497

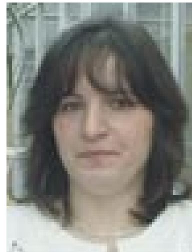

Katrin Dünkel
financial management
phone: -3497

Kirsti Schneider
financial management
phone: -3497

Renate Röhner
accounting and office
phone: -3401

Simone Gutsche
accounting and office
phone: -3401

Torsten Sändig
head of technical engineering
phone: -3415

Olaf Marufke
network administration
phone: -3416

Michael Fischer
technical engineering
phone: -3413

Henry Romanus
scientific coworker
phone: - 3404

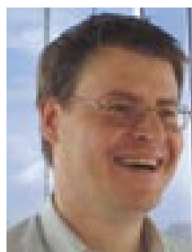

Andreas Schober
scientific coworker
phone: -3486

Michael Gebinoga
scientific coworker
phone: -3486

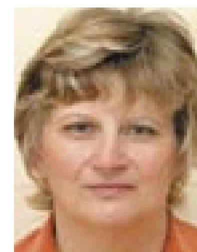

Birgitt Hartmann
technical coworker
phone: -3426

Contact:
Renate Röhner, phone: +49-(0)3677-69-3401
email: renate.roehner@tu-ilmenau.de

Material Science

Department of Metallic Materials and Composite Materials

With the appointment of Prof. Dr.-Ing. habil. H. Kern in 1996 as head of the department of Metallic Materials and Composite Materials Technology, the teaching and research activities related to materials at the Technical University of Ilmenau gained new momentum. The integration of the department into the Faculty of Mechanical Engineering reflects the significance of materials science engineering. The research areas in the department cover metallic, non-metallic, inorganic, and composite materials. The focus of the research is the improvement of available conventional materials, the development of new materials and the creation of innovative material approaches.

Research Activities:

- Tribological behaviour of materials and surface to pography
- Characteristics of ceramic suspensions (rheology)
- Ceramic shaping
- Electrophoretic Deposition
- Materials testing
- Metallography, microscopy and image processing techniques
- Special materials for mechanical engineering
- Composite Materials
- Metal-ceramic and ceramic matrix composites
- Glass matrix composites
- Interfacial characterisation and interface design of composites

Faculty and Staff:

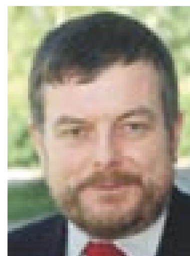

Prof. Dr.-Ing.
Heinrich Kern
head of department
phone: -2450

Kerstin Pfeiffer
technical coworker
phone: -1831

Contact:
Irina Hoffmann, phone: +49-(0)3677-69-2801
email: irina.hoffmann@tu-ilmenau.de

Department of Materials for Electrical Engineering

The department of Materials for Electrical Engineering is concerned with the development of new materials for nanopositioning, as well as the development of new metallisation materials for wide bandgap semiconductor contacts. Furthermore, this department focusses on the analysis of liquid metals and the development of new adaptive materials which have low or negative thermal coefficients. These materials are produced by sputtering of thin films or by electrochemical or electrophoresis methods. Samples of different materials, such as deposited layers and post annealed layers, are also provided from other groups of the university, as well as from industrial partners.

The main focus of this work is analysis with different methods:

- X-ray diffraction in different measurement setups
- X-ray fluorescence spectroscopy, X-ray imaging
- analytical scanning electron microscopy (ESEM, EDX, EBSD)
- analytical transmission electron microscopy (EDX, PEELS, diffraction, high resolution)
- atomic force microscopy
- different electrical methods
- thermo wave inspection system
- classical mechanical testing of materials

Faculty and Staff:

Prof. Dr.-Ing. Dr. rer. nat. Christian Knedlik
head of department
phone: -3611

Lothar Spieß
scientific coworker
phone: -3403

Volkmar Breternitz
scientific coworker
phone: -3134

Andrey Chuvilin
scientific coworker

Maik Gubisch
scientific coworker
phone: -3404

Ute Kaiser
scientific coworker

Thomas Kups
scientific coworker
phone: -3109

Henry Romanus
scientific coworker
phone: -3404

Friedhelm Scharmann
scientific coworker
phone: -3135

Björn Schwenke
scientific coworker

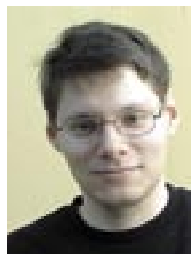

Johannes Biskupek
PhD student

Sören Selve
diploma student
phone: -3404

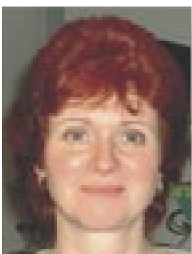

Elvira Remdt
technical coworker
phone: -3446

Jens Schawohl
technical coworker
phone: -3403

Contact:
Brigitte Weiß, phone: +49-(0)3677-69-3610
email: wet@tu-ilmenau.de

Technology

Department of Nanotechnology

Nanotechnology, "the manufacturing technology of the 21st century," should allow us to build a broad range of complex molecular machines (including, not incidentally, molecular computers). This technology will give us the means to build fleets of computer controlled molecular tools that are much smaller than a human cell. Such tools allow medicine, for the first time, to intervene at the cellular and molecular level in a sophisticated and controlled way. They could remove obstructions in the circulatory system, kill cancer cells, or take over the function of subcellular organelles. Just as today, we have the artificial heart, so in the future we may have the artificial cell.
Equally dramatic, Nanotechnology will give us new instruments to examine tissue in unprecedented detail. Sensors smaller than a cell would give us an inside and exquisitely precise look at ongoing cellular functions. Tissue that was either chemically fixed or flash frozen could be analyzed literally down to the molecular level, giving a completely detailed "snapshot" of cellular, subcellular, and molecular activities.
For this purpose, the Chair of Nanotechnology and his members are concentrating on the development of novel materials and nanostructures for electronic devices especially dedicated to sensor applications. Our research topics include hetero- and nanostructures for light detection, extremely light NanoElectroMechanical Systems (NEMS), and piezoelectric sensors for nanolitre droplets which are optimized for the detection of small organic systems such as viruses or single molecules.

Faculty and Staff:

Prof. Dr. rer. nat.
Oliver Ambacher
head of department
phone: -3723

Jörg Pezoldt
scientific coworker
phone: -3412

Majdeddin Ali
scientific coworker
phone: -1172

Maher Al Ibrahim
scientific coworker
phone: -3410

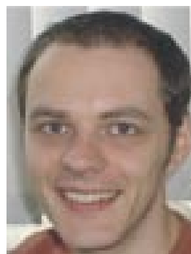

Carsten Buchheim
scientific coworker
phone: -3168 / -3210

Dorin Cengher
scientific coworker
phone: -3352

Genady Cherkashinin
scientific coworker
phone: -3352

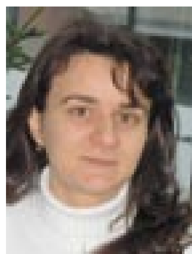

Irina Cimalla
scientific coworker
phone: -3352

Volker Cimalla
scientific coworker
phone: -3408

Gernot Ecke
scientific coworker
phone: -3407

Faculty and Staff:

Christian Förster
scientific coworker
phone: -3352

Ute Kaiser
scientific coworker

Gabriel Kittler
scientific coworker
phone: -1172

Vadim Lebedev
scientific coworker
phone: -3410

Ulrich Liebold
scientific coworker
phone: -2856

Armin Spitznas
scientific coworker
phone: -1172

Thomas Stauden
scientific coworker
phone: -3409

Ronny Wagner
scientific coworker

Petia Weih
scientific coworker

Charbel Zgheib
scientific coworker

Francisco Miguel Morales Sanchez
guest scientist
phone: -3418

Daniel Gäbler
diploma student
phone: -1172

Benedikt Lübbers
diploma student
phone: -1172

Merten Niebelschütz
diploma student
phone: -1549

Oliver Schulz
diploma student

Katja Tonisch
diploma student
phone: -3352

Faculty and Staff:

Chunyu Wang
diploma student
phone: -3409

Florentina Will
diploma student
phone: -3352

Ilona Marquardt
technical coworker
phone: -3407

Silvia Probst
technical coworker
phone: -3230

Dietmar Schäfer
technical coworker
phone: -3230

Willy Schliefke
technical coworker
phone: -3418

Jutta Uziel
technical coworker
phone: -3230

Contact:
Simone Gutsche, phone: +49-(0)3677-69-3724
email: simone.gutsche@tu-ilmenau.de

Department of Microsystems Technology

Microsystem technology combines actuators, sensors and electronic components with functional structures down to micron dimensions. Various principles from all areas of technology (mechanics, actuators, fluidics, optics, and chemistry) could be combined in these microsystems.

Microsystems technology is not limited to a special field of application. It is an enabling technology for new functions and properties for every kind of application which are not achievable through the conventional combination of macro components.

Technologies, such as ink jet printing, arrays and plates for microreactions, and micromixing have been technically realised only through the use of micron sized structures. These systems have begun to approach biological systems in their complexity. In the meantime, first principles of nature are integrated in microsystem devices.
The research in the department of Microsystems Technology is focussed on microfluidics, as well as sensors and actuators containing active piezo layers. The department of Microsystems Technology deals particularly with the outline, design, production and functional measurement of complex micro mechanical and micro fluidic systems. Through the integration of microsystem technology into the Faculty of Mechanical Engineering, there is a symbiosis between the classic disciplines and microsystems technology, this also influences the new field of mechatronics.

Since 1986 a group of experts has dealt with the development of micro components under the direction of Prof. Helmut Wurmus. In 2002 the department moved to the Center for Micro- and Nanotechnologies (ZMN).

Faculty and Staff:

Prof. Dr.-Ing.
Helmut Wurmus
head of department
phone: -2487

Sigmar Hecht
scientific coworker
phone: -2479

Arne Albrecht
scientific coworker
phone: -3426

Mathias Bründel
scientific coworker

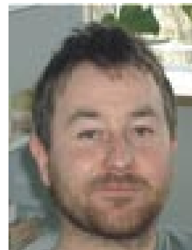

Jörg Burgold
scientific coworker

Tamas Fischl
scientific coworker
phone: -1295

Balázs Horváth
scientific coworker

Matthias Kallenbach
scientific coworker
phone: -3424

Faculty and Staff:

József Król
scientific coworker
phone: -1295

Mike Stubenrauch
scientific coworker
phone: -3422

Heike Bartsch de Torres
scientific coworker
phone: -3424

Frank Weise
scientific coworker
phone: -3423

Julian Botiov
PhD-student

Ole Nagel
diploma student
phone: -3422

Christoph Kremin
diploma student
phone: -3425

Katarina Lilienthal
diploma student
phone: -3424

Sebastian Stoebenau
diploma student
phone: -1806

Lothar Dressler
technical coworker
phone: -3421

Karin Friedel
technical coworker
phone: -3421

Gabriele Harnisch
technical coworker
phone: -3422

Birgitt Hartmann
technical coworker
phone: -3426

Christine Lohmann
technical coworker
phone: -3425

Contact:
Annette Volk, phone: +49-(0)3677-69-2485
email: annette.volk@tu-ilmenau.de

Design

Department of Design and Technology of Electronic Components

Research in the department of Design and Technology of Electronic Components is focused on Computer Aided Design (CAD) of thick film hybrid components including the simulation of thermal behaviour. This work includes the simulation of frequency and time domain behaviour of solid and gridded reference power/ground planes in Low Temperature Cofired Ceramics (LTCC) modules. Available software includes an extensive Computer Aided Engineering (CAE) system from Mentor Graphics® installed on a SUN compute server system.

Other topics include the development of new technologies and materials for environmental friendly production, as well as easy to recycle electronic devices and assemblies.

The laboratories of this group establish an interesting connection with the Microperipheric group (also in the ZMN) which provides technological equipment for production of Printed Circuit Boards (PCB) and LTCC modules. Furthermore, modern analytic facilities at the ZMN allow testing by ultrasonic and X-ray inspection systems.

Faculty and Staff:

Prof. Dr.-Ing.
Gert Winkler
head of department
phone: -2606

Gernot Bischoff
scientific coworker
phone: -1116

Aneta Sutor
scientific coworker
phone: -1119

Thorsten Mülln
scientific coworker
phone: -1118

Ashraf Mokayyes
scientific coworker
phone: -1118

Contact:
Regina Simon, phone: +49-(0)3677-69-2604
email: regina.simon@tu-ilmenau.de

Devices

Department of Solid-State Electronics

The research projects of the department of Solid-State Electronics are focussed on the development and investigation of advanced semiconductor devices. The department consists of four research groups dealing with:

- Polymer devices (organic field-effect transistors, new organic materials for electron devices),
- RF and nanodevices (nanometer MOSFETs, SiGe HBTs, wide bandgap devices),
- Power electronics (IGBTs, reliability issues, control circuits),
- Sensors.

The work of the four groups includes the investigation of basic operation principles, device simulation, device design and optimisation, fabrication, and characterisation. Polymer and wide bandgap devices are fabricated in-house, while other devices, such as SiGe HBTs, are fabricated in the facilities of partners in the semiconductor industry. The research projects of the department are supported by the European Community, German federal agencies (BMBF, DFG), the Federal State of Thuringia, and by industry (e.g. Semicron, Atmel).

Faculty and Staff:

Susanne Scheinert
provisional head of department
phone: -3222

Frank Schwierz
scientific coworker
phone: -3120

Ali Chaybon
scientific coworker
phone: -1589

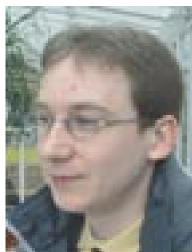

Frank Haase
scientific coworker

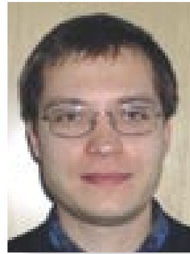

Andrei Herasimovich
scientific coworker
phone: -3406

Ingo Hörselmann
scientific coworker
phone: -3406

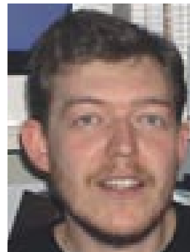

Mario Kittler
scientific coworker
phone: -1550

Christian Fachmann
scientific coworker

Theodor Doll
guest scientist

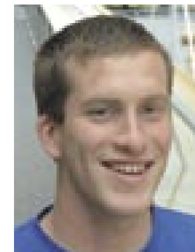

Jochen Weber
diploma student
phone : -3406

Gundis Bauer
technical coworker
phone: -3423

Silvia Klaube
technical coworker
phone: -3222

Contact:
Silvia Herda, phone: +49-(0)3677-69-3717
email: silvia.herda@tu-ilmenau.de

Modules

Department of Microperipherics

The department of Microperipherics covers the field of assembling and connecting technologies, especially thick film and LTCC-hybrid technology.
The main focus is the calculation and modelling of lumped passive elements and transmission line devices. Other fields of activity are the verification of models and the process optimisation.

The laboratories are located at the Center of Micro- and Nanotechnologies (ZMN). The whole equipment for design, screen printing, tape punching, lamination, firing and assembling of PCBs, Thick Film and Low Temperature Cofire Cermic (LTCC)- hybrid circuits and -modules is available there.

Manufacturing of complex microelectronic systems requires hybrid technologies of components, which cannot be integrated into the semiconductor chip by monolithic methods. (MCMs, packages, MST-devices).

The LTCC- (Low Temperature Cofired Ceramics-) technology offers new solutions by a variety of materials (tapes, inks) and a nearly unlimited number of layers.

In addition, LTCC offers possibilities to handle high power dissipation, 3D constructions, microwave applications and better EMC-behaviour. Furthermore, new solutions for sensor and mechatronic applications are thinkable.

Main research topics:

- Integration of buried passive elements, packaging, multilayer and multi chip technologies, RF- and microwave circuits
- characterisation of materials, surface and 3D analysis
- Integration of new materials (e.g. ferrite, high k and low loss dielectrics, high temperature conductivity and PZT). Characterisation of material parameters up to higher limits than provided by suppliers (in view of working temperature, frequencies, environmental pollution conditions, stress or others).
- Optimisation of technologies and process parameters for special applications
- Developing of LTCC technology for integration of sensors, micro optical elements, microacoustic and microfluidic elements to very complex microsytems
- Developing of more exact simulation tools for such new complex modules.

Faculty and Staff:

Prof. Dr.-Ing.
Heiko Thust
head of department
phone: -2605

Karl-Heinz Drüe
scientific coworker
phone: -3429

Waleed Ehrhardt
scientific coworker
phone: -1117

Michael Hintz
scientific coworker
phone: -3430

Ralph Münnich
scientific coworker

Markus Noren
scientific coworker

Ruben Perrone
scientific coworker
phone: -3452

Torsten Theleman
scientific coworker
phone: -1118

Faculty and Staff:

Elisa Morillas
guest scientist

Dorothea Förster
diploma student
phone : -3428

Uwe Genatis
technical coworker
phone: -3427

Ina Koch
technical coworker
phone: -3455

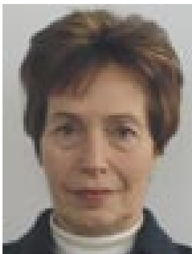

Regina Lenk
technical coworker
phone: -3440

Martina Sieler
technical coworker
phone: -3428

Contact:
Regina Simon, phone: +49-(0)3677-69-2604
email: regina.simon@tu-ilmenau.de

Systems

Department of Process Measurement

The department of Process Measurement, together with the department of Mechanical Engineering Measurement and Production Measurement, forms the institute of Process Measurement and Sensor Technology. At the Technical University of Ilmenau, this institute is in charge of teaching instruction in the areas of process measurement, production measurement, sensor technology for automation engineering, computer-aided processing of measuring values, measurement dynamics, laser and precision measurement, analysis and environmental measurement, and calibration techniques. The institute fulfils its teaching assignments not only in the stage-I- and stage-II-studies for the Faculties of Mechanical Engineering, Electrical Engineering and Information Technology, Computer Science and Automation as well as Business Administration, but it is also responsible for academic training in the branch of study entitled "Process Measurement and Sensor Technology". The highly qualified and practical-oriented training of students is based on extensive research in cooperation with a number of partners from the industry, as well as the BMBF (Federal Ministry of Education and Research), the DFG (German Science Foundation), and the Thuringian Ministry of Culture.

Faculty and Staff:

Prof. Dr.-Ing.
Gerd Jäger
head of department
phone: -2824

Eberhard Manske
scientific coworker
phone: -1250

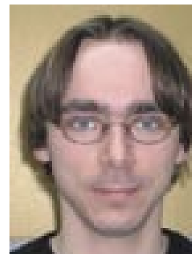

Rostyslav Mastylo
scientific coworker
phone: -1836

Without picture:

Norbert Hofmann
PhD student
phone: -5084

Contact:
Cordula Höring, phone: +49-(0)3677-69-2822
email: cordula.hoering@tu-ilmenau.de

Analytics

Department of Technical Physics

Surface phenomena play an increasingly important role in the age of miniaturisation and nanotechnology. The Department of Technical Physics is involved in research and teaching in numerous areas of surface science, such as functional biointerfaces, surface functionalisation, semiconducting surfaces, and tribology using advanced surface analytical techniques.

The main focus of this research is to investigate the possibilities of controlling the fundamental elements of condensed matter on an atomic scale: atoms and molecules on solid surfaces. The concept of "customised" materials plays an important role in the optimisation of the performance of electronic, optoelectronic, and mechanic devices.

The ability to produce structures atom by atom or molecule by molecule would allow the creation of a large array of specialised materials and functional structures; this is the long-term goal of nanotechnology. It is already possible to manipulate single atoms, for example by using the tip of a scanning tunnelling microscope to influence the position of adsorbed atoms or to investigate chemical reactions of single molecules. The full potential of surface sensitive techniques offers promising possibilities for future research. In this context, our group investigates organic-inorganic interfaces, the mechanical contact between macroscopic and microscopic solid surfaces (including biological systems), as well as the growth and characterisation of carbon layers, specifically C_{60}-molecules and carbon nanotubes.
Another focus of our group's research is the growth and characterisation of compound semiconductors such as silicon carbide and the group III-nitrides. These materials show promise for use as high temperature and high frequency electronic devices for sensor applications. Furthermore, electrical contacts (such as those based on metal carbides) and epitaxially grown insulating layers have a strong influence on device performance.

Research in tribology covers three major areas: Tribology of nanopositioning (friction, wear and lubrication of bearings and couplings used in nanopositioning), Microtribology (adhesion, friction and lubrication of the Micro-Electro-Mechanical Systems), and Tribochemistry (interaction of lubricants and lubricant additives with contacting surfaces).

Additionally, several analytical measurements are performed by our group within collaborative studies with a variety of researchers inside and outside the TU Ilmenau, as well as for companies.

Research topics:
- Processing of ultrathin layers
- Surface and interface properties on an atomic scale
- Structural, electronic and vibronic properties of semiconductors: SiC, InP, and group III-nitrides
- Doping profiles in semiconductors
- Structure formation of organic layers
- C_{60}, nanotubes, nanowires
- Interaction of hydrogen with silicon surfaces
- Tribology of nanopositioning
- Microtribology
- Tribochemistry
- Technical properties of fluorescent lamps

Faculty and Staff:

Prof. Dr. rer. nat.
Jürgen A. Schäfer
head of department
phone: -3609

Stefan Krischok
scientific coworker
phone: -3405

Falko Baier
scientific coworker

Maxim Eremtchenko
scientific coworker
phone: -3712

Wolfram Hild
scientific coworker
phone: -3782

Marcel Himmerlich
diploma student
phone: -3417

Yonghe Liu
scientific coworker
phone: - 5074

Rolf Öttking
scientific coworker
phone: -3215

Vasil Yanev
scientific coworker
phone: -3417

Matthew Zeman
guest scientist

Annette Läffert
technical coworker
phone: -3417

Contact:
Jana Spindler,
phone: +49-(0)3677-69-3608
email: jana.spindler@tu-ilmenau.de

Infrastructure and Equipment

The science center, which holds an overall laboratory space of more than 1000 m², hosts a clean room facility of about 700 m² with various clean room classes. While about 400 m² are classified as clean room class 10,000, the remaining space of 300 m² is classified as class 1,000 or even as low as class 100 in the lithography area.
Outside the clean room there are facilities for different technologies, such as the printing of circuit boards, a laser lab for the trimming and cutting of specimens addressing the packaging applications of devices, and the central application lab which addresses the construction of large and sophisticated complete systems. Furthermore, analytical devices on the nanoscopic scale which require a very low level of vibration are located in the basement of the building.

Technological labs and equipments inside the clean room:

Polymer electronics lab

Evaporation system (Edwards Auto 306)

Glove box used for preparation of polymer films (Braun)

Mask aligner (JUB 2104 Elektromat)

Spin coater (Convac)

Glove-Box

Thin film measurement lab

Optical surface profiler (UBM, UBC 16)
Measurement system for degradation of conductive layers (Karl Süss)
Div. microscopes (Leitz, Zeiss)
Ellipsometer (SD 2300 - Plasmos)
Stress measurement system (TENCOR)
Tactile surface profiler (Ambios Technology)
Film thickness measurement system (Mister)

Optical lithography lab

Anodic bonding tool EV501 (EVG)

Automatic spin coater CEE 4000 (Brewer Science)

Double side mask aligner AL6-2 (EVG)

Semiautomatic spin coater CEE CB100 (Brewer Science)

Spray developer Delta 20 (BLE)

Mask cleaning system (Hamatech) **new**

E-beam lithography system RAITH 150 **new**

Double side mask aligner

Electron beam lithography

Ellipsometer

Wet chemical processes lab

Quick dump rinser

Rinser-dryer (Semitool)

RCA cleaning process

Wet benches for several wet chemical etching processes (Kufner)
(metals, metal oxides, silicon, SiO_2, Si_3N_4 ....)

Wetbench

PVD/RIE lab
(physical vapor deposition / reactive ion etching)

Simple evaporation system for metallic layers (Edwards Auto 306)

Cluster system with ISE, sputtering chamber for metals, e-beam evaporation system (Ardenne LES 250)

Cluster system Ardenne

Cool sputtering system for preparation of SEM samples (Emitec)

ECR dry etching process for silicon carbide (Balzers PLS 500)

ICP dry etching process for silicon (STS - ASE)

Leybold sputtering system (LAB 500)

PECVD system for SiO_2 and Si_3N_4 (STS 310 PC)

Plasma stripper for resists removal (TEPLA 200)

Scanning microscope (Hitachi SD 2700)

RIE dry etching process for SiO_2 and Si_3N_4 (STS 320 PC)

RTP system (Jipelec)

Sputtering system for tungsten carbide und silicide (Ardenne LA 440)

Sputtering system for ZnO-films (Nordiko 2000)

ICP chlorine based dry etching process for GaN (STS-ICP) **new**

RIE chlorine based dry etching process for Al (Alcatel RDE300) **new**

Sputtering system Ardenne

High temperature processing lab

Atmospheric oxidation system for silicon substrates (wet oxide)

4-stock LPCVD system for Si_3N_4, TEOS, poly-Si, doped poly-Si (Tempress Systems)

2- reactor MOCVD system for GaN, AlGaN, AlN and metal oxides like ZnO (Aixtron) **new**

MOCVD system

4-stock LPCVD system

Mounting technologies lab III
(mounting and connection technologies)

Cyberscan

Hole punch for LTCC tapes (PTC)

Isostatic press

Screen exposure system

Screen printer (EKRA)

Screen washing system

Annealing systems (ATV)

Via filling system

Cyberscan

MBE/Surface analytics lab
(Molecular beam epitaxy)

MBE system for SiC, GaN, InN, AlN (Balzers UMS 500)

Surface analytic module with several technologies (OMICRON) (STM, AFM, XPS, UPS, AES, RHEED, PEEM, EELS, MBE)

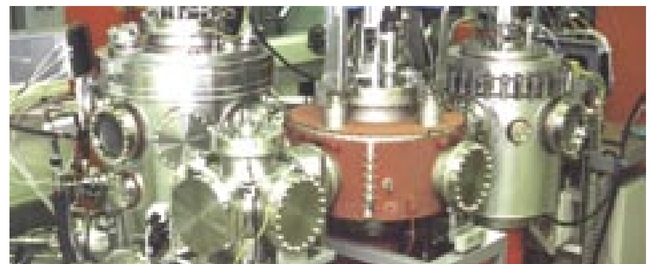

MBE system, detail

Surface analytic module, detail

Solid state analytics lab

Auger electron spectroscopy (AES)
(VG scientific 350) **new**

Photothermical deflection spectroscopy (PDS)

IR ellipsometer (Sentec)

Auger electron spectroscopy (AES)

Electrical characterisation lab

Measurement system for gas sensors

Hall measurement system (Agilent)

Wafer probe station with HP-tools for electrical characterisation (Agilent)

Waferprober

Backend technology lab
(lab for electronics and testing)

Dicing saw DAD-2H/6T (Disco)

Chemical mechanical polishing system PM5 (Logitec)

Wet bench for sample preparation

Mass spectrometer for liquid samples new

Dicing saw

Chemical mechanical polishing

Technological labs outside the clean room

Mounting technologies lab I
(mounting and connection technologies)

Heating press (Schmidt)

NdYAG laser (LPKF)

SMD mounting system

Annealing system (ATV)

Trimming laser system (Aurel)

NdYAG laser

Mounting technologies lab II
(mounting and connection technologies)

Die bonding system (Delvotec)

Wire bonding system (Delvotec)

Fine placer for SMD components

SMD soldering station

Ultrasonic measurement system (Sonoscan)

Wedge bonding system (Delvotec)

Ultrasonic measurement system

X-Ray analytics lab

X-ray diffractometers (Siemens)

X-ray analytics (Feinfocus)

HRX-ray diffractometer (Bruker AXS D8) **new**

X-ray diffractometer

Nanomeasurement technology lab

Nanopositioning and nanomeasurement machine (SIOS)

Vibration free lab benches

Interferometer for surface analysis

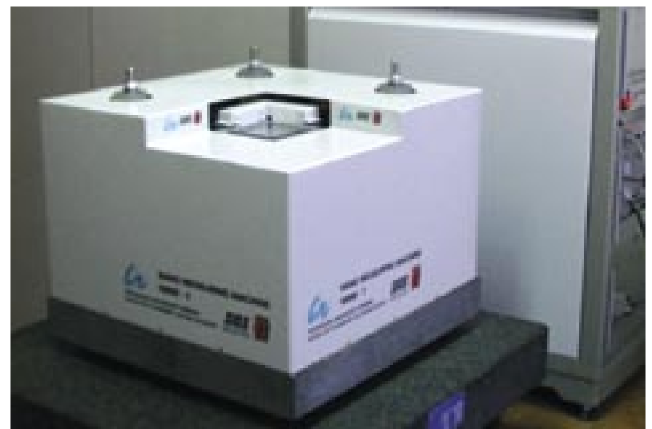

Nanopositioning and nanomeasurement machine

Electron microscopy lab
(transmission and scanning electron microscopy)

Atomic force microscope

Transmission electron microscope
(Phillips TECNAI)

Scanning electron microscope
(Phillips FEI)

Focussed ion beam system
(Phillips FEI, single beam) **new**

Sample preparation for TEM/REM
(Gatan)

Transmission electron microscope

Scanning electron microscope

Fluidics and bionics lab

Surface tension measurement system (Krüss)

Tribometer (Tetra)

Viscometer

Glove box for experiments with biological or chemical samples (Ganuk)

Laminar flow box (Ganuk)

Dosing systems for liquids

Advalytix system to manipulate liquid volumes ranging from picoliters to microliters **new**

Finances

The basic funding for the ZMN is provided by the Technical University of Ilmenau. This covers the costs for the basic operation of the building and the equipment contained within. The total income for ZMN operation amounts to 21,000 €. This funding comes from the following agencies: 7,000 € from the central funding of the university, 7,000 € from the different faculties, and the final 7,000 € is provided by the chairs active in the center. The specific expenditures are listed in detail in Fig. 1.

Research costs are solely provided by a third means, i.e. external funding such as e.g. federal or state government or industry. They amount to 8.4 Mio € in 2004. Fig. 2 gives an overview of the different sources for the year of 2004.

The development of the overall financial volume of the research projects in the time period of 2002 – 2004 is plotted in Fig. 3.

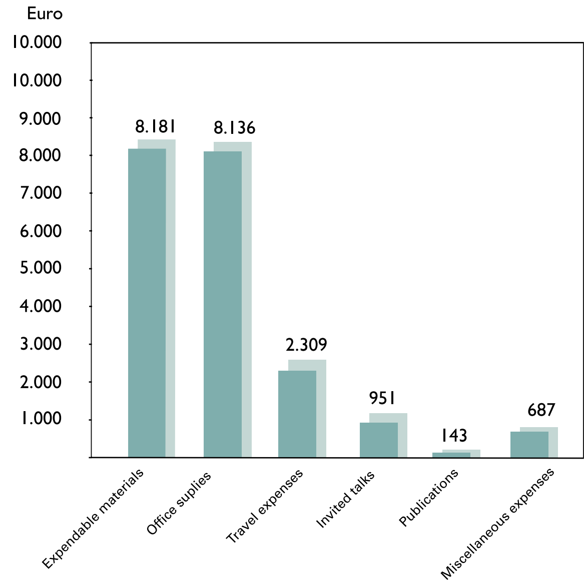

Fig. 1: Household expenses of the ZMN in the year 2004

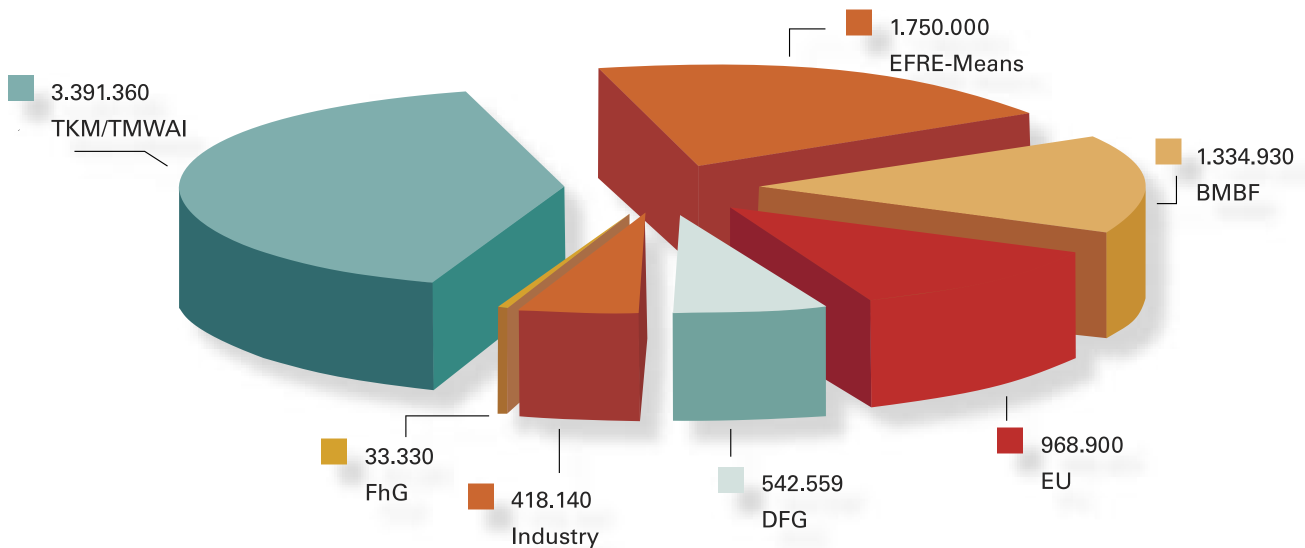

Fig. 2: Current research projects in the year 2004

BMBF	*Federal Ministry of Education and Research*
DFG	*German Science Foundation*
EFRE	*European Fond for Regional Development*
EU	*European Union*
FhG	*Fraunhofer-Gesellschaft*
TKM/TMWAI	*Thuringian Ministries*

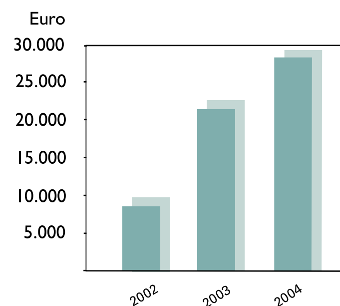

Fig. 3: - Research project development 2002-2004

Electronic structure of the energy gap in hydrogenated amorphous carbon.

G.Yu. Cherkashinin[1,*], Th. Schieffer[2], J. Pezoldt[1], and O. Ambacher[1]
[1] Department of Nanotechnology
[2] Infineon Technologies, Austria

Hydrogenated amorphous carbon (a-C:H) films have attracted considerable attention due to their wide range of technology uses. By changing the deposition parameters via different ion impact energies and the use of certain precursor gases properties of a-C:H can be gradually changed from soft polymer-like films to hard diamond-like carbon (DLC) films. DLC films are covering an extending field application, for example, as passivation layers on semiconductor devices.
Photothermal deflection spectroscopy (PDS) in combination with optical transmission (OT) is useful instrument to probe electronic structure of the hydrogenated amorphous carbon. The attractive feature of PDS is its extremely sensitivity. Absorbance as low as $\alpha d \approx 10^{-5}$ can be detected. It makes attractive to use PDS for monitoring the electronic states localized into gap.

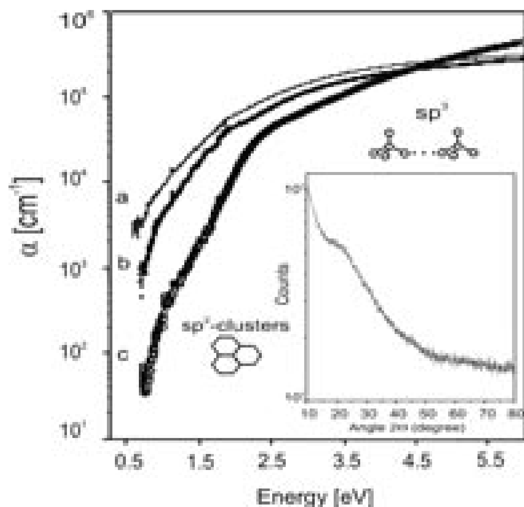

Fig. 1: Absorption spectra of a-C:H (a,b) and a-$C_{1-x}Si_x$:H (c) films grown at the different bias voltage. Insert: X-ray diffraction of a-C:H film; no peaks characteristic for diamond or nano-diamond are observed in the XRD pattern.

<u>A role of hydrogen:</u> Hydrogen saturates free sp^3 bonding orbitales and distorts π-bonded pairs resulting in reduce of the size and concentration of the sp^2 bonded carbon clusters. It gives rise to decrease of concentration of the localized electron states into bandgap, on the one hand, and increase of the band gap, on the other hand. Fig.1 shows the absorption spectra of the three DLC films deposited on the quartz substrates under the different conditions.

Enhanced absorption observed in low energy region of the spectrum, Fig. 1a, is due to the increasing of the density of localized states into the gap: higher impact energies lead to the hydrogen involving from the microstructure of DLC films. The decrease of absorbance observed for the DLC films grown at lower impact energies (Fig. 1b) is, in the first place, due to hydrogen induced defect compensation in hydrogenated amorphous carbon.
<u>A role of silicon:</u> Silicon substitutes carbon atoms in the network and always results in Si atoms being fourfold-coordinated independent on the initial configuration. Incorporation of Si induces the decreasing the fractions of the sp^2 hybridized ring structure and promotes the sp^3 hybridized bond. Essential decrease of absorbance in low energy region of a-$C_{1-x}Si_x$:H, Fig.1c, is due to predominance of the sp^3 phase compared to a-C:H films, Fig. 1(a,b), where absorption is significantly influenced by a range of sp^2 cluster sizes.
<u>The width of band</u> gap is controlled by π-π* states that are within the σ-σ* gap. Therefore, optical properties can be managed by the sp^2/sp^3 ratio. The Tauc band gap, E_{Tauc}, corresponds to optical

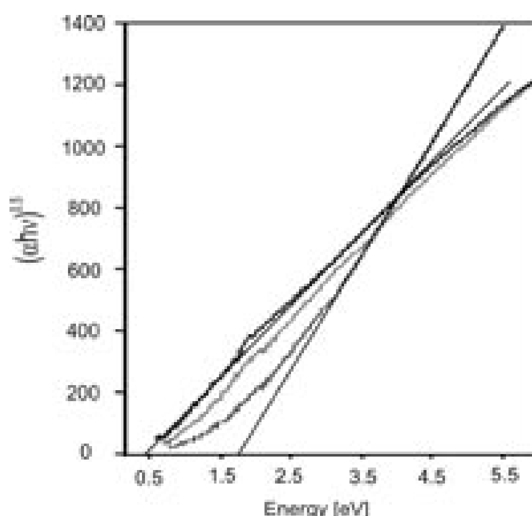

Fig. 2: The Tauc plot: the E_{Tauc} gap determined by the linear interpolation varies from 0.43 and 0.69 eV for a-C:H films grown at 700 and 570 V bias voltage, respectively, up to 1.71 eV for a-$C_{1-x}Si_x$:H (570 V).

* phone: +49-(0)3677-3352, e-mail: genadey.cherkashinin@tu-ilmenau.de

transitions between extended states [1]. In the absence of disorder, the E_{Tauc} is given by the separation between the π-π^* bands ($2E_\pi$). The larger the average size of the sp^2 cluster, the smaller Tauc gap. Fig. 2 demonstrates the influence of the growth conditions on the optical band gap: the width of the gap increases with decreasing value of bias voltage. In the case of the a-$C_{1-x}Si_x$:H films, the increase of the band gap is due to both (i) the increase of the concentration of four-fold coordinated bonds due to silicon incorporation in the network and (ii) atomic hydrogen etching of sp^2 clusters. The estimated E_{Tauc} values for the non-doped a-C:H films indicate rather the DLC nature of a-C:H films than polymer-like one (see Tab. 1). Fig. 3a illustrates decreasing E_{Tauc} as sp^2 fraction increases.

Disorder: the structural and topological ones are associated with the bond-angle distortions within each sp^2 cluster and with size of sp^2 formed clusters, respectively [2]. Not saturated sp^3 sites also induce disorder. The Urbach energy, E_{urb}, is interpreted as a measure of an inhomogeneous disorder associated with different sp^2 cluster sizes and related to the transitions between the extended-to-localized states. Fig. 3b shows the fitting of the absorption spectra plotted in the $\ln(\alpha/\alpha_0)$ vs E scale to determine the E_{urb}. There is a strong correlation between the growth conditions of the DLC films and the E_{urb} magnitude. Fig. 3c shows that the values of the E_{urb} vs E_{Tauc} are grouping at the three sub-groups each of which corresponds to the definite kind of the DLC films. By analysing of each group we can conclude that the E_{urb} decreases as the optical gap increases. By speaking in the disorder terms, the least disorder is characteristic for the a-$C_{1-x}Si_x$:H films, where E_{urb} lies in the 248÷297 meV diapason depending on the film thickness, while the largest one corresponds to the a-C:H films grown at high bias voltage. The Table I sums the values of the E_{urb} as a function of the film thickness, the applied voltage and the optical gap.

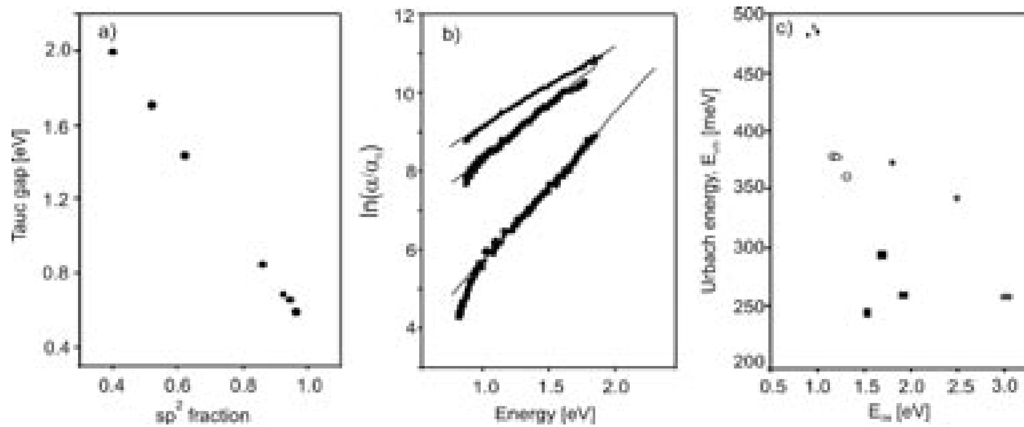

Fig. 3: a) Optical gap versus sp^2 content in a-C:H and a-Si:C:H films (sp^2 content was estimated as E_{Tauc}=3-2.5z, where z is sp^2 content); b) The E_{Urb} estimated as the inverse slope of the fitted line for a-C:H (top and middle) and a-Si:C:H (bottom) films grown at 700 V (top) and 570 V (middle and bottom, respectively; c) The E_{Urb} vs optical gap for a set of the DLC films of the different thickness: cross are a-C:H (700 V), circles are a-C:H (570 V), squares are a-$C_{1-x}Si_x$:H (570 V). The stars are the a-C:H data taken from the work [3].

Tab. 1: The characteristic of the a-C:H and a-$C_{1-x}Si_x$:H films.

Film no.	*Precursor CH_4*	*flow in sccm SiH_4*	*thickness (±15%)in nm*	*neg. DC-bias (V) (±15%)*	*E_{Urb} (meV)*	*E_{04} (eV)*	*E_{Tauc} (eV)*
DLC 00	100		125	570	364±16	1.3	0.86
DLC 01	100		80	570	381±17	1.2	0.69
DLC02	100		30	570	382±55	1.16	0.66
DLCSi1	90	10	145	570	263±13	1.91	2.0
DLCSi2	90	10	90	570	297±29	1.68	1.71
DLCSi3	90	10	25	570	248±20	1.52	1.44
DLC20	100		120	700	487±29	1.0	0.85
DLC21	100		80	700	484±36	0.89	0.43
DLC22	100		30	700	491±39	0.95	0.59

We would like to acknowledge for financial support by the EU project "FLASIC." (G5RD-CT – 2002- 00704).

[1]. J.Tauc in Amorphous and Liquid Semiconductors, ed. by J.Tauc (Plenum London, 1974), Chap.4.
[2]. J.Robertson, Sem.Sci.Tech, **18**, 512 (2003).
[3]. G.Fanchini, A.Tagliaferro, Appl.Phys.Lett., **85**, 730 (2004).

Growth of 3D nanoclusters modelled by KMC

A.A. Schmidt[1], V.S. Kharlamov[1], K.L. Safonov[1], Yu.V. Trushin[1], E.E. Zhurkin[2], and J. Pezoldt[3,*]
[1] A.F. Ioffe Physico-Technical Institute, Russian Federation
[2] St. Petersburg State Polytechnic University, Russian Federation
[3] Department of Nanotechnology

The formation of silicon carbide heterostrucutres containing nanosized SiC-Si clusters on silicon substrates provides a variety of possible applications such as tunneling barriers, heterostructures and antidot structures that could be used as nonlinear scattering centers for two-dimensional electron gas near the surface. SiC has also a number of specific properties, such as high thermal stability and thermal conductivity, breakdown field, carrier saturation velocity, the harsh environments tolerance, high-power and high-frequency operation capability. Thus the attempt to integrate of the SiC-based devices directly into the silicon technology can lead to add on effects if novel nano- and optoelectronic devices are required.

The most suitable technique for the formation of nano-scale SiC on Si is the deposition of carbon on silicon in a ultra high vacuum environment by using solid source molecular beam epitaxy (SSMBE) of C atoms. At different growth temperatures and approximately the same carbon rates and deposition times two principally different clusters nucleation modes were found and two- and three-dimensional SiC clusters were observed [1, 2].

Nowadays different numerical schemes for the simulation of epitaxial growth processes such as different type of rate equation methods [3], discrete Monte Carlo [4], molecular dynamics [5] and *ab initio* [6] methods alongside with the more rare level set approach [7] and continuum Monte Carlo [8] are used. The lattice kinetic Monte Carlo (KMC) method was chosen for the numerical simulation of the cluster growth process, because this method allows to simulate the evolution of a relatively large substrate over a sufficiently long time providing atomic scale precision data on the surface morphology. Previously two-dimensional KMC model was applied to study the low-temperature growth mode of SiC on Si [2] and proper cluster surface concentration and size distribution function were obtained. Nevertheless, a purely two-dimensional model appears to be inappropriate at the temperatures higher then 660°C or in case of a high carbon deposition rate. Thus more general, an essentially three-dimensional model should be developed.

At the early stage of the SiC growth the clusters tend to nucleate coherently to the substrate and so it is reasonable to use a diamond-like lattice with a silicon lattice constant. Si and C atoms occupy some sites of the lattice and the rest are considered as empty virtual sites. Si and C atoms are allowed to jump to the nearest or next to the nearest empty sites. The hop probability depends on the environment of a given atom. For this reason the interaction with atoms in two first coordination spheres was taken into account. Besides the diffusion the deposition events take place according to the carbon atom flux. The diffusion probabilities for the atoms in the system are given by Arrhenius law:

$$P_{diff} = \nu \exp\left(\frac{-E_a}{kT}\right),$$

where ν is a characteristic Debye frequency, T is a substrate temperature. The activation energy of the diffusion of carbon and silicon atoms are given by:

$$E_a^C = \sum_{\substack{1st\,coord.\\sphere}} E^1_{Si-C} + \sum_{\substack{1st\,coord.\\sphere}} E^1_{C-C} + \sum_{\substack{2nd\,coord.\\sphere}} E^2_{Si-C} + \sum_{\substack{2nd\,coord.\\sphere}} E^2_{C-C}$$

$$E_a^{Si} = \sum_{\substack{1st\,coord.\\sphere}} E^1_{Si-C} + \sum_{\substack{1st\,coord.\\sphere}} E^1_{Si-Si} + \sum_{\substack{2nd\,coord.\\sphere}} E^2_{Si-C} + \sum_{\substack{2nd\,coord.\\sphere}} E^2_{Si-Si}$$

Here E_{Si-Si}, E_{C-C} and E_{Si-C} are the effective binding energies for silicon-silicon, carbon-carbon and silicon-carbon atom pairs, respectively, and the upper index denotes the coordination sphere number. The deposition probability is defined by $P_{dep} = \frac{1}{FS} n_{free}$,

where F is the carbon flux, S is the simulation cell area and n_{free} is the number of sites at the surface suitable for the deposition.

The influence of strain on the cluster growth mode was taken into to account by assuming that the effective strain created by each layer is proportional to the number of SiC molecules incorporated in the layer: $E^i_a = k\theta_i^2 N_i$, where k – is effective spring constant, θ_i is an effective misfit in the *i*-th layer as described below, and N is the number of SiC molecules in the layer. Stacking faults are not taken

* phone : +49-(0)3677-69-3412, email: joerg.pezoldt@tu-ilmenau.de

into account, because simulations with excluded strain effects had shown that grown structure is very close to the pure SiC. The effective misfit decreases exponentially with the layer number *i* according to:

$$\theta_i = \theta_0 \exp\left(-\frac{\Lambda(i-1)}{\sqrt{N_0}}\right)$$

where θ_0 is initial misfit between Si and SiC, Λ is a fitting parameter chosen equal to $3\pi/2$ and N_0 is the number of SiC molecules forming the first layer of the cluster. Strain decreases linearly from its maximum value E^i_m and affects all sites of the *i*-th layer within the radius of $\sqrt{N_i}$ sites away from the cluster edge.

According to MD results the binding energies were cho-sen as follows: E^1_{Si-C} = 0.7 eV, E^1_{C-C} = 0.3 eV, E^1_{Si-Si} = 0.2 eV, E^2_{Si-C} = 0.05 eV, E^2_{C-C} = 0.07 eV, E^2_{Si-Si} = 0.06 eV. The higher binding energy for the next to the nearest atoms of the same type enhance the nucleation of SiC without stacking faults.

Fig. 1: Simulated Si-(111) surface after deposition of 4% of a C monolayer. Black and white spheres deno-te substrate atoms and vacancies created by thermal fluc-tuations, respectively. Grey spheres denote both Si and C atoms incorporated into the 2D clusters.

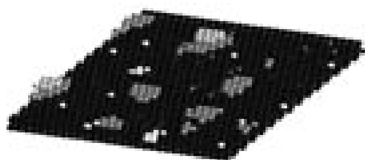

Fig. 2: Simulated Si-(111) surface after deposition of 12% of a C monolayer. Black and white spheres denote substrate atoms and vacancies created by thermal fluctuations, respectively. Dark grey spheres denote C atoms incorporated into the sub-strate. Atoms that are combined into the clusters are shown in light grey (lighter tint is used for upper cluster layers).

The successive snapshots of the silicon surface are shown on Fig. 1 and Fig. 2. At first one should mention, that at given deposition rates the D/F ratio (i.e. the ration between probability of the diffusion and deposition processes) for silicon atoms of the substrate is around 10^5, depending on the local environment. Thus some of silicon atoms leave the substrate and become highly mobile adatoms. The rate of this process increases rapidly, when surface pits start to be formed, because silicon atoms at the edges with their smaller coordination number are bounded weaker. At the same time deposited C adatoms tend to occupy sites at the substrate due to a strong nearest neighbour Si-C bonding. Such site occupation is energetically preferred and leads to the largest energy release in the system. Carbon atoms which could not be incorporated into the silicon substrate start to form 2D SiC clusters (see Fig. 1). These 2D clusters are converted during growth into 3D clusters when the lateral size and so the strain increases. In the present simulation the spring constant was chosen so that the 2D islands with bottom size larger than 50 atoms were energetically unfavourable. Fig. 2 shows two formed clusters with second and partially third double-layer.

A three-dimensional model of the SiC on Si heteroepitaxy process that includes effects of the strain caused by the lattice mismatch was developed. The first stages of the SiC nucleation were studied. All stages of the SiC formation on Si were reproduced in the simulation, i.e. the formation of a $Si_{1-x}C_x$ solid solution followed by the formation of small 2D and then 3D nuclei. Furthermore, the initial phase of the formation of voids in the substrate near the interface was demonstrated. Nevertheless, a relatively simple strain effect model was implemented, the computational resources demands drastically increased because the surface morphology changes affect the diffusion probabilities globally, and the lists of probabilities, that are used, should be significantly updated at each step. Thus for a large-scale simulation further improvements are necessary, e.g. the introduction of the parallel processing of the simulation events on a cluster-type supercomputer.

This work is supported by RFBR grant No. 02-02-17605 and the Russian government program for the support of the leading scientific schools No. 2160.2003.2 and by DAAD within the program "Internationale Qualitätsnetzwerke (IQN): Ilmenauer Koordinationszentrum".

[1] V. Cimalla, J. Pezoldt, Th. Stauden, A.A. Schmidt, K. Zekentes, and O. Ambacher, phys. stat. sol. c 1 (2004) 337.
[2] A.A. Schmidt, K.L. Safonov, Yu.V. Trushin, V. Cimalla, O. Ambacher, and J. Pezoldt, phys. stat. sol. a 201 (2004) 333.
[3] Yu.V. Trushin, Theory of Radiation Processes in Metal Solid Solutions, Nova Science Publish-ers, New York, 1996.
[4] A.C. Levi and M. Kotrla, J. Phys.: Cond. Matter 9 (1997) 299.
[5] P. Allen and D. Tildesley "Computer Simulation of Liquids", Clarendon Press, Oxford 1987.
[6] Y. Yoshimoto, M. Tsukada, Surf. Sci. 423 (1999) 32.
[7] M. Petersen, C. Ratsch, R.E. Caflisch, and A. Zangwill, Phys. Rev. E 64 (2001) 061602.
[8] G. Russo, L.M. Sander, P. Smereka, Phys. Rev. B 69 (2004) 121406(R).

Piezoelectric properties of thin AlN layers for MEMS applications

K. Tonisch[1,*], V. Cimalla[1], Ch. Foerster[1], V. Lebedev[1], D. Dontsov[2], and O. Ambacher[1]
[1] Department of Nanotechnology
[2] SIOS Meßtechnik GmbH, Ilmenau

Micromechanical resonators show significant promise for many sensor applications, including chemical and biological sensing, electrometry, and scanning probe techniques. In these applications, a change in mass, temperature, charge, or any other applied force induces a small shift in the resonance frequency of the oscillator [1]. Typically, resonators require both an actuation and a detection of the resonance frequency. Such responses can be observed through a variety of physical detection methods including electronic and optical effects, i.e. changes in resistance (piezoresistivity), changes in capacitance, and changes in charge (piezoelectricity) [2]. On the other hand, microactuators are usually based on electrostatic, piezoelectric, magnetic, thermal, and pneumatic forces. Although each application of MEMS requires a specific design to satisfy many constraints and conditions, piezoelectric-based MEMS are generally attractive due to their high sensitivity and low electrical noise in sensing applications and high-force output in actuation applications.
The exceptional properties of wide-bandgap III-V nitride semiconductors are promising for such applications. Among the nitrides AlN has the highest thermal conductivity at low temperature, good mechanical strength, high resistivity and corrosion resistance, and the largest piezoelectric coefficients [3]. Thus, AlN resonators are attractive building blocks for electromechanical devices on the micro- and nano scale. Usually, based on surface acoustic wave measurements, a strong c-axis orientation of the AlN is crucial for a high piezoelectric response of the thin film and all process optimization has been performed to achieve such structures. Unfortunately, epitaxial growth of AlN only occurs at high temperatures which make the epitaxial deposition incompatible for the integration in CMOS or other technologies sensitive to heat. Therefore much effort has been made to grow highly textured polycrystalline films with low temperature processes like reactive sputtering. In this work we will show by direct measurement of the piezoresponse in the picometer range that the acceptable tolerance in the crystal orientation is much larger than expected, which opens the way for low temperature integration of piezoelectric thin films into MEMS and NEMS.
AlN thin films of different structural quality have been prepared on conductive (111) silicon wafers by three different methods: (i) plasma induced molecular beam epitaxy (PIMBE), (ii) metalorganic chemical vapor deposition (MOCVD) and (iii) reactive sputtering. The resulting layers have been single crystalline in the case of the PIMBE, polycrystalline with different degree of texture in the case of MOCVD and nanocrystalline in the case of reactive sputtering. The layer thickness was between 100 and 250 nm.

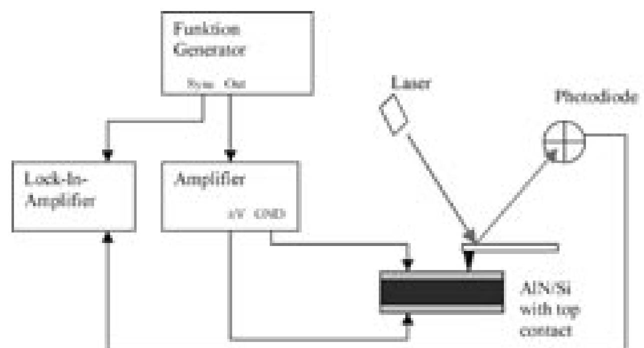

Fig. 1: Piezoelectric Force Microscopy set up to detect thin film expansion of about 10 pm.

For the measurements sputtered Ti/Au contacts were used as top electrodes, while silver glue served as back contact. The estimation of the piezoelectric constants has been performed by piezoelectric response force microscopy (PFM) and by optical interferometry. A modulation voltage is applied between the top electrode and the substrate, which causes the piezoelectric film to oscillate at the same frequency as the applied voltage. In PFM this bias-induced deformation is detected by a common silicon AFM-tip which is brought into contact with the surface of the metallic top electrode [4, 5]. When a modulation voltage is applied to the piezoelectric film, the vertical displacement of the tip follows accurately the piezoelectric motion of the sample surface. The piezoresponse is then detected as the first harmonic component of the deflection signal. Thus, the piezoelectric coefficient can be calculated as the ration between tip displacement Δt and applied

voltage V: $d_3 = \frac{\Delta S_3}{E_3} = \frac{\Delta t}{V}$,

with $\Delta S_3 = \Delta t/t$ is the change of strain along the c-axis and $E_3 = V/t$ the electric field along the c-axis. PFM measurements were performed with a commercial

* phone : +49-(0)3677-69-3352, email: katja.tonisch@stud.tu-ilmenau.de

AFM (ATOS Solver), a function generator (Agilent 33220 A) and a lock-in amplifier (Stanford Research Systems GS). A schematic of the experimental set up is shown in Fig. 1. A homodyne Michelson laser interferometer was used to complement the AFM technique [6].

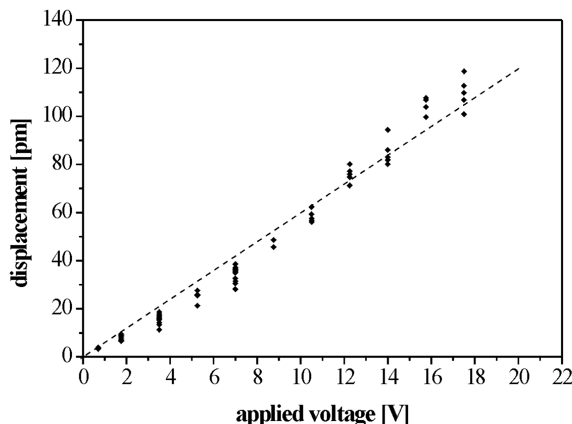

Fig. 2: Typical piezoelectric displacement vs. applied voltage estimated by PFM.

Fig. 2 shows the linear dependence of the displacement of the sample surface from the applied voltage measured at a sputtered aluminium nitride film. The calculation of the displacement versus applied voltage results in a piezoelectric coefficient of 5.36 ± 0.25 pm/V for AlN thin films prepared by both reactive sputtering and by MOCVD, and is in good accordance to reported values [5, 7].

Additional measurements using a homodyne Michelson interferometer supported the above obtained results. Here an integrated spectrum ranging from 5.5 to 22 kHz was recorded. An extract of the spectra for (a) a sputtered and (b) for a MOCVD-grown AlN film ranging from 17.5 to 19 kHz is provided in Fig. 3 and shows the vertical displacement of the sample surface due to the applied voltage of 14 V at a modulation frequency of 18.3 kHz.
The value of the measured piezoelectric coefficient was less affected by the structural quality than expected by other authors [8]. Mostly, the coupling factor k^2 which is measured via surface acoustic wave devices (SAW), is used as a parameter for the

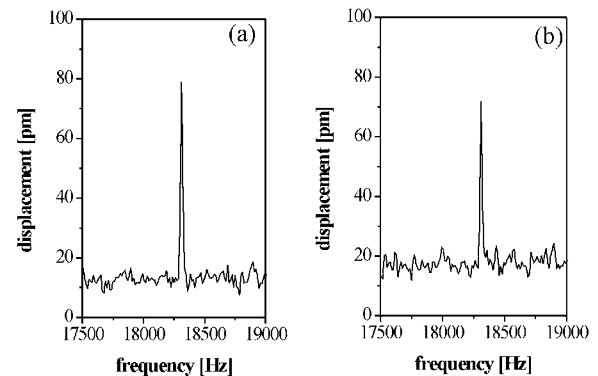

Fig. 3: Typical piezoelectric displacement vs. frequency estimated by optical interferometry for (a) sputtered AlN and (b) MOCVD-grown AlN.

piezoelectric response of thin films. But, while the coupling factor k^2 is reported to decrease dramatically for low degrees of texture [9], the piezoelectric coefficient d_{33} decreases only moderately and only for deviations from the c-axis orientation of about 10 degrees. The reason is that both the PFM method and interferometry are more direct approaches to the piezoelectric polarisation of the film than the analysis of surface acoustic waves is. Thus, though they may not be suited for SAW applications, defect-rich, low temperature grown AlN layers are well suited for piezoelectric applications, which opens the way for the design of advanced integrated MEMS and NEMS structures.

This work has been funded and supported by the Deutsche Forschungsgemeinschaft, SPP 1157: "Integrierte elektrokeramische Funktionsstrukturen", contract no. AM 105/2-1

[1] J. W. Gardner, V. K. Varadan, O. O. Awadelkarim; Microsensors MEMS and Smart Devices, Wiley 2001.
[2] Proc. Int. Conf. Solid State Sensors and Actuators, June 1997; Proc. IEEE Workshop Micro Electro Mechanical Systems, Heidelberg, 1998.
[3] O. Ambacher, J. Phys. D: Appl. Phys. 31 (1998) 2653-2710.
[4] B. J. Rodriguez, D. J. Kim, A. I. Kingon, R. J. Nemanich; Mater. Res. Soc. Symp. Proc. 693 (2002) I9.9.
[5] B. J. Rodriguez, A. Gruvermann, A. I. Kingon, R. J. Nemanich; Appl. Phys. Lett. 80 (2002) 4166-4168.
[6] D. Dontsov, G. Jäger, H. Büchner, U. Gerhardt; Proc. of the 5th Seminar on Quantitative Microscopy Nanoscale PtP-F-44 (2001) 166-173.
[7] I. L. Guy, S. Muensit, E. M. Goldys; Appl. Phys. Lett. 75 (1999) 4133-4135.
[8] R. S. Naik, J. J. Lutsky, R. Reif, C. G. Sodini, A. Becker, L. Fetter, H. Huggins, R. Miller, J. Pastalan, G. Rittenhouse, Y.-H. Wong; IEEE Transactions on Ultrasonics, Ferroelectrics and Frequency Control 47 (2000) 292-296.
[9] L. Vergara, M. Clement, E. Iborra, A. Sanz-Hervas, J. Garcia Lopez, Y. Morilla, J. Sangrador, M. A. Respaldiza, Diamond and Related Materials 13 (2004) 839-842.

SEM and EDX Analyses of Thin-film ITO and Diamond Micro-electrodes Modified by Mercury for the Use in Electrochemical Microsensors

V. Reháček[2], M. Gubisch[1], T. Vitek[2] I. Novotný[2], V. Breternitz[1], L. Spieß[1], H. Tippmann[1], V. Tvarožek[2], and Ch. Knedlik[1,*]

[1] Department of Materials for Electrical Engineering

[2] Department of Microelectronics, Slovac University of Technology, Bratislava, Slovac Republic

There are still increasing requirements for the detection and analysis of trace concentrations of heavy metals like Cu, Pb, and Cd in the world of environment, biochemistry and medicine. Therefore, sensor development in this area is pushed all over the world [1].

Indium-tin-oxide (ITO) thin-film layers are widely used, because of the low resistivity and high transmission of visible radiation. The application of ITO thin-film layers covered with mercury as an electrochemical sensor for detecting trace amounts of heavy metal concentrations is still unpublished. Bearing in mind that the first material for electrochemical sensing of heavy metal traces in solutions were made of polycrystalline diamond thin-film layers modified by mercury, this material was analysed for comparison, as well.

The modified ITO films are used as interdigitated structure in a microelectrode array designed for anodic stripping voltammetry (ASV) in aqueous solutions. ASV has proven to be a powerful tool for trace concentration analysis [2].

Because of its decisive importance for the operation of the sensor device, the morphology of the functional layers is studied in this work.

Experimental

The samples were analysed using the **E**nvironmental **S**canning **E**lectron **M**icroscope (ESEM) Philips XL30 working in ESEM mode in order to avoid complications arising from bad electric conductivity of specimens. **E**nergy **d**ispersive **X**-ray (EDX) analysis has been used to determine the predominant composition in the surface region.

Sample preparation

ITO thin films (thickness 600 nm) were deposited by reactive r.f. sputtering from a target composed of an oxide mixture (90 wt. % In_2O_3 and 10 wt. % SnO_2). Thermally oxidized (111)-Si wafers were used as substrates. The diamond layers (thickness 2 – 3 μm) were grown by CVD from methane and hydrogen (portions 2 % and 98 %, resp.). One part of the samples was terminated in oxygen plasma for 2 min. at room temperature, the second one in a hydrogen atmosphere for 3 h at 620°C.

The Hg deposition was carried out by electroplating in a three electrode setup at a constant electric potential in a solution of 0.01 M Hg^{2+} in 0.1 M KNO_3 as electrolyte.

RESULTS

ITO microelectrodes modified by Hg

The surface of a typical ITO thin-film electrode (diameter 40 μm) modified by Hg is shown in Fig. 1.

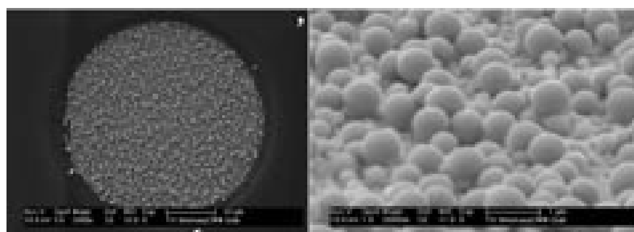

Fig. 1: SEM overview (left) and detail view (right) of an ITO thin-film microelectrode deposited with Hg, sample tilted 70° from horizontal plane, magnification 20,000x

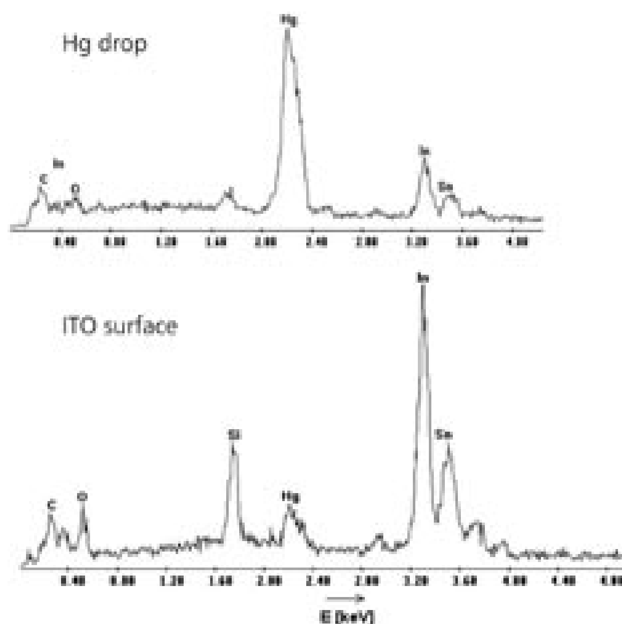

Fig. 2: EDX spectra comparing qualitatively the Hg micro-cluster (left) and an ITO film outside of it (right)

* phone : +49-(0)3677-69-3611, email: christian.knedlik@tu-ilmenau.de

As can be seen from the overview (Fig. 1, left) the surface is fairly studded by mercury, but the latter does not form a continuous film. The detail view (Fig. 1, right) shows that the mercury forms small circular islands with diameters mostly < 500 nm, max. approx. 800 nm.
The thickness and the ideal spherical shape of the Hg drops can be discerned from Fig. 1 (right). This behaviour of Hg to grow on ITO as spherical droplets is an evidence of a bad wetting caused by the high surface tension of mercury, as well as by the high interface tension of the contact area between Hg and ITO. This fact is confirmed by the EDX analysis (see Fig. 2).

Diamond layers terminated in O_2 plasma
Fig. 3 illustrates the morphology of mercury deposited on a diamond film terminated in oxygen plasma. We find almost the same situation as in the case of ITO. The deposited mercury exists as isolated islands. The size ranges from very small droplets (diameter « 1μm) to micro-clusters with diameters up to 20 μm.

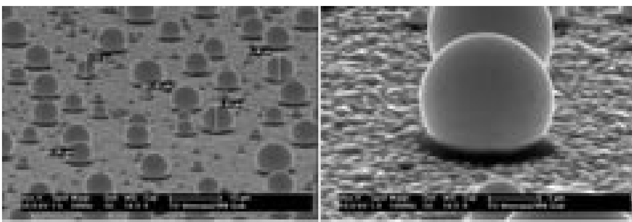

Fig. 3: SEM image of a diamond layer terminated in O_2, sample tilted 70° from horizontal plane, magnification 2,000x (left) and 10,000x (right)

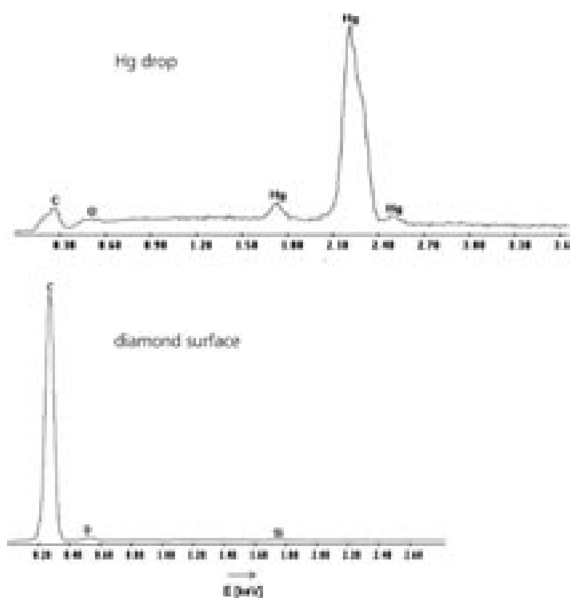

Fig. 4: EDX spectra comparing qualitatively the element composition in (left) and outside (right) of a Hg micro-cluster (diameter approx. 3 μm)

Independently of their size, all the islands have in common an almost spherical shape. The density of covering is notedly lower compared to that on ITO films. This means, that mercury wets diamond films worse than ITO layers even when terminated in oxygen plasma.
The EDX analysis confirms clearly the bad wetting. An unaffected surface without any traces of mercury is measured outside the mercury droplets (see Fig. 4).

Diamond layers terminated in H_2 atmosphere
In the case of mercury on diamond layers terminated in a hydrogen atmosphere at an elevated temperature we find a quite different behaviour compared to the previous two cases (see Fig. 5). Unlike on ITO and oxygen treated diamond layers, the deposited mercury agglomerates to micro-clusters with irregular shapes. Compared to the latter, the volume of separated islands is smaller on average and the surface covering density is higher. Besides these micro-clusters, small Hg particles with dimensions up to approx. 500 nm can be detected. In the top view the nano-clusters have a more or less circular shape. The inclined view suggests wetting angles of the individual droplets <° 90° which indicate a significantly better wetting behaviour as in the first two cases. Reasons for this different behaviour are not clearly defined, yet. A possible change in the degree of crystallisation of the diamond layer, as well as a change of the surface roughness in consequence of the hydrogen termination are possible explanations.

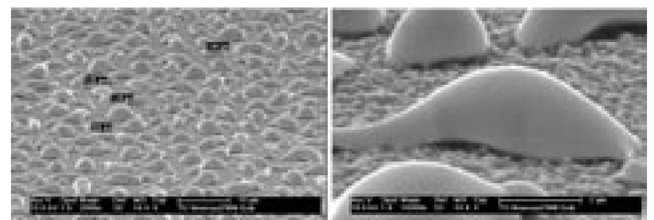

Fig. 5: SEM photographs of a diamond layer terminated in hydrogen atmosphere, sample tilted 70° from horizontal plane, magnification 2,000x (left) and 10,000x (right)

This work is part of the collaboration between the department of Materials for Electrical Engineering and the department of Microelectronics of STU Bratislava and has been supported by DAAD in the framework of the PPP programme (project no. D/03/44409).

[1] Ch.M.A. Brett, Pure Appl. Chem. 73 (2001), no.12, 1969.
[2] P.R.M. Silva, M.A. El Khakani, M. Chaker, A. Dufresne, F. Courchesne, Sensors and Actuators B 76 (2001), 250.

XRD Studies of Solidification Phenomena in Ga-In-Sn Liquid Metals

K. Reinhäckel, V. Breternitz, F. Scharmann, J. Schawohl, and Ch. Knedlik*
Department of Materials for Electrical Engineering

Liquid metals with freezing points below room temperature are of special scientific and technical interest. Alloys on the base of gallium, indium and tin have proved to be particularly promising where the effect of a multi-component eutectic is utilized. There is a still increasing demand for reduction of the solidification point because a lot of practical applications require maintaining the liquid state at very low temperatures, e.g. down to –40°C for electric connector devices in automotive industry. In order to fulfill this need, it is indispensable to improve the knowledge about the phenomena and their interaction during solidification.
In this work the possible application of X-ray diffraction is shown to identify the formation of solid phases.

Experimental

For our experiments a theta-theta X-ray diffractometer (Siemens D5000) has been accessorily equipped with a coolable sample holder (see Fig. 1). The desired temperatures have been maintained by liquid circulation cooling operating with a cryothermostat (Thermo Haake K50) and cooler antifreeze "Algorex" as cooling medium. Unfortunately, the supply tubes of the cooling system permit only a restricted and stepwise sample rotation of about 60°.

Fig. 1: Theta-theta diffractometer equipped with special sample holder operated by liquid circulation cooling (detector not in measuring position)

The parallel X-ray beam configuration, realized by a Goebel mirror and a Soller slit collimator considerably improves the signal intensity because of its lower sensitivity for positioning the sample in the correct z-plane which is beneficial in our case of not well-defined surfaces.
The samples have been visually positioned. A fine-grained glass powder has been used to enable the mechanical fixation of the sample with the best possible thermal contact to the cooled holder and to avoid parasitic diffraction peaks arising from crystalline material.

Samples

From former own experiments and literature it is known that the liquid metal can be undercooled to temperatures significant below the equilibrium eutectic temperature which amounts to 10.7°C [1].
After cooling the liquid down to temperatures of about 0°C, crystals with dimensions of some millimeters could be extracted. Their pyramidal appearance suggests that they should be single-crystalline (see Fig. 2). Some of them are mutually intergrown.

Fig. 2: Crystal extracted from a Ga-In-Sn liquid metal at ca. 0°C

Results

In order to avoid remelting, the samples have been kept at approx. –°5°C during the measurement. Figs. 3 and 4 show typical diffractograms of a single crystal and an intergrown crystal, respectively. Fig. 3 represents the diffractograms of the four side faces of the pyramidal crystal which were adjusted as described above. The diffractograms shown in Fig. 4 have been aquired by using step by step sample

* phone : +49-(0)3677-69-3611, email: christian.knedlik@tu-ilmenau.de

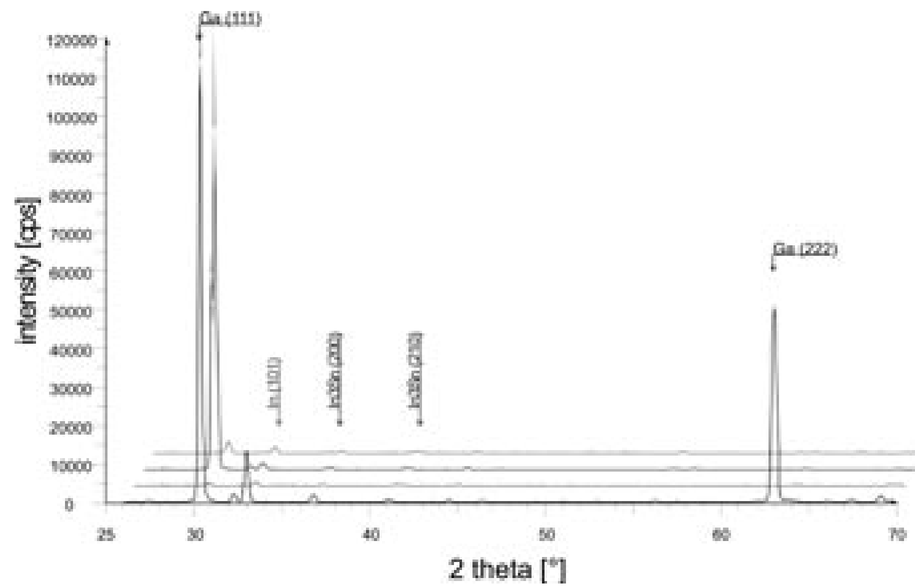

Fig. 3: X-ray diffractograms of a single crystal as shown in Fig. 2 for each pyramid face

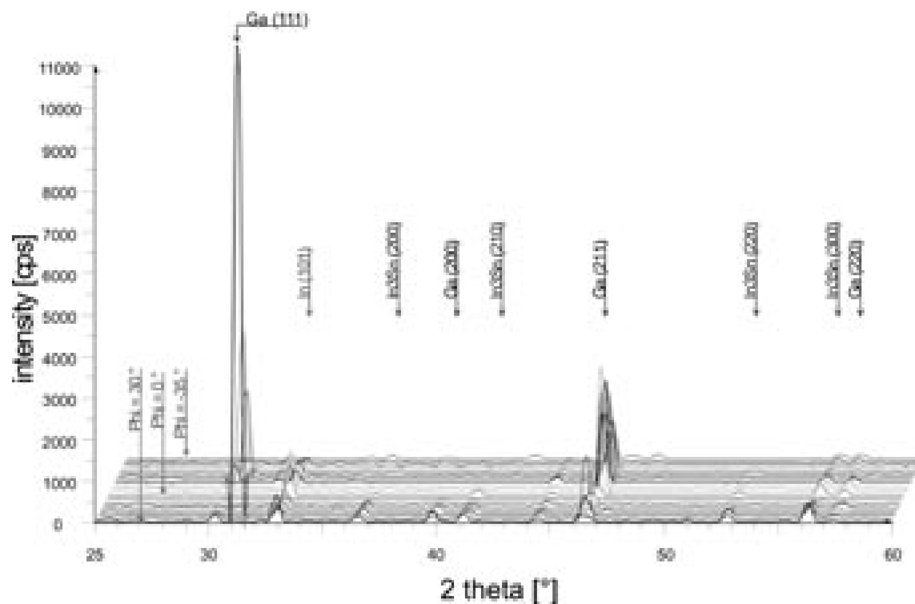

Fig. 4: X-ray diffractograms of an intergrown crystal as a function of the angle of sample rotation j

rotation in an angle range from –35° to 30°. It should be noted that the reference axis (φ = 0°) is not well defined and only determined by the arbitrary sample positioning. In spite of the constraints induced by the special measuring system, some interesting facts can be deduced. As can be seen in Figs. 3 and 4, the diffractograms of single crystals as well as of the intergrown crystals comparably exhibit sharp dominating reflexes arising from gallium. This indicates that the pyramid faces are determined by the (111) lattice plane of gallium. Furthermore there are distinct peaks which can be attributed to indium and intermetallic In_3Sn. All three phases are comprised in the equilibrium phase diagram of the ternary system Ga-In-Sn [1]. In addition some smaller peaks (not designated in Figs. 3 and 4) are probably originating from $InSn_4$. This result corresponds with results in the literature where a decomposition of solid In3Sn at low temperatures has been supposed [1] as a result of XRD investigations [2].

Even though not all phenomena are well understood in detail yet, we can summarize that the modified experimental setup presented in this work is a very helpful tool to clarify phase transformation phenomena in liquid metals.

[1] D.S. Evans, A. Prince, Metal Science 12 (1978), 411.
[2] J. Janczak, R. Kubiak, A. Zaleski; J. Olejniczak, J. Alloys & Compounds 206 (1993), 215.

TEM Investigations of Site Occupancy of Phosphorous Dopants in 4H-SiC

Th. Kups[1,*], A. Chuvilin[1,2], and U. Kaiser[1,2]
[1] Department of Material Science
[2] since 11/04 Faculty of Natural Science, Institute for Physics, University of Ulm

The fabrication of electronic devices using SiC requires a high concentration of dopants. This can be archieved preferentially by ion implantation because of the small diffusion coefficients of dopants in SiC. After implantation, the implanted atoms predominantly oc-cupy interstitial lattice sites [1], where they are usually not electrically active. Therefore, a thermal postimplantation annealing process is necessary to electrically activate the implanted dopants and to reduce the lattice damage. High temperature annealing (>1600°C) reduces implantation induced defects, however for the case of high foreign atom concentration, the SiC matrix remains defective always [2]. One important question which is not fully understood is about the site occu-pancy of p- and n doped SiC.
We addressed the question to Phosphorous (P) doped SiC by using the channeling technique ALCHEMI (atomic location by channelling enhanced microanalysis) and CBED (Convergent Beam Electron Diffraction). By the means of ALCHEMI the site occupancy of atoms within a matrix lattice can be determined [3], [4] by the different x-ray exitation when tilting the electron beam around zone axis, acquisition of x-ray spectrums and comparison of the peakheights of the implanted elements. In the used zone the possible site occupancy of dopants (Si-, C- or interstitial position) can be distinguished (Fig. 1).

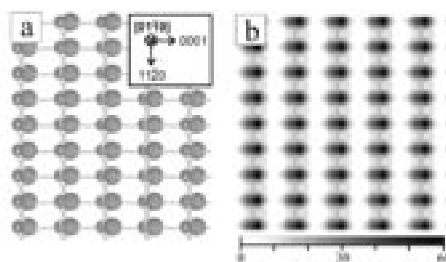

Fig. 1: 4H-SiC model viewed along [01-10] (a) and the projected potential (b). The Si-, C- and interstitial position are separated in projection

The position of higher order Laue zone (HOLZ) lines appearing in convergent beam electron diffraction (CBED) patterns are very sensitive to lattice parameter changes. The advantage of CBED lattice parameter determination against other methods is that the information is received from a tiny specimen volume ([5], [6], [7]).

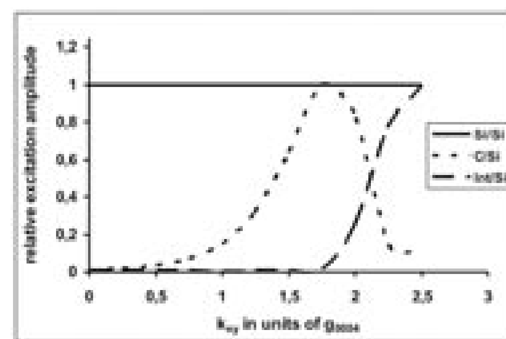

Fig. 2: Calculated exitation amplitudes for [01-10] zone axis and three possible lattice sites (Si-, C- and intersitial position) in relation to the exitation of the Si Bloch state. Full dynamical Bloch wave calculations were made to perform this simulation (program: "mbfit" [8])

Fig. 2 the calculated exitation amplitudes for [01-10] zone axis and three possible lattice sites (Si-, C- and intersitial position) in relation to the exitation of the Si Bloch state is presented. Because of the different shapes it is possible to determine the site occupancy.
P implanted 4H-SiC (concentrations: $1*10^{19}$ cm^{-3} and $5*10^{19}$ cm^{-3}, energy: 160keV, annealed 2min@1600°C at 160mbar Ar atmosphere) have been investigated using a transmission electron microscope (TEM) TECNAI S20 operating at 200kV. EDX analysis was made on [01-10] zone axis incidence for tilts of ±1/2g to ±5/2g with g=0004. The CBED pattern were obtained at [120 80 1] zone axis incidence in the region of the maximum of dopant concentration.
Fig. 3 shows the experimental results of the relative X-ray peak heights for different tilt conditions. The comparison of the graphs of Fig. 2 und 3 shows that in the tendency P is mostly located on interstitials (visible by the general increasing of the relative peak heights). The differences in the slope of the curves for the two dopant doses could be interpreted as the

* phone: +49-(0)3677-69-3109, email: thomas.kups@tu-ilmenau.de

higher amount of dopants on Si-sites (horizontal line at 1) for the high dose compared to the low dose sample.

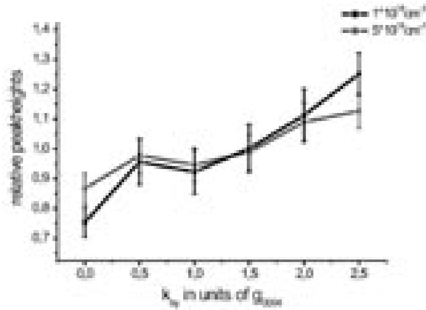

Fig. 3: Experimental results: relative peak heights for different tilt conditions for both P doped samples. The relative measurement error is below 10%.

CBED

Fig. 4 shows the orientation relationship between specimen preparation orientation [11-20] and the used zone [120 80 1] on the P doped samples.

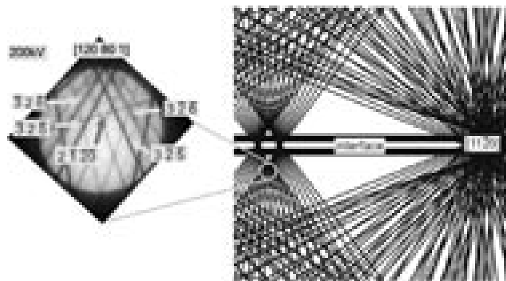

Fig. 4: Relation in reciprocal space of sample orientation [11-20] and the used zone axis incidence [120 80 1] used for an accelerating voltage of 200kV with indexed lines.

The high indexed line (2 –1 –20) is very sensitive to lattice parameter changes in c-direction. All lines are zeroth order except the line (2 -1 -20) which is of first order.

The CBED pattern of region of the maximal dopant concentration (Fig. 5) show a line split of a weak line line (2 -1 -20) which is bigger of the case of the high dose implanted sample (Fig. 5b).

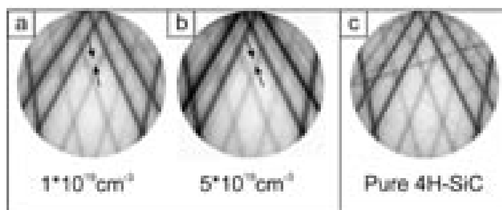

Fig. 5: CBED patterns at [120 80 1] of P ion-implanted 4H-SiC. In the low implanted sample (a) the size of the line split is smaller than in the higher implanted sample (b).(c) for comparison pure 4H-SiC

Fig. 6a presents the scheme of the model (based on the results of Clement et al. [9]) of [120 80 1] with a bend-ing parallel to the electron beam of 0.03 nm and the resulting CBED pattern.

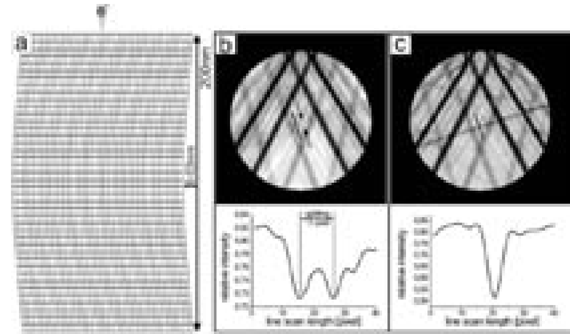

Fig. 6: (a) scheme of the bending of 0.03 nm applied to the model of [320] 4H-SiC. (b) simulated CBED pattern of pure 4H-SiC with the marked split of HOLZ line (2 –1 -20). The line scan below the CBED pattern illustrates the size of line split corresponding to the stress value of 0.04 nm at a thickness of 200nm. c) simulated CBED pattern of pure 4H-SiC for comparison

The line split of the HOLZ line (2 -1 -20) is visible (marked with arrows). The influence of the model bending is presented in the comparison of Fig. 6b and c. Fig. 6b is the simulated CBED pattern of [120 80 1] with a bending of 0.03 nm where the line split is clearly measurable while in Fig. 6c the simulated CBED pattern of pure 4H-SiC [120 80 1] is presented where no line split appears. The size of line split can be change in simulations by changing the bending value.

By this model the bending of the lattice can be caused by the ion implantation process and the differences in bending by higher concentration of atoms in unitcell in the region of maximal amount of dopants.

We showed that the site occupancy of P in 4H-SiC can be determined by ALCHEMI. P is mainly located at interstitial sites. The line split appearing in the CBED patterns occur in all samples which can be interpreted and calculated by the model of a lattice bending per-pendicular to the electron beam.

This work has been supported by DFG.

[1] S. Virdis et.al. Appl. Phys. 91-3 (2002) 1046.
[2] U. Kaiser et al. Nature Materials 1 (2002), 102.
[3] J.C.H. Spence, J. Tafto, J. of Microscopy 130 (1983) 147.
[4] U. Kaiser, J. Electron Microscopy 50 (2001) 251.
[5] J.M. Zuo, M. Kim, R. Holmestead, J. Electron. Microsc. 47 (1998), 121.
[6] U. Kaiser, K. Saitoh, K. Tsuda, M. Tanaka, J. Electron. Microsc. 48 (1999) 221.
[7] S. Krämer, J. Mayer, C. Witt, A. Weickenmeier, M. Rühle, Ultramicroscopy 81 (2000) 245.
[8] K. Tsuda, M. Tanaka, Acta Cryst. A 55 (1999), 939.
[9] L. Clément, R. Pantel, L.F. Tz. Kwakman, J.L. Rouviére, J. Appl. Lett 85(4), (2004), 651.

Modified NiO-layers for gas sensing

L. Spieß[1,*], H. Romanus[1], J. Schawohl[1], I. Hotovy[2], and V. Rehacek[2]
[1] Institute for Materials Engineering
[2] Department of Microelectronics, Slovak University of Technology, Bratislava

Introduction
Nickel oxide, usually taken as model for p-type semiconductors, is an attractive material due to its chemical stability, as well as its excellent optical and electrical properties. Indeed, NiO thin films have been studied for applications in electrochromic devices and also as functional sensing layers for MOS gas sensors. NiO films can be fabricated by different physical and chemical vapour deposition techniques, such as reactive sputtering and plasma-enhanced chemical vapour deposition. The preparation method and the deposition mode are fundamental in determining the properties of NiO thin films, but the effective dependence of the process parameters on the film properties is not well defined. Nevertheless, it is evident that the improvement of the material properties and performance as gas sensor can be reached by adding catalysts or promoters [1, 3, 4].

Experimental
NiO films were deposited by dc reactive magnetron sputtering from a Ni target in a mixture of oxygen and argon atmosphere. Two types of unheated substrates were used: Si and alumina. A sputtering power of 600 W was used. Both argon inert gas and oxygen reactive flow were controlled by mass flow controllers. The relative oxygen partial pressure was 20 %. The total gas pressure was kept at 0.5 Pa. Details of these sputtering deposition conditions are given elsewhere [2]. The NiO film thickness under the conditions described above was 100-150 nm, as measured by a Talystep. On top of these base films thin Pt overlayers (3 and 5 nm) were deposited through a photolithographic mask by magnetron sputtering. After this, the films were annealed in a tube furnace for about 4 h in dry air at 500°C. The crystal structure was identified with a Theta Theta Diffractometer D 5000 with Goebelmirror in Bragg-Brentano focussing, using copper radiation (Cu Ka). The surface morphology and the elemental distribution were investigated by a FEI XL 30 with an energy dispersive X-ray (EDX) analyser based on a silicon detector and an S-UTW-Window operating at an acceleration voltage of 30 kV. Different lateral parts of the sensor structure were analyzed in order to check the elemental distribution.

Results
From XRD spectra of un-doped NiO films it was found that they have a polycrystalline structure (f.c.c. NiO phase). The diffraction pattern showed the presence of diffraction peaks from the (111), (200) and (220) planes of the NiO lattice. The peak positions are located at about 0.7-1.2 degrees below the theoretically predicted values, indicating a larger lattice constant. It was detected that these films have a strong (200) diffraction peak, indicating a preferred orientation along [100] direction. In case of NiO films with a 3 nm thick Pt surface modification no peaks of Pt were observed due to the small amount of platinum deposited. All NiO peaks were suppressed. The SEM pictures, obtained for undoped NiO film with 3 nm Pt displayed in Fig. 1 show different porosity. The morphology of undoped NiO films reveals a rough and compact granular structure, but in the case of Pt modification it is less regular, showing the presence of pores. EDX microanalysis affirm that Pt is present on the NiO films modified with a 3 nm Pt overlayer. Fig. 1 shows EDX spectra measured on samples with different Pt modifications.

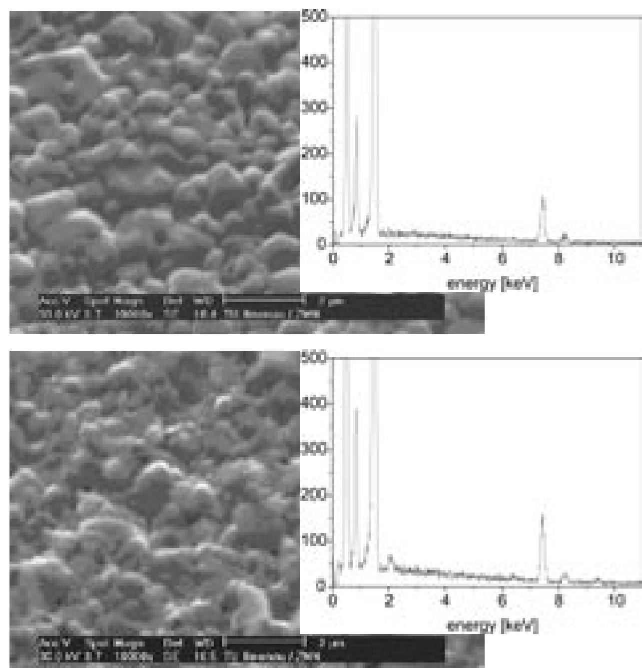

Fig. 1: SEM micrographs of NiO base film and a NiO Film with 5 nm Pt layer and EDX spectra of a NiO film with 3 nm Pt and with 5 nm Pt respectivly.

* phone : +49-(0)3677-69-3403, email: lothar.spiess@tu-ilmenau.de

SEM observations, in secondary electron mode, of the unmodified and of Pt modified NiO films prepared on silicon substrate revealed that the NiO surface of both films was dense, smooth, homogenous and with a uniform morphology which was confirmed by AFM. There were no visible particles. Backscattering SEM mode micrographs of thin Pt overlayers with a thickness of 3 and 5 nm are displayed in Fig. 2. One can see that the Pt film is not continuous and close. It does not cover the NiO surface completely and Pt sputtered atoms create areas of islands and conglomerates. The surface modified by Pt is porous; the density of pores is much higher for a NiO film with a 3 nm Pt overlayer. The surface coverage by Pt islands for NiO film modified by 5 nm of Pt reaches up to 85-90%.

Since the gas sensor structure was realized on raw alumina substrate, the SEM investigation was also done on this substrate to identify the effective morphology of the sensors. It was found that the surface morphology of all samples is characterised by a rough and compact granular structure reflecting the alumina substrate morphology. On single alumina grains we observed the particles and agglomeration of small grains with arbitrary form. The EDX microanalysis performed during SEM observations on different parts of the sensor structure revealed that Pt was present in a small amount on the NiO films modified by a 5 nm Pt overlayer. On the other hand, no Pt signal was recorded from the area not modified by Pt.

Further, an AFM operating in air was used to study the surface morphology and roughness of our films prepared on silicon substrates. Typical AFM images of a NiO base film and a NiO film modified by 3 and 5 nm Pt overlayers prepared on silicon, are mapped. The surfaces of all films were found to be reasonably very smooth and exhibited surface roughness values varying from 0.27 to 0.69 nm. On the other hand, according to a quantitative analysis of the roughness deduced from AFM measurements, the values of roughness changed in dependence on the thickness of the Pt overlayer. The NiO film with 5 nm Pt reveals that the film surface is smoother, containing small grains (about 22 nm) and an average film roughness of 29.8%. In contrast, the film surface of NiO film with Pt of 3 nm shows that the grains create relatively larger crystallites and the value of roughness is higher (32.7%). We assume that these lower values of the average roughness in comparison with NiO base film are due to smaller grains filling the spaces between the larger ones.

To determine the thickness of the Pt overlayers, AFM measurements were performed along the step between NiO and Pt surface prepared on the silicon substrate. According to this measurement, the thicknesses of the Pt overlayers were determined and their average values were about 3 and 5 nm, respectively.

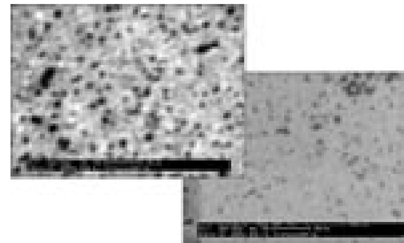

Fig. 2: Backscattering SEM micrographs of Pt thin ovelayer formed on NiO surface prepared on silicon substrate: Pt= 3 nm (a), and Pt= 5 nm (b)

Conclusion

Very thin Pt films with different thickness (about 3 and 5 nm) were sputtered on the surfaces of NiO sensing layers prepared by dc reactive magnetron sputtering. The surface structure and morphology of the unmodified and differently Pt-modified NiO films on both silicon and alumina substrates have been studied. NiO-based sensor devices have been also realized on alumina substrates and their H_2 sensing properties analysed by gas sensing tests in controlled atmospheres. The NiO thin films had a polycrystalline structure (f.c.c. NiO phase) with a relatively low roughness, and a discrete response towards hydrogen. The H_2 gas sensing properties were considerably improved by the catalytic activity of the thin Pt overlayers. The Pt-modified NiO sensors showed high responses and sensitivities to a very low concentration (500-5000 ppm) of H_2 in air by taking into account that the lower explosion limit (LEL) range of H_2 is 40,000 ppm. These results make the Pt-modified NiO sensors promising candidates for implementing hydrogen leak detector. Their gas sensing properties toward hydrogen have been discussed also with reference to the thickness and the morphology of the Pt thin layers. The sensor response to H_2 resulted to be strongly dependent not only on the grain size of Pt cluster islands but also on the porosity of the Pt film on the NiO surface. At low temperatures (~200°C) the NiO sample with a 3 nm thick Pt film showed better properties as H_2 sensors as compared to the NiO sensor with a 5 nm thick Pt film, while at higher temperatures the two differently modified Pt NiO sensors showed similar gas sensing characteristics. This was tentatively explained by supposing a change in the morphology of a 3 nm thick Pt film as function of the temperature.

This work was supported by the Scientific Grant Agency of the Ministry of Education of the Slovak Republic and the Slovak Academy of Sciences, No. 1/0170/03, and partially by a Grant of DLR/Germany No. SVK 01/016 and Grant from DAAD.

[1] A. Salehi, M. Gholizade, Sensors and Actuators B89 (2003), 173-179.
[2] I. Hotovy et al., Sensors and Actuators B78 (2001), 126-132.
[3] M. Matsumiya, W. Shin, N. Izu and N. Murayama, Sensors and Actuators B, 93 (2003) 309-315.
[4] A. Friedberger, P. Kreisl, E. Rose, G. Müller, G. Kühner, J. Wöllenstein and H. Böttner, Sensors and Actuators B, 93 (2003) 345-349.

Tribological characteristics of tungsten carbide films

M. Gubisch[1,*], Y. Liu[2], B. Schwenke[1], L. Spiess[1], S. Krischok[2], G. Ecke[3], J.A. Schaefer[2], and Ch. Knedlik[1]
[1] Institute for Materials Engineering
Departments of Technical Physics[2] and Nanotechnology[3]

Introduction

Tungsten carbide is a commonly used material for precision engineering due to its high degree of hardness, high Young's modulus, high wear resistance, high thermal conductivity, and excellent thermal and dimensional stability. Several crystalline tungsten carbide phases exist in the W-C phase diagram [1]. They consist of the stable phase α-WC with simple hexagonal structure, metastable structure hcp α-W_2C, a high temperature modification of W_2C denoted as β-W_2C and β-WC_1-x with face-centred-cubic structure. All of these phases were reported to be hard and strong. However, their tribological properties, especially in the form of thin films, have not been systematically studied. In this study, we consider the influence of different tungsten carbide phases of WC_{1-x}, W_2C, and WC on the tribological properties of thin film coatings. Our emphasis is on establishing the chemical, structural, mechanical, and tribological properties for such thin film coatings.

Experimental details

Tungsten carbide thin film coatings with dominant phases of WC_{1-x}, W_2C, and WC, respectively were prepared by magnetron sputtering on silicon substrate. Films with a thickness of 700 nm with different phases were obtained by adjusting the sputtering mode, i.e. direct current (DC) or radio frequency (RF), bias voltage, pressure and sputtering gas [2]. As a comparison, a pure W coating with the same thickness was also deposited. The films were analyzed by XRD, SEM, EDS, AES, XPS, and AFM. The hardness and indentation modulus were evaluated by using depth-sensing indentation techniques with a Vickers indenter (normal load of 5 mN). Tribological tests were carried out on a reciprocating micro-tribometer with a chromium steel (100Cr6, grade 5, RMS 50 nm) sphere loaded against coatings at a sliding speed of 336 μm/s. For each coating, the same sphere was employed throughout the entire testing process. All of the tests were performed in ambient environments with approximate humidity and temperature of *r.H.* 35% and 296 °K, respectively.

Results and discussion

The XRD patterns for WC_{1-x}, W_2C and WC coatings obtained by the conventional Bragg-Brentano scan mode are presented in Fig. 1. The XRD pattern for the WC_{1-x} coating in Fig. 1a shows only one peak,the center of which is located at $2\theta = 42.13°$. This peak originates from the diffraction of the (200) plane of WC_{1-x}. In the XRD pattern for the W_2C film we can find three peaks at $2\theta = 34.1°$, 39.9° and 60.8°, see Fig 1b. These peaks correspond to an average lattice spacing of 0.2626, 0.2257, and 0.1521 nm, respectively and are indexed to the (100), (101), and (110) planes of W_2C. The XRD pattern for the WC film shows the highest intensity, as shown in Fig. 1c. Two peaks at $2\theta = 35.4°$ and 74.9° corresponding to an average lattice spacing of 0.2531 nm and 0.1267 nm, are indexed to the (100) of the WC prototype structure and (200), respectively.

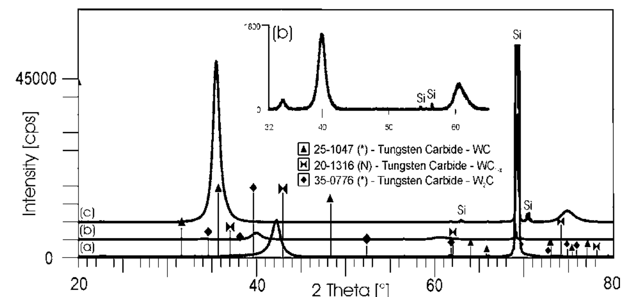

Fig. 1: XRD patterns for (a) WC_{1-x} (b) W_2C and (c) WC films

The carbon content of the WC_{1-x} and W_2C coatings are ~42 and ~22 at.%, respectively, see Fig. 2. The loss of carbon is chiefly from the "resputtering" effect, which removes the light element C from the growing films. The RF mode, with high bias voltage (and hence the high temperature of ~400 °C in the deposition process) contributes to the resputtering effect, therefore W_2C were deposited. The C and N content in the WC films is found to be about 34 at.% and 12 at.%, respectively.

		Chemical composition [at.%]			
sample	method	W	C	N	Ar
W	EDS	99	-	-	1
WC_{1-x}	EDS	57	42	-	1
WC_{1-x}	XPS	53	39	-	-
W_2C	EDS	72	22	-	6
WC	EDS	54	34	12	0
WC	XPS	49	31	12	-

Fig. 2: Chemical composition of sputtered films from EDS and XPS measurements. Both methods give similar results.

* phone : +49-(0)3677-69-3444, email: maik.gubisch@tu-ilmenau.de

The observed WC crystal structure, together with the homogenous N-distribution observed by AES and the missing splitting into a W_2N (or WN) and WC (or WC_{1-x}) phase in our XPS data, are compatible with the following model. A WC prototype crystalline structure is formed, where the N atoms might substitute the missing C atoms in the WC lattice. This substitution seems to be very likely since WC and WN have the same crystalline structure and only very slightly different lattice parameters. Moreover, this model explains the formation of the WC crystal structure and the absence of other structures in XRD.

The friction coefficients for all the coatings are stable in the first 100 cycles, and the lowest friction coefficient is achieved in the WC coating, see Fig. 4. The friction coefficients of W, W_2C, and WC_{1-x} are quite similar. The lowest friction coefficient achieved by WC might be related to the highest hardness with 23 GPa. The similar friction coefficients of W and W_2C can also be explained by their similar hardness with 10 GPa and 12 GPa, respectively. However, these low values might not be the intrinsic properties of W_2C. The high surface roughness and fine grains, shown in Fig. 3c play an important role in determining the hardness. As shown by Greenwood and Williamson [3], higher surface roughness (RMS) and smaller radius of the asperities (grain size in Fig. 3c) result in a higher plasticity index, hence in a lower hardness value from the measurement. However, the hardness is not the only factor that influences friction coefficients. A high μ was obtained in the WC_{1-x} coating, which has a high hardness with 19 GPa. Other influences, such as wear and the formation of the transfer film, also play an important role in determining the friction behavior, especially in terms of life cycle tribology.

Fig. 3: Surface morphology of different WC films due to the deposition process: a) WC_{1-x} (RMS = 1.17 nm), b) WC (RMS = 0.5 nm), c) W_2C (RMS = 3.5 nm)

A large variation of the friction coefficients was observed after 100 cycles in the W, W_2C, and WC_{1-x} coatings, see Fig. 4. A ponounced oscillation of the friction coefficient could be noticed in the curve of the W coating. This behaviour was also observed in the sliding friction of steel and chromium coatings and was attributed to the mild wear and the formation and removal of the oxide films [4]. For the W_2C coating, a steady decrease of the friction coefficient from the beginning of the test to a minimum value of ~0.2 after 1000 cycles was observed. After that, the friction coefficient rose dramatically to about 0.6 in 6,000 cycles and remained there for the next 3,000 cycles, followed by another dramatic rise. Observations by SEM and EDS analysis revealed that the coating was worn through after the tests.

This demonstrates that the drastic increase of the friction coefficient was related to the wear of the coatings. A higher wear rate, i.e. a higher energy dissipation rate, is always accompanied by a drastic increase of the friction coefficient. This finding is also supported by the result from the WC_{1-x} coatings, in which a drastic increase of the friction coefficient from ~0.26 at 100 cycles to a maximum value of ~0.42 at 2,000 cycles was observed.

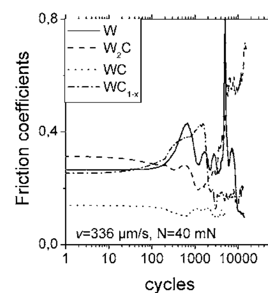

Fig. 4: Friction coefficient as a function of running cycles

This drastic increase is believed to be related to the wear of the coating and the subsequent build-up of the transfer film on the surface of the steel sphere. The wear scar of the sphere after the tests is shown in Fig. 5a. Once a stable transfer film is formed, the subsequent sliding friction becomes small and remains stable as demonstrated by the low friction coefficient at ~0.19 from 2,000 until the end of the test. This value is quite similar to that of the WC coatings at ~0.15 in the whole running process. Fig. 5b shows the wear scars of the sphere after the sliding test on WC on which only a very thin transfer film was identified by EDS analysis. The grooves mainly resulted from particles (indicated by the arrows in the figure) dragging across the surface of the sphere. These hard particles contain W which is partially oxidized as revealed by EDS analysis. From these results, we find that thin transfer film together with the high hardness of the coating make the friction coefficient of WC stable in the long life cycle test.

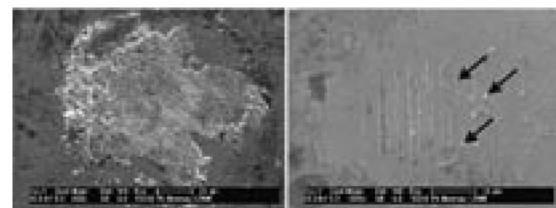

Fig. 5: Wear scar of the steel sphere after the tests of (a) WC_{1-x}, (b) WC coatings.

This research is supported by the German Research Foundation (DFG) under contract SFB 622 and the Thuringian Ministry of Culture.

[1] P. Gustafson, Mat. Sci. Tech. 2 (1986) 653.
[2] M. Gubisch, Y. Liu et al., in G. Dalmaz, A. A. Lubrecht, D. Dowson and M. Priest (ed.), Life cycle Tribology, Proceedings of the 31th Leeds-Lyon Symposium on Tribology (Tribology Series, 44), Leeds, Sept. 2004 (in press).
[3] Greenwood, J. A., and Williamson, J. B. P., 1966, Contact of Nominally Flat Surfaces, Proc. Roy. Soc. Lond., A295, pp. 300-319.
[4] Y. Liu et al., in G. Dalmaz, A. A. Lubrecht, D. Dowson and M. Priest (ed.), Life cycle Tribology, Proceedings of the 31th Leeds-Lyon Symposium on Tribiology (Tribology Series, 44), Leeds, Sept. 2004 (in press).

Wet chemical etching of AlN in KOH solution

I. Cimalla[1*], Ch. Foerster[1*], V. Cimalla[1], V. Lebedev[1], K. Friedel[2], D. Cengher[1], and O. Ambacher[1]
[1] Department of Nanotechnology
[2] Department of Microsystems Technology

Group III-nitride semiconductors have attracted huge research interest in the last years due to their unique properties and potential application for short-wavelength light emitters and detectors as well as for high temperature and high frequency devices. The direct wide band gap of AlN (6.2 eV) and its piezo-electric properties can be utilized to fabricate unique ultraviolet, high brightness, and long-life light emitting diodes and high frequency microelectromechanical systems (MEMS). Most of these devices are three-dimensional (3D) structures and require a patterning followed by an etching. High etch rates have been achieved by chemical dry etching in chlorine containing gases [1]. However, it has a reduced selectivity between different alloys in the group III nitride materials system InGaAlN. On the other hand, KOH-based solutions were found to etch AlN highly selective to GaN and AlGaN [2] and are a fast method to etch sacrificial layers in AlN-AlGaN heterostructures and to create 3D AlN structures. However, KOH based wet chemical etching is strongly dependent on the crystal quality [3].
In this work we investigated the influence of the AlN material quality on the etching rate in KOH-based solutions. Thus, AlN layers were deposited by three different methods on sapphire and silicon substrates (i) by metal organic chemical vapour deposition (MOCVD), (ii) by molecular beam epitaxy (MBE), and (iii) by and reactive sputter deposition.

Fig. 1 shows the atomic force microscopy (AFM) images of representative samples, which were used for the etching experiments. The AlN layers grown by MBE (Fig. 1a) have very smooth surfaces with rms < 1 nm, eventually intermitted by macroscopic defects. The sputtered AlN layers (Fig. 1d) also appear smooth with roughness of rms ~ 2.1 nm. Here, a grain structure on the surface with a mean diameter of 20-30 nm is visible. This grain structure is more pronounced on the MOCVD samples, both on sapphire (Fig. 1b) and on silicon (Fig. 1c). The appearing morphology strongly correlates to the structural properties of the layers as estimated by reflection high-energy electron-diffraction and x-ray diffraction (XRD). Only the MBE grown AlN layer has been single crystalline. The sputtered and the MOCVD grown AlN layers were polycrystalline with a strong (0001) texture with a narrow XRD rocking curve for the MOCVD-AlN (0.4°) on sapphire and a broad curve for AlN on silicon (1-4°). The thickness of the layers before and after etching was measured by reflectometry. Prior to the wet etching all the samples were cleaned by sputter etching in Ar plasma for 2 min, at 30 sccm, a power of 50 W, and a pressure of 8.3×10^{-3} mbar. By this technique a surface layer of 2-3 nm was removed. It was proved that this short sputter etching has no influence on the etching rate. The wet chemical etching we performed in a KOH-based solution with a concentration of 15%.

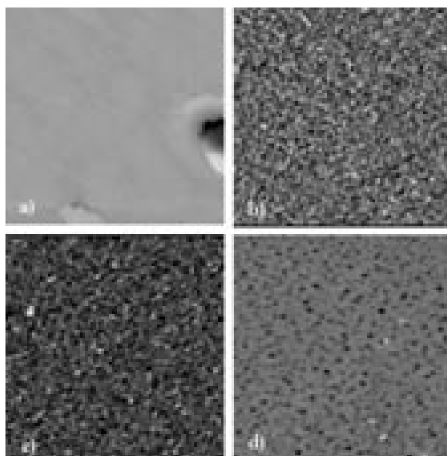

Fig. 1: AFM images (5x5 µm²) of AlN layers before etching: (a) MBE-AlN on sapphire, (b) MOCVD-AlN on sapphire #32, (c) MOCVD-AlN on silicon #48, and (d) sputtered AlN on silicon.

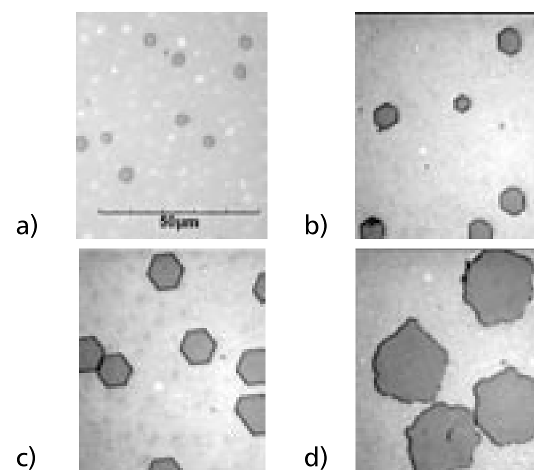

Fig. 2: Evolution of the surface of MBE grown epitaxial AlN during KOH etching at 60°C for: (a) 5 min, (b) 10 min, (c) 15 min, and (d) 30 min.

* phone: +49-(0)3677-69-3352, email: irina.popa@tu-ilmenau.de

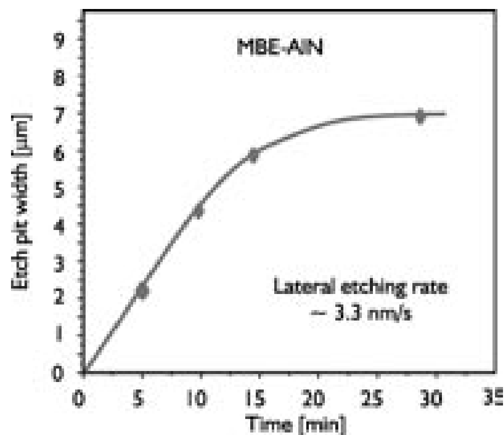

Fig. 3: Width of the etch pits on epitaxial MBE-AlN.

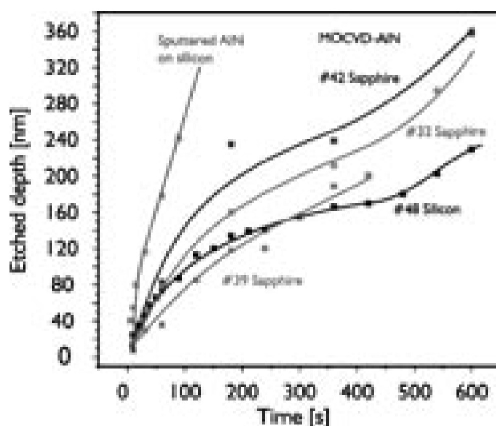

Fig. 4: Kinetics of the wet chemical etching of AlN grown by MOCVD and by sputtering on 15% KOH at room temperature.

The high quality MBE-AlN could not be etched homogeneously. Instead, a very local etching was observed, which results in well-defined hexagons (Fig. 2). The dependence of the width of these hexagons on the etching time is shown in Fig. 3. A lateral etching rate of around 3.3 nm/s can be derived in contrast to no detectable vertical etching. This indicates a pronounced defect etching on threading dislocations and an anistropic etching with a preferred lateral component in $[1\,\bar{2}0]$ direction. At increased temperatures also a vertical etching was observed. At 75°C AlN was etched homogeneously in vertical direction, too.

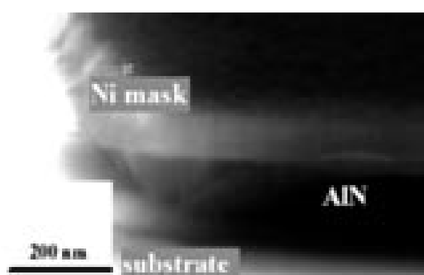

Fig. 5: Undercutting of the Ni mask on sputtered AlN

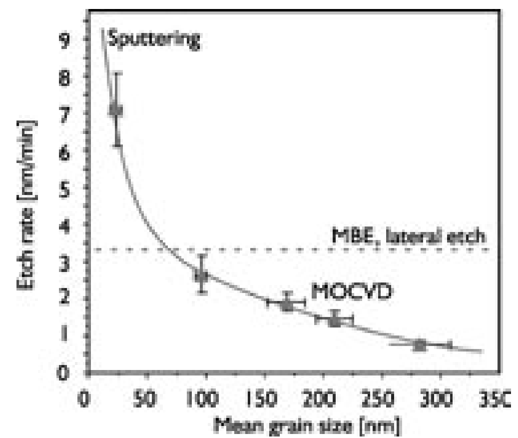

Fig. 6: Averaged etching rate of the AlN layers of different origin in dependence on the lateral grain size. For comparison the lateral etch rate in MBE-AlN is shown as a dashed line.

In contrast, the polycrystalline AlN was etched homogeneously at room temperature. The dependence of the etching depth on the time is shown in Fig. 4. The highest rate was observed for the sputtered AlN layers with an etching rate around 6 – 8 nm/s at room temperature. Again, a strong lateral etching was observed under a Ni mask to create 3D structures (Fig. 5). Here the lateral etching was in the same range as the layer thickness indicating a more isotropic etching compared to the MBE-AlN.

Finally, the etching rate of the MOCVD-AlN layers is strongly dependent on the morphology and the crystal quality. It turned out that both decreasing the texture and the mean grain size in lateral direction increase the etching rate. The coherence between averaged etching rate and the lateral grain size estimated by AFM is shown in Fig. 6. Compared to the lateral etching rate of MBE-AlN there is a faster etching in the case of the sputtered nanocrystalline AlN and a lower rate for the MOCVD-grown AlN where the grain size is in the order of the layer thickness. Thus, depending on the crystal quality a changing from isotropic etching for highly defective and for polycrystalline material to anisotropic etching with a faster component in lateral $[1\,\bar{2}0]$ direction occurs. In conclusion, the wet chemical etching in KOH based solutions at room temperature is principally an etching along defects and grain boundaries. Once an etch pit has been formed the faster etching in $[1\,\bar{2}0]$ direction is responsible for the removal of AlN. Thus, polycystalline AlN with small grain sizes can be etched practically anisotropically, while high quality AlN is etched very locally on defects.

This work has been supported by the Deutsche Forschungsgemeinschaft, SPP 1157 „Integrierte elektrokeramische Funktionsstrukturen", contract AM 105/2-1

[1] C.B. Vartuli, et al, Appl. Phys. Lett. vol. 69, pp. 1426 1996.
[2] C.B. Vartuli, et al, J. Electrochem. Soc. Vol. 143, pp. 3681 1996.
[3] D. Zhuang, and J.H. Edgar, Mater. Sci. Eng. R 48, pp 1 2005.

Growth of AlN nanowires by metalorganic chemical vapor deposition

V. Cimalla*, Ch. Foerster, D. Cengher, and O. Ambacher
Department of Nanotechnology

The exceptional properties of wide-bandgap III-V semiconductors are promising for a broad range of electronical, optoelectronical, electromechanical and sensoric applications. Moreover, the low density of surface states of the nitrides favors this material system for assembling nanoscale devices, where the surface-to-volume ratio is large and the surface related recombination centers in the bandgap would drastically reduce the performance. The first GaN nanowire based devices have been already demonstrated including field effect transistors, Schottky diodes, light emitters and detectors. It demonstrates the high capability for applications for photonic, light-emitting and biological nano devices.
GaN and InN nanowires have been prepared by various techniques including plasma-assisted molecular beam epitaxy, laser ablation, metalorganic chemical vapor deposition and reaction of NH_3 with Ga (In) powder or Ga/Ga_2O_3 (In/In_2O_3) mixtures. In contrary, little was reported on the preparation of AlN nanowires. Among the nitrides AlN has higher thermal conductivity at low temperature, good mechanical strength, high resistivity and corrosion resistance, and the largest piezoelectric coefficients. Thus, AlN nanowires are attractive building blocks for electromechanical devices on the nanoscale.
We have grown AlN nanowires in a commercial horizontal reactor (Aixtron 200RF) using trimethylaluminum, ammonia and nitrogen as a carrier gas. The growth temperature and the pressure were set at 900-1100°C and 100 mbar, respectively. At these conditions the growth rate of a homogeneous AlN layer on silicon was 40 - 120 nm/h. For the nucleation experiments SiO_2 covered silicon wafers have been used as substrates. Both Ni and Au catalyst were used to stimulate the vapor-liquid-solid (VLS) growth (Fig. 1). In this method a nanoscale metal island defines the nucleation center for the nanowire. Aluminum and nitrogen from the gas phase is alloying the metal droplet until saturation is reached.

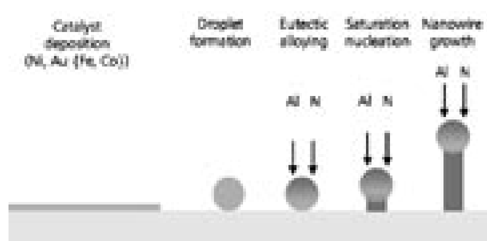

Fig. 1: VLS mechanism of the growth of nanowires.

AlN crystallizes at the interface to the solid while the catalyst droplet remains liquid. Consequently an AlN nanowire is grown with a liquid catalyst cap. The diameter of the catalyst droplet roughly defines the diameter of the nanowire.
A self-organization process was used to create such droplets. First, the metal layers were deposited by electron beam evaporation with a thickness of 2-10 nm. The formation of nanosized catalyst islands was accomplished by an *in situ* annealing in nitrogen prior to the growth. Depending on the initial layer thickness and the annealing time we observed homogenous layers or self-assembled islands with a diameter ranging from 20 nm to 1500 nm.

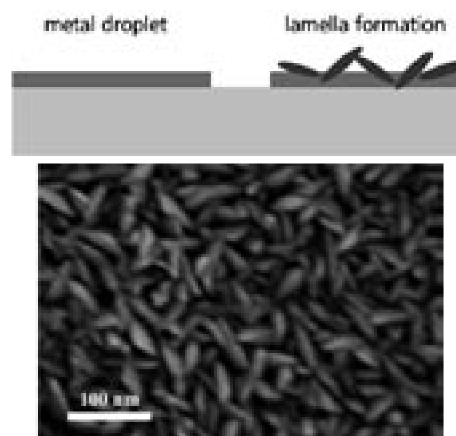

Fig. 2: Lamella formation at high N:Al ratios in the gas phase and low temperatures (950°C).

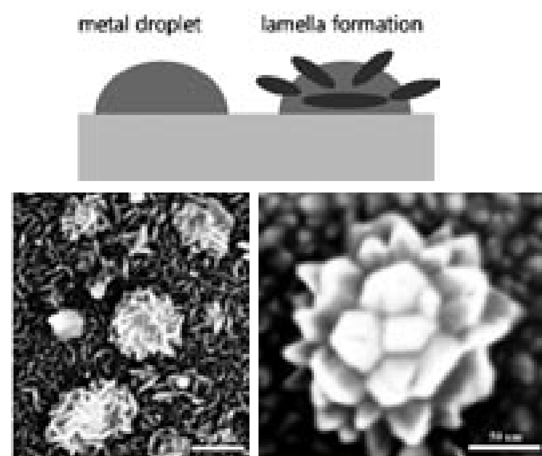

Fig. 3: Lamella formation on large catalyst droplets with 100 – 200 nm diameter at high N:Al ratios in the gas phase and medium temperatures (1000°C).

* phone: +49-(0)3677-69-3408, email: volker.cimalla@tu-ilmenau.de

At high N:Al ratios in the gas phase the growth of a continuous AlN or lamella like nanostructures was observed. The limited diffusion of Al results in a strong gradient and a phase separation inside of the catalyst leading to the formation of nanostructures controlled by the Kirkendall effect. Thus, on homogenous metal layers as well as on very small droplets with a high density the surface is covered by small lamellas (Fig. 2). These lamellas are finally transformed to AlN as proved by x-ray diffraction (XRD).
On larger catalyst droplets with a diameter of 100 – 200 nm three-dimensional nanostructures were formed (Fig. 3). The strong diffusion limitation initiates nucleation centers for these metal structures around the droplet diameter in preferred crystallographic ori-entations resulting in a regular arrangement of the lamellas. They finally appear as nanoflowers.
If the N:Al ration in the gas phase will be reduced, the growth rate of AlN decreases as well. Consequently, during the alloying at the high growth temperatures of 1000-1100°C a remarkable part of the metals is evaporating. In this case the droplets are not homogeneous anymore and stimulate the growth of porous AlN (Fig. 4). However, on medium catalyst droplets (100 nm) eventually AlN nanocolums were grown according to the VLS model (Fig. 5). On small droplets no growth was observed.

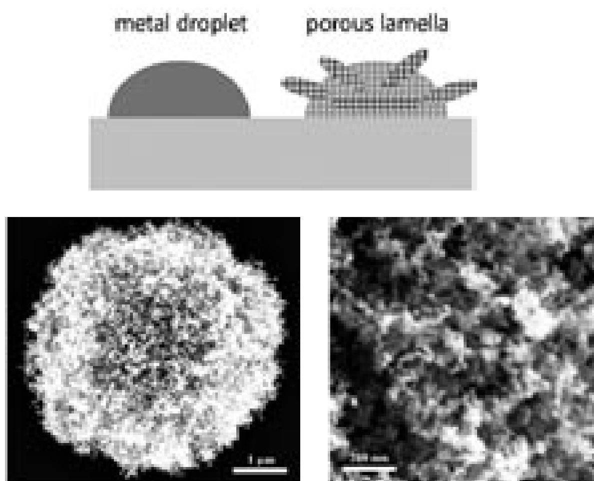

Fig. 4: Porous AlN at medium N:Al ratios in the gas phase and high temperatures (1100°C).

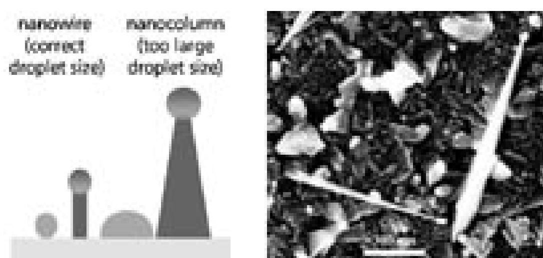

Fig. 5: Growth of nanocolumns on medium droplets (100 nm) at medium N:Al ratio and high temperatures (1100°C).

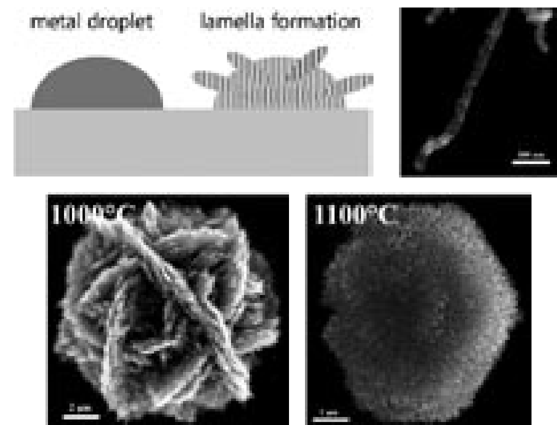

Fig. 6: Growth of nanowires at low N:Al ratio and high temperatures (1000 - 1100°C).

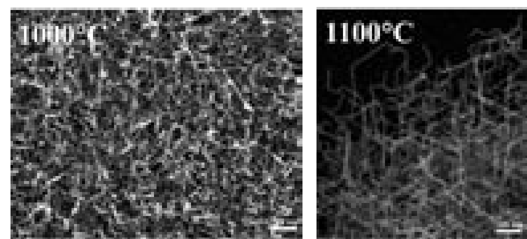

Fig. 7: Higher magnification of nanowires grown at low N:Al ratio and high temperatures (1000 - 1100°C).

Finally, if the N:Al ratio in the gas phase is further reduced the interplay of metal evaporation and nitrogen penetration gives raise to the growth of AlN nanowires with a diameter of 20 nm. Starting point is again the formation of a porous catalyst. However, at these conditions the formation of catalyst droplets with a diameter around 20 nm is achieved inside of the initial droplet. Consequently the preconditions for the VLS growth are fulfilled and AlN nanowires are growing out from the structure. At the end the whole droplet will be transformed into a network of nanowires. (Fig. 6). These networks maintain the basic structure of the droplet after annealing, i.e., the lamella based nanoflower and the more homogeneous spheres at 1000°C and 1100°C, respectively. In addition at higher temperatures a higher order in the nanowire network can be seen. All the wires are connected by angles of 120° (Fig. 7), which results in an overall hexagonal structure of the sphere, too.
In conclusion, AlN nanowires with a diameter of 20 nm were grown stochastically by the VLS method. The high temperatures above 1000°C, which are necessary to grow the nanowires complicate the control of their formation. Small catalyst droplets of 20 nm diameter are not stable due to their evaporation. Thus, nanowire formation could be observed only inside larger 3D structures with diameters up to 5 µm.

This work was supported by the Thuringian ministry of culture (TKM) and the European Union (EFRE program: B 678-03001, 6th frame-work program: GaNano NMP4-CT2003-505614).

Critical points of the band structure of hexagonal AlGaN alloys

C. Buchheim[1,*], R. Goldhahn[2], C. Cobet[3], M. Rakel[3], N. Esser[3], U. Rossow[4], D. Fuhrmann[4], and A. Hangleiter[4]
[1] Department of Nanotechnology
[2] Institute of Physics, Technical University of Ilmenau
[3] Institute for Analytical Sciences, Department Berlin-Adlershof, Berlin
[4] Institute for Technical Physics, Technical University Braunschweig

GaN, AlN and their ternary alloys are used for optical and optoelectronic devices. Short period superlattices have been developed as Bloch oscillators [1] or distributed Bragg reflectors with very high reflectivity [2]. Deep-ultraviolet lasing at 241 nm was reported recently [3]. For the design of such heterostructures and for the evaluation of the achieved properties the detailed knowledge of the complex dielectric function (DF) over an extended range of photon energies is essential. But the current knowledge of the DF for $Al_xGa_{1-x}N$ is rather poor, because most studies are restricted to the transparent region below the band edge [4] or only pseudo-DF's are reported [5]. Here, the DF of GaN and AlGaN with varying Al content is obtained by spectroscopic ellipsometry in the energy range between 0.7 and 9.8 eV. From the data the energetic positions of the critical points of the band structure are extracted. The investigation of samples with different Al content allows the determination of the bowing parameters, which characterise the deviation of the peak shifts from linear behaviour.

The investigated samples are all hexagonal and grown by MOVPE on c-plane sapphire substrates. The GaN sample has a film thickness of 1800 nm. The AlGaN films are 400 nm thick and are grown on 400 nm thick GaN buffers. The growth details have been reported elsewhere [6]. For the VUV measurements (4 to 9.8 eV) the **3m-Normal-Incidence-Monochromator 1a** at BESSY II was used as light source. The ellipsometric parameters Ψ and Δ were recorded at an angle of incidence of 68°. In the low-energy range the data were obtained by using a commercial variable angle ellipsometer (J. A. Woollam Co., Inc.).
Figure 1 shows the real and the imaginary part of the pseudo DF's for AlGaN with Al contents between 0 and 50%. For the samples with higher Al content one can see thickness interferences below the band edge. The critical points of the band structure are much better resolved in comparison to previous studies [5], emphasising the excellent structural quality and surface properties of the films. For GaN their energetic positions are observed at 6.95 eV, 7.89 eV, and

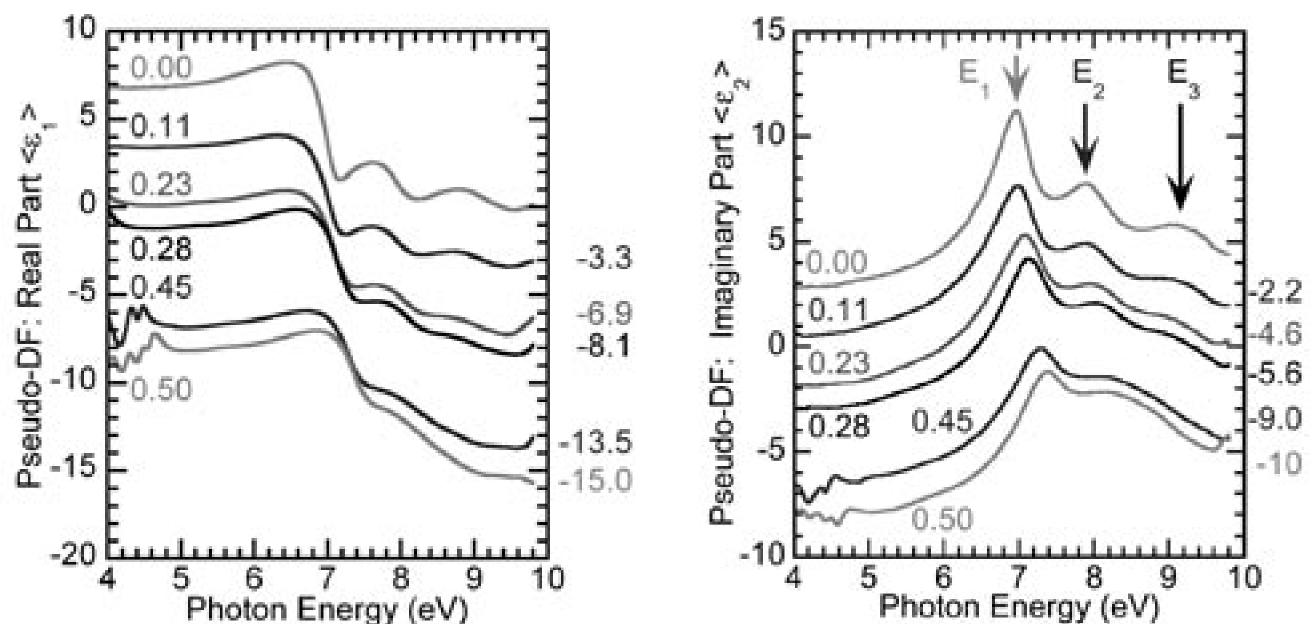

Fig. 1: Real part (left) and imaginary part (right) of the pseudo-dielectric function for hexagonal $Al_xGa_{1-x}N$ alloys. The spectra are shifted proportionally to their Al-content for better clarity. The critical point energies are indicated by arrows.

* phone : +49-(0)3677-69-3168, email: carsten.buchheim@tu-ilmenau.de

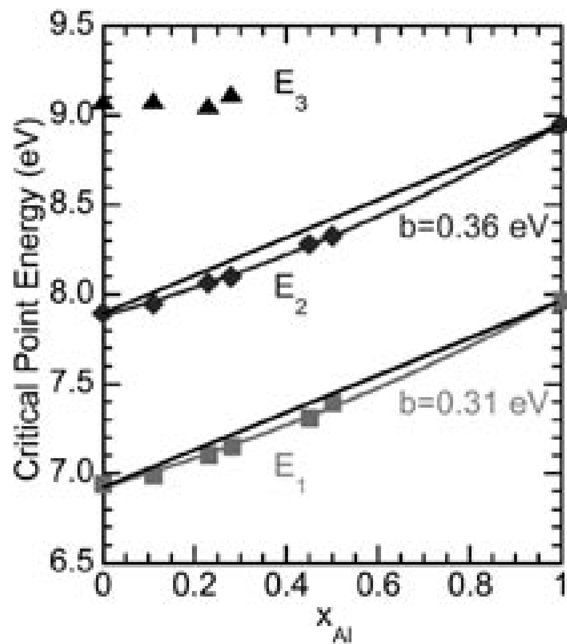

Fig. 2: Dependency of the critical point energies on the $Al_xGa_{1-x}N$ alloy composition (symbols). The solid lines show the difference between fitted bowing and linear behaviour.

9.08 eV. In the figure one can clearly see the shift of the critical points to higher energies with increasing Al content. In Ref. 5 a linear shift has been reported. However, in our studies we find a clear deviation from linear increase for the E_1 and E_2 critical point energies with Al content. For the mathematical description of the behaviour one usually introduces a bowing parameter b, according to the equation:

$$E_{Al_xGa_{1-x}N} = xE_{AlN} + (1-x)E_{GaN} - bx(1-x) \quad (1)$$

As can be seen from Fig. 2 the fit according to Equ. (1) yields bowing parameters of $b = 0.31$ eV and 0.36 eV for E_1 and E_2, respectively, whereas the bandgap (E_0) bowing is well represented by $b = 0.9$ eV (not shown here).

In order to obtain the 'true' dielectric function of the investigated materials and not only pseudo-DF's, one has to fit Ψ and Δ by a layer model, taking into account interfacial layers and rms surface roughness, which is below 1 nm for most samples. The results for

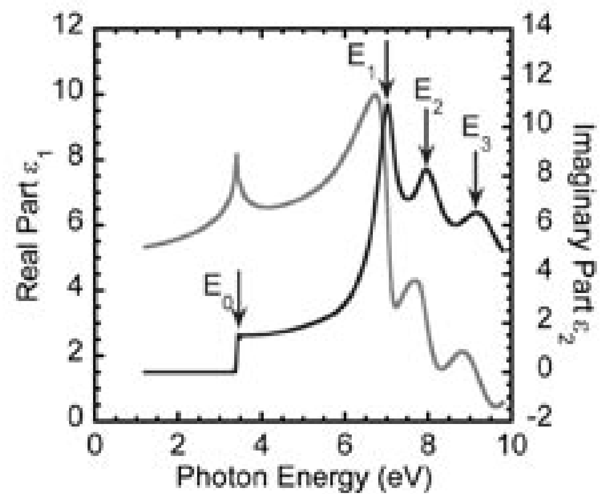

Fig. 3: Real (red) and imaginary part (blue) of the dielectric function of GaN. Critical points are indicated by arrows.

the real (ε_1) and imaginary part (ε_2) of the dielectric function of GaN are shown in Fig. 3. Although the hexagonal material is anisotropic, an isotropic model was used. This is due to the fact, that the growth direction is along the c-axis for all samples and therefore the measurements are not sensitive to the extraordinary DF. In Fig. 3 the spectral features of four critical points are clearly resolved. Below the band edge an excitonic feature is also detected, which is an indication for the high quality of the sample.

As the next step, the ellipsometric data for the AlGaN samples will be fitted in order to obtain the DF in dependence on the Al content.

In summary, the dielectric function of hexagonal GaN is presented as fitted from spectroscopic ellipsometry data. The bandgap and higher energetic critical points of the band structure of AlGaN are resolved for a wide range of Al contents. For the E_1 and E_2 transition energies a small bowing was found for the shift with increasing Al content.

This work has been supported by the BMBF grants 05KS4KTB/3 and 05ES3XBA/5 and the Thuringian ministry of Science, Research and Art (B609-02004).

[1] V. I. Litvinov, A. Manasson, D. Pavlidis, Appl. Phys. Lett. 85, 600 (2004).
[2] T. Ive, O. Brandt, H. Kostial, T. Hesjedal, M. Ramsteiner, K. H. Ploog, Appl. Phys. Lett. 85, 1970 (2004).
[3] T. Takano, Y. Narita, A. Horiuchi, H. Kawanishi, Appl. Phys. Lett. 84, 3567 (2004).
[4] S. Shokhovets et.al., J. Appl. Phys. 94, 307 (2003).
[5] T. Wethkamp, K. Wilmers, N. Esser, W. Richter, O. Ambacher, H. Angerer, G. Jungk, R. L. Johnson, M. Cardona, Thin Solid Films 313-314, 745 (1998).
[6] U. Rossow, D. Fuhrmann, M. Greve, J. Bläsing, A. Krost, G. Ecke, N. Riedel, A. Hangleiter, J. Cryst. Growth 272, 506 (2004).

Resonators for the Micro- and Nanoworld

Ch. Förster[1,*], V. Cimalla[1], K. Tonisch[1], K. Brückner[2], R. Stephan[2], E. Aperathitis[3], M. Hein[2], and O. Ambacher[1]
Departments of Nanotechnology[1] and RF and Microwave Techniques[2]
[3] Microelectronics Research Group, Foundation for Research and Technology-HELLAS, Heraklion, Greece

During the last years strong activities had been performed in the development and applications of micro- and nanoelectromechanical systems (MEMS and NEMS). MEMS and NEMS resonators are a combination between a micro- or nanomechanical structure and an electrical active element for the actuation and read-out of the sensor signal, respectively. Applications for these devices can be found in a wide range, especially for high frequency communication, measuring the viscosity of liquids, operating in nano- and picofluidic systems, sensing and diagnostic of biomolecules. The research on nanoresonators is currently focussed on very high frequency devices operating in the GHz range. This paves the way for new applications like low-power high-frequency devices for portable communication as well as the detection of single biomolecules, like proteins and viruses, in combination with functionalized surfaces of NEMS [1-3]. Resonators down to the sub micron range have been already demonstrated, based on silicon or silicon carbide [4].

In this work we present micro- and nanoelectromechanical 3C-SiC- and AlN-resonator beams with resonant frequencies between 20 kHz and 2 MHz. The operation principle is based on the common magneto motive actuation for these small mechanical elements. A thin conductive metal layer of Au on top of the resonator realizes the actuation and the detection. In Fig. 1 a schematically overview about the work principle of the beams is shown.

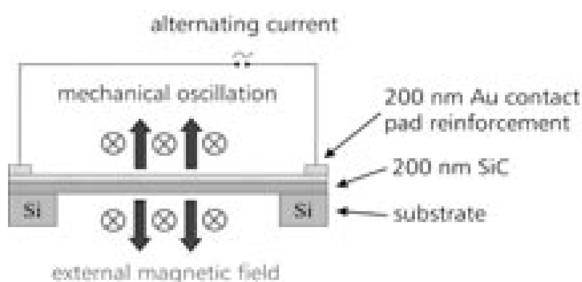

Fig. 1: Principle of the magnetomotive actuation.

The Lorentz force, caused by a RF current through the beams, placed in a static magnetic field of 0.5 T, is used for the actuation. The movement of the beams results in an induced electromotive force, which is proportional to the displacement. The characterisation of the different resonators takes place under ambient conditions, normal pressure and room temperature. The 200 nm thin epitaxial SiC [5] and AlN [6] layers were grown on silicon (100) and (111) oriented substrates, respectively.

Subsequently the beams were dry-etched by an electron cyclotron resonance (ECR) plasma technique with different fluorine and hydro-carbon gases [7, 8]. This new developed plasma based process allows anisotropic as well as isotropic etching for all materials involved. The created freestanding resonator bars have dimensions in the sub-μm to nm-range.

We realized beams with a separate read-out electrode (capacitive) as well as resonator structures with separate actuation and detection signal to solve the problems of the superimposition of actuation and detection. In Fig. 2a a 2 μm wide doubly clamped SiC beam with 250 nm thickness was processed and a capacitive read-out unit is placed very close with a gap of around 1 μm to the resonator. The capacitance between the middle electrode and the beam is changed as the beam is deflected causing a small current if the electrode voltage is kept constant. A second possibility for the separation is shown in Fig. 2b. Three suspended beams are mechanically coupled in the middle, however, electric separated. The two outer beams are supplied with the driving voltage while the beam in the middle is sensing only the induced electromotive force. The underetching of these resonator geometries is much more sophisticated because of the extended middle area where the beams are mechanically coupled. The ECR process for these kinds of resonators must be optimized to underetch the small beams as well as the coupling area without destroying the resonator itself.

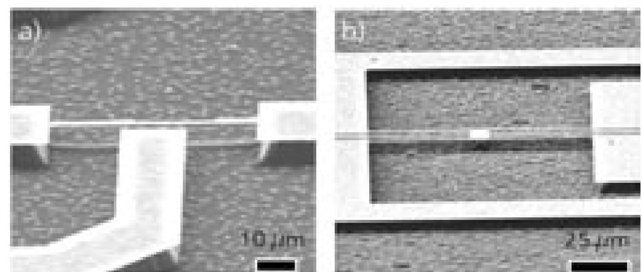

Fig. 2: SEM-Images of different 3C-SiC beams: a) beams with middle electrode for capacitive read out, b) three mechanically coupled beams with electrical separation.

* phone : +49-(0)3677-69-3352, email: christian.foerster@tu-ilmenau.de

The difficulties arose from the different etch times needed for under-etching the resonator beams and the coupling area in the middle. To finish the etch procedure and to guarantee the free standing of the coupled structure a dip in 60°C hot 25% KOH acid was done for several seconds. The wet etching procedure, which only etches the silicon and not the SiC due to the strong chemical inertness, is followed by a dip in hot deionized water and isopropanol in order to inhibit the precipitation out of the salt solution. A nanoresonator with sizes of 10x0.5x0.25 μm^3 is shown in Fig. 3a. An array of beams with different length to realise varying resonance frequencies is visible in Fig. 3b. The width of the resonator structures will be decreased in the future down to 100 nm and less by using the technology of e-beam lithography.

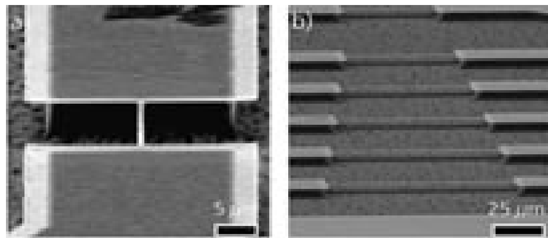

Fig. 3: SEM-images of different beams: a) 500 nm wide and 250 nm thick nanoresonator structure, b) doubly clamped beams of different length.

In Fig. 4a and 4b doubly clamped AlN beams with different length are shown consisting of a 200 nm piezoelectric active AlN film with 50 nm Ni or Au on top. The shown structures are still working using the magnetomotive effect.

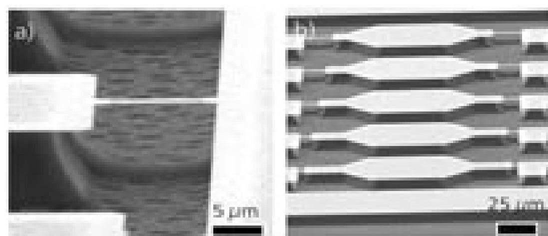

Fig. 4: SEM-images of AlN resonator beams: a) AlN beam with top metallization, b) array of AlN resonator structures with different length.

The piezoelectrical actuation represents a driving and detection scheme without the need of a strong magnetic field and therefore, there is the main focus of our future investigation. This new kind of actuation will open the way to new high sensitive and low energy consuming as well as easy to integrable MEMS and NEMS. The scheme of the actuation of the piezoelectrical active AlN-resonator is presented in Fig. 5.

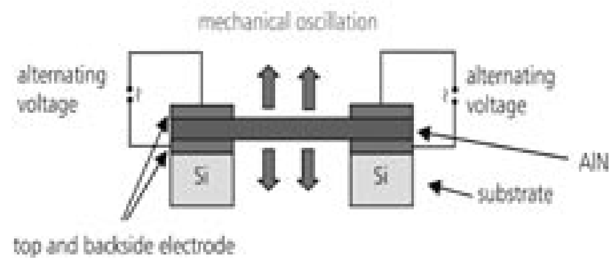

Fig. 5: Principle of the piezoelectric actuation of the AlN beams.

An alternating voltage applied to the AlN-film causes a mechanical expansion and contraction of the AlN-layer, which induces a mechanical oscillation of the suspended beam.

The first AlN micro- and nanoelectromechanical resonators that operate with the new kind of actuation are shown in Fig. 6. An important and difficult technology is the interruption of the top electrode to prevent the short cut over the beam. The careful processing of the beams has to guarantee, that the isolating properties of the AlN layers are kept stable. In the future we will integrate a 2DEG into the beam structure of AlGaN/GaN and use these electron gas for reading out the sensor signal.

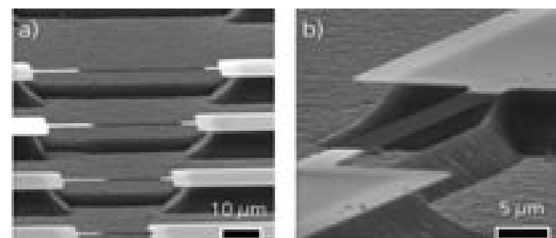

Fig. 6: SEM-images of new AlN piezoelectrical resonator beams: a) array of piezoelectrical AlN resonator structures with different length, b) AlN beam with needed interruption of the top metallization for the piezoelectrical actuation.

This work has been supported by the Deutsche Forschungsgemeinschaft, SPP 1157 „Integrierte elektrokeramische Funktionsstrukturen", contract AM 105/2-1, and DAAD-314/ikyda-dr D/03/40373, PPP-Greece: „Leistungsverhalten von GaN-basierenden UV-Photodetektoren und Lasern".

[1] B. Ilic, D. Czaplewski, M. Zalalutdinov, and H.G. Craighead, "Single cell detectiowith micromechanical oscillators", J. Vac. Sci. Technol. B , vol. 19, no. 6, pp. 2825-8, 2001.
[2] C.T.-C. Nguyen, "Vibrating RF MEMS for low power wireless communications", Proc. 2000 Int. MEMS Workshop (iMEMS'01), Singapore, pp. 21-34, 2001.
[3] S. Pourkamali, R.Abdolvand, and F.Ayazi, "A 600kHz Electrically-Coupled MEMS Bandpass Filter", IEEE MEMS'03, Kyoto, Japan, pp. 702-5, 2003.
[4] Y.T. Yang, K.L. Ekinci, X.M.H. Huang, L.M. Schiavone, M.L. Roukes, C.A. Zorman, and M. Mehregany, "Monocrystalline silicon carbide nanoelectromechanical systems", Appl. Phys. Lett. vol. 78, no. 2, pp. 162-4, 2001.
[5] Ch. Förster, V. Cimalla, O. Ambacher, J. Pezoldt, "Low temperature chemical vapor deposition of 3C-SiC on Si substrates", Mater. Sci. Forum, Silicon Carbide and Related Materials 2004 (ECSCRM 2004), 483-485, pp. 201–204, 2005.
[6] H.P.D. Schenk, G.D. Kipshidze, V.B. Lebedev, S. Shokhovets, R. Goldhahn, J. Kräußlich, A. Fissel, and W. Richter, „Epitaxial growth of AlN and GaN on Si(111) by plasma-assisted molecular beam epitaxy", J. Crystal Growth, vol. 201-202, pp. 359, 1999.
[7] Ch. Förster, V. Cimalla, K. Brueckner, V. Lebedev, R. Stephan, M. Hein, O. Ambacher, "Processing of novel SiC and group III-nitride based micro-and nanomechanical devices", phys. stat. sol.(a) 202, pp. 671-676, 2005.
[8] Ch. Förster, V. Cimalla, R. Kosiba, G. Ecke, P. Weih, O. Ambacher, J. Pezoldt, "Etching of SiC with fluorine ECR plasma", Mater. Sci. Forum, Silicon Carbide and Related Materials 2003 (ICSCRM 2003), 457-460, pp. 821, 2004.

Nucleation control and growth acceleration in FLASiC assisted short time liquid phase epitaxy by melt modification

J. Pezoldt[1,*], Th. Stauden[1], Ch. Förster[1], J. Stoemenos[2], D. Panknin[3], and W. Skorupa[3]
[1] Department of Nanotechnology
[2] Physics Department, Aristotele University Thessaloniki, Greece
[3] Research Centre Rossendorf, Dresden

The only SiC polytype of technological importance which is not available as a single crystal is the cubic form. This is a drawback for different device applications, because this polytype exhibits the highest low field carrier mobility without anisotropy. This makes the material prospective for different device applications, because 3C-SiC exhibits also the lowest interface state densities in a MOS structure compared to other SiC polytypes. But it is very difficult to grow single crystalline 3C by using the classical sublimation technique. This is caused by the fact that 3C-SiC (ß-SiC) is a metastable polytype and phase transition from β to α-SiC occurs at temperatures above 1800°C [1, 2]. This imposes strong restrictions on the classical sublimation technology and led up to now to the situation that no single crystalline 3C-SiC grown by sublimation technology is commercially available. For this reason different methods were tested to produce single crystalline 3C namely, Liquid Phase Epitaxy, Chemical Vapour Deposition, heteroepitaxy on specifically prepared α-SiC and heteroepitaxy of 3C-SiC on silicon or SOI substrates. The last methods suffer from the high lattice and thermal expansion mismatch between Si and SiC leading to a high dislocation density periodically regenerated during the growth of the 3C and a high density of stacking faults. Nevertheless, based on such heteroepitaxial growth, free standing 3C-SiC is now commercially available from HAST, but unfortunately the price to quality ratio for the state of the art material is not favourable compared to 4H and 6H The improvement of this ratio is of high importance especially by lowering the defect density.

The defect density of the heteroepitaxially grown layers mainly results from the high defect density in the seeding layer formed by the carbonization of the silicon substrate which is the mandatory step of the process. A method to reduce the defect density consists in the application of a very powerful irradiation which melts the thin silicon layer beneath carbonisation layer. At the end of this short light pulse, the most defective part of the silicon carbide which has been dissolved recrystallises on the initial layer with a much higher crystalline quality. This is the FLASiC process [3, 4]. To avoid the buckling of the seeding layer and to improve the recrystallisation and growth behavior during the FLASiC process a three layers stack consisting of 3C-SiC/Si/3C-SiC/Si-substrate was used. This composition allows to transform the recrystallisation onto the upper surface of the lower SiC on the Si substrate [4]. To improve the recrystallization compositional changes in the Si by adding C, Ge or both elements were used. The present study reports on the influence of these modifications on the recrystallisation and growth behavior during FLASiC processing.

The layer stacks were grown by solid source molecular beam epitaxy (SSMBE) and/or UHVCVD. The first 3C-SiC layer was grown after a carbonisation step at 1000°C with a growth rate of 1nm/min. The intermediate silicon over layers (SOL) were grown at 620°C. The second 3C-SiC layer was grown identical to the first one. The composition of the intermediate silicon layers (SOL) was varied by adjusting the parallel operating silicon, carbon and germanium sources. Subsequently to the growth process the prepared wafer stacks were FLASiC processed at 800°C and two different flash voltages 3.1 and 3.2 kV. The light pulse duration was 20 ms. The resulting layers were analysed by cross-section, plane view and high resolution transmission electron microscopy as well as cross section transmission electron microscopy (XTEM) accompanied with EDX.

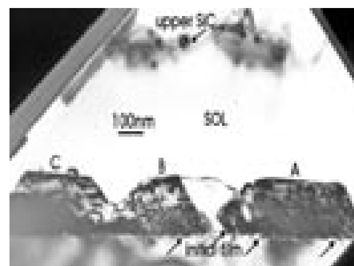

Fig. 1: XTEM micrograph of a 3.1 kV at 800°C FLASiC processed 35 nm SiC/300 nm $Si_{0.93}C_{0.03}Ge_{0.04}$/35 nm SiC initial wafer stack.

Fig. 1 displays a typical XTEM micrograph of a FLASiC processed layers stack. This resulting structure is typical and independent of the composition of the melt if the Ge content is below 10 %. As it is evident the thickness of the lower 3C-SiC layer increases

* phone : +49-(0)3677-69-3412, email: joerg.pezoldt@tu-ilmenau.de

during the flash lamp annealing. The thickened 3C-SiC layer consists of four different parts: (1) small trapezoidal pyramids at the interface of the first 3C-SiC layer and the Si substrate (shown with arrows in Fig. 1), (2) the initial but thermal annealed 3C-SiC layer (marked with > < in Fig. 1), (3) the melted and recrystallised 3C-SiC layer and (4) a liquid phase epitaxial grown 3C-SiC layer with large trapezoidal pyramids (TP). The large TP's are denoted in Fig. 1 with A, B and C. The dislocation density within the melted and recrystallised layer as well as in the TP's is around one order of magnitude lower compared to the dislocation density of the initial lower SiC layer. The average dislocation density in the uppermost part of the 3C-SiC layer is around 2 to $3x10^{10}$ cm^{-2} [4, 5]. The second 3C-SiC layer on top of the SOL layer after the flash lamp annealing is discontinuous. This typical multilayer structure is caused by the ongoing processes during the flash lamp annealing procedure. The SOL layer is melted during the FLASiC process. The formed Si melt dissolves the uppermost part of the lower 3C-SiC layer and the lower part of the capping 3C-SiC layer. The remaining parts of the nondissolved SiC layers undergo only a thermal annealing procedure. In a second step at the end of the light pulse the solidification starts. This process leads to a liquid phase epitaxial nucleation and growth of 3C-SiC with a lower defect density. During this step the temperature of the near substrate region is lower than the temperature of the surface of the multilayer system. Due to the existing temperature gradient the dissolved carbon of the melt is transferred to the surface of the lower 3C-SiC layer leading to a liquid epitaxial thickening of the lower 3C-SiC layer. The partial dissolution of the capping SiC layer lead to the disruptive structure of the upper SiC layer observed after the FLASiC processing by TEM (Fig. 1). The small TP's formed at the 3C-SiC/Si-substrate interface are caused by a partially melting process of the substrate near the interface, in agreement with [4, 5]. They can be avoided by adjusting carefully the flash lamp conditions [4].

Ge and C additions to the SOL and subsequent FLASiC processing lead to an substantial increase of the TP size. The mean size of the TP's was observed to be 300 nm. In the case of flash lamp processing at 3.2 kV 500 nm was achieved. Furthermore, the averaged thickness of the grown 3C-SiC layer is 150 nm corresponding to a growth rate of 7.5 μm/s. The determined grain size dependence as a function of the additions to the SOL is the following: $D_{Si} < D_{Si+Ge} < D_{Si+C} < D_{Si+Ge+C}$. Additionally it was observed that if carbon was added to the SOL the remaining thickness of the upper SiC layer was smaller than in the case of the pure Si and Si + Ge melts. That means that carbon additions to the melt not only support the growth of the 3C-SiC on the lower SiC layer but also lead to a stronger dissolution process of the upper SiC layer and therefore to an enhancement of the carbon concentration in the SOL leading to an enhanced growth rate on the lower 3C-SiC layer.

The self enhancement of the dissolution of the upper SiC layer might be caused by the reduction of the Si band gap as a consequence of the C incorporation. In dependence on the substitutional C content the Si band gap reduces from 1.1 eV for pure Si up to 0.82 eV for C concentrations exceeding 3% [6]. The lower band gap increases the absorption coefficient and therefore the SOL temperature during FLASiC processing. The increased melt temperature leads to a stronger dissolution of the upper SiC layer. If the used Ge content is small, i.e. below 10 %, the effect on the band gap and the melting temperature of the solid solution can be neglected. In this case the reason of the increase of the TP size might be explained by the fact that Ge additions increases the carbon adatom mobility on the growing surface and the carbon transport through the Si melt during the flash lamp annealing. If both elements are added an additive effect appears. The increase of the grain size by adding Ge into the growth environment was also observed in the case of SiC nucleation on the Si surfaces [7].

If the Ge content of the SOL and the FLASiC conditions are properly chosen a homogeneous layer with a 3C-SiC thickness between 150 and 200 nm can be achieved (Fig. 2).

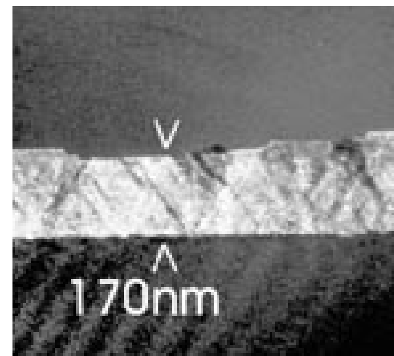

Fig. 2: 3C-SiC layer after FLASiC processing and a SOL composition of $Si_{0.55}Ge_{0.45}$

Significant improvement of the TP's size and the deposited layer thickness was achieved if Ge and C is added to the SOL. This effect is caused by the modification of the optical properties and the mass transport properties of the SOL.

This work was supported by the European Union within under grant No. G5RD-CT-2002-00704.

[1] H. Jagodzinski, Neues Jahrb. Miner. Monatsh. 3 (1954), 49.
[2] J. Pezoldt, Mater. Sci. Eng. B29 (1995), 99.
[3] D. Panknin, J. Stoemenos, M. Eickhoff, V. Heera, N. Vourouzis, G. Krötz and W. Skorupa, Mater. Sci. Forum 353-356 (2001), 151.
[4] W. Skorupa, D. Panknin, W. Anwand, M. Voelskow, G. Ferro, Y. Monteil, A. Leycuras, J. Pezoldt, R. McMahon, M. Smith, J. Camassel, J. Stoemenos, E. Polychroniadis, P. Godignon, N. Mestres, D. Turover, S. Rushworth and A. Friedberger, Mater. Sci. Forum 457-460 (2004), 175.
[5] E. Polychroniadis, J. Stoemenos, G. Ferro, Y. Monteil, D. Panknin and W. Skorupa, Mater. Sci. Forum 457-460 (2004), 351.
[6] H.J. Osten, Thin Solid Films 367 (2000), 101.
[7] T. Wöhner, Th. Stauden, J.A. Schaefer and J. Pezoldt, Mater. Sci. Forum 338-342 (2000), 281.

Heteropolytype structures based on SiC

F. M. Morales*, Ch. Förster, O. Ambacher, and J. Pezoldt
Department of Nanotechnology

The SiC family of crystals are suitable materials for the formation of heterostructures since the difference in gap energies among the SiC polytypes is relatively high (2.2 eV for β (3C) and 3.4 eV for α (2H)). Actually, the intentional control of polytype transitions on alternative SiC layers open an attractive door in the field of modulated band-gap engineering based on chemically homogeneous heteropolytypic structures. In this context, it is important to work out rules for a desired polytype change as a consequence of changing technological relevant parameters. It is known that α to β transitions can be promoted by providing α-SiC polytypes of a higher energy by ion implantation and annealing or either mechanical, thermal or pressure chocking [1-5]. Cubic SiC was also grown on hexagonal templates by sublimation epitaxy [6], atomic layer epitaxy [7] or molecular beam epitaxy [8]. Heteroepitaxial growth of β-SiC on α-SiC (0001) substrates was carried out in cold wall chemical vapor deposition (CVD) reactors [9,10] while pulsed laser deposition allow the formation of β (3C) or α (2H or 4H-SiC) polytypes on sapphire [11].

It is definitely of higher difficulty to induce the transition from cubic (β) to hexagonal and/or rhombohedral (α) SiC, and even more difficult when the conditions do not vary during the growth process as it is in the current experiments. Relative good control of heteropolytypic transitions from the cubic phase to the hexagonal one was achieved only with solid source molecular beam epitaxy (MBE) [12] or by a combination of sublimation growth and ion implantation [13]. If Si is used as substrate, β-SiC is often heteroepitaxially grown by CVD or MBE. Nevertheless, up to now there is no reliable technique to grow hexagonal or rhombohedral SiC polytypes on the cubic phase. A few attempts by CVD have shown the presence of hexagonal domains included in cubic SiC layers on Si [14] or via nano-sized silicon nitride precursors, not fully orientated α-SiC could be grown on Si [15].

In this report, a technique to nucleate and grow epitaxially nanoscale α-SiC (0001) on β-SiC(111)/Si(111) substrates is presented. The method consists in controlling the adjustments of the Si to C ratio during heteroepitaxial growth. In this way, hexagonal and/or rhombohedral SiC nuclei, mainly 4H-SiC, are developed on SiC cubic layers, after different thicknesses depending on the selected growth parameters: Si/C ratio and temperature. It has been possible to delimitate the regions where the β to α transition occurs for the ultra-high vacuum CVD process. These original structures, and their defects (stacking faults, twins, polycrystalline top clusters) are investigated by reflection high-energy electron diffraction (RHEED) and transmission electron microscopy (TEM).

The deposition was carried out in an UHV chamber with a base pressure of $1x10^{-8}$ mbar. For the growth of the heteroepitaxial layers, a mixture of silane (SiH_4), ethene (C_2H_4) and hydrogen (H_2) is used. The RCA cleaned Si (111) wafers were loaded and transferred into the deposition chamber, out-gassed at 350°C for 30 min and heated to 450°C. In order to carbonize the Si surface, C_2H_4 was introduced with a flow rate of 7 sccm. After 10 min, the temperature was increased up to 940°C with a heating rate of 0.3 K/s. Thereafter the flow rates of H_2 and C_2H_4 were set up to 10 and 1 sccm respectively while SiH_4 was varied between 1 and 2 sccm. The substrate temperature was selected to be between 950 and 1050°C with a deposition time between 60 and 720 min. Finally, the substrate was cooled down at 2 K/s. RHEED experiments were carried with a Staib EK35R system. TEM was implemented in both TECNAI 20S-TWIN (FEI) and JEOL 2010F electron microscopes.

Fig. 1 shows two kind of typical RHEED patterns found for the whole set of grown samples: (a) only 3C-SiC reflections and (b) α-SiC reflections: ordered dots placed along the 01-1N streaked row of reflections indicating long range ordering in the sequence of stacking faults parallel to the surface, related to hexagonal and/or rhombohedral SiC polytypes. In Fig. 1 (b) the arrowed brighter reflections are caused by the 4H-SiC polytype, which was found to be the most common phase among the α-SiC.

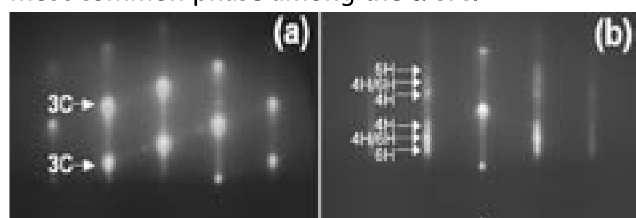

Fig. 1: RHEED patterns along <110> azimuth.

* phone : +49-(0)3677-69-3412, email: paco.morales@tu-ilmenau.de

RHEED patterns for an intermediate state with reflections related to 3C-SiC, twins and streaks associated to disordered and/or ordered stacking faults were also observed.

Fig. 2 (a) shows the common structure of one of the samples where the β to α transition occurs. 3D nuclei of α-SiC develops after a definite thickness of β-SiC; 50 nm for this example of a sample grown at 1000°C with a Si/C ratio of 1.45. The α and β SiC layers are epitaxially orientated on the Si substrate and exhibit some characteristic defects as voids at the interface beneath the SiC layer, stacking faults and twins oblique and parallel to the interface plane in the β-SiC structure, faceting of α-SiC nuclei often continuing {111} walls dividing cubic SiC domains and top polycrystalline SiC hillocks [16, 17]. As it is displayed in the high-resolution micrograph of Fig. 2 (b), the ABCA... stacking sequence of closed packed layers along the [111] direction in the β layer is disrupted and subsequently long range ordered.

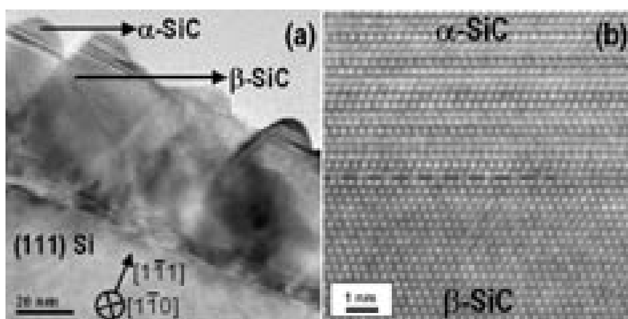

Fig. 2: TEM micrographs showing the structure of specimens with α-SiC nucleation on top.

Fig. 3 shows the temperature - Si/C-ratio - phase diagram where α and/or β SiC is present at the surface region of the grown epitaxial layer. Hexagonal or rhombohedral nuclei form under the use of relatively C rich conditions (Si/C ratio=1.3-1.9) compared to the growth conditions were only β-SiC is stabilized (Si/C ratio >2). Additionally, Si reach conditions allowed faster growth rates of SiC layers on top of Si. From these experimental observations it can be concluded that the α-SiC develops after the formation of an effective cubic capping thickness when Si stops to out-diffuse from the substrate and new thermodynamic conditions (C rich conditions) make the ordered cubic structure to develop disordered stacking faults giving rise to longer range ordering and new polytypes formation.

As a summary, in UHV-CVD, the formation of nanoscale α-SiC on β-SiC/Si(111) templates is possible at low temperatures (950-1050°C) by adjusting Si/C ratios during the growth. This event is independent on the carbonization procedure used for the β-SiC/Si(111) pseudo substrate fabrication. The main reason for the favoured formation of the α-SiC/β-SiC nanoheteropolytypic structures was found to be the nucleation and growth under carbon-rich conditions.

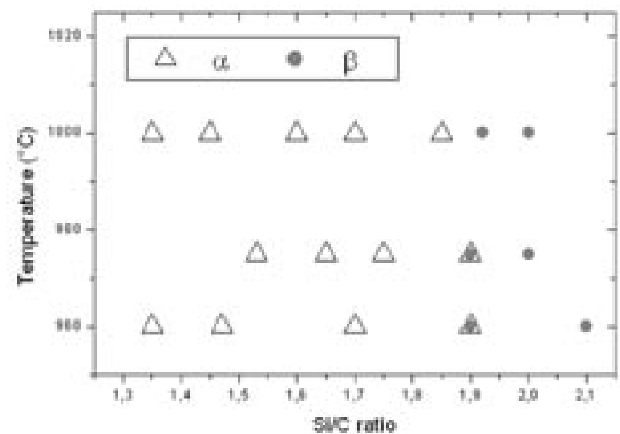

Fig. 3: Relation of SiH_4/C_2H4 fluxes where only β-SiC or α-SiC nucleation on β-SiC layers were observed at different temperatures.

F. M. Morales would like to thank Alexander von Humboldt Foundation by the economic support under a Humboldt Research Fellowship (SPA/1114640 STP).

[1] A. A. Kalnin, J. Pezoldt and Yu. M. Tairov, Sov. Phys. Sol. State 29 (1987) 575-577.
[2] J. Pezoldt, A. A. Kalnin, D. R. Moskwina and W. D. Savelyev, Nucl. Instr. Meth. B80 (1993) 943-948.
[3] P. A. Kistler-De Coppi and R. Richarz, Int. J. High Tech. Ceram. 2 (1986) 99-113.
[4] X. Y. Yang, Y. K. Wu and H. Q. Ye, Phil. Mag. Lett. 80 (2000) 333-339.
[5] Y. Q. Zhu, T. Sekine, T. Kobayashi and E. Takazawa, J. Mater. Sci. 33 (1998) 5883-5890.
[6] A. A. Levedev, N. S. Savkina, A. M. Strelchuk, A. S. Tregugova and M. P. Scheglov, Mat. Sci. Eng. B46 (1997)168-170.
[7] T. Yoshinobu, H. Mitsui, I. Izumikawa, T. Fuyuki and H. Matsunami, Appl. Phys. Lett. 60 (1992) 824-826.
[8] M. Diani, L. Simon, L. Kluber, D. Aubel, I. Matko, B. Chenevier, R. Madar and M. Audier, J. Cryst. Growth 235 (2002) 95-102.
[9] S. Nakamura, T. Kimoto and H. Matsunami, J. Cryst. Growth 270 (2004) 455-461.
[10] H. Matsunami and T. Kimoto, Mater. Sci. Eng. R20 (1997) 125-166.
[11] T. Kusumori, H. Muto and M. E. Brito, Appl. Phys. Lett. 84 (2004) 1272-1274.
[12] A. Fissel, Phys. Rep. 149 (2003) 149-255.
[13] J. Pezoldt, A. A. Kalnin and W. D. Savelyev, Nucl. Instr. Meth. B65 (1992) 361-365.
[14] K. Pfenninghaus, A. Fissel, U. Kaiser, M. Wendt, J. Kräußlich, G. Peiter, B. Schröter and W. Richter, Mat. Sci. Eng. B46 (1997) 164-167.
[15] R. Liu, B. Yang,Z. Fu,Q. Chen,L. Hong, M. Li, Z. Liu and Y. Ruan, Thin Sol. Films, 345 (1999) 188-1911.
[16] F. M. Morales, Ch. Förster, O. Ambacher and J. Pezoldt, Proc. Electrochem. Soc. (in press).
[17] F. M. Morales, Ch. Förster, O. Ambacher and J. Pezoldt, Inst. Phys. Conf. Ser. (in press).

Ion Beam Synthesis of $(Si_{1-x}C_{1-y})Ge_{x+y}$ Solid Solutions

P. Weih[1,*], Th. Stauden[1], G. Ecke[1], S. Shokhovets[2], Th. Kups[3], M. Voelskow[4], W. Skorupa[4], and J. Pezoldt[1]
Departments of Nanotechnology[1], Experimental Physics[2], and Materials for Electrical Engineering
[4] Research Centre Rossendorf, Dresden

Silicon Carbide provides, because of its excellent material properties, a great potential for applications in electronic devices, operating at high temperatures, high frequencies and harsh environment conditions. The relative low carrier mobility, the absence of well developed techniques and heterostructure materials for band-gap and strain engineering in the SiC technology limit the applications of this material in electronic devices. The incorporation of isovalent Ge atoms in the Silicon Carbide lattice could be able to change the structural, electrical and optical properties of the SiC material and enlarge the application fields and strengthen the role of SiC in electronics. It is expected that the larger atomic size of the Ge atoms will increase the lattice parameter of SiC [1]. This could be of importance for the further growth of materials with larger lattice constants such as e. g. GaN on SiC. For these two reasons the formation of $(Si_{1-x}C_{1-y})Ge_{x+y}$ semiconductor solid solutions could be of great interest.

The immiscibility of Ge in the SiC lattice, the low desorption temperature of Ge on the SiC surface and the tendency of Si- and Ge- to cluster formation are challenges that make the epitaxial growth of low defect density ternary alloys very difficult. Up to now only a few experimental works reporting on the epitaxial growth of $(Si_{1-x}C_{1-y})Ge_{x+y}$ alloys on silicon and silicon cabide substrates are available [2 - 6].

Ion implantation of Ge in SiC is an alternative technique providing the possibility to overcome the obstacles attendant to the growth process. This material synthesis method allows the incorporation of Ge with concentrations exceeding the thermodynamical Ge miscibility limit and leads to the formation of $(Si_{1-x}C_{1-y})Ge_{x+y}$ alloys. Up to now, only a few works are available reporting on the Ge implantation into hexagonal SiC (4H-SiC and 6H-SiC). They were carried out at different implantation conditions and post implant treatments. The obtained results can be summarized as follows: (1) amorphisation of the SiC lattice occurs at room temperature implantation with a Ge dose of about $3x10^{14}$ cm^{-2} [7, 8], (2) polytype phase transitions from hexagonal into cubic polytype were observed during high temperature annealing process at 1400-1600°C [9], (3) phase separation of Ge nanocrystals in the SiC host material is possible at annealing temperatures higher than 1400°C [10, 11], (4) formation of compressive strained 4H-SiC:Ge layers was obtained as a consequence of high temperature ion implantation at temperature von 1000°C [12]. In the present study the effort was to stimulate Ge incorporation into the 3C-SiC and 4H-SiC lattice by ion beam synthesis in order to create a metast-able $(Si_{1-x}C_{1-y})Ge_{x+y}$ alloy.

The ion implantation was carried out into 3C-SiC thin films with two different layer thicknesses of 120 nm and 300 nm. They were grown by Solid Source Molecular Beam Epitaxy on (111)-oriented on-axis Si wafers. In the case of 4H-SiC single crystalline substrates from Cree were used. The implantation was carried out at elevated temperatures (600°C) in order to prevent the material amorphisation and to minimize the defect formation in the crystal lattice of the host material.

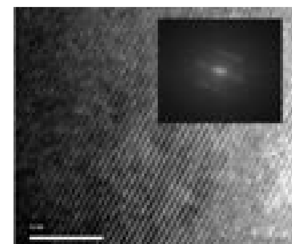

Fig. 1: TEM image of the implanted part of the 4H-SiC crystal. The inlet shows a fast Fourier transformation of the image.

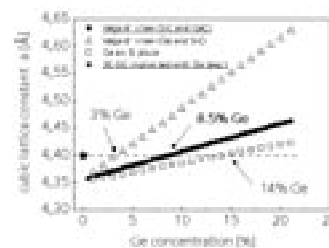

Fig. 2: Dependence of the $(Si_{1-x}C_{1-y})Ge_{x+y}$ cubic lattice constant versus Ge concentration based on different models.

The chosen implantation temperature was motivated by a previously achieved result, where it was shown that the optimal implantation temperature for the formation of a $(SiC)_{1-x}(AlN)_x$ pseudobinary solid solution is around 600°C where the lattice damage can be kept low and the cubic to hexagonal polytype

* phone : +49-(0)3677-69-3352, email: petia.weih@tu-ilmenau.de

transition can be suppressed [12]. TRIM simulations were carried out in order to choose the value of the implantation energy so that the implantation maximum is located in the middle of the 120 nm and in the upper 1/3 of the 300 nm thick SiC layer, respectively. Two series of experiments were carried out. In the first case Ge was implanted in 120 nm 3C-SiC heteroepitaxial layers. The implantation energy for these experiments was chosen to be 140 keV and the ion dose was $1x10^{17}$ cm^{-2}. In the second case Ge was implanted into 300 nm 3C-SiC heteroepitaxial layers and the 4H-SiC crystals with an implantation energy of 200 keV and an ion dose of $4.7x10^{16}$ cm^{-2}. The lower implantation energy experiment leads to a Ge peak concentration of approximately 18 at.%. The higher implantation energy experiment leads to a Ge peak concentration of approximately 5.8 at.%. Thermal annealing experiments were carried out for 1 minute in a rapid thermal annealing (RTA) equipment in Ar-atmosphere. The annealing temperature was chosen to be below the melting point of Si. Annealing experiments were carried out at different temperatures in the range between 800°C and 1300°C. The structural and composition were investigated by x-ray diffraction, transmission electron microscopy (TEM), Auger electron spectroscopy. Furthermore, electrical and optical measurements were carried out to asses changes in the physical properties of the synthesized layers.

TEM investigations revealed that only weak lattice dam-age was introduced into the host lattice during the ion beam synthesis process under the chosen implantation conditions (Fig. 1).

The deviation of the lattice constant of the 3C-SiC layers after ion implantation in comparison to an unimplanted sample was investigated by x-ray diffraction methods. After converting the measured (111) plane distance for this sample to the cubic lattice parameter a lattice parameter equal to 4.3999 Å was calculated for the implanted layer. Under the assumption that theoretical proposed deviation [1] of the lattice constant with increasing incorporation of Ge is valid, the measured value corresponds to a substitutional incorporation of Ge atoms into SiC between 3% (assumtpion: Vegard`s law between SiC and Ge) and 14% (assumption: Ge occupies only Si places in the crystal lattice) depending on the used theoretical model [1]. Applying a simple linear regression between the lattice parameters of cubic SiC and GeC the Ge concentration was calculated to be about 8.5%. This value corresponds to an incomplete substitutional incorporation of Ge atoms into the SiC lattice (Fig. 2). The average fraction is about 50%. For this estimation the theoretical calculated value for the lattice constant of cubic GeC from [12] was used.

Spectroscopic ellipsometry studies showed that the implanted layers possess a significantly larger absorption coefficient compared to the unimplanted 3C-SiC and demonstrate an absorption edge at lower photon energies (Fig. 3). These observations might be an indication of a band gap reduction as a consequence of Ge incorporation in the SiC lattice. Furthermore electrical and Raman measurements carried out on the 4H-SiC samples revealed a reduction of the specific resistance and a increase of the carrier concentration, respectively. This observation indicates on an incorporation of Ge on V_{Si} and V_C lattice sites and their complexes. This defects exhibit large activation energies and are therefore deep centres acting as traps for free carriers. If Ge now enters such a lattice position their concentration is lowered and the carrier concentration increases despite the fact that Ge is an isovalent nondoping group IV element.

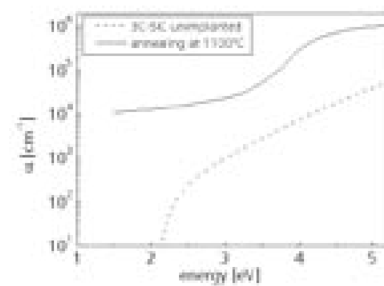

Fig. 3: Spectral dependence of the absorption coefficient for a 3C-SiC sample annealed at 1100°C (solid line) and a high 3C-SiC layer (dotted line) for comparison.

In conclusion ion beam synthesis is a suitable method for the formation of a metastable $(Si_{1-x}C_{1-y})Ge_{x+y}$ alloy exhibiting different properties compared to single SiC polytypes.

This work has been supported by the Thuringian Ministry of Culture under contract B 607-02006

[1] C. Guedj and J. Kolodzey, Appl. Phys. Lett. 74, 691 (1999).
[2] S. Mitchell, M. G. Spencer and K. Wongchotigul, Mater. Sci. Forum 264-268, 231 (1998).
[3] W. L. Sarney and M. C. Wood, J. Appl. Phys. 91, 668 (2002).
[4] P. Weih, V. Cimalla, Th. Stauden, R. Kosiba, G. Ecke, L. Spiess, H. Romanus, M. Gubisch, W. Bock, Th. Freitag, P. Fricke, O. Ambacher and J. Pezoldt, phys. stat. sol. (c) 1, 347 (2003).
[5] M. Diani, L. Kubler, L. Simon, D. Aubel, I. Matko, and B. Chenevier, Phys. Rev. B 67, 125316 (2003).
[6] P. Weih, V. Cimalla, Th. Stauden, R. Kosiba, L. Spieß, H. Romanus, M. Gubisch, W. Bock, Th. Freitag, P. Fricke, O. Ambacher and J. Pezoldt, Mater. Sci. Forum 457-460, 297 (2004).
[7] Y. Pacaud, J. Stoemenos, G. Brauer, R. Yankov, V. Heera, M. Voelskow, R. Kögler, W. Skorupa, Nucl. Instr. and Meth. in Phys. Res. 120, 177 (1996).
[8] V. Heera, J. Stoemenos, R. Kögler, W. Skorupa, J. Appl. Phys. 77, 2999 (1995).
[9] Ch. Schubert, U. Kaiser, A. Hedler and W. Wesch, J. Appl. Phys. 91, 1520 (2002).
[10] U. Kaiser, Journal of Electron Microscopy 50, 251 (2001).
[11] G. Heß, J. Kraeusslich, B. Wunderlich, W. Wunderlich, ESRF report from 06.11.2002, experiment number Me 309, http://ftp.esrf.fr/pub/smis1.esrf.fr/21179_A.pdf, (2002).
[12] R. Pandey, M. Rerat, C. Darrigan, M. Causa, J. Appl. Phys. 88, 6462 (2000).

Epitaxial stabilization of cubic AlN polytype on 3C-SiC/Si(111) templates

V. Lebedev*, U. Kaiser, V. Cimalla, J. Pezoldt, C. Förster, and O. Ambacher
Department of Nanotechnology

Among III-nitrides, AlN (E_g = 6.2 eV) is being intensely investigated for possible electronic and optoelectronic applications since the early 90th. The wide bandgap afforded by aluminum nitride, coupled with favorable transport properties and heterojunction capability, pave the way for UV optoelectronics [1] and high power electronic applications.
Three common crystal structures are shared by the tetrahedrally coordinated binary nitrides: rocksalt ($Fm\underline{3}m$), wurtzite (2H, $P6_3mc$) and zinc blende (3C, $F\underline{4}3m$). The two latter structures differ only in the relative handedness of the fourth interatomic bond along the (111) chain. These rather subtle structural differences and relatively small differences in the internal energies ($\Delta E_{W\text{-}ZB}$) are manifested by the well known 2H-3C polytypism. Depending on the epitaxial conditions, AlN thin films can be deposited in either forms [2]. However, the largest among the III-nitrides 2H-3C energy difference ($\Delta E_{W\text{-}ZB}$ ~ -18.41 meV/atom) forces the 2H-phase of AlN to dominate at the usual growth conditions. There were a few reports on the epitaxy of cubic AlN films stabilized by the lattice replication, but the crystal quality of the 3C- and rocksalt AlN epilayers is still a challenge.

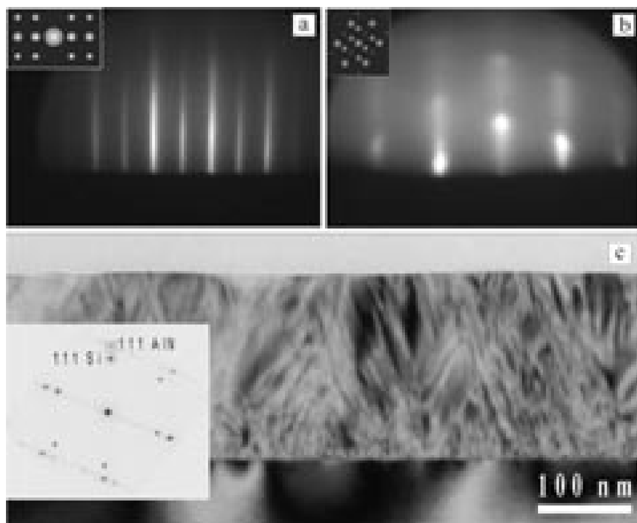

Fig. 1: RHEED pattern of a) 2H-AlN layer on 3C-SiC(111) RTCVD template (2x1 along < $2\bar{1}0$ >) and b) 3C-AlN layer on 3C-SiC(111) CVD template (1x1 along <112>). Inserts: RHEED pattern simulations. c) 110 TEM bright-field image of the 3C-AlN layer grown on the CVD 3C-SiC(111) "waved" template showing stacking faults and twins in inclined {111} planes (insert: corresponding selected area electron diffraction (SAED) pattern).

In this work, nominally undoped AlN epilayers were grown on 3C-SiC/Si(111) templates by plasma induced molecular beam epitaxy (PIMBE). The templates have been prepared by carbonization of Si substrates using (i) an ultra high vacuum chemical vapor deposition (CVD), and (ii) a rapid thermal CVD (RTCVD). The RTCVD processing results in a well oriented single-crystalline 3C-SiC layer with an average thickness of ~ 3 nm. The growth process can be described by the "complete condensation" mode [3] occurring at high supersaturations and results in the flat SiC layer. High-quality 2H-AlN(0001) epilayers have been grown on RTCVD prepared 3C-SiC(111) thin layers. The nucleation and subsequent 2H-AlN growth have been maintained in the two-dimensional (2D) mode (Fig. 1a).
In opposite to the RTCVD case, the CVD process has been performed in the "incomplete condensation" mode leading to formation of 3C-SiC islands. This mode provides a characteristic "waved" surface consisting of well developed SiC islands having the same epitaxial relationship with Si as in the case of RTCVD surrounded by the Si pits. This important feature of the "incomplete condensation" has been used in our experiments. The 3C-AlN(111) growth has been performed at low supersaturation, just on the boundary between 3D and 2D epitaxy (Fig. 1b). The higher supersaturations resulted in the 2H-AlN nuclei formation followed by 2D growth of the 2H-phase. Fig. 1c shows the TEM micrograph of 3C-AlN epilayer. As a result of the low stacking fault (SF) energy in 3C-AlN, a high density of SFs/twins are created in {111} planes.
To analyze the experimental findings, we will consider the growth mode models for both cases: 2H-AlN(0001)/3C-SiC/Si(111) and 3C-AlN(111)/3C-SiC/Si(111). In the simplest case, the growth mode is determined by the balance between the formation energies of the film surface σ_{film}, the template surface σ_{sub}, and the interfacial energy E_I. One can write the conditions for the 2D growth of strained thin film as

$$\sigma_{sub} > \sigma_{film} + E_{I} - \Delta\mu / 2A_{(hkl)} + n_{lat} \cdot E_{str} \qquad (1)$$

where n_{lat} = 3 for hexagonal cell, E_{str} is the macroscopic stress energy, and A(hkl) is an intersection of the

* phone : +49-(0)3677-69-3410, email: vadim.lebedev@tu-ilmenau.de

elemental cell with the surface plane (hkl). Two last terms in (1) represent the formation energy of the epilayer [4]. $\Delta\mu$ is a difference in the chemical potentials of the bulk and gas phases representing the actual growth. At the low supersaturations used, this term is of ~0.05 Jm^{-2} and does not affect the overall energy balance.

The Eq. 1 has two valuable terms influencing the growth mode - the macroscopic stress E_{str} and the interfacial energy E_{int}. A contribution of E_{int} to the total film energy is in a reverse proportion to the layer thickness and has no impact on the long-term epitaxy. A contribution of the macroscopic stress energy E_{str} can be estimated on the basis of XRD and HRTEM analysis. It is not surprising, that the most stable 2H-AlN/Si(111) 5:4-matched system represents a minima in the macroscopic stress energy resulting in the stable 2D growth. When we consider 3C-AlN/SiC on Si(111) and 2H-AlN on 3C-SiC/Si(111), the magnitude of the biaxial stress is high in both cases, but the 2H phase has a certain advantage (-10.9 GPa vs. -9.7 GPa). This advantage plus the thermodynamical stability results in the stable 2H-AlN epitaxy on the flat RTCVD-SiC templates. To explain the observed stabilization of the 3C phase on the CVD templates, two features relating to the "waved" character of the surface are to be considered. Firstly,

$$\sigma_{sub} > (\sigma_{film} - \Delta E_M) + E_{int} - \Delta\mu / 2A_{(hkl)} + n_{hkl} \cdot E_{str}$$

the new term ΔE_M has to be introduced in the Eq. (1): where $\Delta E_M = (-\sigma xx^2/2Y)(A\lambda/2) + 2A\sigma_{sub}$ states for the reduction in the total energy of the system due to the sinusoidal undulations at the 3C-AlN/SiC interface showed in Fig. 2b (A~3 nm and λ~5-10 nm are the amplitude and period of the surface wave, respectively, Y is the Young's modulus) [4]. Secondly, in case of the flat surface conditions (RTCVD-SiC), a replication of the template crystal structure is the long-range order interatomic interaction. The lattice replication can be easily overcome by the thermodynamical stability of the 2H phase. In opposite, the "waved" surface (CVD-SiC) provides the vicinal planes for the nucleation (for instance {121}), see Fig. 2b and Fig. 2c). In this case, 2H lateral nucleation leads to the short-range topological incompatibility and a huge uniaxial strain (ϵ_u~0.018), which suppress 2H formation and favors the 3C-AlN polytype epitaxy. Fig. 2a demonstrates that small 2H-AlN domain originates only at the flat interface area. In contrast, 3C-AlN nucleation starts on sinuous-shaped rough interfaces (as can be seen in Fig. 2a and b). The dominant 3C-phase overgrows the hexagonal inclusion forming incoherent 3C-2H boundaries (Fig. 2a).

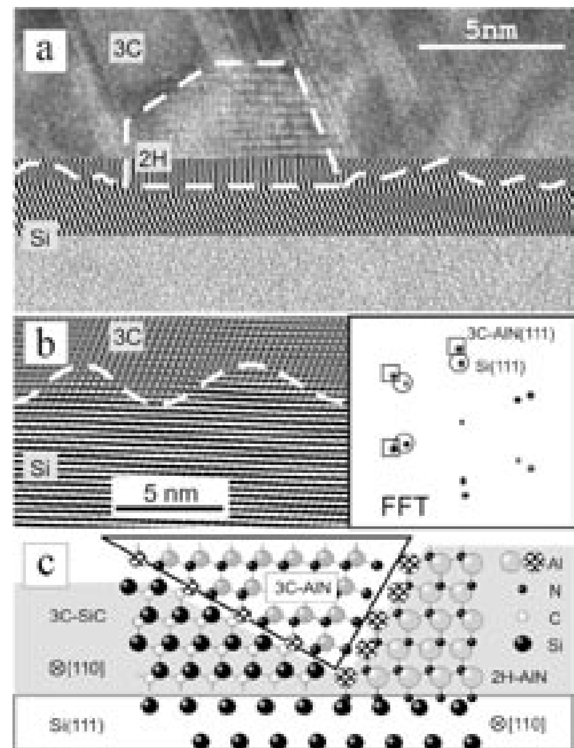

Fig. 2: a)-b) 110 HRTEM filtered images of the AlN/SiC/Si(111) interface show: a) 2H-AlN domain (marked by dashes) originating at the flat bottom of the Si pit formed during carbonization in the "incomplete condensation" mode (the image is FFT-filtered at the interface area), b) FFT-filtered HRTEM image highlighting the "waved" 3C-AlN/3C-SiC/Si(111) interface (as marked) together with FFT-pattern showing the reflections used for filtering. c) Schematic view of the atomic arrangement at the interface demonstrates the mechanism of the lateral nucleation of 3C-AlN.

Summarizing, we conclude that the growth of 3C-AlN polytype can be epitaxially stabilized on the 3C-SiC(111) surface by the polytype replication due to the lateral character of the nucleation and the reduction in the total energy of the film provided by the "waved" character of the template surface.

This work was supported by the TMWTA and TKM (project B609-02004). The authors also acknowledge an ONR NICOP (grant 04PR02823-00).

[1] C. Miskys, J. Garrido, C. Nebel, M. Hermann, O. Ambacher, M. Eickhoff, M. Stutzmann, Appl. Phys. Lett. 82, 290 (2003).
[2] V. Lebedev, W. Richter in Vacuum Science and Technology: Nitrides as seen by the technology, ed. by T. Paskova and B. Monemar (Research Signpost, India, 2002).
[3] W. Attenberger, J. Linder, V. Cimalla, J. Pezoldt, Mat. Scien.&Eng. B, 61-62, 544 (1999).
[4] J. Howe, Interfaces in Materials (J. Wiley & Sons, New York, 1997).

Surface-phonon-polariton response of a silicon carbide based metamaterial

C. Rockstuhl[1], H.P. Herzig[1], Ch. Förster[2], A. Leycuras[3], O. Ambacher[2], and J. Pezoldt[2,*]
[1] Institute of Microtechnology, University of Neuchatel, Switzerland
[2] Department of Nanotechnology
[3] CRHEA, CNRS, Valbonne, France

Phonon-polaritons are resonant vibrational states that can be excited in the lattice of bipolar dielectric materials such as silicon carbide (SiC) in the mid-infrared for wavelengths between approximately 10 μm and 13 μm [1]. The real part of the dielectric constant of SiC takes negative values in this spectral domain. As the imaginary part is low, the excitation of phonons is highly efficient causing well pronounced resonances [2]. In small particles made of SiC, the excitation of surface-phonon-polaritons (SPP) leads to a distinct scattering response of light into the far-field and a large near-field amplitude in the vicinity of the particle over a small spectral domain [3]. Additionally, it was experimentally shown that the absorption of SiC particles is greatly enhanced at the phonon resonance wavelength [4]. For two-dimensional structures as analyzed in the present work, the excitation of SPP is only possible if the illuminating light field is TM polarized, meaning that the magnetic field oscillates parallel along the invariant third dimension of the grating. All of these phenomena are similar to the behavior of some metals such as silver and gold in the visible part of the spectrum, in which the excitation of surface-plasmon-polaritons is the physical underlying effect responsible for this behavior [5]. The excitation of SPPs in gratings made of SiC was investigated in the past for an application as a thermal light source. By choosing proper geometrical parameters, it is possible to obtain directed coherent emitters [6].

The present investigation demonstrates the determination of the SPP response of a metamaterial consisting of binary one-dimensional gratings made of SiC on silicon as a function of the grating geometry and the polarization of the electromagnetic excitation. The chosen geometry of the subwavelength period of the metamaterial dominates the transmission property

For the fabrication of the samples, 3C-SiC films have been grown by chemical vapor deposition on a (100) oriented Si substrate. The thicknesses of the used films have been 1.9 μm, 2.4 μm, and 2.7 μm. Subsequently aluminum gratings were deposited on the surface of the SiC films using i-line photolithography. The periods of the gratings were chosen to be 6 μm, 8 μm, 10 μm, and 14 μm. For each period eight different gratings with varying fill-factors were fabricated. In regions uncovered with aluminium, the subjacent SiC was removed using anisotropic dry etching by an ECR-plasma etch process as described in [7]. An example of the fabricated gratings is shown in Fig. 1. The transmission efficiency of the zero order for the fabricated gratings was measured with a FTIR spectrometer Magna IR 860 from Nicolet. As reference for the subsequent measurements we used the transmission of the uncoated substrate. The wavelength resolution of the spectrometer was chosen such that Fabry-Perot oscillations in the measured spectrum due to multiple reflections of transmitted light in the substrate were suppressed (2 cm^{-1}).

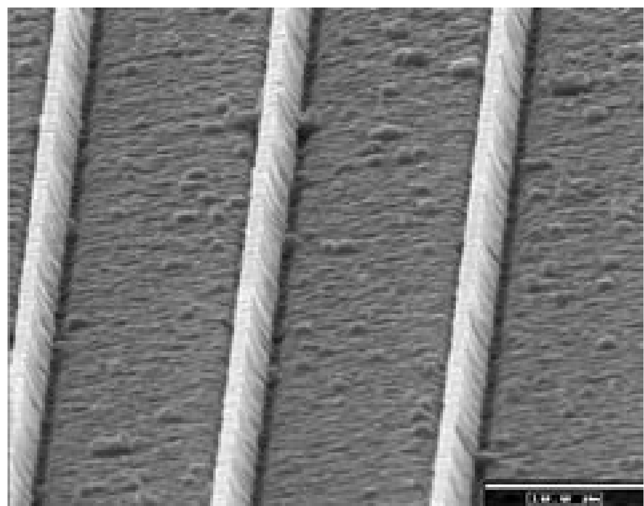

Fig. 1: ß-SiC grating fabricated on (100)Si. The dimensions are 2.7 µm (height) x 0.8 µm (width) x 2 mm (length) and 14 µm periodicity.

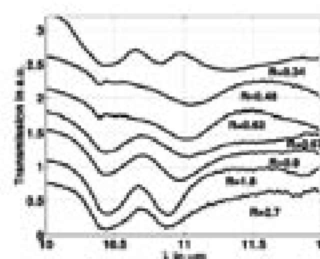

Fig. 2: Wavelength dependent transmission spectra for a grating with a period of 8 mm as a function of the axis ratios using TM-polarized light for the illumination.

* phone : +49-(0)3677-69-3412, email: joerg.pezoldt@tu-ilmenau.de

The size of the fabricated gratings was 2 mm x 2 mm and the gratings were illuminated with a slightly defocused Gaussian beam. Results for a series of measurements with a grating of 10 μm period by using TM polarized light for the illumination are shown in Fig. 2 for wavelengths between 10 μm and 12 μm. The transmission is shown as a function of the axis ratio R, which is defined as the height of the structure divided by the width of the wires. For an unambiguous representation of the results, an arbitrary offset was added to each spectrum such that they appear well separated. It can be seen that two well-pronounced dips appear in the spectra, which are associated with an excitation of a SPP in the micro- and nanostructures due to an enhanced scattering as well as enhanced absorption at these wavelengths4. For the structure with the highest axis ratio, they appear approximately at 10.4 μm and 10.9 μm. At these wavelengths SPPs are comparably excited at the free standing non-periodic objects [3]. The measured phonons are consequently associated with the geometrical cross section of the wire. By decreasing the axis ratio R of the structure, the SPP resonance at 10.4 μm appears to a good approximation at the same wavelength but its strength is lowered, whereas the second resonance is continuously shifted towards higher wavelengths. For the smallest axis ratio the corresponding wavelength is 11.3 μm, as it can be seen also from Fig. 3, where the wave-length of the second SPP is shown as the function of the axis ratio R. It can be seen that generally there is a continuous shift in the phonon wavelength by increasing the axis ratio. As the criteria for the phonon wavelength we have used the local minima in the transmission spectra of each grating. For comparison with a theoretical prediction, the figure shows likewise the calculated phonon wavelengths for the corresponding structures. The calculations have been done with the Fourier Modal Method [8] and for the dielectric constant published values from literature have been used [9].

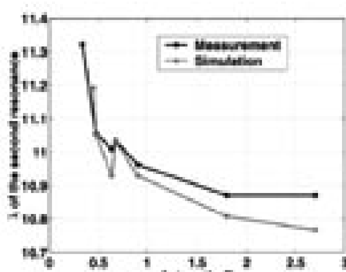

Fig. 3: Wavelength of the second SPP as a function of the axis ratio for a grating of 10 µm period using TM-polarized light for the illumination.

As three different heights of the structures were used for the measurements, an additional small red-shift appears for gratings with a higher thickness, even if their axis ratio might be somewhat larger. This shift towards higher wavelengths for the phonon excitation, which appears for large structures led to a discontinuity versus R. The period of the grating has only a minor influence on the response of the structures, which is dominated by the phonon excitation in each of the single rectangular wires. The basic behavior could be observed for gratings with all four periods. The two dips in the transmission spectra (Fig. 2) indicate on the excitation of a phonon appear to a good approximation at the same wavelength. This observed behavior shows that the measured resonances in the transmission spectra are notgrating resonances that employ the periodicity of the structure, such as the Rayleigh anomaly. Another parameter that influences the transmission spectra and which was investigated experimentally, is the polarization state of the illuminating wave-field. Surface-phonon-polaritons are not excited by using TE-polarized light for the illumination, as it is necessary to confine locally the electric field in the structure over a small spatial extension. In carried out wavelength dependent transmission spectra measurements no resonances appear and with an increase of the width of the wire structure. The determined curves at this polarization tend to show the response from a thin film made of SiC. Such a film is highly reflecting in the corresponding spectral domain, due to the large negative real part in the dielectric constant. This behavior could be also observed and theoretically verified in numerical simulations by using rigorous diffraction theory.

In summary, we have shown results of the measurements of the excitation of surface phonon-polaritons in periodically arranged wires made of SiC with a rectangular geometrical cross-section. The wavelength of excitation is tunable and depends on the geometry of the wire. A SPP can be only excited if the light is TM-polarized and no resonances appeared if the illuminating wave field is TE-polarized. Based on these two properties, the structures can be used in principle as a polarization filter, or more general as a color band-pass filter by exploiting their wavelength dependent transmission of only TM-polarized light. For possible filter elements that should show no sensitivity to the polarization, biperiodic structures could be used.

This work was supported by the European Union within the framework of the Future and Emerging Technologies-SLAM program under grant No. IST-2000-26479.

[1] H. Mutschke, A.C. Andersen, D. Clément, Th. Henning, and G. Peiter, Astron. Astrophys. 345, 187 (1999).
[2] R. Hillenbrand, T. Taubner, and F. Keilmann, Nature (London) 418, 159 (2002).
[3] C. Rockstuhl, M Salt, and H. P. Herzig, accepted for publication in JOSA B.
[4] M. S. Anderson, Appl. Phys. Lett. 83, 2964 (2003).
[5] G. Schider, J. R. Krenn, W. Gotschy, B. Lamprecht, H. Ditlbacher, A. Leitner, and F. R. Ausse-negg, J. Appl. Phys. 90, 3825 (2001).
[6] J. J. Greffet, R. Carminati, K. Joulain, J. P. Mulet, S. Mainguy, and Y. Chen, Nature (London) 416, 61 (2002).
[7] Ch. Förster, V. Cimalla, R. Kosiba, G. Ecke, P. Weih, O. Ambacher, and J. Pezoldt, Mater. Sci. Forum 457, 821 (2004).
[8] J. Turunen, in Micro-optics, edited by H. P. Herzig (CRC Press, London, 1997).
[9] S. S. Mitra, in Handbook of optical constants, edited by E. D. Palik (Academic, New York, 1985).

Bulk Materials in LTCC Multilayers

M. Hintz*, R. Perrone, I. Koch, and H. Thust
Department of Microperipherics

Abstract
Over the last years, the thickfilm technology for LTCC (**L**ow **T**emperature **C**ofired **C**eramics) has constantly been improved. Using fine-line and photo-imageable techniques, the possible resolution is improved up to 30 µm. A problem is that the thickfilm technology is based on pastes or inks which limit conductivity, accuracy, resolution, and chemical processability. The reason for this is the particle structure of pastes and inks. For both screen printing and jet printing, well-defined properties are necessary. Furthermore, the typical cofiring process requires special sintering conditions. Therefore, the particle size and the material composition are limited.
In this work, various zero-shrinkage techniques for LTCC and especially PAS (**P**ressure **A**ssisted **S**intering) are described and a process for the realisation of buried bulk materials is explained. Structures of this type are compared with screen printed structures.
Structured metallic bulk materials can also be used to realise special kinds of cavities. In contrast to organic inlays, they are formed by etching after sintering which ensures that the cavities maintain their accuracy during the whole process. This helps to produce large and filigree membranes and channels and to modify the inner surface of the cavities.
The new technologies can help to provide inner layers with more functions and can increase the spectrum of LTCC multilayers, especially in the fields of radio frequency, power, and fluidic applications.

Introduction Zero-Shrink-Techniques
In the last years, different zero-shrink-techniques were introduced. These techniques use different constraining mechanisms to limit the x/y-shrinkage during sintering, thus to end up with lower tolerances. The traditional zero-shrink-technique is TOS (**T**ape **o**n **S**ubstrate). Another method for reducing the x/y-shrinkage is the use of release tapes on the surface of the laminated body. This process is called PLAS (**P**ressureless **A**ssisted **S**intering). After firing the release tape can be removed by sand blasting or water blasting. The PAS (**P**ressure **A**ssisted **S**intering) uses an uniaxial pressure during sintering, mostly in combination with release tapes.
The SCS (**S**elf **c**onstrained **S**intering) also known as SCPLAS (**S**elf **c**onstrained **PLAS**) is based on a similar principle as PLAS but the constraining material is integrated in the inner layers or direct in the LTCC tapes. Well defined chemical and mechanical properties of the different materials and a symmetrical mounting are necessary for this technology.

Bulk Materials in LTCC
Today, the most frequently discussed advantage of zero-shrinkage is the advanced dimensional accuracy. In addition, it also offers another very special advantage: It allows cofired structures to be used without shrinkage during sintering. Thus, it is possible to integrate bulk materials like metals, ceramics, or silicon. The materials should be preferentially flat with a TCE value close to that of LTCC and with a high elasticity. The chemical properties should be compatible.
Tests with metallic inlays and inlays made of silicon were done. Because of the low elasticity, Silicon is critical for larger inlays. Metals, especially silver, have shown better results.
At present, for LTCC applications only screen printing is used to realise cofired conductors. With disadvantages like low conductivity of the pastes, limited resolution, and low edge accuracy, this process narrows the application fields. Most of these disadvantages could be avoided by using bulk metal structures (Fig. 1). Today, such structures are only used in postfiring processes. The problem is to integrate this kind of structures into multilayers, because it is necessary to apply the structures on the unfired tapes. For instance, the direct contact of green LTCC foils with liquids especially acids is critical.
At the TU Ilmenau a new process has been developed to solve this problem. A special organic layer was used to cover the green foils and to allow the chemical structuring of the bulk metal. During the PAS the cover layer totally sublimates. In this way it is possible to integrate structured bulk metals in LTCC multilayers.

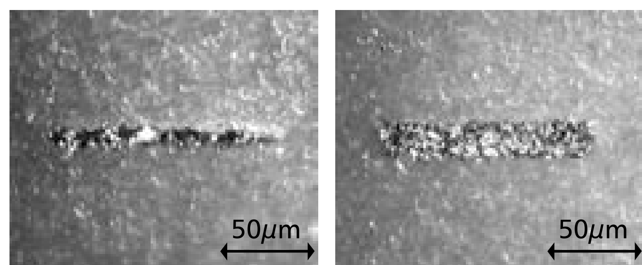

Fig. 1: Screen print (left) versus bulk conductor

* phone : +49-(0)3677-69-3430, email: michael.hintz@tu-ilmenau.de

Electrical and RF Properties

Some simple meander structures were used to determine the DC properties of buried printings and bulk metals.

Pure Ag has a specific ohmic resistance of about 0.016×10^{-6} Ωm compared with Ag-paste with approximately 0.04×10^{-6} Ωm [1]. Bulk metal structures are more capable to use this potential. The measurements of the buried meander show a quite better performance of the bulk materials.

The resistance was much lower than the resistance of printed lines (Fig. 2). A higher thickness and edge accuracy (Fig. 1), as well as a significantly lower specific resistance are the reasons for this behaviour.

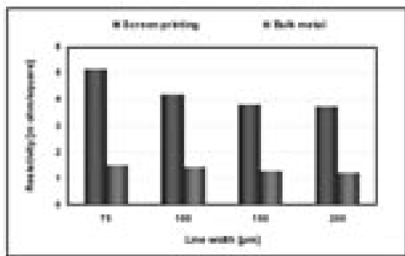

Fig. 2: Resistivity of printed lines and bulk metal

These properties are advantageous for high power applications and high frequency structures.

For RF applications usually buried shielded striplines are used to control transmission wave modes and to decrease cross coupling. The aim of the investigation was to improve the RF performances of such structures. To this end a buried ring resonator was manufactured to clarify the advantages and disadvantages of bulk conductors at frequencies above 5 GHz.

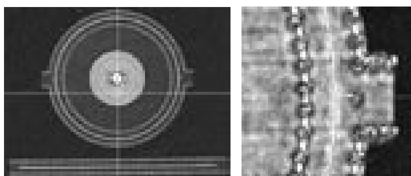

Fig. 3: Sonoscan pictures of the RF structure

Structures with buried printed pastes (Ag) and buried etched foils (Ag) were manufactured. The S- parameters of these structures were measured at different frequencies. From the S21 at the resonance frequencies the transmission losses of the lines were calculated.

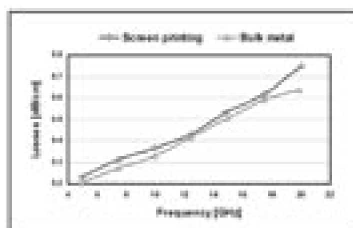

Fig. 4: Losses of printed lines and bulk metal

The obtained results are promising. The losses of the bulk metallic lines are nearly 10% lower than those of printed lines. A problem of the bulk metallic lines was the underetching of the edges. That is why the lines were about 15% narrower than simulated. Consequently, the line impedance was higher. With comparable line widths the losses of the bulk lines should be even lower than the measured values.

Bulk Materials for Cavity Formation

Formation of cavities in LTCC multilayers and keeping the geometrical accuracy is very difficult. In the case of inner structures only three ways are possible:

- use of very low lamination pressures
- use of sublimating inlays
- use of etchable inlays (openings necessery)

Only in the last process the cavity is fixed during the whole sintering process and allows to minimise deformations. In case of the other processes lamination pressure and sintering shrinkage might be responsible for deformation and warping.

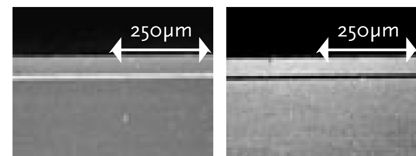

Fig. 5: Chamber with Membrane before (left) and after etching of the bulk metal

Etchable bulk materials are advantageous especially for realising fluidic channels and chambers with very thin membranes. Fig. 5 shows a chamber with a thin membrane. Without fixing the ceramic during sintering by a bulk metal the geometrical accuracy is not stable.

The formed metallic inlay was situated in the substrate and embossed the green ceramic during lamination. After sintering the metallic inlay was etched by using the fluidic channels.

Summary

Zero-shrink-techniques, especially pressure assisted sintering, allow the cofired integration of bulk materials. A way to integrate and structure bulk metals was shown. Advantages of such structures are a high electrical and thermal conductivity and better RF properties. Furthermore, structures with excellent edge geometry, low roughness, high aspect ratio, and high resolution are possible.

Bulk materials can also help to realize filigree cavities and membranes.

In this way, the technology described is qualified for new applications in the fields of power devices, radio frequencies and 3D- structuring.

This work has been supported by the TMWFK (Az.: B609-02003)

[1] Albrecht, A., Botiov, J., Fischer, M., Drüe, K.H., Hintz, M.Wurmus," Alternative Ansätze zur Herstellung hochstromtragfähiger Leiter in LTCC", IMAPS Germany 2003, Munich.

[2] Barnwell, P., Amaya, E., Lautzen „ HeraLock Self-constrained LTCC Tape", IMAPS Nordic 2002, Stockholm.

[3] Rabe, T., Schiller, W.A., Hintz, M., Thust, H.,"Sintern von LTCC- Substraten ohne laterale Schrumpfung", DKG Jahrestagung, Karlsruhe, October 12, 2004.

Electric controlling of hybrid integrated functional liquid crystalline elastomers (FULCE)

T. Fischl[1,*], A. Albrecht[1], H. Wurmus[1], and A. Sánchez-Ferrer[2]

[1] Department of Microsystems Technology

[2] University of Freiburg, Institute of Macromolecular Chemistry

The objective of the European research project FULCE is the integration of **Fu**nctional **L**iquid **C**rystalline **E**lastomers into the microtechnics technologies. The FULCE materials open a new field of actuator materials and give new possibilities in microtechnics. They are promising actuator materials with great movements and low stresses.

The aim of the research is to explore possible applications for FULCE materials. Additional to the existing other actuator materials like memory shape alloys or piezoceramics the functional liquid crystalline elastomers open new directions of applications. The differing chemical and physical properties together with the different behaviour during the switch process provide innovation of the material.

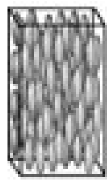

Fig. 1: The schematic presentation of the nematic phase

The functional liquid crystalline elastomers are often named "artificial muscle". This term refers to the usage of the material as an actuator. The crystalline molecules (mesogenic groups) of the aligned elastomers lose their orientation when the temperature is increased under the switch process (nematic-isotropic transition), which results in macroscopic shrinkage of the film (Fig.1). The switch (shortening) process characteristic of the FULCE material is shown in Fig. 2.

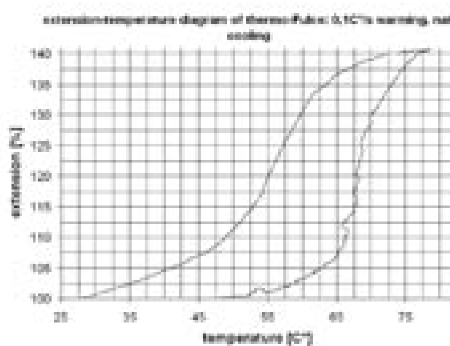

Fig. 2: The temperature-extension diagram (nematic-isotropic transition) of FULCE actuator film with thermal active molecule
Extension: $e = (L_0/L_{actually}) \cdot 100$ [%],
(L: sample length)

The non sufficient precision to control this process with heat radiation restricts the use in microtechnical applications. To solve this problem, we developed an elastic heat source which is able to heat the elastomer material and to follow its movement during the switch process. This second layer is electrically conductive with a resistance especially adapted to match the requirements of modern mechatronics. We mixed electrically conductive carbon particles (Printex XE2 from Degussa AG) into the pre-elastomer solution of FULCE. The primary particle size was 30 nm. After dispersing, the solution was sprayed onto the surface by airbrush using an operative pressure of 3 bar. The solution can include 7-10 m% carbon particles. This black quantity is sufficient for the formation of an electrically conductive network in the layer (Tab. 1).
We used side chain polymers as pre-elastomer solution which was cross-linked by exposition to light with a wavelength of 365 nm.

Black ratio in mixture	Electric Resistance
0,5 m%	>2 MΩ
3 m%	>2 MΩ
5 m%	1230 Ω
7,5 m%	970 Ω
10 m%	120 Ω
~22! m%	*97 Ω*

Tab. 1: Mass ratio of carbon particles in the FULCE pre-elastomer mixture

The electric conductive layer heats up by its own resistance during current flow. The heat is transmitted to the actuator material and it shrinks when the transition temperature is reached. The secondary elastomer layer has nearly the same elasticity as the actuator material underneath it, but the mesogenic groups are unaligned in this film (Fig. 2). The experiment on a beam structure has shown, that the conductive layer constrained the movement of the actuator material only by a few percent. The advantage of this layer is the possibility of static controlling.

* phone : +49-(0)3677 -69-1295, email: tamas.fischl@tu-ilmenau.de

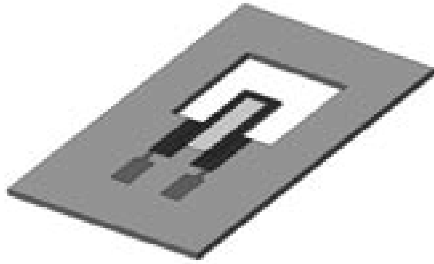

Fig. 3: Solid model of the beam structure

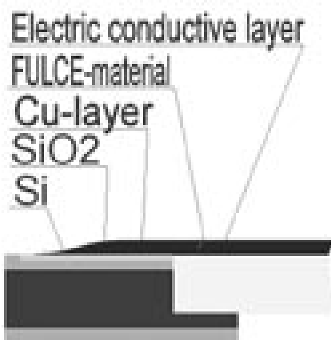

Fig. 4: Layer arrangement on the microtechnical

Demonstrator

The method mentioned above can be used for hybrid integration of microtechnical structures. We built a beam structure to demonstrate the movement with this method (Fig. 3-4). A structure was made with classical microtechnologies. We started with a silicon wafer (thickness: 525 μm) with oxide-layers on both sides. Electric contacts were realised by deposition of chromium and copper in combination with a lift-off process. Standard lithography was applied to produce the actuator structure. Dry etch processes like RIE and ICP were used to etch the structure into the silicon. After removal of the photo-resist, the actuator film was embedded in silicon rubber. The silicon rubber was cross-linked and then the electrically conductive layer was sprayed onto the surface through a metal or a plastic mask onto the surface. The thickness of the conductive layer was 90μm and the thickness of the actuator film was 280 μm. The specific electric resistance of the measured layer was $\rho=9.6$ Ωcm at room temperature and a cross section $A=8.1 \cdot 10^{-4}$ cm^2 (Fig. 5). The electric current necessary to heat up the actuator material can be calculated with the next equations.

$$R = \rho \cdot \frac{l}{A}$$

$$U = \sqrt{P \cdot R}$$

For a complete nematic-isotropic transition an electric power of about 0.1 Watt is necessary with the geometrical parameters mentioned above. The optimal electric resistance was about 11.81 kΩ with the used experimental setup with low distances (max. 10 mm). The resistance of the conductive layer depends on the concentration of the carbon particles within the material and on the length and cross section of the layer.

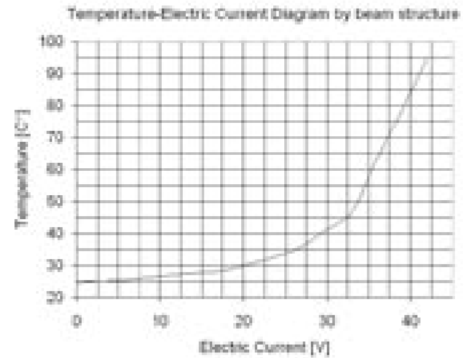

Fig. 5: Length-Electric Resistance diagram of the electrically conductive layer

The current-temperature dependance of the elastic conductive layer in case of the beam structure is shown in Fig. 6. The diagram was determined through measurements with a pyrometer and a digital multimeter.

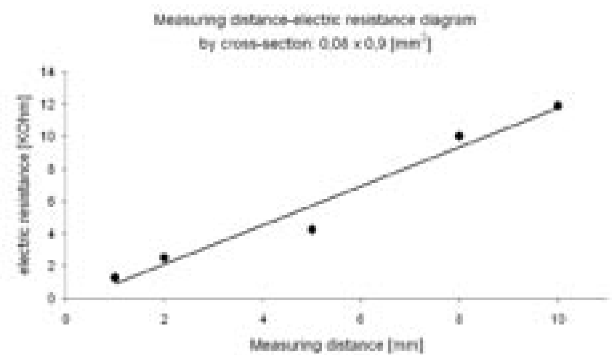

Fig. 6: Temperature-current diagram by the beam structure. Cross section and length of the electrically conductive layer: $A=8.1 \cdot 10^{-4}$ cm^2, l=1cm

Summary

We showed that it is possible to control hybrid integrated functional liquid crystalline films with electric current. The developed film is able to follow the nematic-isotropic transition process efficiently in macroscopic dimensions. We got a more accurate and really adaptable control method for future applications like switches, grippers, valves or pumps etc. More complicated applications are possible in a computer controlled system.

The project is funded by the European Union , contract no. HPRN-CT-2002-00169. Special thanks to Dr. Bernd Halbedel and Michael Jakob from the TU Ilmenau for their help to develop the electrically conductive layers.

Microcombustion system in MEMS technology

M. Stubenrauch[1,*] and N. Schwesinger[2]

[1] Department of Microsystems Technology

[2] Department of Microstructured Mechatronical Systems, Technical University of Munich

Background

In the context of the ongoing global trend to miniaturise standard systems and technologies into microsystems, even combustion processes are taken into consideration. Several publications like a micro spectrometer [1] that is powered with hydrogen and oxygen, show the approach of continuous combustors. A pulsed system in MEMS technologies is presented in [2], where a combustion driven motor has been created. Spacecraft propulsion systems are described for example in [3] and [4]. They use various gaseous or solid propellants to create thrust for small satellites. All these systems are designed for special applications and use a lot of different technologies and processes. A simple and common approach in standard MEMS technology would be helpful to combine the advantages of these solutions and to cover several applications with a single basic design and peripheral setup.

Design and Technology

We suggest a microfluidic device for the continuous or pulsed combustion of bipropellants, e.g. hydrogen and oxygen.

The microfluidic elements consist of two to four gas inlets, the backflame preventers, a mixer and a homogeniser, the reaction chamber, the nozzle area,

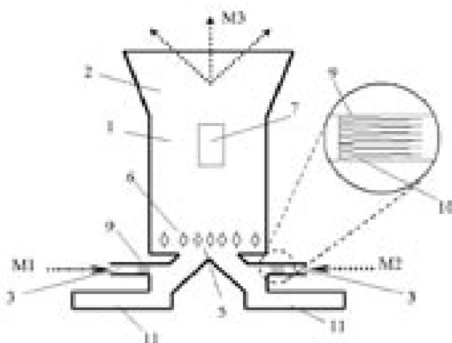

Fig. 1: Design of the fluidic structur with gas inlets (M), backflame preventers (10), mixer and homogeniser (5, 6), reaction chamber (1), nozzle area (2), and ignition system (7)

and the ignition system (see Fig. 1). We used H_2 as fuel and O_2 as oxidiser. The ignition system can be provided by external electrodes (lateral or perpendicular to the silicon surface) or by integrated electrodes. We use a constantly charged capacitor to supply the necessary energy for ignition. At an impulse from the control unit, a high voltage transistor transfers this energy to the electrodes in the system. In this way we can realise transitions in a range of a few μsec.

The structures are manufactured in a 4" MEMS process chain as shown in Fig. 2. After oxidation and doublesided lithography, the two wafers are bonded and diced.

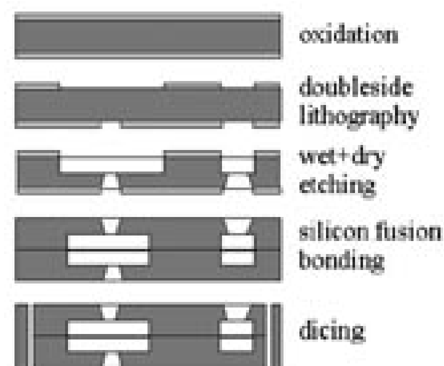

Fig. 2: Technology steps

The systems have an extension of 40x27 mm^2 and fit into special fluidic adapters to connect them with standard tubings. For the first tests, external valves and wire electrodes were used (see Fig. 3).

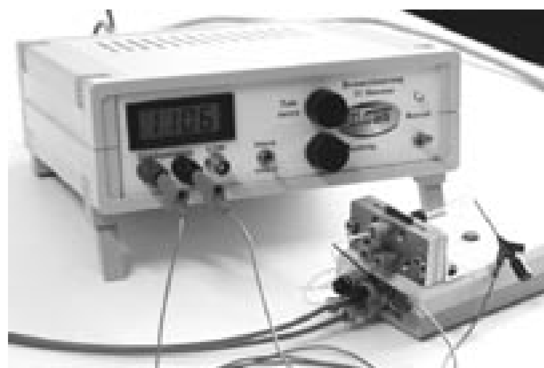

Fig. 3: Actual setup of microcombustor with control unit, electrodes and gas supply

* phone : +49-(0)3677-69-3421, email: mike.stubenrauch@tu-ilmenau.de

Experiments
The microburner was tested with a stoichiometric mixture of H_2/O_2. The gas was supplied in pulses between 50 and 100 msec to fill the system with 7 mm^3 of gas (internal volume). The system works stable for several hours without damaging the silicon structure.

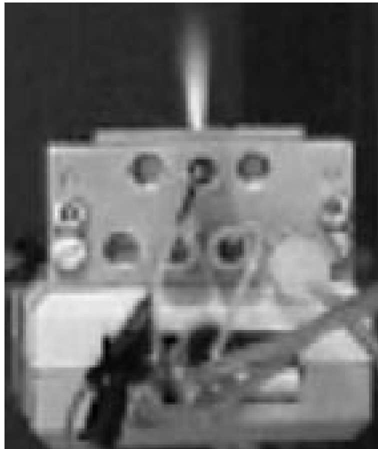

Fig. 4: Snapshot of an operating system

The core temperature of the flame (see Fig. 4) was estimated to be in the range of 2000-3000 K, but the temperature of the system did not exceed 80°C due to the fast heat transfer from the silicon to the fluidic adapter and the surrounding air. Other fuels and oxidisers were used in different modes of operation, pulsed and continuously driven (see Tab. 1). For some chemical reactions no continuous flame could be established due to the extremely high velocity of the flame. With propane the system did not work stable in pulsed mode. The maximum pressure for the system in a static load was 15-30 psi depending on the substrate thickness between 250 and 300 μm. During pulsed operation the pressure is orders of magnitude higher. Obviously, the elasticity of the gases and the silicon membranes absorb this energy during these fast transitions.

fuel system	continuous mode	impulse mode
H_2, O_2 / 1:2		X
H_2, air	X	X
H_2, O_2 / not 1:2	X	X
C_3H_8, O_2	X	
SiH_4, O_2		X
SiH_4, air		X

Tab. 1: Operation modes with different gases

Applications
The main application for the pulsed combustion of stoichiometric hydrogen and oxygen is a propulsion system for small spacecrafts. It allows reproducible small amounts of water and electrical power generated by solar energy. Another use for the microburner could be an ignition system for gas powered cars. The microflame will be injected into the motor cylinder and lead to a homogeneous explosion, less toxic exhaust gases and lower fuel consumption. It is also possible to decompose and destroy toxic chemicals and gases from chemical or biological weapons or waste dumps. A third line in the fluidic structure will inject the gas to be destroyed in the hot zone of the microcombustor.
Conclusions
The first tests with the presented microcombustors (microthrusters) show the ability to be used for various applications. It is a robust system and has a simple design that can be adapted to different fields of usage without major changes in technology. The machines and processes used are common in all microsystem facilities worldwide. More functions like valves, sensors (pressure, temperature) can be integrated easily.
Parallelisation will enable the system to be used even in applications with much higher energy consumption than possible with other MEMS.

[1] S. Zimmermann, B. Riepenhusen, J. Müller; Micromachined Flame Analyzers, Atomic Emission Flame Spectrometer (AES) and Flame Ionisation Detector (FID), Proc. µTAS ´98, Banff, 473-476.
[2] D. Lee, D. Park, J. Yoon, S. Kwon, E. Yoon, Fabrication and test of a MEMS combustor and reciprocating device, in: Journal of Micromechanics and Microengineering 12, 2002. 26-34.
[3] A. London, A. Ayón, A. Epstein, S. Spearing, T. Harrison, Y. Peles, J. Kerrebrock, Microfabrication of a high pressure bipropellant rocket engine, in: Sensors and Actuators A 92, 2001. 351-357.
[4] C. Rossi, S. Orieux, B. Larangot, T. Conto, D. Esteve, Design, fabrication and modeling of solid propellant microrocket-application to micropropulsion, in: Sensors and Actuators A 99 , 2002. 125-133.

Design and fabrication of a single-bead microreactor for high-throughput experimentation in heterogeneous catalysis

T. Zech[1], G. Bohner[1], O. Laus[1], M. Fischer[2,*], J. Klein[1]
[1] hte AG Heidelberg
[2] Center for Micro- and Nanotechnologies

Introduction
The development of novel and better catalysts for chemical processes is mainly an empirical process utilizing the existing technical know-how and experiences. The vision to reduce expenditures of time and costs provoked powerful activities for the development of high-throughput technologies for the application in heterogeneous and homogeneous catalysis systems. The main target in primary screening is the identification of hits out of large catalyst libraries. The number of catalysts tested in parallel should be a few hundred on a small reactor footprint. Therefore, specific library preparation methods resulting in very low amounts of the single materials are required.
Generally, some challenging requirements that have to be met by primary screening reactors are: The reactor design has to accomodate catalysts made by a simple, fast and scalable catalyst preparation method. Many catalysts should be tested simultaneously under steady-state conditions and continuous flow.
In this work, we present a unique approach to high-throughput catalyst testing that is based on using individual beads in a massively parallel arrangement of microreaction chambers on a chip.

System design and catalytic materials
The basis of the single-bead concept is the use of single shaped bodies as the catalytic material of interest. These particles may in principle be of any shape, but usually spherical particles are applied. In accordance with approaches known from combinatorial chemistry, such spherical particles are called „beads". Each bead represents one catalyst as a member of a library of solid catalysts. It consists of an unporous material like α-Al_2O_3 or Steatit or of typical porous support materials like γ-Al_2O_3, SiO_2, or TiO_2.
These beads can be subjected to different synthesis procedures and sequences like impregnation, coating etc. In addition, full mixed metal oxide catalysts can also be formed to spherical particles.
The reactor suitable for testing single bead catalysts in a highly parallel fashion, the so-called „single-bead reactor", is designed as two-dimensional arrangement of microreaction chambers that can hold one catalytic bead each. The partial cross section of a single-bead reactor is shown in Fig. 1.

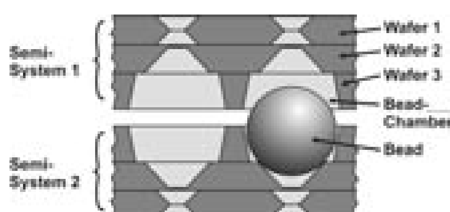

Fig. 1: Cross section of a single-bead reactor

The reactor is made up of two identical semi systems. Having filled the base part with beads, the top part is pressed, sealed, or bonded against the base part to encapsulate each bead in a single, independent microreaction chamber and to avoid fluidic cross-talk between adjacent reaction chambers. The beads sit loosely in the reaction chambers, allowing continuous fluid flow through the micro reactor. Using the top-down direction as fluid flow path and the small footprint of a single microreaction chamber allows the extensions of the reactor arrangement in two dimensions resulting in a very high number of reactors on a small chip area.
For reactors having several hundred parallel reaction chambers an active control of fluid flow is not a viable option. Therefore, fluidic networks have to be realised where a limited number of feed sources connected to the parallel reactors and further downstream to the analytics. Accordingly, adjusting the pressure drop along the fluid flow path is the key for controlling the fluid flow rate. A powerful solution of the aforementioned problem is the use of single, independent flow restrictors for each reaction chamber.
For example, the pressure drop of fluid flow through narrow and short channels or pores can be calculated using the law of Hagen-Poiseuille:

$$\Delta p = \frac{8}{\pi} l_P \dot{V}_B \eta \frac{1}{r_P^4 N}$$

l_P = pore length, V_B = flow rate, η = viscosity, r_P = pore radius, N = pore number

Depending on the pore number and the pore radius a considerable pressure drop can be generated. Especially, reduced pore radii result in a strong increase of the pressure drop. Considering this rough calculation it becomes clear, that such arrangements of narrow

* phone : +49-(0)3677-69-3413, email: michael.fischer@tu-ilmenau.de

and short pores allow the generation of an equal flow distribution. Therefore, the fluid access ports of the microreaction chambers have been designed as flow restrictors in our „single-bead approach". These flow restrictors are microstructured membranes as a collection of a defined number of short straight pores with a very small diameter. Computational fluid dynamics simulations proved the functioning of this approach [1]. In that case, the feed stream is entering a small chamber above the reaction chamber inlets via a standard stainless steel tube with a typical laminar flow distribution. However, by means of the pressure drop caused by the individual pore membranes at the inlet of every reaction chamber, this single stream is equally divided into sub-streams flowing through each reaction chamber.

Reactor fabrication

Because of the high demands regarding the accuracy of the microstructures as well as of its excellent thermal stability and heat conductivity, silicon was chosen as primary reactor material. Accordingly, a number of processes known from silicon micromachining were applied in the fabrication of the different parts of the reactor.

Every semi system of the reactor consists of 3 wafers assembled by silicon fusion bonding. Wafer 1 (Fig. 1) is a 400 μm silicon wafer which is structured by wet chemical anisotropic etching. Due to the crystal orientation of the silicon (100) the square holes are etched on both sides under an angle of 54.74° into the substrate. For a higher chemical stability the wafer is oxidised thermally after the structuring process to obtain a thin SiO_2-coating on the inner reactor surface. A thin silicon membrane is manufactured by etching a cavity from the bottom side into wafer 2 (Fig. 2). Afterwards, pores are etched into the membrane by Reactive Ion Etching (etching gases: sulfur hexafluoride and oxygen). After realizing the pore structure a SiO_2-coating of the cavities and pores is done by a re-oxidation. The holes in wafer 3 which form one half of the bead chamber are produced by micro powder blasting. A metal mask structure will be transferred into an oxidized silicon wafer with an air pressure jet carrying a very fine-grained blasting abrasive. Compared with the Deep Reactive ion Etching or the „Bosch process" the micro powder blasting is an economical alternative for a complete via structuring of a 525 μm thick wafer. By the simultaneous powder blasting of the SiO_2 layer this can be used as a masking for the following isotropic etching (mixture of HNO_3, HF and CH_3COOH) of the silicon wafer. By the use of isotropic etching a rounding and a smoothing of the chamber wall is achieved. After the completion of all silicon wafers for one semi system (wafer 1 to 3) the several substrates are combined by silicon fusion bonding.

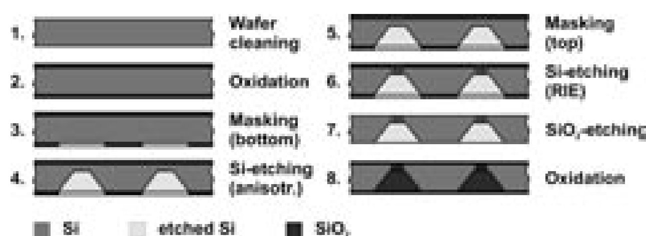

Fig. 2: Processing scheme of wafer 2

Typically, one semi system of the reactor is filled with beads, then the other semi system is pressed against it during reaction to achieve fluidic separation between adjacent reaction chambers, because of the manufactured half systems are designed completely symmetrically. However, it is also possible to combine these in a non-detachable manner by two bond processes. In that case, the beads need to be inserted into the reactor before the final bonding step. Therefore, a bonding process leading to a hermetically sealed connection must be used that does not alter the properties of the beads. In our case, the connection was realized by anodic bonding with an inbetween glass wafer (structured Borofloat).

Application and conclusion

The selective oxidation of CO in hydrogen was chosen as a model reaction in order to validate the 625-parallel reactor against each other. As a reference, a library of catalysts containing 96 different materials was designed in order to test them in the reactor. The library consists of single-component catalysts and binary and ternary mixtures of active components [2]. The reactor was filled with catalysts and mounted into a stainless steel flange (Fig. 3). Afterwards the selective CO oxidation in H_2 was tested at different operating conditions.

Using our system, identical results in the high-throughput screening of heterogeneous catalysts with regard to the relative performance of different catalysts and observed catalytic trends can be obtained [2]. Thus, efficient high throughput experimentation could be realised by the single-bead concept for heterogeneously catalyzed gas phase reactions.

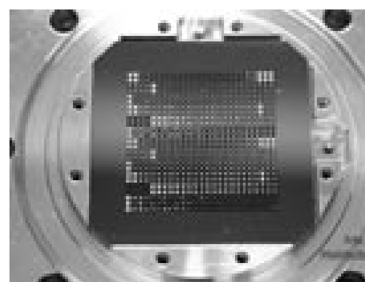

Fig. 3: Filled single-bead reactor mounted into stainless steel flange for catalyst testing

[1] T. Zech, J. Klein, S. A. Schunk, T. Johann, F. Schüth, S. Kleditzsch, and O. Deutschmann, High-throughput analysis - A tool for combinatorial materials science, chapter Miniaturized reactor concepts and advanced analytics for primary screening in high-throughput experimentation, pages 491-523, Kluwer Academic/ Plenum Publishers, New York, 2003.

[2] T. Zech, G. Bohner, O. Laus, J. Klein, and M. Fischer, Design, fabrication, and application of a massively parallel single-bead microreactor system for high-throughput experimentation in heterogeneous catalysis Volume 76, Issue 6, Review of Scientific Instruments, 2005.

Dosing Systems and their Fields of Application

F. Weise*, J. Burgold, and H. Wurmus
Department of Microsystems Technology

The dosing technology developed at ZMN is a contactless process for a precise dosing of the smallest amounts of fluids. The key technology is bases on the structuring of silicon.
We are able to manufacture dosing systems within the range from 30 pl up to 10 nl and dropping frequencies between 100 Hz and some kHz. Depending on the application, these systems can work with the drop on demand (DoD) or the continuous jet principle. The driver unit is a piezoactuator. It can be used either as a bimorphous or as a stacked actuator, depending on the application. An application-specific housing has been developed and produced for the fluidic, electric and mechanical connect on the silicon chips (Fig. 1).

Fig. 1: Dosing chip with housing

In the silicon chips layout, a distinction is made between front and side shooter (Fig. 2). The advantages of the side shooter are its easier manufacturing and, depending on the design, better ability to be filled. For the front shooter, on the other hand, it is simpler to shape the nozzle region and also to make surface modifications in this area for a defined wetting behavior.

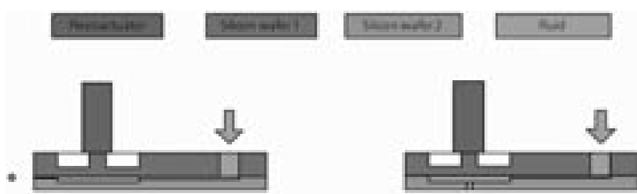

Fig. 2: Front shooter *Side shooter*

In order to have a precisely defined droplet break-off, the geometry in the nozzle region must be structured very precisely. Likewise, the surface properties in and around the nozzle must be defined. For this reason, the surfaces inside the nozzle and the channel structures have been coated with SiO_2. This means that the surface is hydrophilic to aqueous solutions and chemically resistant. In order to avoid the spreading of fluid outside the nozzle, the region around the nozzle was made hydrophobic. For this purpose, two alternative ways have been tested. On one hand, FC layers have been deposited on the nozzle region. These are very hydrophobic, but not mechanically resistant. On the other hand, the surface has been treated with trichlo rooctadecylsilane. This layer is not as hydrophobic as the FC layer, but much more mechanically resistant, allowing the region around the nozzle to be cleaned.

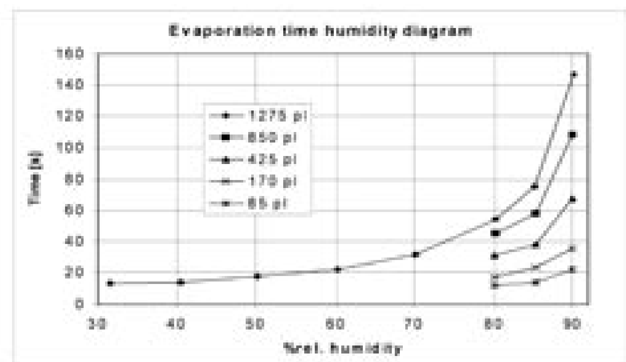

Fig. 3: Evaporation of water droplets

Within the scope of the research project „Picofluidic“, a dosing head (Fig. 1) has been developed for applying smallest fluid volumes (50 pl) on to a sensor. These fluids are aqueous solutions. Due to the demands on positioning precision, the system is configured in such a way that the dosing head can be positioned up to 250 μm from the target. In the case of droplets with volumes in the range of nano to picoliters, surface effects, e.g. evaporation, have a large influence. In Fig. 3, the evaporation of water droplets in dependence of the relative air humidity is represented.

For permitting the study of the droplets for a longer period of time, a special atmosphere had to be created. For this purpose, the entire experiment setup was built in a controlled environmental chamber.

* phone: +49-(0)3677-69-3423, email: frank.weise@tu-ilmenau.de

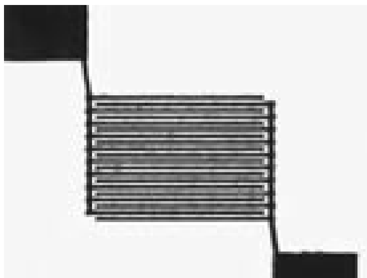

Fig. 4: Printed gate electrode pattern for a polymer transistor (line width 45 µm)

Another important application for dosing systems comes from the area of polymer electronics (Fig. 4). Conductor tracks and other electronic components can be manufactured using adequate polymers. It has been shown in [1] how PATAC (poly-bis-alkylthio-acetylene), an insulating polymer, can be converted into a conducting polymer using lasers. The conductivity can be raised up to 16 orders of magnitude. This corresponds to the conductivity of highly doped silicon. The polymer is solved in toluol in order to be able to be dispensed. Another polymer used was PANI (polyaniline). It is solved in DMPU and allows to directly write the conductor tracks. The conductor tracks should have a width of 50 µm, which means the droplet diameter should be about 40 µm. For PATAC, the film thickness shall not be larger than 2 µm, and for this reason we have worked with a very low polymer concentration.
In higher polymer concentrations, the solution viscosities increase strongly. For this reason, a heatable casing was adopted. Fig. 5 shows a chip for printing the polymer.

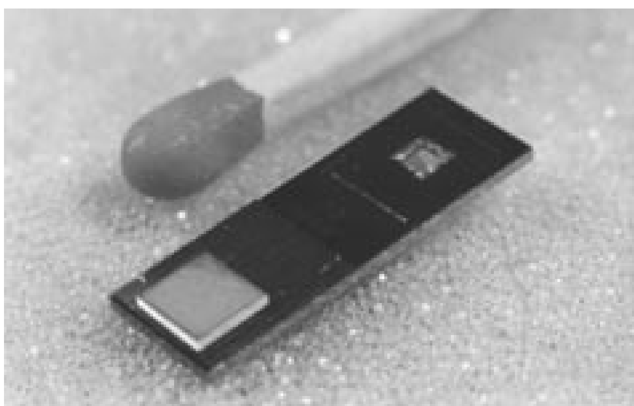

Fig. 5: Dosing chip for polymer printing with a bimorph actuator

For various dosing systems built at the TU Ilmenau, the tested fluids, their respective nozzle diameters, operating voltages and maximal dropping frequency are listed in Tab. 1. The droplet volumes are not shown, since they depend not only on the nozzle size and its geometry, but also on the temporal progression of the driving pulse. Fig. 6 shows the droplet break-off for two different pulse forms but with the same nozzle.

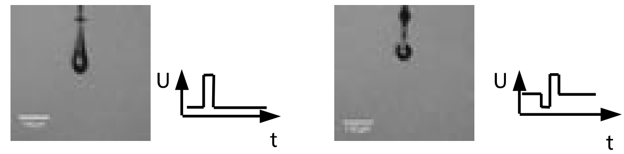

Fig. 6: 100 pl droplet 50 pl droplet

The next step of the project is to work on improving the handling of these systems in order to make them more robust and fail-safe.

Tab. 1: Data of different dosing systems

Device	Sort of liquid	Nozzle fluidic diameter [µm]	Operating voltage [V]	Droplet max. frequency [Hz]
1	water	35 … 100	30 … 100	30 … 100
2	water	30 … 45	60 … 120	3000
	toluene		30 … 60	8000
	DMSO		40 … 80	4000
	polymer (heated)		150 … 180	1000
3	water	40 … 100	100 … 150	3000
	ethanol		50 … 80	6000
4	water	40 … 100	100 … 150	3000
	ethanol		50 … 80	6000
	DMSO		60 … 100	4000
	polymer (diluted)		150 … 200	2000
	polymer (heated)		150 … 200	1500
	solder (heated)		160 … 200	500
	wax (heated)		80 … 120	1000
5	water	35 … 60	60 … 100	4000
	ethanol		50 … 80	6000
	enzym solution		60 … 120	5000
6	water	35 … 60	30 … 60	3000
	ethanol		10 … 40	4000
	enzym solution		30 … 80	2000
7	water	100 … 300	50 … 200	100
	DMSO		50 … 100	150
8	water	80 … 300	30 … 80	200
	polymer (diluted)		60 … 150	100
	polymer (heated)		80 … 200	60
	solder (heated)		120 … 200	100

The project is supported by the Thuringian department for culture (TKM) and the European Union (EFRE program: project number B 678-03001).

[1] H.-K. Roth, C.D. Skordoulis, M. Schroedner, I. Stohn, A. Bolovinos, E. Bakalis; "Excimer-laser-induced permanent electrically conducting sites in polymers for microelectronic applications"; SPIE Proceedings Vol. 3423, 1998, pp.344-347.

Wide Bandgap Heterostructures: AlGaN/GaN vs. 4H/3C SiC

V. Polyakov* and F. Schwierz
Department of Solid-State Electronics

Introduction
During the past few years, AlGaN/GaN HEMTs (high electron mobility transistor) gained a lot of attention. These devices are promising candidates for high-power amplifiers operating in the GHz range. They show frequency limits (cutoff frequency f_T and maximum frequency of oscillation f_{max}) in excess of 100 GHz, high breakdown voltages, and extremely high output power densities [1].
The unique performance of AlGaN/GaN HEMTs is mainly related to the properties of the polarization-induced 2DEG (two-dimensional electron gas) that forms at the AlGaN/GaN interface and to the wide bandgaps of AlGaN (4 eV for $Al_{0.3}Ga_{0.7}N$) and GaN (3.4 eV).
Recently it has been shown that heterostructures from another wide bandgap material system, namely hexagonal/cubic SiC, can be grown [2]. So far, it is not known if 2DEGs with high sheet density in hexagonal/cubic SiC structures do exist and if such structures can be used for HEMTs.
In the present work we investigate the formation of 2DEGs in heterostructures consisting of 4H (hexagonal) and 3C (cubic) SiC by numerical simulation and compare the calculated free electron distributions and sheet densities with those obtained for AlGaN/GaN structures.

Model Description and Heterostructure Design
For the calculation of the electron distributions and the resulting 2DEG sheet densities, the one-dimensional Schrödinger and Poisson equations are solved self-consistently. Polarization effects are taken into account for both material systems (AlGaN/GaN and 4H/3C SiC).

The investigated AlGaN/GaN heterostructures consist of a 25 nm $Al_{0.3}Ga_{0.7}N$ barrier layer and a thick GaN substrate. The combination of spontaneous and piezoelectric polarizations induce a net positive bound charge σ of 1.36×10^{13} q/cm^2 at the AlGaN/GaN interface (q is the elementary charge). The conduction band offset at the interface is 0.38 eV. The 4H/3C SiC structure has a 25 nm 4H SiC barrier layer and a thick 3C SiC substrate. In this structure, only the spontaneous polarization of the 4H SiC is responsible for the net positive bound charge ($\sigma = 1.348 \times 10^{13}$ q/cm^2). The conduction band offset at the 4H/3C interface is 0.99 eV. The other parameters necessary for the calculations (effective masses, dielectric constants, etc.) were collected from the literature. In both structures a metal gate is placed on top of the barrier layer.

Results and Discussion
First, we consider undoped structures, i.e., both the barrier layers and the substrates are undoped. Fig. 1 shows the calculated electron density profiles and conduction band edges of the undoped AlGaN/GaN and 4H/3C SiC structures. Clearly in both structures a

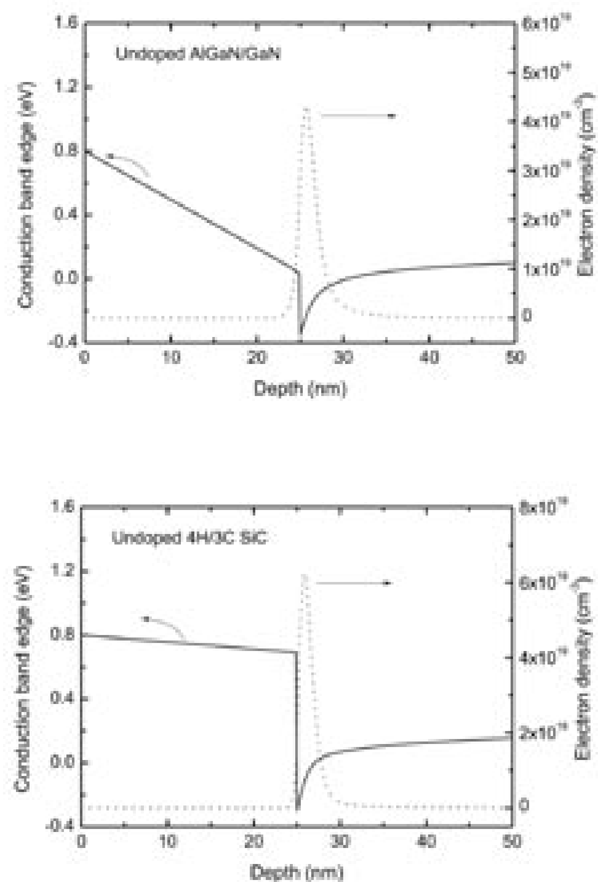

Fig. 1: Electron density profiles (dotted lines) and conduction band edges (full lines) of the undoped AlGaN/GaN and 4H/3C SiC structures. The surface potential is 0.8 eV.

* phone : +49-(0)3677-69-3120, email: vladimir.polyakov@tu-ilmenau.de

2DEG is formed. The 2DEG sheet densities obtained by integrating the electron density over the depth (from the interface to the bottom of the substrate) are $1.05x10^{13}$ cm^{-2} for the AlGaN/GaN structure and $1.28x10^{13}$ cm^{-2} for the 4H/3C SiC structure.
The promising result for the SiC structure is a consequence of the large interface bound charge (comparable to $Al_{0.3}Ga_{0.7}N$/GaN) and the extremely large conduction band offset (substantially larger than that in $Al_{0.3}Ga_{0.7}N$/GaN). It should be noted that a high 2DEG sheet density is a key design goal for HEMTs.

Next, we take a look on how efficiently the 2DEG sheet density can be controlled by the gate voltage. In Fig. 2 the sheet density is shown as a function of the surface potential. The surface potential includes the Schottky barrier height (of the gate/barrier layer junction) and the applied gate voltage. If, for example, a Schottky barrier of 1 eV is assumed, a surface potential V_{surf} of 5 eV corresponds to an applied gate voltage of -4 V.

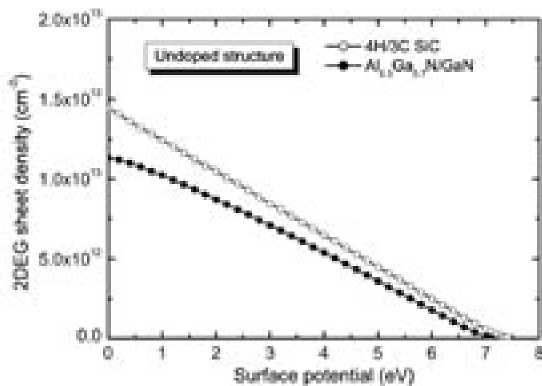

Fig. 2: Calculated 2DEG sheet density as a function of the surface potential for the undoped AlGaN/GaN and 4H/3C SiC structures.

In both structures the sheet density gradually decreases with increasing surface potential (i.e., for more negative gate voltages) and the 2DEG channels become completely depleted of free electrons at $V_{surf} \approx 7$ eV. Clearly the sheet density for the 4H/3C heterostructure is larger over the whole range of surface potential variation.
Simulations of AlGaN/GaN and 4H/3C structures with different barrier layer thicknesses revealed that the 2DEG sheet density in the SiC structure is much less sensitive to the barrier thickness than in the AlGaN/GaN structure.
Next, we consider the influence of a barrier layer doping on the 2DEG. For this case, the 25 nm barrier layer is assumed to be composed of three successive sublayers: a 5 nm undoped cap layer, an intermediate 15 doped supply layer with a donor concentration of 10^{19} cm^{-3}, and a 5 nm undoped spacer. In the AlGaN/GaN structure the barrier layer doping leads only to a slight increase of the 2DEG density from $1.05x10^{13}$ cm^{-2} (undoped case) to $1.15x10^{13}$ cm^{-2} for a surface potential of 0.8 V. On the other hand, in the 4H/3C structure, the 2DEG density increases by more than 30% from $1.28x10^{13}$ cm^{-2} (undoped) to $1.69x10^{13}$ cm^{-2} in the doped structure.
The results of the present study show that 2DEGs with very high sheet densities are formed in 4H/3C SiC heterostructures. This makes SiC-based heterostructures a potential candidate for high-power HEMTs, provided that a reliable growth technique is available. More work has to be done to investigate to which degree the high sheet densities in 4H/3C structures translate to a high output power and to estimate the frequency limits (f_T and f_{max}) of SiC-based HEMTs.

This work has partially been supported by DFG (Gz. Schw729/2-3).

[1] F. Schwierz and O. Ambacher, Proc. IEEE EDMO, pp. 204-209 (2003).
[2] A. Fissel, Physics Reports, pp. 149-255 (2003).

Effects of solvent and annealing on the performance of solar cells based on poly(3-hexylthiophene): fullerene

M. Al-Ibrahim[1,2,*], O. Ambacher[1], and S. Sensfuss[2]
[1] Department of Nanotechnology
[2] TITK Institute, Department of Functional Polymer Systems, Rudolstadt

During the last couple of years, increased efforts of many research groups were devoted to the development of solar cells based on conjugated polymers. Using poly[2-methoxy-5-(3′,7′-dimethyloctyloxy)-1,4-phenylene vinylene]:[6,6]-phenyl-C61-butyric acid methyl ester (MDMO-PPV: PCBM), polymer solar cells with white light power conversion efficiency of 3.3% on glass substrates[1] and of 3% on flexible substrates[2] were realized. Regioregular poly(3-hexylthiophene) (P3HT) appears to be one of the most suitable conjugated polymers to date for polymer solar cells.

In this work we report on the effects of the processing conditions on the light absorption of P3HT:PCBM layer and on the performance of the polymer solar cells processed from these layers.

Figure 1 shows the absorption spectra of P3HT:PCBM composite films (1:2 wt.-%) casted from chloroform (CF) and chlorobenzene (CB) solutions before and after thermal annealing at 100°C.

The absorption maximum of the film casted from chloroform solution is observed at a wave length of 460 nm. This maximum is observed at 510 nm when the film is casted from chlorobenzene solution.

The absorption band edge of the films casted from chloroform and chlorobenzene solutions are observed at 600 nm and 630 nm, respectively.

The peak at 335 nm in both spectra is caused by PCBM[3]. This indicates that the degree of the P3HT chain ordering [4] is higher in the case of using chlorobenzene.

After thermal annealing of the two layers the PCBM peak as well as the whole spectrum of the film casted from chlorobenzene remains unchanged, while the absorption spectra of the film casted from chloroform changes significantly. The maximum absorption peak is red shifted by 50 nm, the absorption band edge is shifted from about 600 nm to 630 nm. The changes in the absorption spectrum of the film casted from chloroform solution upon annealing are due to the molecular diffusion of PCBM out of the polymer matrix, which increases the degree of the P3HT chain ordering [5]. Using a P3HT:PCBM composite (1:1 wt.-%) and the two solvents chlorobenzene and chloroform we found the same behaviour.

We conclude that molecular diffusion of PCBM in the P3HT matrix is higher in films casted from chloroform in comparison to films casted from chlorobenzene solutions, which destroys the self- organization structure of P3HT and reduces the absorption of the organic layers in the green spectral region. This effect depends on the amount of PCBM in the composite and is very pronounced in the case of using chloroform solution. After thermal annealing the absorption around 510 nm is further increased. This effect is due to the improved ordering of the conjugated polymers in the film by reducing the free volume and the defect density at the interface created during solvent evaporation [6] as well as by the improved interchain interactions [7]. The effect of the solvent and the thermal annealing on the morphology is investigated by X-ray diffraction. $2\theta/\theta$ scans prove that P3HT crystallizes after annealing.

Polymer solar cells were fabricated using 5x5 cm^2 flexible ITO coated polyester foils. The device design is described elsewhere [2].

Table I summarizes the photovoltaic parameters of the cells investigated during this work. Fig. 2 shows the current-voltage characteristics of PET-foil/ITO/PEDOT:PSS/P3HT:PCBM/Al solar cells under white light illumination (100 mW/cm^2) for P3HT:PCBM 1:1 and 1:2 wt.-% using chlorobenzene (CB) solvent. The open circuit voltage (V_{OC}) of the cell based on a 1:2 composition is 100 mV higher than that of the cell based on a 1:1 composition. This can be explained by the partial coverage of the cathode by PCBM [8], which is higher by using the 1:2 than by 1:1 composition.

The short circuit current (I_{SC}) of the cell based on a 1:1 composition is obviously higher than that of the cell based on 1:2 composition.

This significant difference is due to the differences in optical density and to the different absorption in the green spectral region of the photoactive layer.

The energy conversion efficiency of the cell based on 1:1 composition ($\eta_{AM1.5}$ = 2.2%) is higher than that of the cell based on 1:2 composition (1.0%). No enhancement in the performance of both cells was obtained after annealing of the cells.

* phone : +49-(0)3677-69-3410, email: maher.al-ibrahim@tu-ilmenau.de

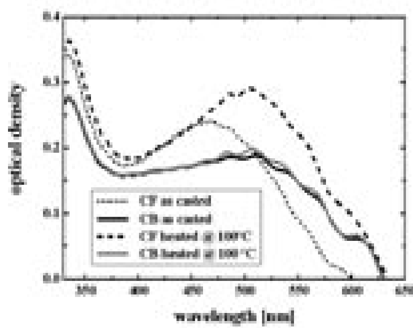

Fig. 1: Absorption spectra of P3HT:PCBM composite films (1:2 wt.-%).

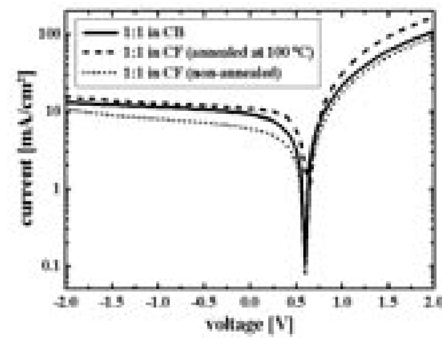

Fig. 2: I/U characteristics of P3HT:PCBM solar cells under white light illumination (100 mW/cm²).

A change of the solvent used for the 1:1 P3HT:PCBM composition from chlorobenzene to chloroform leads to lower I_{SC} and $\eta_{AM1.5}$. V_{OC} and FF do not change (Tab. 1). After thermal annealing of the cell prepared using 1:1 P3HT:PCBM composite from chloroform solution the performance of the cell is improved. V_{OC} becomes 30 mV higher, I_{SC} and FF increase to 10.9 mA/cm² and 0.49, respectively, and as a consequence, $\eta_{AM1.5}$ amounts to 3.4%.

Tab. 1. Comparison of device parameters of polymer solar cells with different P3HT:PCBM compositions and process by different solvents (chlorobenzene CB and chloroform CF).

Composite	V_{OC} (mV)	I_{SC} (mA cm²)	FF	$\eta_{AM1.5}$ (%)
1:1 in CB	600	9.2	0.4	2.2
1:2 in CB	700	3.6	3.6	1.0
1:1 in CF non-annealed	600	6.2	6.2	1.5
1:1 in CF annealed	630	10.9	0.49	3.4

In summary, we have found that the processing conditions (solvent, P3HT:PCBM composition, thermal annealing) strongly effect the optical properties of the P3HT:PCBM films. The improved absorption of the composite films, the enhancement of the degree of polymer chain ordering lead to an improved performance of polymer solar cells based on poly (3-hexylthiophene):fullerene.

We thank Bundes Ministerium for Bildung und Forschung (BMBF Germany) and Thüringer Kultusministerium (TKM Thuringian/ Germany) for financial support.

[1] C.J. Brabec, S.E. Shaheen, C. Winder, N.S. Sariciftci, P. Denk; Appl. Phys. Lett. 80, 1288 (2002).
[2] M. Al-Ibrahim, H.-K. Roth, S. Sensfuss; Appl. Phys. Lett. 85, 1481 (2004).
[3] M. Al-Ibrahim, H.-K. Roth, U. Zhokhavets, G. Gobsch, S. Sensfuss; Solar Energy Materials & Solar Cells Vol. 85 (1) (2005) 13-20.
[4] M. Theander, O. Inganas, W. Mammo, T. Olinga, M. Svensson, M. Andersson; J. Phys. Chem. B. 103, 7771 (1999).
[5] D. Chirvase, J. Parisi, J.C. Hummelen, V. Dyakonov; Nanotechnology 15, 1317 (2004).
[6] T. Ahn, H. L. Sein-Ho Ha; Appl. Phys. Lett. 80, 392 (2002).
[7] P. J. Brown, D. S. Thomas, A. Köhler, J. Wilson, J.-S. Kim, C. Ramsdale, H. Sirringhaus, R. H. Friend; Phys. Rev. B 67, 064203 (2003).
[8] J. Liu, Y. Shi, Y. Yang; Adv. Funct. Mater. 11, 420 (2001).

Polymer Solar Cells with Normal and Inverse Architectures

M. Al-Ibrahim[1,2,*] , O. Ambacher[1], and S. Sensfuss[2]
[1] Department of Nanotechnology
[2] TITK Institute, Department of Functional Polymer Systems, Rudolstadt

Aside from further needed improvements in electronic performance and lifetime, innovation in manufacturing methods is necessary for a future success of organic photovoltaic devices. The manufacturing methods depend on the architecture of the cell. Fig. 1 shows two possible design of the polymer solar cell (normal and inverse). The first electrode and the substrate in the normal design must be transparent. Usually indium tin oxide (ITO) is used as anode and PET-foil [1-5] or glass as substrate [6-8]. The second electrode (cathode) is normally a metal such as Al, Ca or Mg. With this design polymer solar cells could be realized with an external AM1.5 power conversion efficiency of 3% [4], 1.5% [5], 3.5% [6] and 3.3% [7]. In the inverse design the top electrode must be transparent. We report about the inverse architecture and compare between normal and inverse architectures of polymer based solar cells. A spin coated poly(3-hexylthiophene)/[6,6]-phenyl-C61-butyric acid methyl ester (P3HT/PCBM) composite layer is used as photoactive layer. The chemical structures of P3HT and PCBM are described elsewhere [6]. In [5] we have already reported about the optical and electrochemical properties of P3HT/PCBM composite and about the possible charge transfer from P3HT to PCBM. For the normal architecture we use PET-foil as substrate, ITO as transparent anode, and Al as cathode [4], while in the inverse cell Au is the transparent anode, Ti is the cathode and a Si wafer is the substrate. The device preparation with normal and inverse design is described in [9].

Fig. 2 shows the absorption spectra of films based on P3HT in comparison to the transmission spectra of PET/ITO and an Au ultrathin layer (8 nm). The absorption maximum of P3HT can be observed at 2.48 eV (λ_{max} = 500 nm). The band gap of the polymer is about 1.9 eV (λ = 650 nm). The transmission of PET/ITO (175 μm/100 nm) in the spectral range 350-450 nm is lower than the one of Au (8 nm layer), while it is higher for light with wave length more than 450 nm. However both show nearly comparable transmission in the range where P3HT absorbs and therefore they both can be used as transparent contacts in solar cells based on P3HT.

Following the electron transfer from P3HT to PCBM the electrons must be injected from the LUMO of the acceptor (PCBM) into the cathode (Al or Ti) and the excited holes must be transferred from the HOMO of the donor into the anode (ITO or Au). Thus, to obtain a high photocurrent from the solar cell the barrier height for the holes and the electrons must be as low as possible. Fig. 3 shows the band diagram with HOMO/LUMO levels of the donor polymer P3HT and acceptor PCBM in relation to the work function of ITO, Au, Ti and Al. For the normal design of the cell (ITO as anode and Al as cathode) the barrier height for the holes is 0.50 eV and for the electrons 0.53 eV. For the inverse design (Au as anode and Ti as cathode) the barrier height for the holes (0.1 eV) is significantly lower than that in normal design. The barrier for the electrons in the inverse design is only 0.05 eV higher than the one of the normal design. The difference in the work function values in the normal design (ITO, Al) is 0.42 eV and in the inverse one (Au, Ti) 0.77 eV.

Tab. I summarizes the parameters of both cells. The open circuit voltage of the normal cell (V_{oc} = 600 mV) is slightly higher than that one of the inverse cell (550 mV) despite using different electrode materials but the same photoactive materials. The open circuit voltage of the polymer solar cells depends on the energy difference LUMOacceptor-HOMOdonor [2,8]. The short circuit current (I_{sc}) of the normal cell (6.6 mA/cm^2) is slightly higher in comparison to the inverse cell (6.25 mA/cm^2). The short circuit current of the polymer solar cell depends on the amount of the absorbed light in the photoactive layer, on the carrier mobility of the donor and acceptor region, on the morphology of the photoactive layer, on the nature of the contacts between the photoactive layer and the electrodes as well as on the conductivity of the electrode materials. Because of same donor and acceptor materials used in the photoactive layer of the normal and inverse cell and because of the same preparation conditions for this layer in the two types of cells, the effects of the morphology and the charge mobility can be neglected. Nevertheless, we note from the slightly different fill factor values, defined as (I_{max} x V_{max})/(I_{sc} x V_{oc}), with I_{max} and V_{max}

* phone : +49-(0)3677-69-3410, email: maher.al-ibrahim@tu-ilmenau.de

corresponding to the maximum power point, for the two cells (0,39 for normal and 0,33 for inverse cell) that there might be a small difference in the

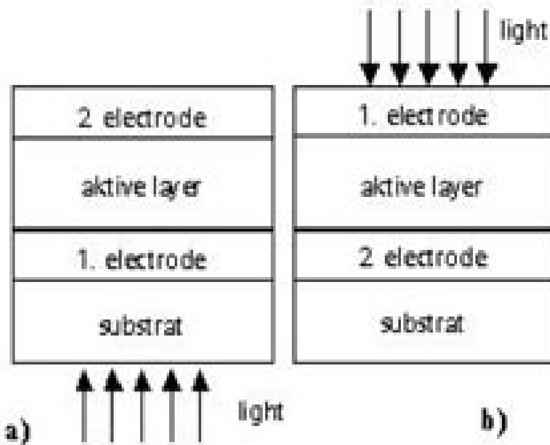

Fig. 1: Architectures of polymer solar cells: a) normal b) inverse.

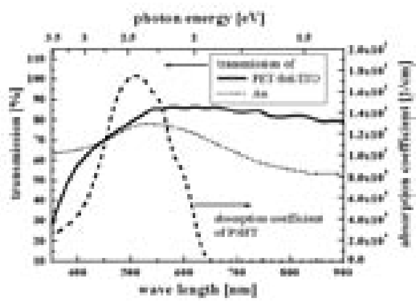

Fig. 2: Transmission of the PET-foil (175 µm)/ITO (100 nm) and Au layer (8 nm) and absorption spectrum of P3HT film.

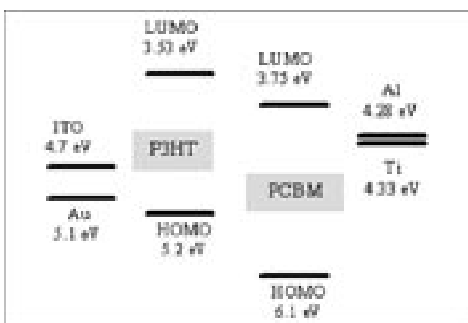

Fig. 3: Band diagram with HOMO/ LUMO levels of donor polymer P3HT and acceptor PCBM in relation to the work function of ITO, Au, Ti and Al.

morphology of the photoactive layer or in the electronic properties of the contact/polymer interface. The transmission of the PET/ITO is slightly higher in comparison to the transmission of the Au layer in the range of 450-650 nm (Fig. 2). As a consequence the photoactive layer in the normal cell absorbs slightly more light than that of the inverse cell. The barrier height for the electrons (acceptor/Al) in the normal cell and in the inverse cell (acceptor/ Ti) are comparable. The advantage of the inverse cell with Au anode is that the barrier height for the holes (donor/Au: 0.1 eV) is lower than the one in the normal cell (donor/ITO: 0.5 eV) (Fig. 3). For these reasons the current in the normal cell is comparable to that in the inverse cell.
Consequently, the power conversion efficiency $\eta_{AM1.5}$ of the normal and the inverse cell is 1.54% and 1.12%, respectively.

Tab. 1. Photovoltaic performance of normal and inverse cell under illumination with 100 mW/cm² of AM1.5.

Cell	V_{OC} [mV]	I_{SC} [mA/cm²]	FF[%]	$\eta_{AM1.5}$[%]
norma	600	6.60	39	1.54
inverse	550	6.25	33	33

Presently, the material costs for a future polymer solar cell are essentially determined by the relatively expensive ITO substrate. Inverse polymer solar cell architectures starting with a metal coated instead of an ITO coated substrate are a conceivable alternative. A first intermediate step on this way is demonstrated preparing an ITO-free polymer solar cell. Further research and developments are needed to apply these results to flexible substrates and low-price metal electrodes with suitable work functions.

We thank Bundesministerium für Bildung und Forschung (BMBF Germany) and Thüringer Kultusministerium (TKM Thuringia/Germany) for financial support.

[1] S. Sensfuss, A. Konkin, H.-K. Roth, M. Al-Ibrahim, U. Zhokhavets, G. Gobsch, V.I. Krinichnyi, G.A. Nazmutdinova, E. Klemm, Synth. Met. 137 (2003) 1433-1434.
[2] M. Al-Ibrahim, H.-K. Roth, M. Schroedner, A. Konkin, U. Zhokhavets, G. Gobsch, S. Sensfuss, Organic Electronics 6(2) (2005) 65-77.
[3] M. Al-Ibrahim, A. Konkin, H.-K. Roth, D.A.M. Egbe, E. Klemm, U. Zhokhavets, G. Gobsch, S. Sensfuss, Thin Solid Films 474 (1-2) (2005) 201-210.
[4] M. Al-Ibrahim, H.-K. Roth, S. Sensfuss, Applied Physics Letters 85 (9) (2004) 1481-1483.
[5] M. Al-Ibrahim, H.-K. Roth, U. Zhokhavets, G. Gobsch, S. Sensfuss, Solar Energy Materials & Solar Cells 85 (1) (2005) 13-20.
[6] F. Padinger, R. S. Rittberger, N. S. Sariciftci, Adv. Funct. Mater. 11(13) (2003) 1-4.
[7] C.J. Brabec, N.S. Sariciftci; J.C. Hummelen, Adv. Funct. Mater. 11 (2001) 15.
[8] C. J. Brabec , A. Cravino, D. Meissner, N. S. Sariciftci, T. Fromherz, M. T. Rispens, L. Sanchez, J. C. Hummelen, Adv. Funct. Mater. 11(5) (2001) 374.
[9] M. Al-Ibrahim, S. Sensfuss, J. Uziel, G. Ecke, O. Ambacher, Solar Energy Materials & Solar Cells 85 (2) (2005) 277-283.

InO/SnO/SiC FET for the Detection of NO_x and O_2

M. Ali[1,*], V. Tilak[2], Th. Stauden[1], V. Cimalla1, and O. Ambacher[1]
[1] Department of Nanotechnology
[2] General Electric Company, Niskayuna, USA

Demands for exact monitoring of nitrogen oxide gases (NO_x), which are air pollutants released from combustion facilities and automobiles, have become more serious all over the world in recent years. For air quality monitoring or exhaust gas control, NO_x is the main gas to be detected, and the concentration range to be measured is about 0-10 ppm. Semiconductor NOx sensors using metal oxides have been investigated by many researchers [1, 2, 3]. Most semiconductor metal oxides undergo surface interactions, such as physisorption, and chemisorption, with gas molecules at elevated temperatures (300 to 600°C). Since most active layer of semiconductor sensors are polycrystalline (composed of multiple crystallite grains pressed or sintered into a continuous structure incorporating grain boundaries), the adsorbed gases have significant electronic effects on the individual crystalline particles. The gas-solid interactions, result in a change in electron (or hole) density at the surface (i.e., a space charge forms), which in turn results in a change in overall conductivity of the semiconductor oxide. This behaviour has been widely exploited to produce rugged, low cost ceramic sensors that are widely used in many applications with varying degrees of success. Up to now SnO_2 based sensors were the mainly investigated and also of commercial interest. They are, however not very selective and usually operate at elevated temperature. The addition of an appropriate amount of metal additives (e.g., Pt, Ir, Pd) or different semiconducting metal oxide (ZnO, InO, V_2O_5, etc.) have been shown to improve the detection of various kinds of gases via the enhancement of the sensor response and decrease of temperature of maximum sensor response [1,4,5,6]. A decrease in response time and better selectivity are also claimed to be achievable by using these additives. In this work the NO_x and O_2 sensing properties of InO/SnO films in dependence of the operation temperature have been investigated.

The sensor structure is shown in Fig. 1. The structure includes SiC-based field effect transistor (FET) with InO/SnO gate as a gas sensitive layer. InO and SnO films, of 40 nm thickness, were deposited via RF magnetron reactive sputtering. The channel has doping of 10^{17} and thickness of 0.25 μm. The gate and source are shorted. The experiments were performed in a vacuum chamber reaching a base pressure of 4×10^{-8} mbar.

Fig. 1: Schematic diagram of the SIC-based FET NO_x gas sensor processed by General Electric.

Current/voltage characteristics have been carried out at different gas concentrations on sensors, which were heated at different temperatures. using a furnace. The temperature was measured by a thermocouple a few millimetres above the sensor. In all cases the applied source drain voltage varied between 0 V and 20 V in steps of 40 mV while the respective values of the current were measured.

Fig. 2 shows the I-V characteristics of SiC-based FET with InO/SnO gate in vacuum and in presence of 2 ppm of NO_x at 350°C.

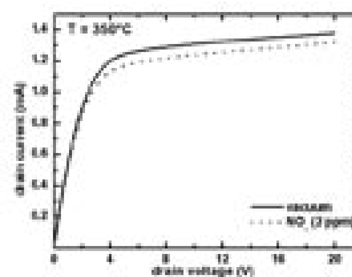

Fig. 2: I-V characteristics of the sensor operated at 350°C in vacuum (solid line) and in presence of 2 ppm of NOx (dotted line).

The zero bias resistance of this device in vacuum at U_{ds} = 20 V was 14.5 kΩ. After the exposure to 2 ppm of NO_x the resistance increased to 15.4 kΩ. The response to NO_x can be understood by considering the interaction between NO_x and n-type InO/SnO films. Adsorption of oxidizing gases (such as NO_x, O_2,..) reduces the number of free electrons in metal oxides and, thus reduces the conductivity. This change in the conductivity of the gas sensitive layer in our FET is reflected by a change in the drain current. We have found that the exposure to the oxidizing gases NO_x and O_2 results in decrease in the drain current.

* phone : +49-(0)3677-69-1172, email: majdeddin.ali@tu-ilmenau.de

Fig. 3 shows the sensitivity of the sensor operated at 350°C to different concentrations of NO_x (from 2 to 1016 ppm). We have defined the sensitivity as the relative current variation at constant voltage expressed in percent:

$$S = \frac{I_v - I_g}{I_g} \times 100$$

whereby I_v and I_g are the current of the sensor in vacuum and in presence of gas.

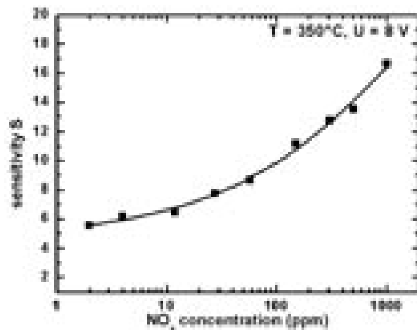

Fig. 3: Sensitivity of the sensor to different concentrations of NO_x at 350°C. The measurements were performed at a constant voltage of U = 8 V.

Fig. 4 shows the sensitivity of the sensor operated at 400°C to different concentrations of O_2 (from 2 to 40466 ppm).

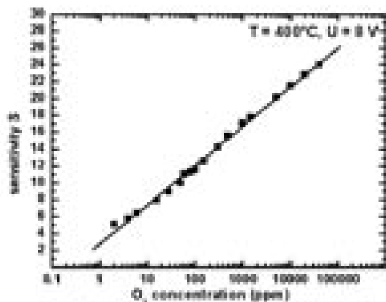

Fig. 4: Sensitivity of the sensor to different concentrations of O_2 at 400°C.

We have found that the sensitivity increases non-linearly with an increasing concentration of NO_x and linearly with an increasing concentration of O_2. Fig. 5 shows the dependence of the sensitivity to 12, 150, and 504 ppm of NO_x on the operating temperature. As seen from Fig. 5, the optimum detection temperatures occur in the 325-375°C rang for NO_x.

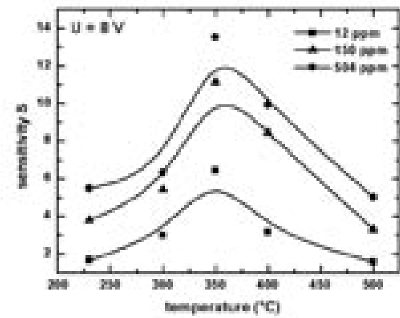

Fig. 5: Dependence of sensitivity versus temperature for 12, 150, and 504 ppm of NO_X.

Fig. 6 shows the dependence of the sensitivity to 80, 150, 302, and 504 ppm of O_2 on the operating temperature. As seen from Fig. 6, the optimum detection temperatures occur in the 375-425°C rang for O_2.

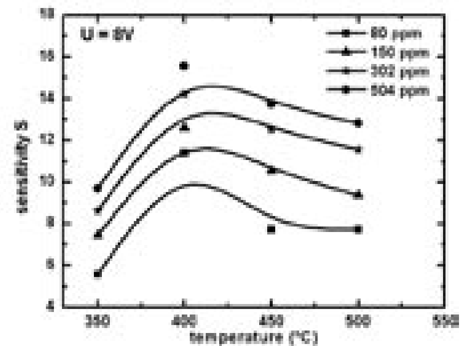

Fig. 6: Dependence of sensitivity versus temperature for 80, 150, 302, and 504 ppm of O_2.

Conclusion:
(1) Maximal sensitivity to NO_x and O_2 was observed at 350°C and 400°C, respectively.
(2) The optimum detection temperatures occur in the 325-375°C rang for NO_x. and in the 375-425°C range for O_2.

This work was performed in cooperation with V. Tilak, P. Sandvik, and D. Merfeld from General Electric.

This work was supported by the Thuringian ministry of culture (TKM) and European Union.

[1] A. Dieguez, A. Romano-Rodiguez, J. R. Morante, J. Kappler, N. Barman, and W. Göpel, Sensors and Actuators B60 , 125-137 (1999).
[2] E. Comini, G. Faglia, G. Sberveglieria, Zhengwei Pan and Zhong L. Wang, Appl. Phys. Lett. 81,1869 (2002).
[3] C. Winnie Chu, M. Jamal Deen,b and Ross H. Hula, J. Electrochem. Soc.,145,4219-4225 (1998).
[4] A. V. Tadeev, G. Delabouglise, and M. Labeau, Materials Science and Engineerin B57, 76-83 (1998).
[5] O. Renault, A. V. Tadeev, G. Delabouglise, and M. Labeau, Sensors and Actuators B59, 260-264 (1999).
[6] N. Yamazoe, Y. Kurkawa, and T. Seiyman, Sensors and Actuators B4, 283-289 (1983).

Optical Design of Integrated Microoptical-Microfluidic Systems for Biomedical Applications

M. Amberg[1,*], J. Enger[2], M. Göksor[2], D. Hanstrop[2], and S. Sinzinger[1]
[1] Department of Technical Optics
[2] Department of Physics, Göteborg University, Sweden

Introduction
Microfluidic systems gain importance for a large variety of applications in biomedicine and life sciences. One of the problems occurring in practical systems is the adhesion of cells and micro-particles to the walls of microfluidic channels and reservoirs. For scientific examinations, e.g. for drug testing, it is necessary to expose specific test cells to different media. The cells are moved between the reservoirs, e.g. by optical tweezers, and kept there for a specific period of time. This is a very time consuming experiment as the cell under examination must be kept in the laser trap during the whole reaction cycle. If the cell, on the other hand, is left untrapped in the reservoirs it will stick to the walls of the micro-reservoir and removing is not possible without damaging the cell. Therefore, there is a strong need for a matrix of fixed traps in the reservoir keeping a couple of cells, each in his own trap, away from the surfaces. In this case the movable optical trap is just needed for transport from one reservoir to another. In this project we investigate possibilities to integrate optical functionality in the microfluidic system to generate the static weak optical traps without additional optical components which need to be aligned to the microfluidic system. Further on, this system setup could be used to generate light distributions for sorting particles within a volume flow [5].

Goal of the work
Until now, the microfluidic and the optical systems are not integrated into the same substrate. Using planar integrated free space optical systems (PIFSO), it is possible to integrate both functionalities within one substrate. The idea of PIFSO systems is to integrate common free space optics into a glass substrate [1]. This means that the optical axis is folded and the light travels on a zig-zag path between the reflection coated surfaces (see Fig. 1). The optical elements, commonly diffractive elements, need to be corrected for the oblique incidence of light and are etched with submicron precision into the surfaces of the substrate. No optomechanical alignment of the individual optical components is necessary since the system is integrated monolithically. These systems are ready for use immediately after fabrication. It was shown by various authors that such PIFSO systems can be used e.g. for optical communication and security applications [2, 3]. Combined with a microfluidic system, both applications use the same fabrication techniques and could be combined very well. Up to now, these PIFSO systems are fairly inefficient and need to be optimised, e.g. by integration of refractive components [4].

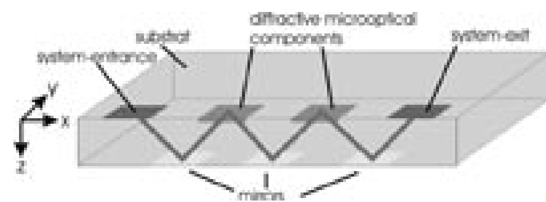

Fig. 1: Principle setup of a PIFSO system

Basic requirements for optical trapping
Optical tweezing systems are a common technology and commercially available. Most of the tweezing systems are single trap tweezing systems. Thus, just one test particle can be handled at a time. Optical tweezers normally consist of microscope objectives with a high numerical aperture, e.g. a magnification of 100x, and a numerical aperture NA = 1.3 with oil immersion. These objectives are well corrected for aberrations and focus the light to a diffraction limited focus. The focussed wave field exerts two kinds of forces on "larger" (>wavelength) particles which allow the trapping. The first one is the radiation pressure, pushing the particles along the optical axis out of the focus and the second one is the axial gradient force pulling the elements into the focus. For optical tweezing it is necessary that the gradient force is stronger than the radiation pressure to keep the particles within the focus of the laser beam. For smaller objects (down to 5nm), the trapping is based on the formation of an electric dipole momentum in response to the ligth's electric field [5].

Preliminary experimental setup
A preliminary experiment demonstrates that it is possible to generate the spot pattern which is required for keeping particles away from the walls, within a semi-integrated system (see Fig. 2). The

* phone : +49-(0)3677-69-1806, email: martin.amberg@tu-ilmenau.de

channel system is built up by a microscope cover slip with a PDMS layer containing the microfluidic system. The combination of these materials allows one to setup a system sealed against leakage of the liquids. On the other side of the cover slip is a silica substrate. This substrate contains the diffractive beam splitter, calculated to generate four spots in a square. For the preliminary test system the distance between the spots amounts 15μm and the distance to the channel surface (Δz - d) is in the range between 2 - 20μm.

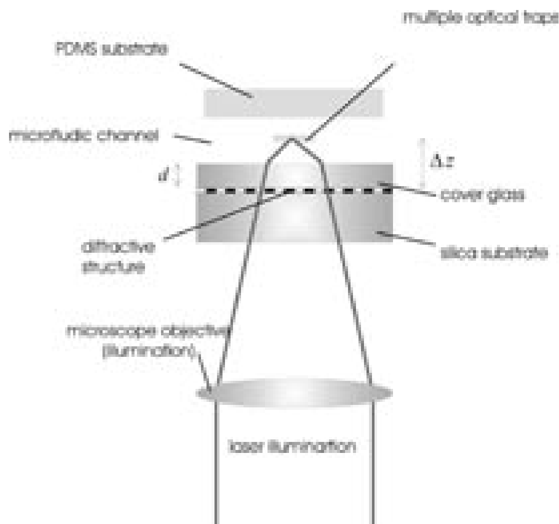

Fig. 2: Preliminary experiment setup

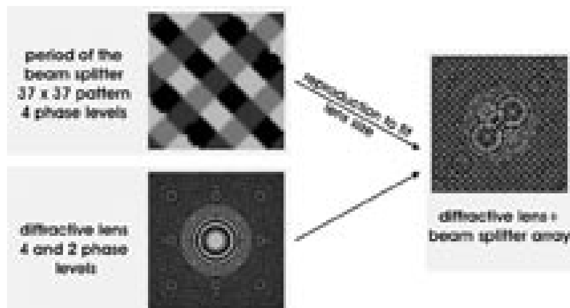

Fig. 3: Combination of a diffractive beam splitter and a diffractive lens

Therefore, various beam splitters have been designed to meet this requirement. In order to achieve the largest possible numerical aperture for higher trapping forces, an additional diffractive lens is integrated in the diffractive optical element which provides additional focussing power. The lithographic fabrication of diffractive optics allows to combine the beam splitter and the additional lens within one substrate. Hence, the phase structure of both elements has to be added. This basic procedure is shown in Fig. 3. As the beam splitter is an element of about 37 by 37 pixels, it needs to be replicated periodically in order to fit the size of the lens (approx. 350 by 350 pixels). When varying the minimum feature size (s_{min}= 2μm - 1μm) of the diffractive elements the numerical aperture varies: NA of 1.01 - 1.28. This is good enough to trap at least smaller particles within the system. To move the particles from one reservoir to another, it is necessary to improve the setup so that it is possible to reach the channel from both sides with a microscope objective.

After design and fabrication of the diffractive optical elements, currently first test experiments are under way.

The authors gratefully acknowledge the financial support provided by Deutsche Forschungsgemeinschaft (DFG) through the SONS Programme of the European Science Foundation, which is also funded by the European Commission, Sixth Framework Program. We gratefully acknowledge the support of T. Seiler and Prof. J. Jahns, University of Hagen with the fabrication of the integrated diffractive optical element.

[1] J. Jahn and A. Huang, "Planar packaging of free space optical interconnections", Proc. of the IEEE 82, 1623-1631 (1994).
[2] S. Sinzinger, "Microoptically integrated correlators for security applications", Opt. Comm. 290, 69-74 (2002).
[3] M. Gruber, "Planar-integrierte photonische Mikrosysteme zur parallelen optischen Kommunikation in der Informationstechnik von morgen", Logos Verlag Berlin (2003).
[4] M. Amberg and S. Sinzinger, " Design Consideration for Efficient Planar-Optical Systems", Opt. Comm. submitted (2005).
[5] D. G. Grier, "A revolution in optical manupilation", Nature 424, 810-816 (2003).

Improved low-cost fabrication of submicrometer polymer field effect transistors

S. Scheinert[1,*], G. Paasch[2], A. Herasimovich[1], and I. Hörselmann[1]

[1] Department of Solid State Electronics

[2] Leibniz Institute for Solid State and Material Research IFW Dresden

Recently, we developed a novel low-cost technology [1] using underetching technique, in combination with low-resolution photolithographic steps and further standard microelectronic processes, for the inexpensive preparation of organic short-channel transistors. In order to impede short-channel effects thin insulator layers are necessary. Different organic materials have been investigated as an alternative for inorganic gate insulators. Layers with high break-through voltages at thicknesses down to 150nm have been achieved already, but for short-channel transistors 50nm or less are needed. Since such organic insulators are not yet available, we used a hybrid design with silicon dioxide as gate insulator and a highly doped silicon wafer as gate.

In spite of the good overall performance, the first preparations led to a low mobility and a nonlinear increase of the drain current at low drain voltages. A possibility to increase the mobility is the HMDS treatment of the silicon dioxide interface. The increase of the mobility was only obtained operating the process on the pure oxide layer but not on an oxide with prepared source/drain contacts. The effect of the nonlinear drain current increase has been investigated by 2D simulations considering the source/drain contacts. One contact is a sputtered gold layer and the other one an evaporated composite layer made from chromium/gold since the chromium improves the adhesion of the evaporated contact. Fig. 1 shows the output characteristics and drain conductance of a 1μm channel length transistor using gold as source and the composite contact as drain and for interchanged contacts. The drain current is higher using the composite Cr/Au-contact as drain. Furthermore, there is a non-linearity of the curves at low drain voltages in both cases resulting in a maximum of the drain conductance. This maximum occurs at higher drain voltages for the Cr/Au-contact as source. Our simulations have indicated the low work function of the chromium to cause a Schottky contact to the polymer resulting in the non-linear behavior at low drain voltages in both cases. This Schottky contact is reverse-biased with Cr/Au as source and forward-biased in the other case. Consequently, the drain current is lower for the composite contact as source. However, by contrast to the experiments (Fig.1), the maximum of the drain conductance occurs at nearly the same drain voltage in both cases. Consequently, there are further influences as for example fixed charges near the composite contact determining the position of the maximum.

Another important aspect demonstrated by the simulations is the estimation of the mobility applying the simple Shockley equation. The variation of the drain current in both the linear and saturation region

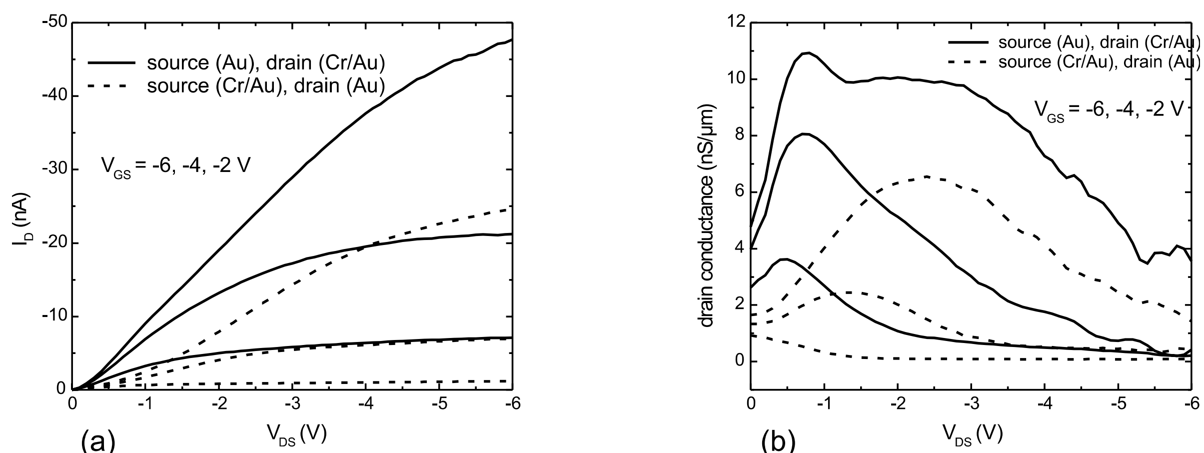

Fig. 1: Output characteristics (a) and drain conductance (b) for a P3HT transistor with L=1µm and w=500µm and a composite contact.

* phone : +49-(0)3677-69-3222, email: susanne.scheinert@tu-ilmenau.de

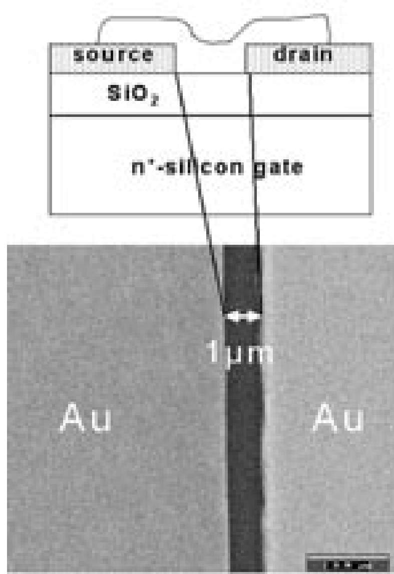

Fig. 2: Cross section and scanning electron micrograph of the varied transistor design

depends on the work function of the contacts. Therefore, applying the simple Shockley equation results in wrong values for the mobility estimated directly from the current-voltage characteristics.
As a result of these simulations we prepared transistors without composite contacts. The schematic cross section and a scanning electron micrograph are shown in Fig. 2. The measured characteristics of such a transistor are given in Fig. 3. As visible, there is a linear increase of the current in the active region and no maximum in the drain conductance. However, the drain currents are different interchanging the contacts. This phenomenon is the well known problem of the current dependency on the antecedent measurements. However, the reason for this effect is not clear. As a result we conclude, the demonstrated technology enables the preparation of organic field effect transistors with well-defined and controllable channel lengths in the submicrometer region with improvement of the performance by using only high work function contacts.

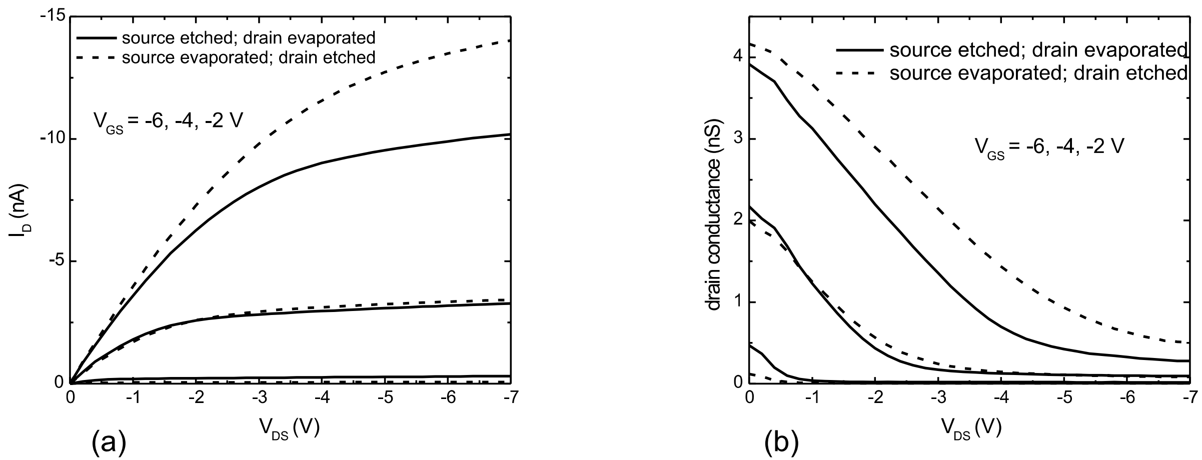

Fig. 3: Output characteristics (a) and drain conductance (b) for a P3HT transistor with L=1µm and w=500µm without composite contact.

This work has been supported by the DFG.

[1] S. Scheinert, A. Scherer, T. Doll, G. Paasch, and I. Hörselmann, Appl. Phys. Lett. 84, 4427 (2004).

GaN-based pH-Sensors

G. Kittler*, A. Spitznas, C. Buchheim, V. Lebedev, and O. Ambacher
Department of Nanotechnology

The pH-value is a crucial parameter in biological and chemical systems determining reaction kinetics and lifetime of cell cultures or other biological systems. Therefore pH-sensors are used in laboratories, industry, and medical facilities. GaN-based pH-sensors would combine the possibility to measure pH-value and to realize a simultaneous optical spectroscopy.
The sensor-structure consists of an AlGaN/GaN-heterostructure grown on a 2" sapphire substrate by plasma-induced molecular beam epitaxy (PIMBE). Because of strong spontaneous and piezoelectric polarization within the different crystal-layers and an abrupt change in polarization between AlGaN and GaN a two-dimensional electron gas (2DEG) is confined close to the interface [1]. The electrons are blocked in their motion perpendicular to the crystal interface leading to a sheet carrier concentration of around 10^{13} cm^{-2} and a very high room-temperature mobility of 800 cm^2/Vs. The schematic cross section of an AlGaN/GaN-heterostructure is shown in Fig. 1.

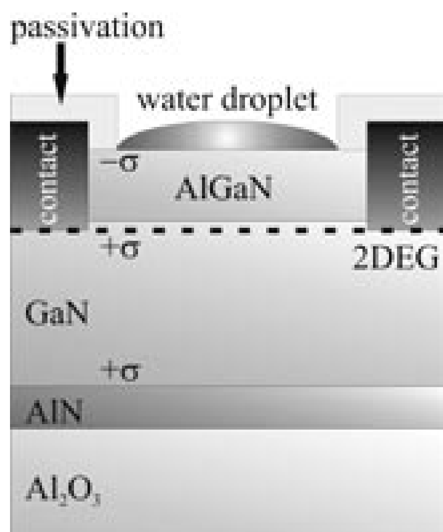

Fig. 1: Schematic view of an AlGaN/GaN with fixed polarization charges σ at the interfaces and a 2DEG.

The carrier concentration of the 2DEG is sensitive to any change of the surface charges disturbing the balance of charges within the whole structure [2]. The surface sensitivity to charges is used to measure the pH-value of solutions wetting the open-gate area of the sensor [3]. According to the site-dissociation theory by Bergveld [4] amphoteric hydroxyl groups are formed at oxidized surfaces contacting an aqueous solution. At these surface sites chemical reactions can occur, i.e. hydroxyl groups can be neutral, protonized , or deprotonized leading to an additional pH-dependent surface charge. This charge causes a depletion or an enhancement of electrons in the 2DEG influencing the current flowing through the transistor structure.
In order to prevent an electrochemical decomposition of the metal contacts different materials were tested to passivate the sensor surface and contacts. Fluorocarbon layers (FC-layers) were investigated because they were used to modify wetting behaviour of GaN-based sensors analyzing the contact angle of small water droplets. But within solutions FC-layers did not prevent an electrochemical reaction, i.e. the FC-layers were not leak-proof in solution as it is shown in Fig. 2.

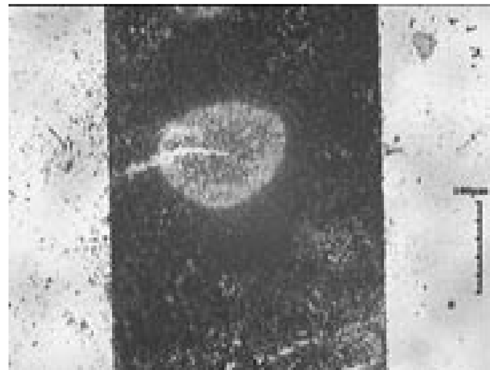

Fig. 2: Destroyed FC-layer and metal contact by an electrochemical reaction.

The most promising material for passivating the sensor surface is soldering-stop resist. The electrical resistance of this 8 μm thick layer is higher than $2 \cdot 10^8$ Ohm, i.e. the metal contact are well electrically isolated against the solution. The chemical and electrochemical stability of this material is good, although one has to pay attention to the operating point of the transistor, especially to the potentials applied to the drain- and source-contact in order to avoid decomposition.
To measure the pH-value of a solution the passivated and connected sensor is immersed in liquid. The only part of the sensor exposed to solution is the open-gate area, i.e. the active area. In order to control and to measure the gate potential an Ag/AgCl-reference

* phone: +49 (0) 3677-69 1172; email: gabriel.kittler@tu-ilmenau.de

electrode is used. The present pH-value of the solution is measured with a standard pH-instrument. Simultaneously the temperature of the solution is measured in order to avoid measurement errors. Fig. 3 shows the pH-setup.

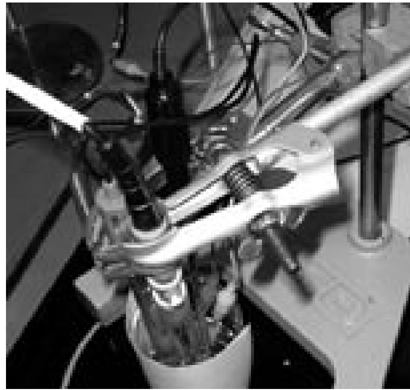

Fig. 3: pH-measurement setup with GaN-based sensor, Ag/AgCl-reference electrode, pH-instrument, and temperature sensor.

The sensitivity of a pH-measuring device is the most important parameter. To determine the sensitivity the characteristic of drain-current (I_D) versus reference potential (U_{Ref}) depending on the pH-value is measured. A typical result is shown in Fig. 4.

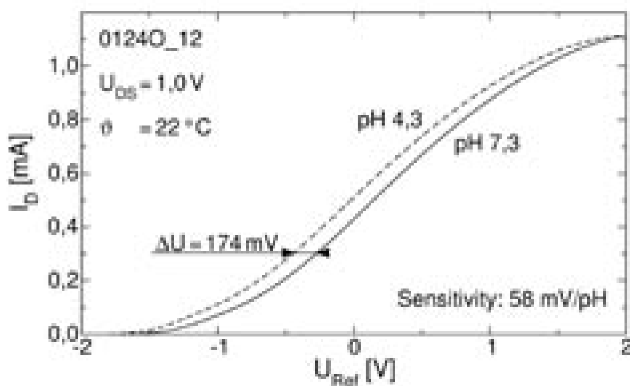

Fig. 4: I_D vs. U_{Ref} characteristic of an GaN-based pH-sensor showing a sensitivity of 58 mV/pH.

With decreasing pH-value the curve is shifted parallel to the x-axis. That means if the solution becomes more acid a lower reference-potential is necessary to get the same value of drain-current. The sensitivity is calculated from the potential-shift of the curves divided by the change of pH-value leading to a sensitivity of 58 mV/pH. The best theoretical value at 22°C calculated from Nernstian equation is 58,5 mV/pH. Taking into account a decrease of sensitivity during long-term measurement the GaN-based sensors show almost ideal Nernstian behaviour.

For a continuous pH-measurement a fixed reference potential is chosen from the position of the maximum slope in the I_D-U_{Ref}-diagram. Only close to this value the curve shows almost linear behaviour leading to a nearly linear behaviour of I_D-pH-dependence as it is shown in Fig. 5 for a different sensor. For this sensor and the chosen voltages it is possible to correlate a current value to a certain pH-value, i.e. the sensor can work as a pH-sensor.

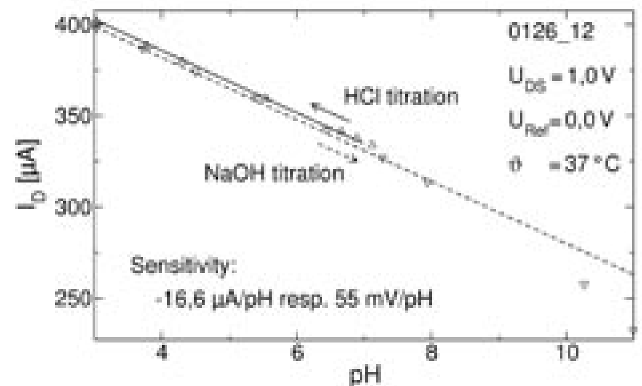

Fig. 5: I_D-pH-characteristic during a titration process.

A time resolved pH-measurement with constant reference potential is shown in Fig. 6. The correlation between I_D and pH is deduced from the I_D-pH-measurement or from the difference of I_D in the I_D-U_{Ref}-diagram at the chosen reference potential.

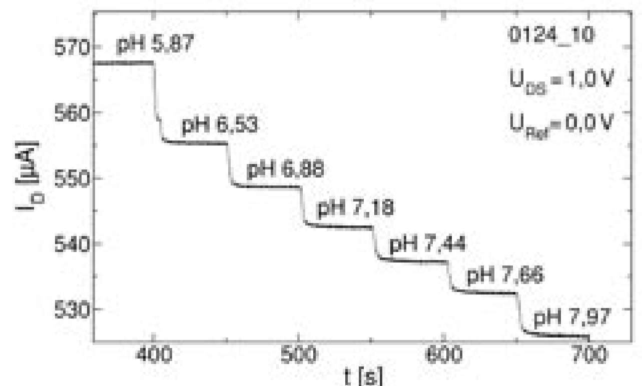

Fig. 6: Time resolved pH-measurement with constant reference potential.

The next steps will be the use of this sensors for different applications in biochemical assays, the integration of such sensors in small bioreactors, and the combination of pH- and optical measurements. Another challenge will be the integration of a reference electrode onto the sensor-chip.

This work was supported by the Thuringian ministry of culture (TKM) and the European Union (EFRE program: B 678-03001, 6th framework program: GaNano NMP4-CT2003-505614).

[1] O. Ambacher et al.: Two-dimensional electron gases induced by spontaneous and piezoelectric polarization charges in N- and Ga-face AlGaN/GaN heterostructures, J. Appl. Phys. 85, 3222(1999).
[2] R. Neuberger, G. Müller, O. Ambacher, M.Stutzmann: High-Electron-Mobility AlGaN/GaN Transistors (HEMTs) for Fluid Monitoring Applications, phys. stat. sol. (a) 185, No. 1, 85 (2001).
[3] G. Steinhoff, M. Hermann, W.J. Schaff, L.F. Eastmann, M. Stutzmann, M. Eickhoff: pH response of GaN surfaces and ist application for pH-sensitive field-effect transistors, Appl. Phys. Lett. 83, 177 (2003).
[4] P. Bergveld, A. Sibbald: Analytical and biomedical applications of ion-selective field-effect transistors, Comprehensive Analytical Chemistry, Vol. XXIII, Elsevier 1988.

Precise Drilling and Structuring of LTCC Materials using a 355 nm YAG-Laser

K.-H. Drüe * and I. Koch
Department of Microperipherics

Introduction

The interconnection density of LTCC circuits is increasing steadily. This density is limited by the manufacturability of structures on the tapes and the size of cavities and vias inside the tapes. In the last years progress was made concerning fine line printing and the use of photoimageable inks. Lines and spaces of 50 μm and below are state of the art. Drilling and filling of microvias and milling and cutting of tapes with high accuracy and reliability are still a challenge. In this field mechanical and laser methods compete. Mechanical punching is widely used in mass production. This method shows a high throughput and allows via-diameters of 100 μm and below. Lasers are also used for cutting and drilling of LTCC. They are universal tools without any wear and tear. One example is the tripled YAG laser with a wavelength of 355 nm.

Equipment

The investigations were performed using such a laser. The system uses a Q-switch with a frequency range from 15 to 50 kHz and a precision XY-table [1]. This table is used for the cutting process and for drilling of big vias (>0.8 mm). For small round vias a so called TurboCut module is used. This is a rotating optical device that diffracts the laser beam away from its central position and allows a trepanning cut. The maximum diameter of vias that can be drilled with this system is given by the diameter of the cutting nozzle. The software of the TurboCut control assures that the first pulse after the shutter opening is always located inside the circle to cut. The LTCC technology allows 3D-constructions with cavities, channels and trenches.
Laser cutting of the individual tapes is a very simple way to create these elements. The following examples will descibe the advantages.

Applications for precise structuring

The first application is a carrier for a sensor array for picofluidic investigations. The sensor chips in this application should not stand out from the carrier; therefore they are mounted in cavities. A slot is situated under the chips to allow spectral measurements of the small amounts of liquids on the transparent sensors. Fig. 1 shows the structure produced.
The next example is an optical device shown in Fig. 2. In this case a laser diode and some other optical elements had to be mounted on a common LTCC substrate. The LTCC carrier had to assure the electrical connections, the cooling by thermal vias and the exact positioning of the optical elements. The latter was done by cutting structures of different shapes using the UV laser system.

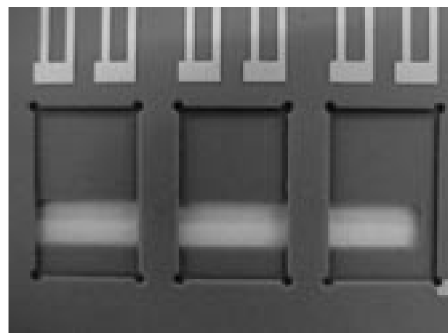

*Fig. 1: Sensor carrier with cavities in the dimension of 5 * 8 mm² for picofluidic investigations*

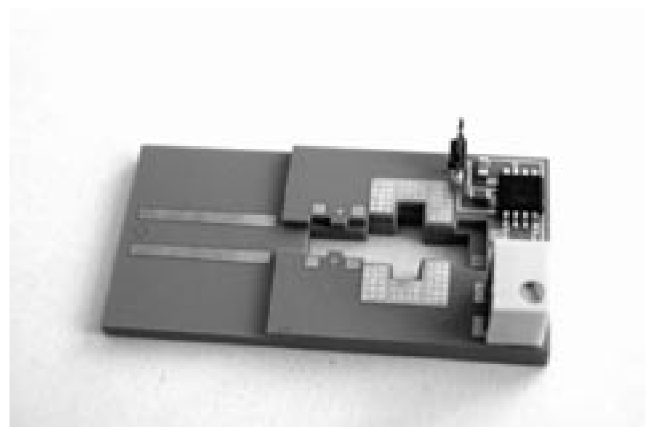

Fig. 2: Laser cut LTCC substrate as carrier for a laser diode (Design Fraunhofer IOF, Jena)

Investigations of microvias

Laser cutting of LTCC tapes shows differences to the cutting of homogeneous foils like metals or polyimides. These materials allow to focus the laser beam very exactly and the width of the cutting gap is in the scale of the laser spot. LTCC tapes are mixed materials and show a different behaviour. The different components react in different ways with

* phone : +49-(0)3677-69-3429, email: karl-heinz.drue@tu-ilmenau.de

the introduced laser energy, which density shows a gaussian distribution. For that reason we found "influenced zones" with vitrifications and colour changes beside the cut, where the whole material is vaporized.

Therefore the "effective gap width" of the cut is larger than the beam diameter [3]. For cutting an averaged laser power of about one Watt is necessary. This corresponds to a power density of about 0.32 MW/cm^2 at a spot diameter of 20 μm. Engraving is possible with a laser power of about 0.1 Watts.
Engraving was used in RF structures to create buried cavities in order to reduce the parasitic capacitance in coils. [2].
In laser cutting of LTCC one can differentiate between 3 cases:
1. Big cavities, with the possibility to push out the cut area after cutting
2. Very small vias, where the whole material is vaporized
3. "Medium sized" structures (size 80..200 μm), where it is impossible to push out the drill core mechanically.
Micro vias and medium sized ones in different materials were investigated. The test objects were via arrays with different via diameters and pitches and structures for RF applications.
Bigger vias with a diameter of 0.5 mm were used to determine possible cut widths for different tapes.

Results
One standard test to evaluate the properties of different materials was to cut the above mentioned 0.5 mm vias with an average laser power of one Watt (Q-switch frequency 32 kHz, pulse energy 31μJ). For tape materials of 114 μm thickness a cut width of about 20 μm was possible. Some debris was located in and around the gap. Some test samples were covered with a protective layer to reduce the "influenced" zone during laser treatment.
The TurboCut was used for all investigations of microvias to get a circular cut geometry. The best results were obtained with multiple phase processes. This means, every via was cut multiple times (up to 4, best results with 3) with different laser parameters like Q-switch frequency (influences the laser power) and beam expander position. For thicker tapes (maximum thickness 254 μm) it was always necessary to change the focal plane during the cutting process.
Fig. 3 and 4 show via arrays cut in LTCC of a thickness of 114 μm. A protective layer was used. The arrays have a pitch of 150 μm and the vias have a diameter of about 35 μm. In the moment this is the minimum achieved with our system. To cut these vias the laser beam was moved on a circle with a diameter of 5 microns.

Engraved cavities under coils of 50 μm line width and 100 μm line space with 1.5 to 3.5 turns reduced the parasitic capacitance of these coils to about 50% [2].

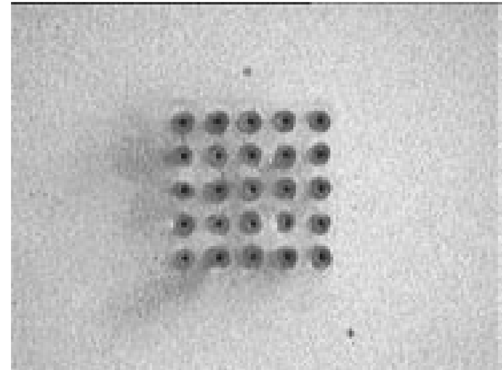

Fig. 3: Via array on LTCC, pitch 150 µm, 3 production phases, unfired

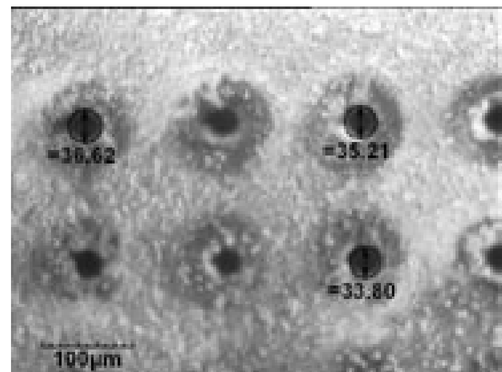

Fig. 4: Dimensions of single vias, detailed view of the via array in Fig. 3

Conclusions
Laser processing of LTCC materials allows reducing the dimensions of the structures to 50 μm and below. Limitations are given not only by the size of the focused laser beam and the exact motion control, but also by the properties of the tapes, the backings and the support (e.g. vacuum chuck) of the laser equipment. UV-lasers are especially suited
for precise cutting of tapes and for the drilling of microvias. The use of protective layers during processing can improve the cut geometry on the tape. Further investigations are necessary in this field.

The work was supported by the German Space Agency DLR (project KERAMIS) and the Thuringian Ministry of Culture (project Picofluidik).

[1] K.-H. Drüe, T. Thelemann, H. Thust "Laser Processing of LTCC with different machine concepts", 14th European Microelectronics and Packaging Conference & Exhibition,
Friedrichshafen, Germany, 23-25 June 2003 pp. 248-253.
[2] R. Perrone, H. Thust, K.-H. Drüe "Progress in the Integration of planar and 3D Coils by using photoimageable Inks", 2004 International Symposium on Microelectronics, 14-18 November 2004, Long Beach, CA.
[3] E. Elvey, G. Wang, F. Barlow, A. Elshabini "Micro Vias in LTCC Substrates", 2004 International Symposium on Microelectronics, 14-18 November 2004, Long Beach, CA.

Progress in the Integration of Planar and 3D Coils on LTCC by Using Photoimageable Inks

R. Perrone*, H. Thust, and K.-H. Drüe
Department of Microperipherics

Introduction
An actual trend is to develop new applications for higher frequencies and to integrate as many functions and passive components in a module as possible. Thus, the LTCC technology plays a very important role because it offers a wide range of possibilities to produce multi-layer circuits and permits the integration of passive elements, such as planar, buried planar, as well as 3D inductors into the LTCC module.
Standard "thick-film" inductors have a limited bandwidth of at most 1-3 GHz due to the fact that the resolution of the standard screen printing technology does not allow to pattern lines smaller than 100 to 80 µm. The size of inductors is also limited by the via diameter (standard 100 to 150 µm) and the stacking tolerances. In order to achieve an increased bandwidth, the dimensions of the coils must be reduced.
To reduce the size of coils, photoimageable inks were used in combination with microvias.
Photoimageable inks allow to pattern lines at the top layers with a maximal line resolution of 13 µm/ 21 µm line width/line space [1]. Fig. 1 shows some small parallel lines.

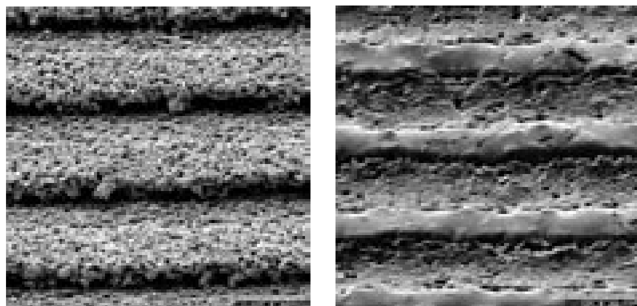

Fig. 1: Fodel parallel lines. Line width/space 30 µm/ 30 µm (l. – green/REM; r. – cofired/REM)

All microvias have a diameter of about 60 µm and were drilled with a multifunctional laser on the green sheets as in the process described in [2]. They were filled with a conducting ink by means of a via fill machine and a metal via fill mask. The metal mask was manufactured with the same laser.

Test Inductors and Measurements
Planar-spirals and planar-symmetricals with over-crossed turns have been manufactured. These turn shapes are shown in Fig. 2. In Tab. 1 the geometrical properties of the manufactured coils are summarised.
The inductivity of spiral coils as a function of the aperture width and line width was investigated. The results for inductors with 1.5 turns are shown in Fig. 3. It can be seen, that a reduction of the dimensions of the coils increases their cut-off frequency and makes the inductance curve more planar. The cut-off frequency of the inductors with an aperture width of 1 mm and 0.5 mm is higher than 8 GHz.

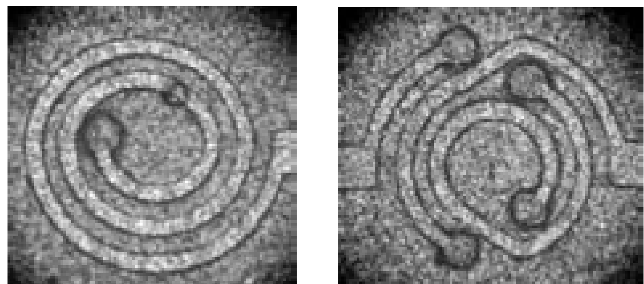

Fig. 2: Inductor shapes (l. - spiral, r. - symmetrical). Aperture: 0.5 mm, line width/space 50 µm/100 µm.

Aperture [mm]	0.5*	1	2
Turn shape	round		square
Number of turns	1.5	2.5	3.5
ine width [µm]	L30	50	70
Line space [µm]	100*		200
Tape thickness [µm]	475		

* Coils with microvias

Tab. 1: Properties of coils

* phone : +49-(0)3677-69-3452, email: ruben.perrone@tu-ilmenau.de

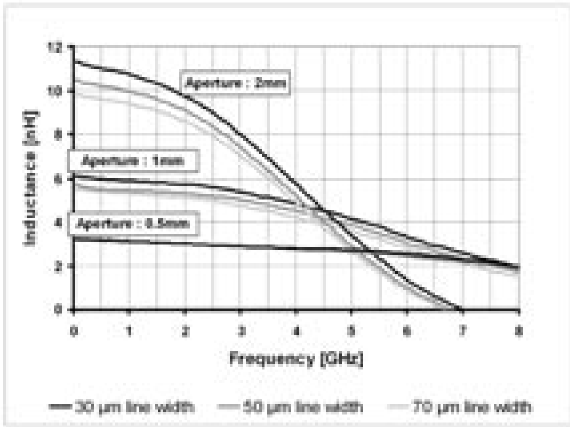

Fig. 3: Inductivity of spiral coils for different apertures and line widths.

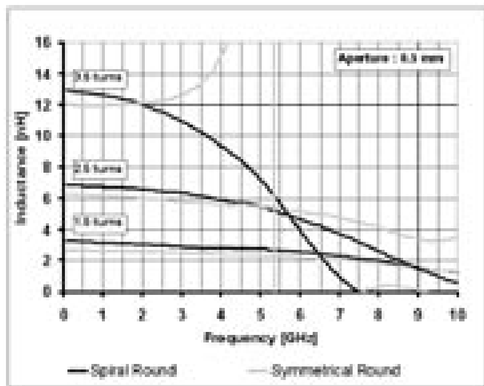

Fig. 4: Inductivity of planar-spiral and planar-symmetrical coils.

In Fig. 4 the inductivity is compared with the frequency of spiral and symmetrical coils with a line width of 50 µm. The measurements show that the inductivity of symmetrical inductors remains constant over a wider frequency range as the inductivity of spiral inductors. Some coils have not reached their cut-off frequency up to 10 GHz.
The parasitic capacitance of coils can be reduced by integrating cavities between them and their ground plane. Fig. 5 shows a photo of a buried cavity. The reduction of this capacitance causes a rising of the cut-off frequency and leads to a more flat inductance over the frequency as shown in Fig. 6.

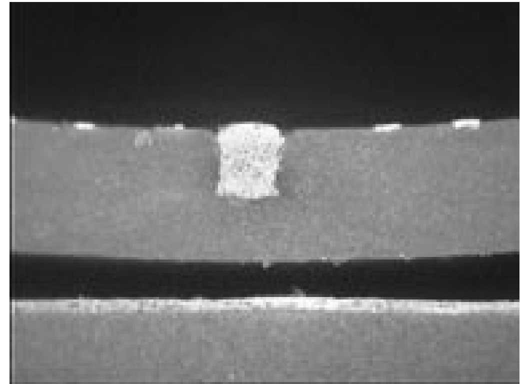

Fig. 5: Buried cavity.

Conclusion
In summary, the RF-properties of thick-film coils were improved by:
a) reducing their size by using photoimageable inks in combination with microvias,
b) using a symmetrical turn arrangement, and
c) integrating cavities between the coils and their ground plane.

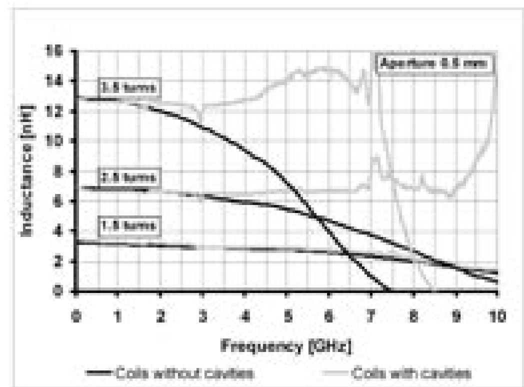

Fig. 6: Inductivity of coils with and without cavities.

[1] R. Perrone, M. Hintz, K-H. Drüe, R. Münnich and H. Thust, "Photostrukturierte Elemente und Leitungen in LTCC", PLUS, Januar 2004, Band 6, Nº1, pp. 126-132.
[2] Karl-Heinz Drüe, Torsten Theleman and Heiko Thust, "Laser Processing of LTCC with different Machine Con-cepts", 14th European Microelectronics and Packaging Conference & Exhi-bition, Friedrichshafen, Germany, 23-25 June 2003.

Low-Temperature Co-Fired Ceramic Microwave Switch Matrix for Satellite Communications

J. F. Trabert[1,*], M. A. Hein[1], J. Müller[3], R. A. Perrone[2], R. Stephan[1], and H. Thust[2]
Departments of RF- and Microwave Techniques[1] and Microperipherics[2]
[3] Micro Systems Engineering GmbH & Co., Schlegelweg 17, 95180 Berg

Introduction
We develop reliable and inexpensive components for future applications in microwave-based multimedia satellite communications. The architecture should be modular and provide a high functional density with good microwave performance. DC power consumption, manufacturing costs, weight, and volume should be kept at a minimum. Robustness, high durability and reliability, longterm stability, hermiticity and space qualification are further key requirements.
Up to now, compact microwave circuits are layed out like singlelayer printed circuit boards. Typically, connections between the RF components are placed on the top layer and the bottom layer is used as ground. This is a serious limitation for the complexity. Several multilayer techniques have been proposed to overcome this limitation. Most of these techniques have to cope with organic materials that usually suffer from poor dielectric properties, i.e. the losses of the dielectric layers prevent applications at K-band operating frequencies. One promising solution is the LTCC (low-temperature co-fired ceramic) technology which incorporates multi-layer thick-film ceramic structures with good RF and microwave performance in a single module. This technology improves the packing density of RF circuits significantly, although at the expense of challenges related to the RF design.
This paper focuses on the description of a 4x4 reconfigurable switch matrix as one example of a highly integrated modular package. Other examples, like modules for solid-state power amplification and frequency synthesis, are developed by our project partners [1]. The functionality and small size of all of these demonstrators are due to the needs of satellite-based communication systems. In this work, the principle of operation and the potential benefits of a RSM for satellite-based systems are demonstrated.

LTCC Technology
The aim of our research is to achieve a truly three-dimensional hybrid integration of passive and active components, including biasing networks, DC-blocks, power splitters et cetera, in a single LTCC multi-layer structure. At the same time, reduction of semiconductor expenses can be achieved by minimising the complexity of the semiconductor components, e.g., by transferring matching and decoupling circuits into the ceramic tile instead of being monolithically integrated on-chip. Such benefits imply that the LTCC microwave components are manufactured by reliable technological processes with reproducibly high quality and high yield. Furthermore, it is necessary to develop suitable RF interconnects, like transitions between different layers (vertical connects) or different types of transmission lines, second-level interconnects between the ceramic module and the main board (in our case: the micro-wave wafer probing station), and transitions suitable for a hermetic housing.
The LTCC process used in this work combines conventional silk-screen printing for ground layers and DC bias circuitry with a high-tech fine-line photo-imaging method as described in detail in [2, 3]. The latter technique allows to pattern microwave transmission lines with high precision, whereas standard screen-printed lines are limited in terms of minimum achievable line width, accuracy, and edge definition. Using fine-line printing, the advantages of thick-film and thin-film techniques can be exploited simultaneously at moderate costs, to manufacture microwave transmission lines, high-definition interconnects, and precise impedance matching circuits. Another important ingredient for high-quality microwave components are vias of small diameter and high placement accuracy.

Reconfigurable Switch Matrix (RSM)
We have integrated active semiconductor switching circuits with high-resolution passive components into a ceramic module for a 4x4 single-pole multi-throw reconfigurable switch matrix. A RSM provides a variety of digitally controllable signal paths for adaptation, recon-figuration, and functional multiplexing.
The modular design includes different types of transmission lines, transitions, impedance matching circuits, and biasing and decoupling networks enabling digitally controlled reconfiguration. As a first step towards a complete, hermetically sealed, package, we have designed and characterised sub-modules incorporating individual active and passive components. In the course of iterative optimisation steps, we have redesigned distinctive passive components as described in the following.

Coplanar-stripline-microstrip transition
A coplanar ground-signal-ground structure with a pitch width of 200 μm was used for the 2nd-level intercon-

* phone : +49-(0)3677-69-1592, email: johannes.trabert@tu-ilmenau.de

nect. Fig. 1 shows the waveguide transitions from the probe-tip port to a bond-pad of the switch-IC.

Fig. 1: Geometry of the applied coplanar-stripline-microstrip transition. The two encasing via-fences shift substrate-propagation-modes to higher frequencies, define the line impedance, and they decrease the coupling to adjacent transmission lines. The transparent grey areas embody the LTCC substrate material (DuPont 951).

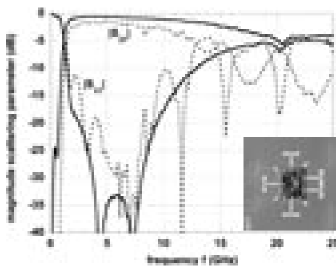

Fig. 2: Measured scattering parameters of an activated RF-junction (solid curves) in comparison with the scattering parameters of a complete RSM I/O signal path (dotted curves). Inset: photograph of the switch-IC mounted in the test-fixture.

The coplanar waveguide is first converted into buried strip-stripline and finally to a microstrip line. The electrical characterisation exhibits a good impedance matching from 15-21 GHz with $|S_{11}|$ < -15 dB and also a reasonable low insertion loss with $|S_{21}|$ of less than 1 dB.

Analysis of a single switch junction

Fig. 2 presents the microwave properties of an individual switch-IC mounted in a LTCC test module [4]. The inset to Fig. 2 shows a photograph of this module. It consists of a cavity into which the chip is embedded, gold-wire bonds with a span of about 500 μm and a diameter of 25 μm for the DC and micro-wave signals, microstrip lines, and the coplanar-microstrip transitions for RF probing. The measured S-parameters reflect the uncompensated broadband response of a series circuit consisting of two coplanar-microstrip transitions including the microstrip lines, two single bond-wires, and the RF-junction switched into its on-state. The S-parameters indicate fairly good performance up to about 12 GHz but degrade at higher frequencies: $|S_{11}|$ increases up to 5 dB and $|S_{21}|$ decreases to about -5 dB at 20 GHz. The source of this degradation could be associated with the hybrid integration of the switches including the wire bonds. Fig. 2 compares the S-parameters with the results for a complete prototype RSM. The similarity of the frequency-dependent S-parameters is striking, confirming the limiting effect of the individual switch ICs on the overall performance of the RSM.

At the same time, the reproducibility of the data confirms the suitability of the LTCC technology for dense three-dimensional microwave circuits. One possibility to improve the performance of the switch matrix is to implement compensation networks for each chip, optimised for the frequency range of interest.

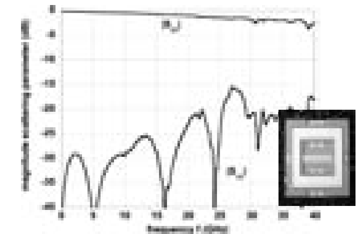

Fig. 3: Measured scattering parameters of a hermetically sealed module. Inset: photograph of the module with coplanar interface and CPWG transmission line before sealing.

Hermetic package with coplanar waveguide ports

To achieve space qualification, LTCC modules must be sealed hermetically. We have designed and tested different hermetic packages suitable for microwave frequencies. The inset to Fig. 3 depicts the 1-mm high module of base dimensions 12 mm × 14 mm which showed the best performance. Like the open modules it was manufactured with *DuPont 951*-tape and the recommended gold-based paste. The module contained an embedded coplanar waveguide with a lower ground plane (CPWG) and with an identical geometry the CPWG interfaces needed for RF probing. The micro-wave signal transmission illustrated by the main panel of Fig. 3 is very promising. The insertion loss is 0.9 dB at 20 GHz (0.7 dB/cm), and the return loss remains below 20 dB up to, at least, 25 GHz.

Conclusions

First steps have been undertaken successfully towards the realisation of a compact 4x4 reconfigurable LTCC switch matrix for satellite communications. Measurements of individual components and sealed packages revealed promising microwave response in the frequency band of interest. Ways for further improvements have been identified, illustrating the potential for realistic satellite applications. The necessity to employ narrow-band compensation networks in combination with a precise layout of the microwave transmission lines, the transitions between different types of waveguides, and the bond wiring to the chips has been illustrated.

This work has been supported by the German Federal Ministry of Education and Research (BMBF, No. 50YB0313). We gratefully acknowledge valuable contri-butions from K. Drüe and S. Rentsch at TU Ilmenau, and M. Spinnler and B. Hespeler at Tesat-Spacecom GmbH.

[1] A. Jacob et al., R. Kulke et al., Interim Report of project KERAMIS (No. 50YB0313), DLR, Germany, unpublished.
[2] R. Perrone, H.Thust, K.-H. Drüe, “Progress in passive integration of planar and 3D coils by using photoimage-able inks on and into LTCC”, 2004 IMAPS, 37th Int. Symposium on Microelectronics, Long Beach, California, USA, November 2004.
[3] T.R. Suess, M.A. Skurski, “Fodel®, Photoprintable Thick Film; Materials and Processing”, DuPont Company, Microcircuit Materials, RTP Research Triangle Park, North Carolina, USA, www.dupont.com/mcm/pdfs/fodel.pdf.
[4] J. Trabert, M. Hein, J. Müller, R. Perrone, R. Stephan, H. Thust, “High functional density low-temperature co-fired ceramic modules for satellite communications ”, submitted to European Microwave Conference, EuMW, Paris, France, October 2005.

Polymeta – A Novel Technology for Printed Circuit Boards on the Basis of Physical Vapor Deposition

G. Winkler[1,*], G. Bischoff[1], A. Sutor[1], S. Griehl[2], and T. Müller[2]

[1] Department of Design and Technology of Electronic Components

[2] CREAVAC, Creative Vakuumbeschichtung GmbH, Dresden

New applications in electronics require improved thermal management which can be achieved by new materials for PCB's. In a former paper at the IMAPS Poland 2003 [1] a new flexible material for PCB's with some proposals for new technologies was described. In this paper the newly developed technology on the basis of PVD will be presented. This includes the possibility to realize a second connexion layer with vias based on this technology. The problem of thermal load during the PVD process due to the restricted thermal durability was to be solved.
As application the replacement of conventional glow lamps by high power LED's was chosen and will be presented. In this application the possibilities for a better thermal management are crucial and will be compared to conventional FR4 material.
Due to the flexibility of this material a reel to reel production is possible.

Introduction
The paper mentioned in the abstract closed among others with the conclusion: "It is a challenging task to develop compensatory technologies that would outpace the current ones by their quality and yet be affordable in mass production". This paper describes such new technologies based on a flexible material designed for the application as thermal conductive foils. The brand is KERATHERM® 86/xx [2] – a ceramic filled silicon material reinforced by glass fabrics. The process of forming the conductive pattern should avoid the conventional etching technology by means of PVD technology in conjunction with proper electrolytic deposition and, if necessary, short time etching. The excellent possibilities for thermal management have been shown already. The challenge of mass production could be solved by a technology which allows a reel to reel production. The work was done in cooperation between Technical University of Ilmenau, CREAVAC GmbH, and Kerafol GmbH, all located in Germany.

Process
Two different technologies were taken into consideration. The first is a semi additive process and the second a fully additive one. The basis for both processes was a copper layer applied to the substrate by PVD.

Investigations have been carried out to determine the pull strength of the final connecting copper layer for different substrate materials, process parameters and technology variations. It could be shown that the generation of vias is possible. In Fig. 1 such a via is shown. The hole was punched by a LTCC punching equipment with a diameter of 0.5 mm, the thickness of substrate was less than 1 mm.

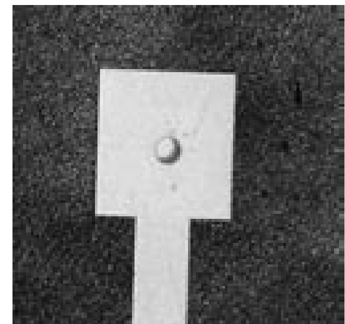

Fig. 1: Via

Semi Additive Technology
This process uses the PVD to produce a thin copper layer in the range of μm. A photo resist is used as a galvanic resist to clad the basic copper layer in a way that the galvanic reinforcement produces the final conductive pattern. A short etch removes the thin copper layer. Fig. 2 shows the different steps of this process.

It could be shown, that only a restricted choice of substrate materials produces visibly good surfaces, as well as sufficient pull strength values after the PVD process. Measured values for the pull strength are shown in Fig 3. With additional interposer layers (Palladium, Aluminium and Nickel / Chromium) the pull strength values could be improved on the expense of additional etching steps.
Additional to Kerafol materials, some thermoplastic materials for a low cost application were included in these investigations: PET (50μm), PEN (125μm), and Kapton PI (25μm).

Additive Technology
The additive technology is shown in Fig. 4. It is carried out without chemical etching. Instead, structuring is done by proper masking of the PVD deposition.
Crucially for this technology is the masking resist which has to withstand relatively high temperatures during the PVD process. Some screen printable materials showed sufficient resistivity in this respect.

* phone : +49-(0)3677-69-2606, email: gert.winkler@tu-ilmenau.de

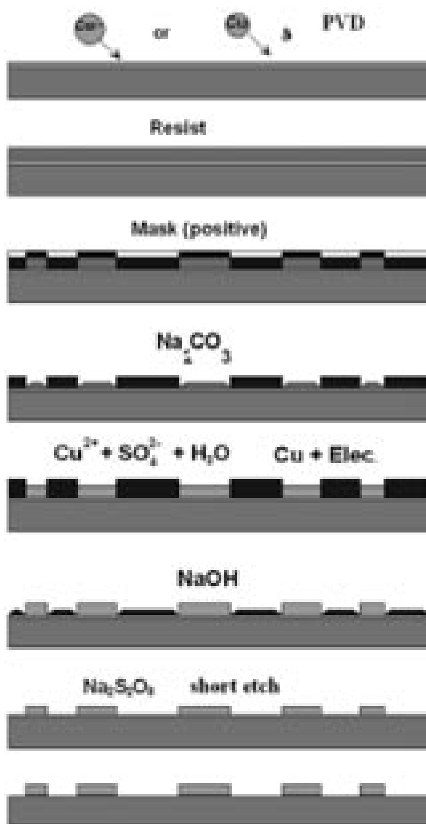

Fig. 2: Semiadditive technology

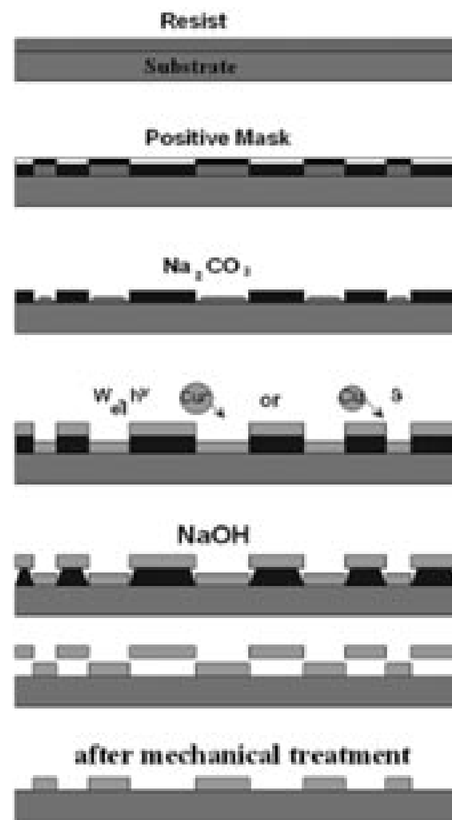

Fig. 4: Additive technology

Equipment
The PVD process has been realized at CREAVAC GmbH with equipment provided by them. Fig. 5 shows a source for continuous metal vaporisation. As mentioned before a reel to reel production could provide benefits for mass production.
Investigations proved that this is possible with adapted equipment.

Fig. 5: Source for vaporisation

Applications
One possible application benefitting from the technology described above could be the assembly of high power LED's. Here, the thermal management can become important due to the relatively high power dissipation. Flexible substrates make possible the application of "light bands" to illuminate steps or path in airplanes. Fig. 6a shows the test layout and Fig. 6b an assembled circuit. As a second application, Fig. 7 shows another LED module assembled in an automatic process.

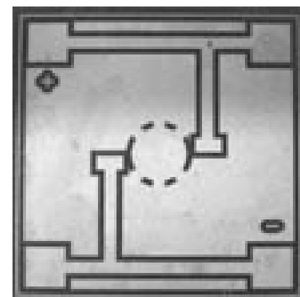
Fig. 6a: Test layout

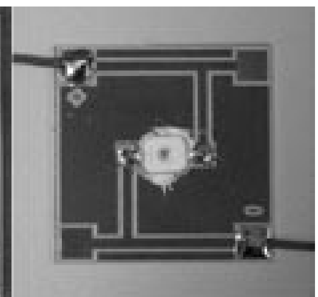
Fig. 6b: Assembled module

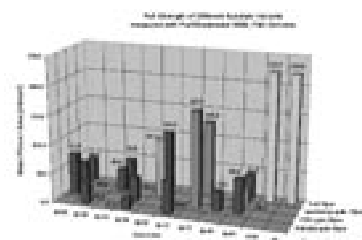
Fig. 3: Pull Strength on different substrates

Conclusions
It could be shown that new technologies based on PVD processes in conjunction with new substrate materials can result in new products which can compete very well with standard PCB technology in terms of functional, economical, and ecological aspects.

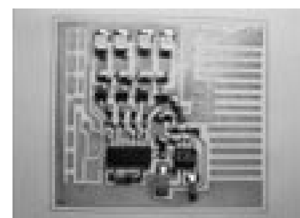
Fig. 7: Automatically assembled LED module

[1] Gert Winkler, Gernot Bischoff, Aneta Sutor: „New Materials and Technologies for Printed Circuit Boards", Proceedings of the 27th International Conference and Exhibition IMAPS – Poland 2003, pp. 88-100.
[2] Kerafol: Katalog KERATHERM, Keramische Folien GmbH Eschenbach (Germany), 2002.

Chemical and Biochemical syntheses optimised for Micro-structured Glass Chips

M. Gebinoga[1,*], Arne Albrecht[2], and A. Schober[1]
[1] Center for Micro- and Nanotechnologies
[2] Department of Microsystems Technology

Summary
The SynSort Technology is a combination of chemical solid-phase syntheses using planar polymer films and a magnetic handling device. The functionalised polymers will be connected at small, magnetic glass-chips. 50 – 100 of these chips will be arranged on a magnetic glass array. It is possible to use this technology for a spatial resolved combinatorial synthesis on a solid support. One powerful combinatorial synthesis is the Split&Mix technique for the synthesis of large libraries of compounds. One of the most important disadvantages of this technique is the analysis of the synthesised compounds. For such syntheses a coding of each polymer carrier will be necessary, unless a time-consuming deconvolution strategy for the product mixtures will be used.

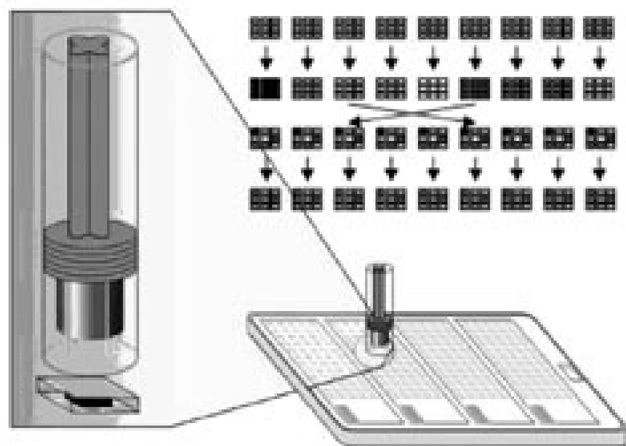

Fig. 1: Sketch of a MTP chip carrier with the magnetic pen to move the magnetic glass-chips. Above are outlined the combination strategy following a Split&Mix technique but with spatial addressable glass-chips.

The SynSort technology allows an easy spatial arrangement and each glass-chip can be used for special reactions to synthesise a compound. For the common washing steps in solid-phase synthesis all glass-chips together will be washed on the magnetic glass array. For a new synthesis with other reactions the glass-chips can be rearranged following the combinatorial synthesis strategy.

After all steps are done, each glass-chip with a single compound can be easily identified only by the first position at the array, and the following rearrangement steps.

Split&Mix technique
The Split&Mix technique (also known as "one-bead, one-peptide" concept) synthesised on a statistic approach a large number of different peptides on polystyrene beads (∅ 10-50 μm). Each bead carry exactly one peptide of a specific sequence. In a synthesis well there are some thousand beads. For an analysis there must be analysed in the first step some thousand peptides. Active mixtures will be distributed a couple of times and re-analysed (deconvolution strategy). It is obvious, that this strategy carry some serious problems:

- Mixtures can exhibit different characteristics as pure substances (an enhancement as well as a suppression will be problematic for the screening).
- Isolation of pure substances can be very tedious.

The SynSort approach overcomes these problems by a spatial arrangement that enable a rapid identification of each peptide.

Chemical Part
The SynSort chemistry is an adapted solid phase peptide synthesis (SPPS), based on FMOC chemistry by resin coated glass-chips. The coating with an appropriate resin-linker structure will be done by our project partner *IPHT e.V.* in Jena. Normal FMOC based SPPS use resins with linkers to build up single peptides or many different peptides ("peptide library"). The peptide library of the SynSort project deals with the Vancomycin binder motif. This is of a particular interest, because this interaction between the antibiotic Vancomycin and different binding (or non-binding) peptides can give some answers in respect to the antibiotic defense of resistant bacteria strains (e.g. *Staphylococcus aureus*).

* phone : +49-(0)3677-69-3468, email: michael.gebinoga@tu-ilmenau.de

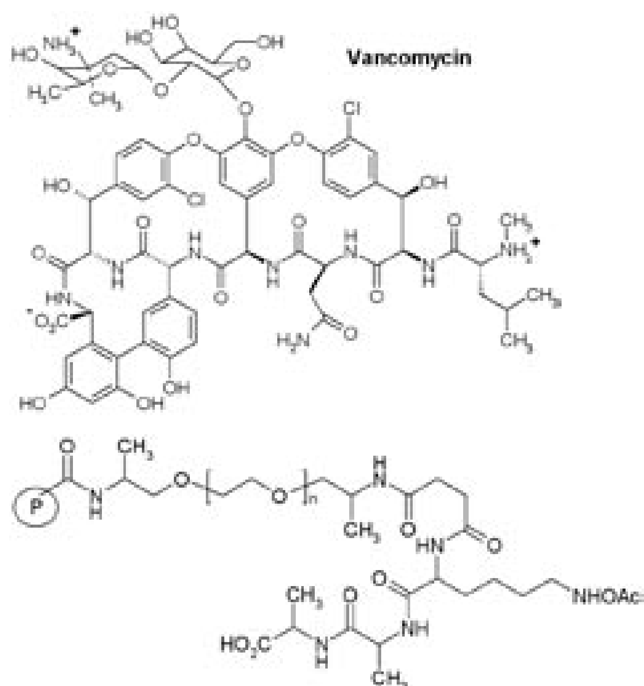

Fig. 2: Molecular structures of Vancomycin (above) and a reference peptide coupled on the resin. The encircled P stand for the high molecular resin.

A crucial point of this synthesis is the adaptation of the glued glass-chips to the harsh reaction conditions of SPPS. Especially two of the used chemicals (dichloromethane (DCM) and trifluoro acetic acid (TFA)) are very aggressive to the glass-chips. The glass-chips, produced by *Little Things Factory GmbH* (one of our project partners) by sand-blasting are now sufficient resistant.

	Resistance to		
Glass-chips	**DCM**	**TFA**	**DCM/TFA**
1. generation	<30min	1 h	<15min
2. generation	~2 h	6 h	~ 1 h
3. generation	>16 h	> 16 h	~ 12 h

Mechano-Electronic part

A xyz table with a special constructed magnetic grip arm will be developed for the sorting operations with the system. The dimensions of this table are 400x200 mm^2 and the table can carry two microtiterplates (MTP). Each MTP holds 4 chip-carrier with 60 glass-chips. (see Fig. 1 and 2).

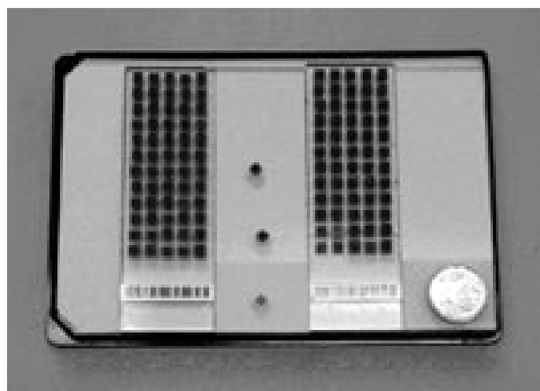

Fig. 3: Picture of a MTP carrier with two of four chip-carrier. Each chip-carrier can carry 60 glass-chips.

One of the project partners - the *IPHT* - adapts a commercially available system to this task whereas the *TU-Ilmenau* will develop the magnetic grip arm for taking off and positioning of the magnetic chips on the magnetic carrier plates.
The first sketch of this system consists of a moveable ferro magnetic inner pen inside a plastic capillary. This capillary is positioned on the chip to be gripped. The magnetic pen causes a magnetic force for the take off of the chips. When the chip is positioned onto the magnetic carrier plate the magnetic pen is withdrawn by an electromagnetic actuated placing system and a fixed connection between both systems is realised.

Collaborating project partners are T. Henkel (IPHT e.V., Jena) and T. Frank (Little Things Factory GmbH, Ilmenau).
This work has been supported by the DBU (Az.: 21847).

New Investigations with the Nanopositioning and Nanomeasuring Machine in Combination with a High Resolution Focus Sensor

R. Mastylo*, E. Manske, and G. Jäger
Department of Process Measurement

The development of the focus sensor, as well as its integration into the nanopositioning and -measuring machine have already been described and the first investigations of the metrological properties have been reported [1].

The following steps were included in the overall design. As described earlier [2], the focus sensor is combined with a CCD camera microscope, which allows the user to trace the point of optical scanning on the sample surface. The first design of this microscope contained a LED for realising the lighting by means of a 100 µm optical fiber. In this case a strong unevenness and an incomplete image illumination were observed. In order to realise a very homogeneous, adjustable image illumination (contrast and field) the microscope was completely modified according to the rules of Köhler's illumination. Here, the light for the camera illumination is supplied by a cold-light illuminator via an optical fiber. Fig. 1 shows the modified overall structure (nanopositioning and -measuring machine + focus sensor + CCD-microscope), whereas Fig. 2 shows the CCD camera image on the observation monitor during measurement. Here, the measurement of a Si-structure is shown.

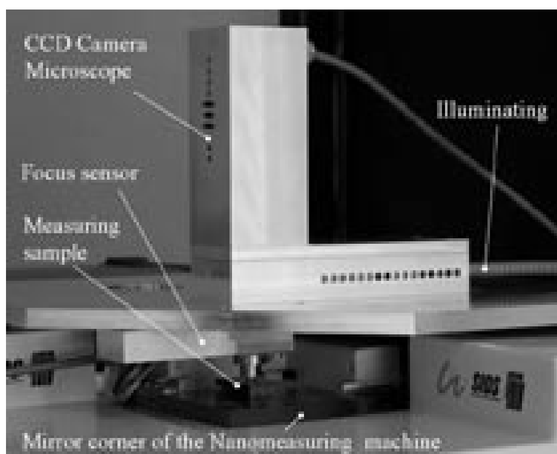

Fig. 1: Nanomeasuring machine with integrated focus sensor und new CCD microscope.

The lateral size of the structure is approximately 80 mm and the height amounts to approximately 10 mm. The white spot in the middle of the image is the focussed laser spot of the focus sensor, i.e., the point at the measuring surface where the measurement is carried out at a certain moment.

The improved properties of the microscope permit the combination of the focus sensor and the CCD microscope with an image-processing measuring technique.

The spot size (approximately 1 µm) of the focus sensor limits the lateral resolution [2]. Therefore, the smallest measurable structure width cannot be less than 5 µm. In order to increase the lateral resolution of the focus sensor and to be able to use the focus sensor for width measurements, the diffraction phenomena (Batwings effect) occurring at the edges must be evaluated according to the diffraction theory [2, 3]. Measurements related to this issue have shown that the batwings are reproducible in the nanometer range, which makes it possible to increase the lateral resolution considerably.

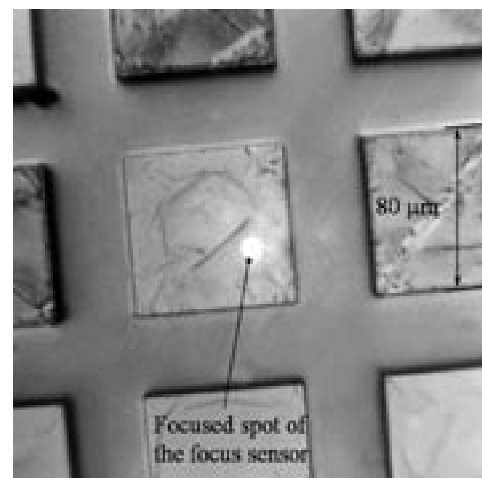

Fig. 2: CCD camera image with laser spot during measurement.

New possible applications of the focus sensor were tested in the framework of the funded research project "Picofluidic" at the ZMN. Due to its height and its diameter, the volume of a drop of liquid can be calculated on the basis of the "Sessile Drop Method". The nanopositioning and -measuring machine with integrated focus sensor has been used to determine

* phone : +49-(0)3677-69-3442 email: rostyslav.mastylo@tu-ilmenau.de

these two parameters. Fig. 3 shows line scans of an evaporating water drop. Measurements 1 to 5 were made at a time interval of 30 s (starting from 1) each time. Below a certain height (scan no. 5), the measurements become incorrect. This is where limits are set to this measuring technique.

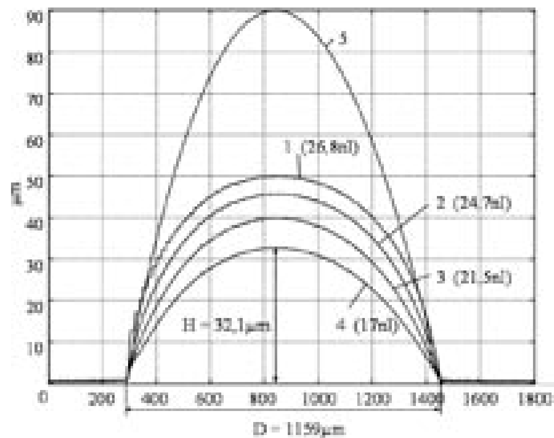

Fig. 3: Line scans of an evaporating water drop.

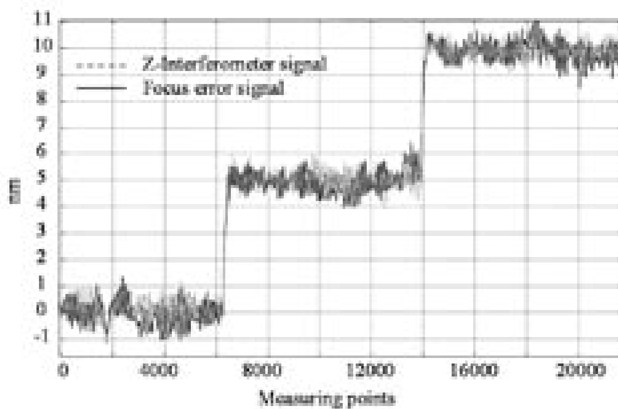

Fig. 4: Positioning of the 5 nm-steps in z-direction.

The error results from the focus measuring principle. Below a certain height of the water drop (approximately 30 mm), the laser beam of the focus sensor is reflected additionally by the surface of the carrier material, thus exerting an influence on the measuring signal (defocusing). Thus, the smallest measurable drop volume amounts to about 17 nl … 20 nl. In order to minimise the influence of defocussing in this experiment, coated glass (reflection factor < 1 %) was used as carrier material. From the experiments carried out, the following conclusions can be drawn: In order to determine smaller drop volumes (< 17 nl), the carrier material and the liquid should possess the same refractive index, if possible. In this case, no defocussing effect is produced. Thus, experiments shall be carried out with carrier materials and liquids with different refractive indices.

Furthermore, investigations concerning the positioning accuracy of the focus sensor were made. In this case, the sensor had to be decoupled from the nanopositioning and –measuring machine. First, the sensor was calibrated using the nanopositioning and –measuring machine [1]. Then, the mirror corner of the nanomeasuring machine (with the measuring sample) was moved in z-direction until the sensor signal reached its zero position. From this position 5 nm-steps were carried out with the nanomeasuring machine in z-direction.

Fig. 4 shows the signals of the z-interferometer and of the focus sensor. Both signals are nearly identical. Even the occurring irregularities of about 2 nm (caused by acoustic vibrations) correlate. This experiment proves the extremely high positioning and measuring accuracy of the focus sensor.

Another option is the combination of the focus sensor with an AFM attachment. Here, the sensor is constantly focussed on the back of the cantilever. A number of corresponding test measurements were made. However, compared to the method of optical scanning, only very limited scanning speeds can be realised (up to 10 mm/s). This limitation is due to the dynamic behaviour of the nanopositioning and -measuring machine. Future research work will be focussed on the improvement of the scanning speed by inserting an additional piezoelectric actuator which shall allow a follow-up control of the cantilever.

[1] Mastylo R., Manske, E.; Jäger, G.: Development of a focus sensor and its integration into the nanopositioning and nanomeasuring machine, OPTO 2004 6th International Conference, Nuremberg, May 2004, pp. 123-126.
[2] Mastylo R., Manske, E.; Jäger, G.: Investigation of the metrological characteristics of the nanopositioning and nanomeasuring machine with integrated focus sensor, Jahresbericht ZMN 2003.
[3] Harasaki, A.; Wyant, J.C.: Fringe modulation skewing effect in white light vertical scanning interferometry, Applied Optics Vol. 39, No. 13, 2000, pp 2101-2106.

Practise of new Sensors and Pipettors for Biotechnological Applications

A. Schober*, G. Kittler, C. Buchheim, M. Ali, V. Cimalla, M. Fischer, V. Yanev, M. Himmerlich, S. Krischok, J.A. Schaefer, H. Romanus, T. Sändig, J. Burgold, F. Weise, H. Wurmus, K.H. Drüe, M. Hintz, H. Thust, M. Kittler, E. Manske, R. Mastylo, G. Jäger, Ch. Knedlik, G. Winkler, H. Kern, R. Hoffmann, L. Spiess, and O. Ambacher

All departments of the Center for Micro- and Nanotechnologies

Introduction

New microfluidic and nanosensoric devices have become valuable tools in the pharmaceutical arena: miniaturisation means more assays, in less time, with less costs and higher information content. According to the aims of the picoproject, we realised the integration of novel sensors on the base of AlGaN/GaN heterostructure nitrides together with new dosing devices, for the measurement of biomedical and biotechnological assay systems.

After the successful implementation of the infrastructure first biological tests have been performed with the set-up. The whole system consisting of sensor, micro periphery and electronics combined with pico- and nanofluidic dispensers, was tested and optimised using the expertise of the nine departments of the ZMN (see Fig. 1).

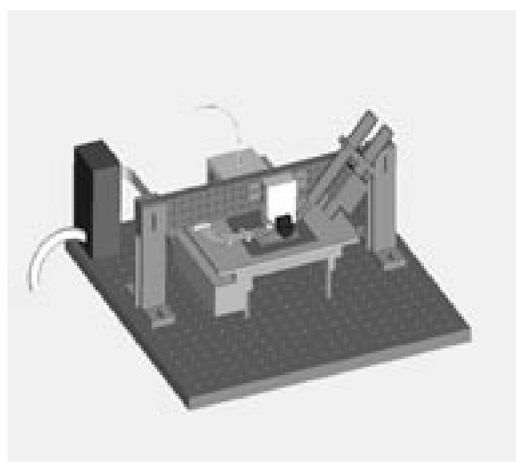

Fig. 1: Scetch of the system. A xyz table is combined with a microscope, the dispenser, and the frame with the sensor array.

Technical optimisation

New dispensers adapted to viscous liquids and with better filling properties have been developed (see report of F. Weise). The heterostructure sensor systems have been employed for pH-measurements and are in an ongoing development process for the application for electrophysiological measurements where the pH value for instance is an important parameter for the "turn around" rates of the metabolism (see report of G. Kittler). The whole system performance was optimised and is tested with respect to electronics, periphery and system behaviour (see reports of M. Kittler, K. H. Drüe, Fig. 2). The sensor fabrication process is controlled by analytical tools like REM and the interaction of the biological substrate and the sensor surface is examined with the tools of surface science (see report of V. Yanev).

Fig. 2: Set-up of the experiment with the dispenser module, the microscope, and the frame with the sensor.

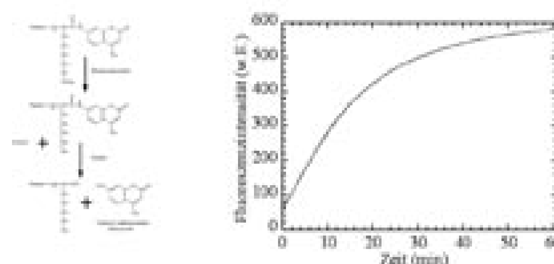

Fig. 3: Enzymatical assay. Left: Scetch of the fluorescence principle of the HDAC assay. Right: Measurement of the activity of the HDAC enzyme.

Biological experiments

First experiments concerning the influence of AlGaN surfaces to biological materials have been performed. Both enzymatical assays and cell adherence experiments have been realized on sensor surfaces.

(1) Enzymatical assay: The DNA of eukaryotic cells is packed in helper-proteins named histons. For reading the genetic code the DNA must be accessable for the replication apparatus and for transcription. This is the task of specialised enzymes: the histondeacetylases.

* phone : +49-(0)3677-69-3486, email: andreas.schober@tu-ilmenau.de

The histondeacetylases catalyses the cleavage of the acetyl group of the Histon-DNA-Complex. In this way this enzyme modulates the Histone-Code as antagonists of the Histonacetyltransferases (HAT) (Strahl and Allis, 2000). To some extend the degree of the condensation of the chromatin, this is the complex of DNA and histon, is regulated in such a way that the transcription is inhibited. The HDAC is regarded as a relevant target in the medicinal chemistry (Marks et al., 2000; Yoshida et al., 2003). HDAC inhibitors are considered as high potentials in cancer treatment (Jung, 2001; Kim et al., 2003; Remiszewski, 2002).
The possibility to pipett the high viscous enzyme mix with the picodispenser has been tested. Furthermore it could be shown that the sensor surface does not affect the activity of the enzyme (see Fig. 3).
Examinations of pH changes in different enzymatical assays have been performed.
(2) Cell adherence: The biocompatability of the semiconductor heterostructure with cells is examined and shows – as a first result – no strong interference (Fig. 4).

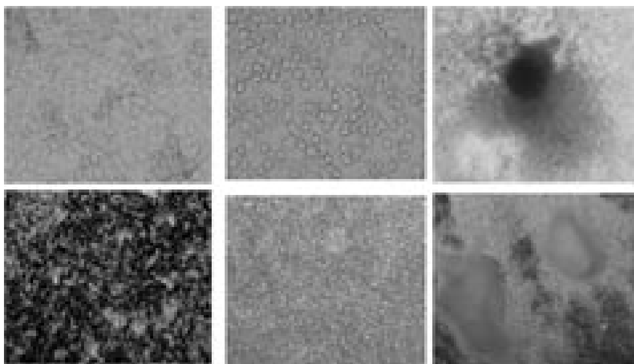

Fig. 4: Biocompatablilty experiments: left column HepG2-cells, midst - fibroblasts (L-cells), right: heart myo cells cultivated from the pluripotent P19 cell line. The line above always the cells in the petri dish as a control, below - the adherent cells on AlGaN.

HepG2 cells, fibroblasts, and heart myo cells differentiated from the pluripotent P19 cell line have been placed on oxidised and non oxidised sensor surfaces in petri dishes with nutrition media, whereas those areas of the petri dish which are not covered with sensor chips serve as a control, where cell material was cultivated as well. The microscopic images show that all three cell lines adhere to the sensor surfaces, whereas there is a morphological difference between the cells on the sensor and those on the petri dish surface, indicating a less strong adherence on the sensor surface. Nevertheless, the cells could not be removed without enzymatic help. Further investigations will be performed with different cell lines using fluorescence based viability tests.

Conclusions
Ongoing research is focused on the application of the system to enzymatical assays and to establish microfluidic and nanosensoric devices for electrophysiological measurements of cells.

The work was supported by the Thüringer Kultusministerium (TKM) and the European Community (EFRE program, 6th framework program: Project number: B 678-03001).

Jung, M. (2001). Inhibitors of histone deacetylase as new anticancer agents. Curr Med Chem, (8), 1505-11.
Kim, D.H., Kim, M. and Kwon, H.J. (2003). Histone deacetylase in carcinogenesis and its inhibitors as anti-cancer agents. J Biochem Mol Biol, (36), 110-9.
Marks, P.A., Richon, V.M. and Rifkind, R.A. (2000). Histone deacetylase inhibitors: inducers of differentiation or apoptosis of transformed cells. J Natl Cancer Inst, (92), 1210-6.
Remiszewski, S.W. (2002). Recent advances in the discovery of small molecule histone deacetylase inhibitors. Curr Opin Drug Discov Devel, (5), 487-99.
Strahl, B.D. and Allis, C.D. (2000). The language of covalent histone modifications. Nature, (403), 41-5.
Yoshida, M., Matsuyama, A., Komatsu, Y. and Nishino, N. (2003). From discovery to the coming generation of histone deacetylase inhibitors. Curr Med Chem, (10), 2351-8.
E. Gottwald and A. Schober, The shape of things to come, European Pharmaceutical Review, Issue 4 2004.
O. Ambacher et al.: Two-dimensional electron gases induced by spontaneous and piezoelectric polarization charges in N- and Ga-face AlGaN/GaN heterostructures, J. Appl. Phys. 85, 3222 (1999).
R. Neuberger, G. Müller, O. Ambacher, M.Stutzmann: High-Electron-Mobility AlGaN/GaN Transistors (HEMTs) for Fluid Monitoring Applications, phys. stat. sol. (a) 185, No. 1, 85 (2001).
G. Steinhoff, M. Hermann, W. J. Schaff, L. F. Eastman, M. Stutzmann, M. Eickhoff: pH response of GaN surfaces and ist application for pH-sensitive field-effect transistors, Appl. Phys. Lett., Vol. 83, No. 1, 177 (2003).
J. Burgold, F. Weise, M. Fischer, G. Schlingloff, Th. Henkel, J. Albert, G. Mayer, A. Schober "Evolution and Operating Experiences with Different Drop-On-Demand Systems, Macromol. Rapid Commun. 2005, 26, 265–280.
A. Schober , G. Kittler, C. Buchheim, A. Majdeddin, V. Cimalla, M. Fischer, V. Yanev, M. Himmerlich, S. Krischok, J.A. Schaefer H. Ro-manus, T. Sändig, J. Burgold, F. Weise, H. Wurmus, K.H. Drüe, M. Hintz, H. Thust, J. Gessner, M. Kittler, F. Schwierz,Th. Doll, E. Manske, R. Mastylo, G. Jäger, Ch. Knedlik, G. Winkler, H. Kern, R. Hoffmann, L. Spiess, A. Spitznas, E. Gottwald, K-F. Weibezahn, D. Wegener, A. Schwienhorst, O. Ambacher. „A novel class of sensors for system integrative concepts in biotechnological applications" 12. Heiligenstädter Kolloqium S. 163-169, Dieter Beckmann, Manfred Meister (hrsg.), 2004, ISBN 3-00-015042-0.

Characterisation of MEMS-Resonators under Ambient Conditions

K. Brueckner[1,*], Ch. Förster[2], K. Tonisch[2], V. Cimalla[2], O. Ambacher[2], R. Stephan[1], K. Blau[1], and M. A. Hein[1]
[1] Department of RF and Microwave Techniques
[2] Department of Nanotechnoly

Semiconductor production processes originally designed for manufacturing integrated circuits can be used to make complex-shaped and well defined electro-mechanical structures. Even if the technology is based on planar concepts, the combination of etching and lift-off processes allows the design of various three-dimensional structures. These patterned semiconductors can form mechanical resonators and, by metallisation, they can be coupled to electrical circuits. The single-crystalline semiconductor material allows the preparation of surfaces and volumes with a low density of defects, which is essential for high mechanical quality factors. The mechanical oscillation of the resonators is affected by various physical parameters, e.g. mass, friction, tension, and temperature. Detecting these parameters electrically would allow a variety of sensor applications. With respect to a high sensitivity, in all cases a high resonant frequency is beneficial which requires small geometries. Among future applications of mechanical high-frequency resonators are filters and other RF applications that would benefit from the integration of active and passive components on the same chip.

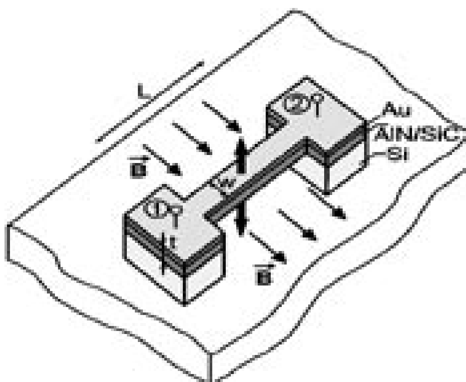

Fig. 1: Mechanical resonator of beam length L, width w and thickness t, with contact areas 1 and 2, in an external magnetic field of flux density B. The bold arrows indicate the direction of the Lorentz force and the resulting beam deflection.

Mechanical oscillations in semiconductor materials have been demonstrated recently by several groups, [1], [2]. Typically, the mechanical resonance is stimulated by a periodic energy supply, and the resulting vibration is detected electrically. Here, the basic resonator structure is a doubly clamped beam that is actuated magnetomotively, i.e., a Lorentz force is generated by placing the beam in a permanent magnetic field and applying an RF current to it, as illustrated in Fig. 1.

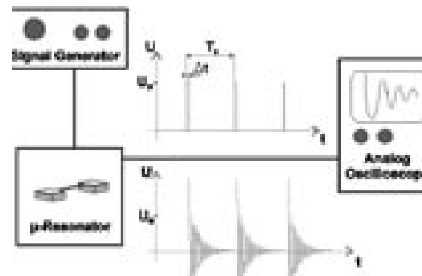

Fig. 2: Schematic measurement setup, diagrams of excitation and read-out time signal.

Using optical lithography, beams with various dimensions were prepared. They consisted of an ~102-nm thick AlN or SiC(100) layer with a 50-nm thick gold metallisation on top. The beams vary in length and width from 10 to 500 µm and 500 nm to 8 µm, respectively. Based on the Euler-Bernoulli theory [3] and recent extensions [4], the fundamental resonant frequencies f_{res} of the beams can be estimated by

$$f_{res} = 1.03\sqrt{\frac{E}{\rho}} \cdot \frac{t}{L^2} \cdot c(\varepsilon) \quad , \qquad (1)$$

where E is Young's modulus, ρ the mass density, t the thickness, and L the length of the beam. The factor $c(\varepsilon) \approx [1 + 0.3 \times (L/t)^2 \times \varepsilon]^{1/2}$ accounts for the effect of tensile or compressive strain (ε > or < 0) on f_{res} [4]. In addition to the analytical approach, the resonant frequencies were calculated numerically (for $\varepsilon = 0$) using a commercial finite-element simulation software [5], leading to f_{sim}-values ranging from 3 kHz to 1 MHz for AlN, and 26 kHz to 17 MHz for SiC. The oscillation of the beams is caused by an RF current at several MHz, driven by a primary voltage of the order of Volts. The secondary voltage, induced by the periodic displacement, is much smaller than the primary voltage, in the range of µV, and therefore

* phone : +49-(0)3677-69-1580, email: klemens.brueckner@tu-ilmenau.de

very difficult to detect as a tiny background signal. To overcome this problem, we propose to separate the excitation signal and the response of the resonator in time. With a period of T_0 = 1 ms, the beam is excited by short voltage pulses of duration Δt = 15 μs and amplitude U_D = 300 mV, as sketched in Fig. 2.
The free decay of the resonator can be monitored with an oscilloscope. The periodic response yields the information on the resonant frequency fres and the loaded quality factor Q of the resonator. The maximum induced voltages reached 120 μV and were obtained for the longest beams, while the response of short beams dropped to as little as 10 μV due to the smaller amplitudes of the mechanical oscillation.

Fig. 3: Basic equivalent circuit model of the micro-electromechanical resonators.

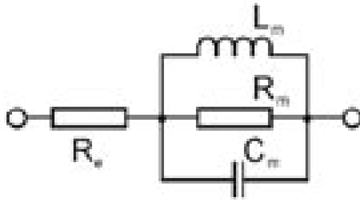

The mechanical elements of the resonators form a damped mass-spring system whose behaviour can be modelled by an equivalent electrical circuit as demonstrated in Fig. 3. While the electrical resistance R_e of the metallisation layer of the beams can be measured directly, the other parameters R_m, L_m, and C_m can be extracted only by comparing the solution of the equation of motion of the system with the experimentally obtained decay curves. The parameters are necessary for a computer simulation of the system and are in the order as shown in Tab. 1 for two examples.

	example 1 AlN beam	example 2 SiC beam
L (μm)	125	125
f_{res} (kHz)	233	800
Q	125	250
R_e (Ω	34.6	34.3
R_m (mΩ)	840	307
L_m (nH)	4.59	0.241
C_m (μF)	101.7	164.1

Tab. 1: Equivalent circuit parameters for two selected resonator beams of different materials.

The measured f_{res}-values covered the range from 6 to 750 kHz for the AlN beams, and 0.32 to 1.5 MHz for the SiC beams. In Fig. 4 the dependence of the resonant frequencies (left-hand axis) and the ratio of measured to calculated resonant frequencies, $\nu = f_{res}/f_{sim}$ (right-hand axis), on beam length for both materials, are compared. The resonant frequencies of the SiC beams are higher than for AlN beams of identical geometry, mainly caused by the higher Young's modulus, see eq. (1).
We note a linear increase of the ν(L)-curves. This implies that the resonant frequencies scale like 1/L rather than $1/L^2$, as expected for relaxed beams. According to eq. (1), this is a typical behav-iour of strained material. Similar conclusions were drawn for MEMS resonators made of polycrystalline Si [4]. Thus, for a given film thickness, the slope dν/dL is thus a direct measure of the residual strain ε. Obviously, the AlN beams are much less strained ($\varepsilon \approx +5\times10^{-5}$) than the SiC beams ($\varepsilon \approx +5\times10^{-4}$). This difference could be caused by a higher density of defects in the sputtered AlN films compared to the evaporated SiC films, facilitating relaxation of residual strain.

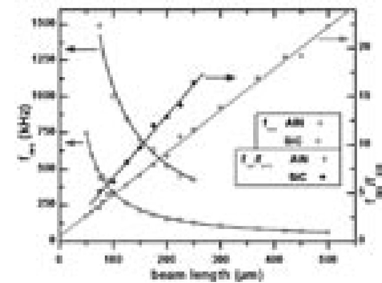

Fig. 4: Frequency versus beam length for the doubly clamped SiC and AlN beams.

In conclusion, we have successfully realised free-standing resonator beams of widely varied geometries from heteroepitaxial SiC and AlN films on Si. The resonant properties of the beams actuated under ambient conditions in a static magnetic field, were investigated by a pulsed measurement scheme. Using this technique, the weak resonant response could be separated from the strong excitation with high accuracy.
The quality factors of the resonators, covering frequencies from 50 to 1500 kHz, reached values around 200. The moderate *Q*-values, as well as the linear scaling of the resonant frequencies with beam length, indicate residual tensile strain and hence the potential for further improvement.

This work has been funded by the German Science Foundation (DFG), Priority Programme 1157: "Integrierte elektrokeramische Funktionsstrukturen", contract no. AM 105/2 1.

[1] C. T.-C. Nguyen, "Vibrating RF MEMS for low power wireless communications" , Proc. 2000 Int. MEMS Workshop (iMEMS'01), Singapore, pp. 21-34, 2001.
[2] S. Pourkamali, R. Abdolvand, and F. Ayazi, "A 600kHz electrically-coupled MEMS bandpass filter", IEEE MEMS'03, Kyoto, Japan, pp. 702-5, 2003.
[3] A. N. Cleland, M. Pophoristic, and I. Ferguson, "Single-crystal aluminum nitride nanomechanical resonators", App. Phys. Let., vol. 79, no. 13, pp. 2070-2, 2001.
[4] T. Ikehara, R. A. F. Zwijze, K. Ikeda, "New method for an accurate determination of residual strain in polycrystalline silicon films by analysing resonant frequencies of mi-cromachined beams", J. Micromech. Microeng., vol. 11, no. 1, pp. 55-60, 2001.
[5] ANSYS 8.1 Simulation Suite.

Surface Conductivity of Epitaxial InN

G. Ecke*, V. Cimalla, M. Niebelschütz, and O. Ambacher
Department of Nanotechnology

Thin films of InN show high n-type conductivity, for which the origin is not completely identified up to date. Recent improvements in the heteroepitaxial growth allowed the preparation of InN layers with carrier concentrations down to 10^{17} cm^{-3} [1]. A conclusive model for the observed decreasing conductivity with increasing layer thickness is the confinement of a high carrier concentration at the interface to the substrate due to piezoelectric charges and at the surface due to doping by oxygen [2, 3]. Up to date, attempts to prove the electron accumulation at the surface include C-V- profiling, measurement of the sheet carrier density versus thickness, both accomplished on air, and high-resolution electron-energy-loss spectroscopy (HREELS) on clean InN surfaces in ultrahigh vacuum [4,5]. Excess sheet carrier densities between 1.5 and 4.7 x 10^{13} cm^{-2} have been determined. Recently the electron accumulation was explained as an intrinsic property of InN layers ascribed to the specific properties of the band structure of InN. In this work we show that an oxidised surface built by the contact to air results in very similar electron accumulation.
In these investigations we used the experimental setup of Auger electron spectrometer with integrated ion beam sputtering possibility to detect the lateral conductivity of epitaxial InN layers during sputtering. Ion beam sputtering must be done carefully under special conditions avoiding the development of metallic In droplets [6]. Fig. 1 shows the experimental setup and the special sample holder construction for these measurements.

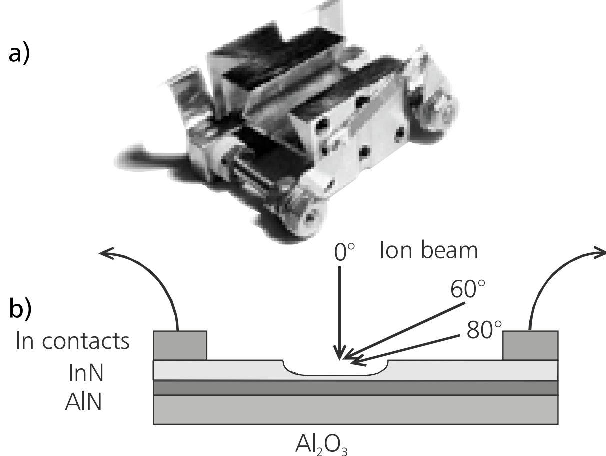

Fig.1: a) Sample holder construction and b) scheme of the conductivity measurements.

The measured resistance during the sputtering of an InN layer is shown in Fig. 2. As expected, with decreasing layer thickness the resistance increases. However, two typical features disturb this almost linear trend. First, there is a strong increasing of the resistance during the removal of the first 5 nm of the InN layer (shown in the insert). This strong increase of the resistivity confirms the existence of a highly conductive surface layer. The second feature, marked as "Interruption", appeared after stopping of the sputtering process and exposing the sample to air. After loading to ultra high vacuum the resistivity dropped down. However, it recovered to the previous trend after continuing sputtering of around 5 nm.

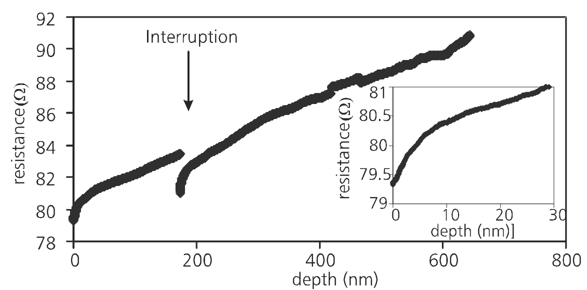

Fig. 2: Measured resistance versus depth during the grazing incidence sputtering of 1.8 µm thick InN layer, insert: evolution of resistance at the beginning of the sputtering.

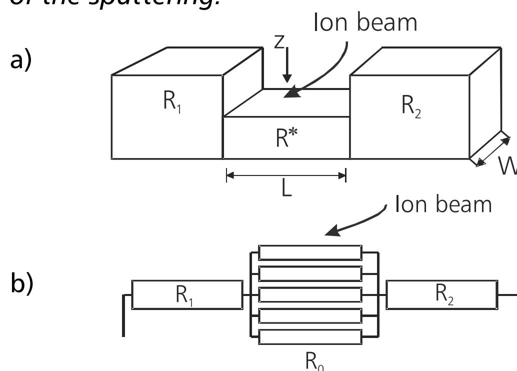

Fig. 3: a) Geometrical scheme for the sputtering of the InN stripe and b) equivalent circuit diagram.

The measured curves can be understood as an indicator of the conductivity profile of the InN layer. If we assume the geometrical scheme and circuit diagram of Fig. 3 we can get the conductivity σ by the deviation of the measured data according to

* phone : +49-(0)3677-69-3407, email: gernot.ecke@tu-ilmenau.de

$$\sigma(z) = -\frac{L}{W}\frac{d\left(\frac{1}{R(z)-(R_1+R_2)}\right)}{dz} \quad (1) \qquad \sigma = e\cdot\mu_n\cdot n \quad (2)$$

with σ being the conductivity, z the depth, R the measured resistance, L and W the geometrical dimensions according to Fig. 3 and R_1 and R_2 the resistance of the unsputtered parts of the sample. For the calculation of the free electron density using formula (2) one needs the mobility of the electrons in InN which is found to be dependent on the carrier density itself. Using the integrated values estimated by Hall measurements on InN layers with different thickness [1] we get the empirical relationship ($n=8\cdot10^{13}\mu^{3/4}$ (n in cm^{-3} and μ in cm^2/Vs). With the help of this approximation we can calculate the following electron densities seen in Fig. 4 after the measured curve of Fig. 2.

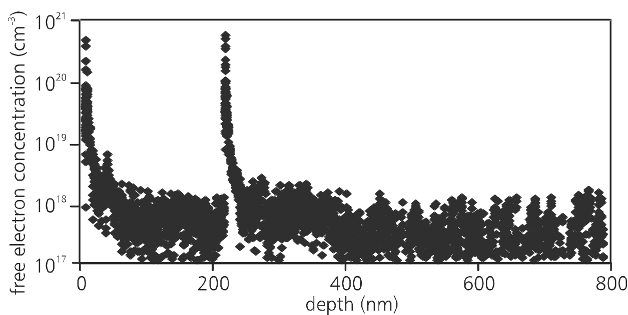

Fig. 4: Depth profile of the free electron concentration calculated from the resistance evolution in Fig. 2.

Obviously the exposure to air results in a very highly localised carrier concentration of more then 10^{20} cm^{-3} at the surface. This behaviour was fully reproduced after interruption of the sputtering and exposure to air. This layer at the surface might be the result of the contamination from air, most probably due to the incorporation of oxygen atoms, which act as dopants and create free carriers close to the surface. AES depth profiling proved the existence of oxygen in the near surface region. The correlation between the depth profiles for the concentration of oxygen and electrons supports the assumption that oxygen plays the major role in the high conductivity of air exposed InN layers. Moreover, after removing of the oxidised layer the electron concentration reaches an equilibrium value of 4.5×10^{17} cm^{-3} in good agreement with the best values measured on thick InN layers (3×10^{17} cm^{-3} for 7500 μm [2]). Consequently these surface effects do not affect the bulk properties of the InN layers.

Finally, by integration of the excess electron density close to the surface versus depth a surface sheet carrier density of 2.2×10^{13} cm^{-2} is obtained. The estimated electron accumulation agrees very well with the results obtained by HREELS on clean InN surfaces [5] as well as on air exposed InN by C-V depth profiling [2], where carrier concentrations up to around 2×10^{20} cm^{-3} close to the surface were observed.

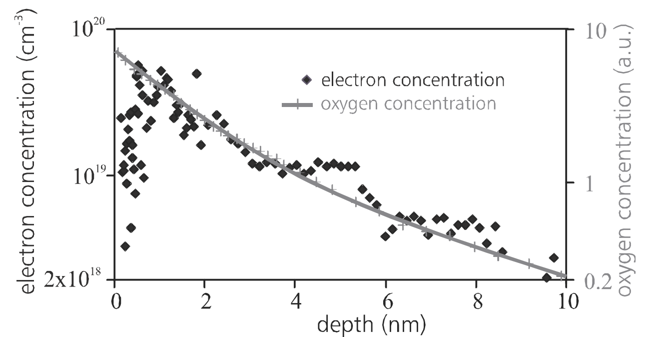

Fig. 5: Depth profiles of the electron (diamonds, from Fig. 3, left ordinate) and oxygen concentration by AES (line, right ordinate).

Conclusions

The correlation of the concentration profiles of oxygen and free electrons close to the surface of InN as well as the reproducible recovering of the highly conductive surface by exposing the sample to air clearly confirms the important role of oxygen for the electron accumulation. After 10 nm sputtering oxygen was not detectable anymore by AES and the estimated bulk electron density agrees very well with the best MBE grown samples. However, here the interface charges between InN and the buffer layer are still affecting the estimated values. The accuracy of the geometrical values (especially the sputter crater width) critically determines the accuracy of the estimated data. The future work will concentrate on the investigation of the electron concentration evolution close to the interface after sputtering through the whole layer, and the kinetics of re-oxidation by exposing of a clean InN surface by a defined amount of oxygen and simultaneous measurements of the incorporated oxygen and the resistance of the InN layer.

This work was supported by the Thüringer Kultusministerium (project B609-02004).
The authors also acknowledge an ONR NICOP Grant.

[1] H. Lu, W.J. Schaff, L.F. Eastman, J. Wu, W. Walukiewicz, D. C. Look, and R.J. Molnar, MRS Symp. Proc. 743, L4.10.1 (2003).
[2] H. Lu, W.J. Schaff, L.F. Eastman, and C.E. Stutz, Appl. Phys. Lett. 82, 1736 (2003).
[3] V. Cimalla, Ch. Foerster, G. Kittler, I. Cimalla, R. Kosiba, G. Ecke, O. Ambacher, R. Goldhahn, S. Shokhovets, A. Georgakilas, H. Lu, and W.J. Schaff, phys. stat. sol. (c) 0, 2818 (2003).
[4] I. Mahboob, T.D. Veal, C.F.McConville, H.Lu, and W.J. Schaff, Phys. Rev. Lett. 92, 036804 (2004).
[5] I. Mahboob, T.D. Veal, L.F.J. Piper, C.F.McConville, H.Lu, W.J. Schaff, J. Furthmüller, and F. Bechstedt, Phys. Rev. B 69, 201307 (R) (2004).
[6] R. Kosiba, G. Ecke, V. Cimalla, L. Spieß, S. Krischok, J.A. Schaefer, O. Ambacher, W.J. Schaff, Nucl. Instr. Meth. Phys. Res. B215, 486 (2004).

Growth of Semiconducting Molecular Films: Interface Interaction and Ordering

M. Eremtchenko[1,*], F.S. Tautz[1, 2], S. Krischok[1], R. Öttking[1], T. Stolz[1], A. Opitz[1, 3], and J.A. Schaefer[1]
[1] Department of Technical Physics
[2] School of Engineering and Science, IU Bremen
[3] Experimentalphysik IV, University of Augsburg

The fast development of organic electronics has shown a high potential for semiconducting molecular films in technological applications. Having a number of advantages which make the molecular based devices very attractive for different market segments, the improvement of semiconducting properties of grown organic structures is still one of the key issues.
It is well known that the electronic properties are significantly limited by structural heterogeneities, this limits the mobility. Therefore, the performance of organic devices is defined by the quality of the molecular films and is strongly coupled to the conditions of the structure formation. In this context, the improvement of semiconducting properties of molecular films requires comprehensive investigations of the growth process and a deep understanding of related features.
The structure of thin films is strongly dependent on the interactions at the interface between the substrate and the molecules which is still not optimised, although significant experimental data were collected during the last decade. Our work is related to the investigation of various molecular-solid interfaces in order to recognise the driving forces of the formation of interface structures. The spectroscopic and microscopic data linked to the quantum chemical calculations allow to analyse the bonding at the interfaces on an intramolecular scale. The selection of the active parts of molecules opens a way for a purposeful tuning of the bonding strength by functionalisation [1], [2] which allows to optimise the search for well ordered interfaces.
The intramolecular analysis of bonding was carried out for the case of five-ring polyaromatic hydrocarbon perylene and it is well known derivative PTCDA adsorbed on Ag(111) [1]-[4]. Analysing the coupling between the molecular vibrational modes and the charge transfer in these interfaces, the presumable bonding by the central carbon ring was established and the role of the functionalisation on the adsorption strength was outlined. The variation of the bonding centre activity leads to drastic changes in the interface structures. Instead of the well known commensurate herring-bone structure of the PTCDA/Ag(111) interface, the incommensurate liquid-like hexagonal monolayer of flat lying perylene molecules on the same substrate was observed [4] (see Fig. 1). These features illustrate the variety of effects at organic/inorganic interfaces and surprising growth modes of molecular films.

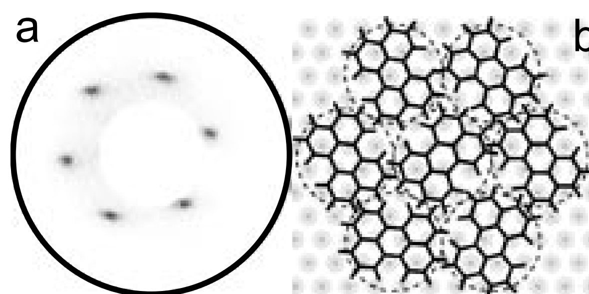

Fig. 1: Structure of perylene/Ag(111). LEED (a) and schematic real space (b) images.

The next object of our experiments was pentacene which is rather similar to perylene. It is hydrocarbon consisting of five aromatic rings ordered in-line. This material demonstrates the best p-type semiconducting properties among organic films and is the most favourable candidate for molecular electronics. We have studied the formation of the pentacene/Ag(111) interface which has an unusual structure. The first molecular layer is formed by flat lying disordered molecules. Note that the structure was unambiguously derived from the vibronic spectra [5]. Further molecule deposition leads to the formation of a bulk-like structure with tilted molecules [5]. Therefore, pentacene itself produces an accommodation layer at the interface which allows to decouple the molecular structure from the substrate. This property could promote the formation of pentacene films with a small number of defects which might be one of the reasons for the relatively high carrier mobility reported for pentacene semiconductors.
For the design of integrated circuits the complimentary application of both p- and n-type semiconductors is necessary. In the case of molecular electronics, having appropriate p-type pentacene films, the formation of n-type material is still problematic. The carrier mobility is in the region of 1 cm^2/Vs for some molecular materials, such as fullerene C_{60} which

* phone : +49-(0)3677-69-3712, email: maxim.eremtchenko@tu-ilmenau.de

was well investigated during the last decade. It may be a candidate for several applications due to its semiconducting properties. The fullerene growth was investigated on several substrates, but only little is known about its growth on indium phosphide. There is a remarkable coincidence of the lattice parameters for the InP(001)-(2x4) surface and C_{60} which allows to expect the formation of well ordered molecular structures.

We investigated the growth of single domain fcc fullerene crystals on InP. The short- and the long-range order was confirmed by STM and LEED measurements, respectively (see Fig. 2). Interestingly, initial 3D island growth leads to a single domain structure of multilayers [6], [7]. The stability of the film growth with respect to the common surface defects was also investigated. The present study shows again the large variety of unusual growth modes which are important for understanding the molecule-solid interaction.

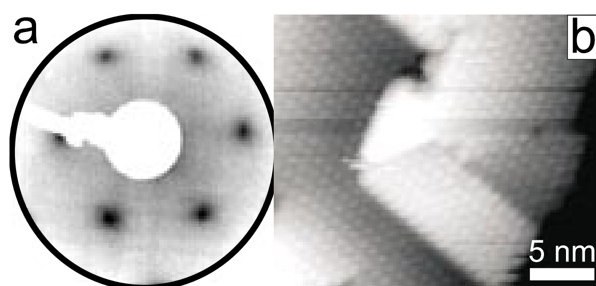

Fig. 2: Structure of C_{60}/InP(001)-(2x4). LEED (a) and STM (b) images.

The use of fullerenes for electronic applications is limited by the penetration of contaminants into the molecular structure which drastically decreases its semiconducting properties. Studying the surface reaction of C_{60} with atomic hydrogen, the formation of hydrocarbon layeres was observed. The hydrogenation was proposed for the protection of the molecular films [8] in analogy to inorganic semiconductors, where this technique is well developed.

Summarising we note, that complimentary spectroscopic and microscopic studies of molecular films allow to identify growth on an atomic scale which leads to a deep understanding of related processes. Furthermore, our results supplemented by calculations provide information about bonding already on a submolecular scale and open a way for tuning and even engineering molecular structures.

We greatfully acknowledge the continuous support by DFG and TKM.

[1] M. Eremtchenko, J.A. Schaefer, F.S. Tautz, Nature 425 (2003) 602.
[2] F. S. Tautz, M. Eremtchenko, J.A. Schaefer, Pico 8 (2004) 4.
[3] M. Eremtchenko, D. Bauer, J.A. Schaefer, F. S. Tautz, New Journal of Physics 6 (2004) 4.
[4] M. Eremtchenko, D. Bauer, J.A. Schaefer, F.S. Tautz, Journal of Materials Research 9 (2004) 2028 (special issue on organic electronics).
[5] M. Eremtchenko, R. Temirov, D. Bauer, J.A. Schaefer, F.S. Tautz, submitted to Phys. Rev. B, 2004.
[6] J.A. Schaefer, G. Cherkashinin, S. Döring, M. Eremtchenko, S. Krischok, D. Malsch, A. Opitz, T. Stolz, R. Temirov, „Frontiers of multifunctional integrated nanosystems“, NATO Science Series, Vol. 152, Kluwer Academic Publishers (2004) 131.
[7] M. Eremtchenko, S. Döring, R. Temirov, and J.A. Schaefer, Phys. Rev. B 71 (2005) 045410 (selected paper for Virtual Journal of Nanoscale Science & Technology).
[8] M. Eremtchenko, R. Öttking, S. Krischok, S. Döring, R. Temirov, and J.A. Schaefer, Fullerenes, Nanotubes, and Carbon Materials, accepted for publication 2004.

Thermal Decomposition of Indium Phosphide: Metallic Cluster Growth

M. Himmerlich[1,*], M. Eremtchenko[1], S. Krischok[1], Th. Stolz[1], M.C. Zeman [1,3], M. Gubisch[2], R.J. Nemanich[3], and J.A. Schaefer[1]
[1] Department of Technical Physics
[2] Institute for Materials Engineering
[3] North Carolina State University, Raleigh, USA

Indium phosphide as semiconductor material has attracted a considerable technological and scientific interest because of its applications in various electronic and photonic devices [1], [2]. The well known instability of this material under annealing reveals itself in the formation of metallic indium clusters on the surface as a consequence of phosphorus evaporation by thermal decomposition of the material [3], [4]. As a widespread structural defect, metallic droplets strongly affect the properties of semiconductor surfaces and need to be considered in the design of electronic devices, as well as for the growth of layered semiconducting structures. A combination of microscopic methods and local probing of the chemical composition and the spectroscopic properties of the InP(001) surface, before and after ion bombardment and subsequent annealing cycles, is presented.

Experiments were performed in UHV using atomic force microscopy (AFM) and photoemission electron microscopy (PEEM), as well as laterally resolved ultraviolet photoelectron spectroscopy (UPS). InP(001) wafers (S-doped, n=3 x 10^{18} cm^{-3}) were chemically cleaned and then annealed for 20 hours at 370 K in UHV. The remaining surface contamination was removed by gentle sputtering with Ar^+ ions (energy 0.5 keV, ion current density about 1 $\mu A/cm^2$). The annealing steps were carried out by heating the sample to the desired temperature within 5 min, remaining it at this temperature for 5 min, and then gradually cooling down to room temperature. The phosphorus desorption from the sample surface was controlled by quadrupole mass spectrometry (QMS). After this treatment the structures were examined ex situ using scanning electron microscopy (SEM) in combination with energy dispersive X-ray spectroscopy (EDX).

A careful microscopic investigation after each preparation step gives insight into the evolution of the surface topography. The AFM image of the surface relief before sputtering is presented in Fig. 1a. Although, a contamination layer with a thickness of ~0.2 nm consisting of carbon and oxygen impurities was detected by XPS, terraces with a step height of 2 Å are resolved. Ion bombardment leads to the formation of small clusters (Fig. 1b), which have diameters of about 20 nm and a height of a few nm. The formation of these small clusters results from the preferential sputtering of phosphorous from the InP surface [5].
Annealing of the surface improves the order as shown by LEED. A regularly ordered indium rich (2x4) reconstruction of the InP(001) surface is obtained after annealing at 600 K, and a surface state near the top of the valence band can be detected by UPS [6], [7].

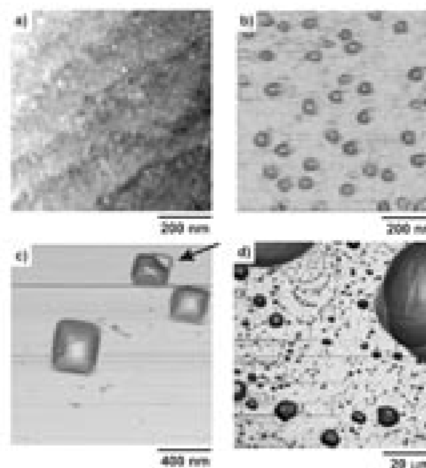

Fig. 1: AFM micrographs of the InP(001) relief after consecutive treatments: a) as loaded, b) after Ar^+ sputtering, and additional annealing at c) 670 K and d) 770 K.

Further annealing at 670 K leads to the onset of thermal decomposition. As a consequence, the surface is etched by phosphorus evaporation and larger metallic clusters (diameter ~200 nm, height ~40 nm) arise due to the remaining indium on the surface (see Fig. 1c). At 670 K the islands have a relatively narrow size distribution and cover the surface homogeneously. At this stage the observed islands have a rectangular shape which can be ascribed to the lower etching rates of the (111) and (100) planes [3], resulting in the formation of subsurface depressions beneath the clusters. The arrow in Fig. 1c points to such a

* phone : +49-(0)3677-69-3417, email: marcel.himmerlich@tu-ilmenau.de

depression, visualised by displacement of the island by the scanning AFM tip.
With rising annealing temperature, larger structures form and the island diameters vary from several 10 nm to droplets in the micrometer range. The small clusters seem to migrate towards the large droplets driven by the tendency to minimise the surface energy.
The phosphorus depletion becomes significant and is favoured at terrace boundaries. This leads to the formation of large depression regions which are no longer completely covered by clusters. The edges of these depressions act as diffusion barrier for small clusters migrating towards the large droplets. This effect can be deduced from the in-line circular arrangement of the relatively small clusters around the large ones (Fig. 1d).
In situ AFM investigations of the sample topography are limited to an area of 5x5 μm^2 using the UHV equipment. Therefore, additional surface sensitive microscopic techniques are needed to obtain a broader overview of the island distribution on the surface. The formation of the metallic indium phase on InP is an ideal object for investigation in a Photoelectron Emission Microscope (PEEM). The very high contrast between islands and semiconductor surface when using UV light generated by a mercury lamp, is related to the large difference in photothreshold of indium (ϕ=4.1eV) compared to that of InP (5.7 eV). Figs. 2a-c illustrate the changes in the cluster distribution after annealing at different temperatures.

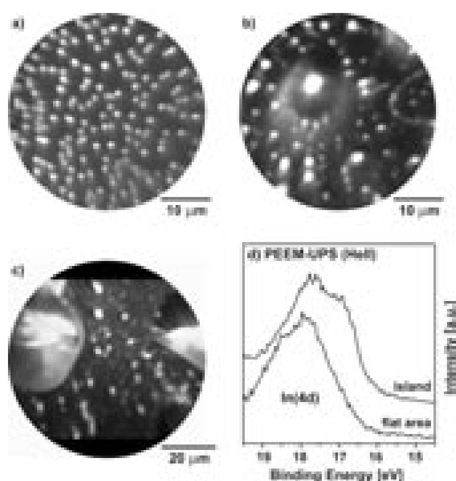

Fig. 2: PEEM images of the InP(001) surface after consecutive treatments: a) 670 K, b) 720 K and c) 770 K annealing, d) laterally resolved UPS (investigated area ~200 µm²).

Laterally resolved UPS (HeII) spectra using the spectroscopic mode of PEEM indicate a different chemical composition of the cluster in contrast to the surface. For flat areas the In(4d) core level is located at a binding energy typical for InP, whereas the peak is shifted by 0.8 eV towards lower binding energies if UPS data is collected from a single cluster (see Fig. 2d). The observed peak position corresponds to that expected for metallic indium [8].
Besides an increase of the average cluster size, drastic differences in the cluster shape are also visible. Mainly two species of large clusters are found: spherical and pyramidal islands [3] and transition states between these two. The shape is optimally visualised by SEM, which was performed after removing the sample from UHV conditions. The SEM images presented in Fig. 3 show the typical surface morphology after annealing at 770 K.

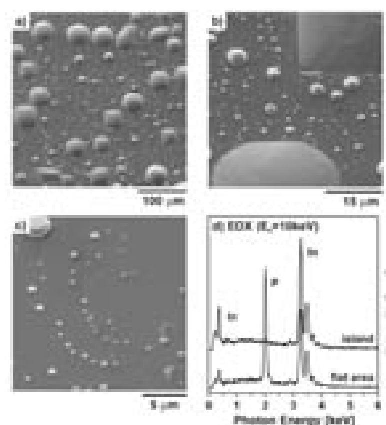

Fig. 3: a) – c) SEM images (E_0 = 10 keV) of the InP(001) surface after annealing at 770 K, d) EDX scans performed on a single island and a flat surrounding area .

The complex dynamic of the cluster growth is related to the competition of two processes: first, the nucleation of small indium clusters at surface steps and second, the ripening process, leading to the growth of large clusters at the expense of small ones. The different effects contributing to the island formation result in a rather complex growth dynamic on the InP surface.
To recapitulate, the difference in composition was locally probed on the flat area and on a single cluster using EDX. The spectra shown in Fig. 3d clearly indicate that the formed clusters only consist of metallic indium while the surrounding area is InP [6]. Therefore, both laterally resolved UPS (HeII) and EDX prove the formation of metallic indium clusters in contrast to the bare InP surface.

The authors gratefully acknowledge the continuous financial support by DFG and TKM.

[1] Indium phosphide and related materials: processing, technology and devices, ed. A. Katz, Artech House, Inc., 1992.
[2] Properties, processing and applications of indium phosphide, ed. T. Pearsall, No. 21 in EMIS Datareviews Series, London, INSPEC, 2000.
[3] T. D. Lowes, M. Zinke-Allmang, Phys. Rev. B 49(23) (1994), 16678.
[4] F. Riesz, L. Dobos, C. Vignali, C. Pelosi, Mat. Sci. Eng. B 80 (2001), 54.
[5] M. M. Sung, S. H. Lee, S. M. Lee, D. Marton, S. S. Perry, J. W. Rabalais, Surf. Sci. 382 (1997), 147.
[6] F. Lodders, J. Westhof, J.A. Schaefer, H. Höpfinger, A. Goldmann, S. Witzel, Z. Phys. B – Condensed Matter 83 (1991), 263.
[7] M. Himmerlich, diploma thesis, TU Ilmenau (2005).
[8] J. Woll, Th. Allinger, V. Polyakov, J.A. Schaefer, A. Goldmann, W. Erfurth, Surf. Sci. 315 (1994), 293.

TEM investigations on biological samples

H. Romanus[1,*], M. Frant[2], E. Remdt[1], K. Liefeith[2], and L. Spieß[1]
[1] Institute for Materials Engineering
[2] Institute for Bioprocessing and Analytical Measurement Techniques (iba), Heiligenstadt

Motivation of study
The objective of the relevant research project of *iba* is the validation of a new biomimetic surface coating which shall be applied as an effective antifouling concept for sensor surfaces in aqueous environments. At present the continuous use of optical and electrochemical measuring systems, respectively sensor systems for a longer period of time in aqueous surroundings (drinking water, river water, waste water, etc.) is strongly limited, respectively impossible due to their unsatisfactory resistance against superficial biofilm accumulation (fouling), Fig. 1.

Fig. 1: Biofilm accumulation on measuring systems

In spite of the fact that initial biofilm formation is controlled by thermodynamic phenomena the monomolecular tetraetherlipid coating shall adapt the physico-chemical nature of the sensor surface in dependence of the surrounding aqueous system. In particular during the performance control all laboratory tests necessary to check the antifouling potential of different tetraetherlipid systems should be carried out under simulated microbiological conditions. Therefore, various laboratory models were established and validated representing the different microbiological situations in drinking water, river water and waste water. As a result three laboratory models exist including defined media conditions and five specific bacterial strains, respectively. These bacterial strains isolated from real water systems were characterised as typical fast and strongly colonizers on different well-defined substrate materials. A comprehensive identification and characterisation of all used micro organisms was performed focussing on microscopic evaluation (optical microscopy – Fig. 2, REM and TEM) to describe typical morphologic and surface specific characteristics of the bacteria.

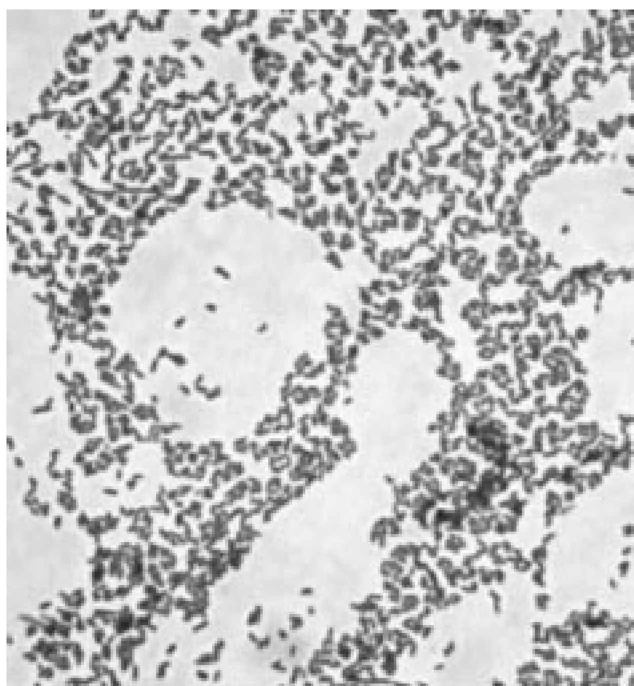

Fig. 2: Optical microscopy of strain 2.5 – Aeromonas hydrophila/caviae

Negative staining
Negative staining is an extremely powerful electron microscope technique for studying the ultrastructur of flagella, fimbriae, and fibrils. Unstained biological specimens have very low contrast in the electron microscope. To introduce contrast, a thin film of an electron dense negative stain with high atomic number is used to surround and embed the specimen [1].
In this work bacteria (15 different strains) were gently placed onto Quantifoil grids and negatively stained using 2% phosphotungstic acid. The resulting images are comparable with images presented in literature [1, 2].

* phone : +49-(0)3677-69-3404, email: henry.romanus@tu-ilmenau.de

Results

Each sample was examined at 5 representative spots. Very different structures were found, see Fig. 3-5. The morphology was mainly circular, oval, and rodshaped. All investigated biological organisms do not show an internal structure.

For example Aeromonas hydrophyla/caviae bacteria predominantly arise in oval shapes with sizes between 0.53-0.79 x 1-1.28 μm (some with flagellas, Fig. 3a) and in circular shape with diameter between 0.87-0.91 μm, Fig. 3b.

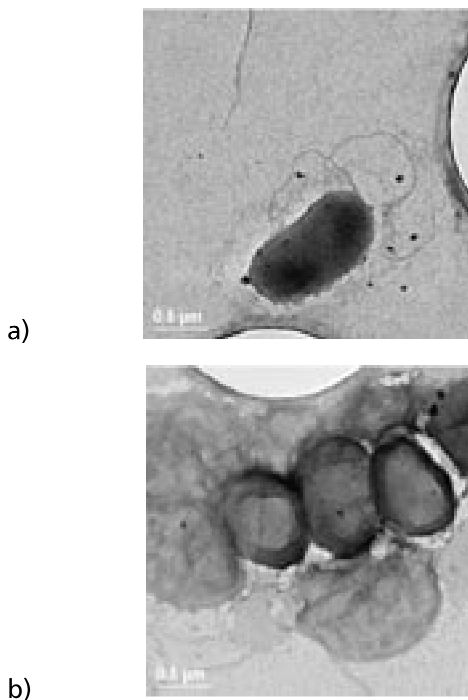

Fig. 3: TEM images of negatively stained strain 2.5 – Aeromonas hydrophila/caviae a) 1-1.7 μm long flagellas on bacterium (0.67 x 1.28 μm), b) circular shapes

Pasteurella pneumotropika/haemolitika possesses mainly a circulare structure which was identified as coccoid and capsule, Fig. 4. Flagellas could not be proven clearly. With the Bacillus cereus long rods (Fig. 5a) and endospores (Fig. 5b) can be differentiated.

Conclusions

The morphology of 15 different strains was examined by TEM. With these 3 examples presented it could be shown that negative staining is a powerful electron microscope technique. However, it is difficult to examine unstained samples.

Compared with the optical microscopy images shapes, size differences, and some flagellas of micro organisms could be determined more exact. It was possible to describe typical morphologic and surface specific characteristics of bacteria. For further works an optimisation of the preparation will be necessary.

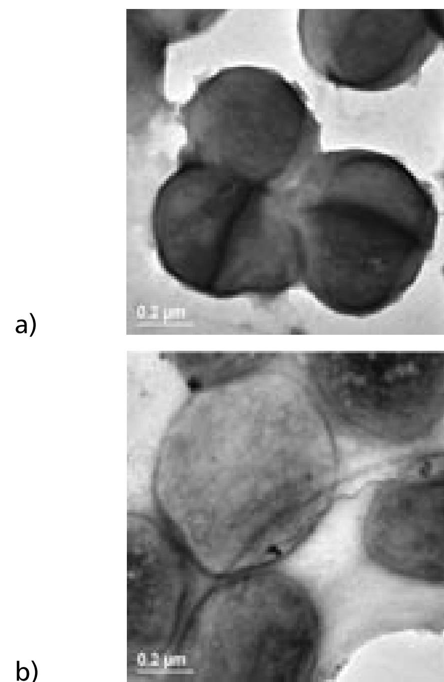

Fig. 4: TEM images of negatively stained strain 4.1 – Pasteurella pneumotropika/haemolitika a) small circular (0.43-0.58 μm), b) large circular (0.60-0.98 μm)

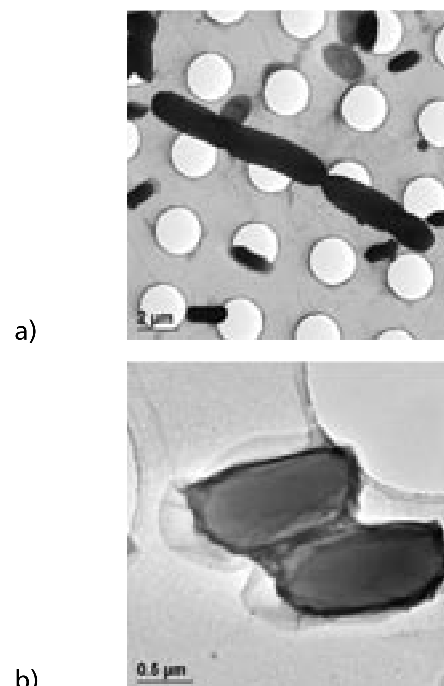

Fig. 5: TEM images of negatively stained strain 6.7 – Bacillus cereus a) long rods 1.65 x 4.31 μm, 1.60 x 4.84 μm and 1.63 x 3.93 μm, b) endospores 0.98 x 1.9 μm and 0.88 x 1.94 μm

This work is supported by the BMBF project "Wassertechnologie".

[1] Handley, P. S.: Negative staining. In: Mozes, N.; Handley, P. S.; Busscher, H. J. und Rouxhet, P. G.: Microbial cell surface analysis - Structural and physicochemical methods. 1. Ed. Weinheim: VCH Verlagsgesellschaft, 1991. ISBN 3-527-27987-3, p. 63-86.

[2] Gavín, R.; Rabaan, A. A.; Merino, S.; Tomás, J. M.; Gryllos, I.; Shaw, J. G.: Lateral flagella of Aeromonas species are essential for epithelial cell adherence and biofilm formation. Molecular Microbiology 43 (2002) 2, p. 383-397.

SEM/TEM Investigation of Ceramic Layers

Th. Kups[1,*] A. Knote[2], S. Selve[1], H. G. Krüger[2], L. Spieß[1], and H. Kern[2]
Departments of Materials for Electrical Engineering[1] and Metallic Materials and Composite Materials[2]

Introduction and Experimental
The aim of the present tests is to develop a surface coating for investigating the interface between the ceramic layer and the substrate. Ceramic layers for these investigations were made by ZrO_2 electrophoretically and then sintered in an open-porous layered structure.
The starting material for the electrophoretic coating was the commercial available powder of zirconium oxide ZrO_2 with 8% Yttrium (Tosoh TZ8Y). For SEM investigations the stainless steel X5Cr17 was used as a coating substrate. Because of the low sputter rate of steel it was not used as substrate for TEM investigations. For this investigation the ceramic was coated on a silicon substrate. The coating occurred at a voltage of 60 V, a coating period of up to 5 s and an electrode spacing of 3 cm in a homogenous and constant electrical field.
After the layer had dried, the sintering was carried out at a heating and cooling speed of 6 K/min in vacuum (holding time of 3 h). After sintering the layer structures were characterised by TEM and SEM. The (sintering) parameters of the produced layers are presented in the following table. The SEM samples were broken after cooling to the temperature of liquid N2 to avoid the etching influence of the etching beam. In Tab. 1 the specimen parameters are presented.

ZrO_2Ceramic	Substrate	(Sintering) parameter	Prepared for…by
TZ8Y	X5Cr17	3h@1200°C	SEM/Etching edge/cold break edge
TZ8Y	X5Cr17	3h@1150°C	SEM/cold break edge/
TZ8Y	Si		TEM

Tab. 1: Parameters of the specimens investigated

Results and Discussion
The first sample was prepared with breaking at cooled conditions. The overview image is shown in Fig. 1 where one can see that the whole layer was completely separated from the substrate. Thus, the bonding of the layer to the substrate must be very weak compared to the mechanical stress during the breaking process.

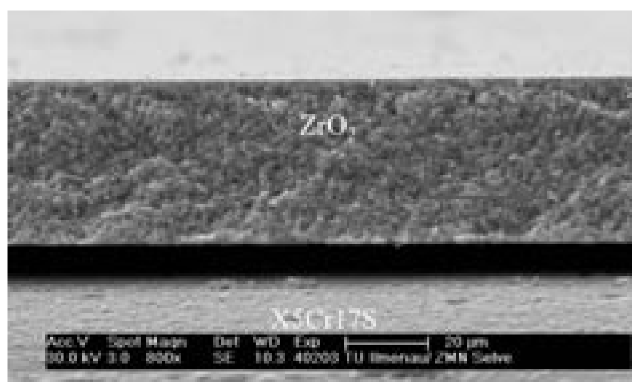

Fig. 1: Overview of the first sample, the layer was completely separated from the substrate

Therefore, to see the conditions of bonding of the layer and the substrate the sample was prepared by etching a small edge into the layer with Ar atoms (Fig. 2). A EDX map was recorded at the region marked with the rectangle (Fig. 3).

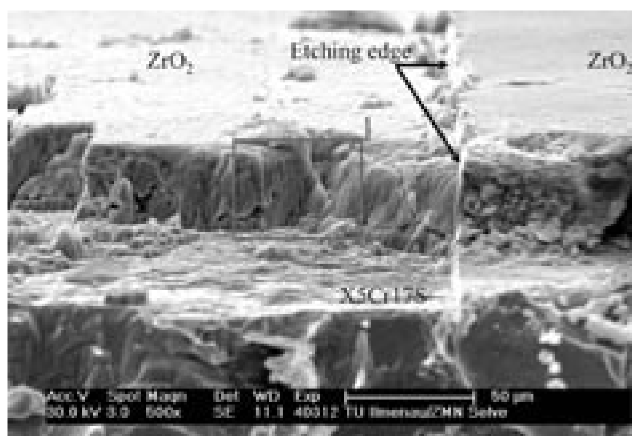

Fig. 2: Overview of the sample prepared by etching an edge

The column like structure one can seen the SEM images consist of the substrate material which must be very thick because no signal of the probable layer (Zr, Y and O) behind this column was measured. Thus, an intermixing of layer and substrate might have occurred. This column like structure is a preparation effect which only appears when etching a small edge into the layer.
Therefore, to see the layer structure as it is, the specimen has to be broken at temperatures of liquid N_2.

* phone: +49-(0)3677-69-3109, email: thomas.kups@tu-ilmenau.de

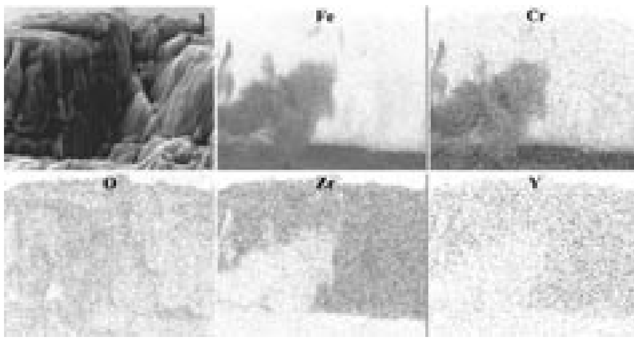

Fig. 3: EDX mappings of the ceramic layer and substrate for 5 elements. The column like structure one can seen in the SEM images is a preparation effect and consists of the substrate material which must be very thick because no signal of the probable layer (Zr, Y and O) behind this column was measured.

Fig. 4 shows the SEM image of the second specimen. The layer was separated from the substrate, only small portions of the layer remained on the substrate. The region of the porous layer structure marked with the rectangle was used for further investigation (Fig. 5).

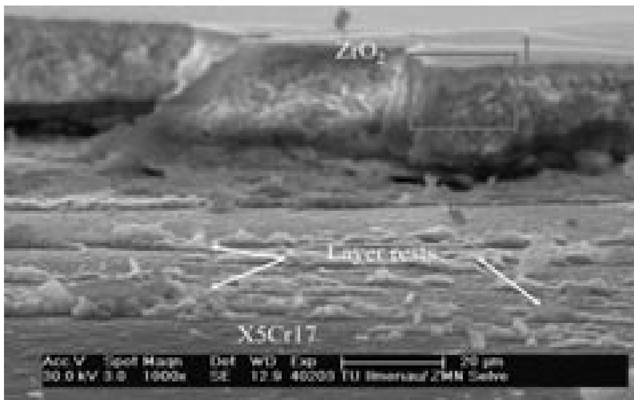

Fig. 4: Overview of the second specimen. The layer was separated from the substrate nearly totally. Only small portions of the layer remained on the substrate.

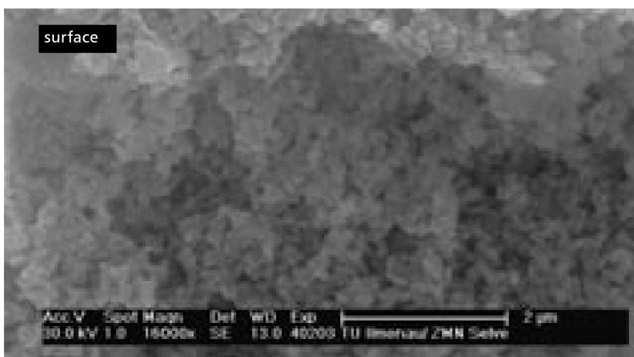

Fig. 5: Closer look on the ceramic layer near the surface. The porosity of the ceramic layer is clearly visible.

The porous structure of the ceramic layer of this sample is presented in Fig. 2. In Fig. 3, a closer look at such a layer left over as marked in Fig. 4 is shown. One can see that the surface is provided with small imprints which probably are caused by the ZrO_2 particles imprinting the substrate during the sintering process.

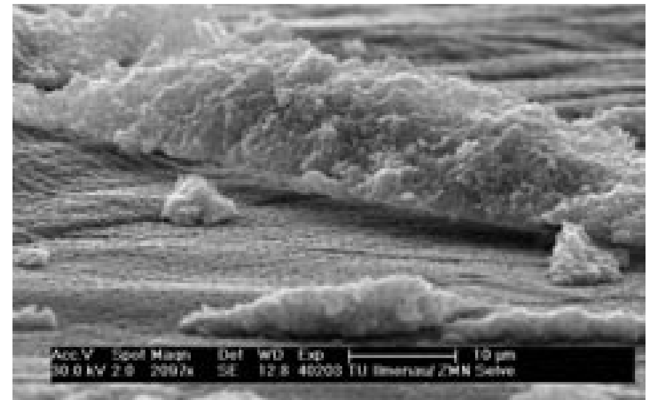

Fig. 6: Detailed image of the layer left overs. One can see the imprints of the former layer on the substrate

In Fig. 7 the results of the TEM investigations of the third sample on Si substrate is presented. The layer has not separated from the substrate and shows the typical ceramic porous structure. The EDX map of this area shows for the three main elements (Zr, Si, O) the expected results without any mixing of layers or diffusion of Si into the layer.

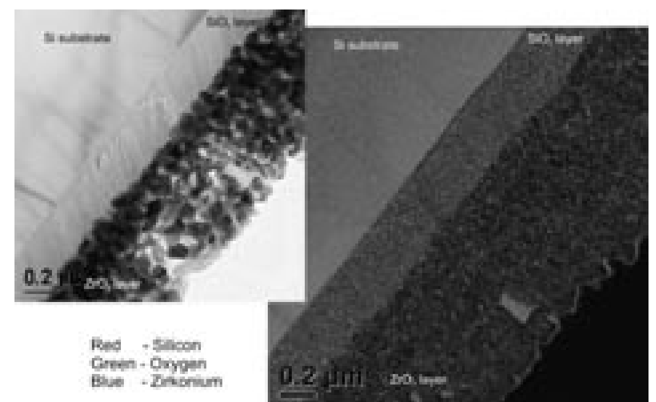

Fig. 7: TEM overview of sample 3. The porous structure is visible and the EDX map shows no extra properties.

This work was supported by DFG KE359/7-1.

Dry Sliding of Copper: The Influence of Adsorption

Y. Liu[1,*], M. Gubisch[2], M. Himmerlich[1], S. Krischok[1], L. Spiess[2], M. Scherge[1], and J. A. Schaefer[1]

[1] Department of Technical Physics

[2] Institute for Materials Engineering

Micro-Electro-Mechanical Systems (MEMS) is the integration of mechanical elements, sensors, actuators, and electronics in a common silicon substrate through microfabrication technology. Copper's usefulness in the MEMS technology is based on its high electrical and thermal conductivity, and its good mechanical properties. Several studies have shown that tribology (friction and wear) is an important factor affecting the performance and reliability of MEMS which usually operate at very low working loads and speeds. Under these conditions, mild wear was observed in sliding tests of copper and its alloys. The mild wear is usually related to the formation of oxide films and influenced by adsorbates from the environment. In addition, it is also affected by the hardness of the substrates. If the oxide film remains after slider passes, and the substrate is hard enough to support the oxide film, the sliding occurs between the oxides, and thus low wear and a low coefficient of friction are expected. We examined this scenario by dry sliding tests of pure copper using microtribometers in air and in vacuum. The oxide films in the wear tracks were studied with scanning electron microscopy and photoelectron emission microscopy combined with laterally resolved photoelectron spectroscopy. The deformation band underneath the wear tracks was revealed by conventional metallographic method and was observed by orientation imaging microscopy.

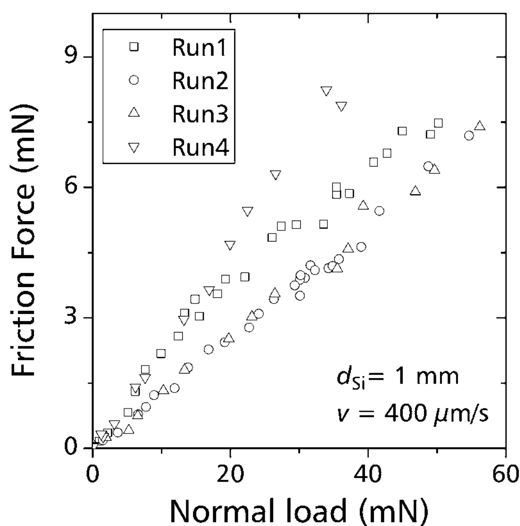

Fig. 1: Friction behaviour of copper in air

Friction in air

The friction force F of copper sliding against a silicon sphere of 1 mm diameter tested in air is presented in Fig. 1. In the first run, F increases linearly with normal load L for L<18 mN. After a transition at L ~18 mN, F still increases linearly with normal load, but with a smaller slope. In the consecutive next two runs, run 2 and run 3, F increases linearly in the whole range of normal load. The slopes of curves in run 2 and run 3 are nearly the same as those in the first run when L>18 mN. If we take the slopes of the curves as friction coefficients μ, we can observe a higher μ when copper is covered with adsorption layers. Once the adsorption layer is damaged, μ turns smaller and stable. This result is also supported by the higher slope of the curve in run 4 which was tested 12 hours after run 3. After such a long dwelling time, a stable adsorption layer was built up at the surface again. Due to the heavy intermixing at the contact, both chemically and mechanically, the newly formed adsorption layer was thicker and more resistant to damage. Therefore, no transition to a low value of μ was observed in the range of L<40 mN.

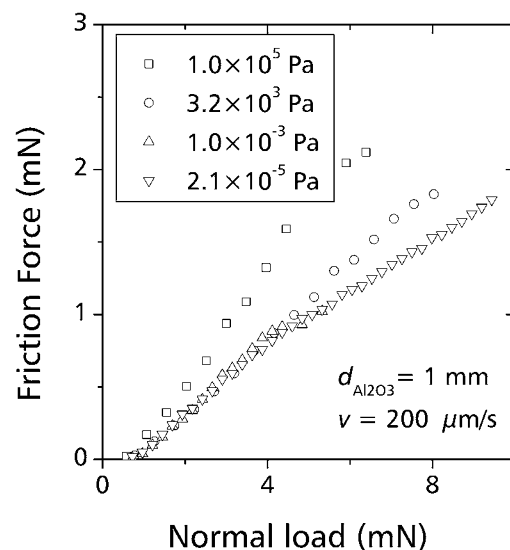

Fig. 2: Friction behaviour of copper in vacuum

Friction in vacuum

The friction force F of copper sliding against a sapphire sphere of 1 mm diameter tested in vacuum is presented in Fig. 2. The testing sequence is first a friction test under normal pressure, then pumping to a lower pressure to perform the friction test at the

* phone : +49-(0)3677-69-5074, email: yonghe.liu@tu-ilmenau.de

same place until the lowest pressure of the vacuum chamber is reached. Like the results tested in air, a higher μ was observed when the copper surface was covered with adsorption layers as shown by the curve at 1.0×10^5 Pa. Again, a transition to a lower μ was observed at a normal load of ~5 mN. A decrease of pressure can reduce μ to a lower value as shown by the curve at 3.0×10^3 Pa. When L<5 mN. A further decrease of pressure does not reduce friction. In contrast, when L>5 mN, the friction can be further reduced with a decrease of pressure. These results show that the adsorption changes not only with running time, but also with the pressure.

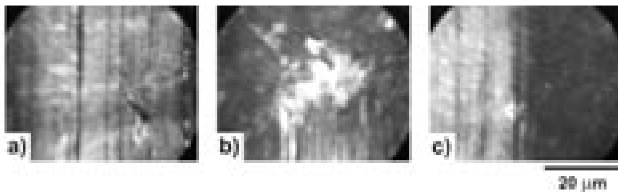

Fig. 3: PEEM images of the wear tracks in copper produced by tribological tests in air: a) trenches inside the wear marks, b) worn material at the end of the track, c) border between the worn area (left) and the untreated flat copper surface (right).

Composition of wear tracks: PEEM and UPS studies

After tribological tests, the samples were examined in UHV using Photoelectron Spectroscopy (XPS, UPS) and Photoelectron Emission Microscopy (PEEM). Typical PEEM images of different regions of one wear track are presented in Fig. 3. The non ideal tribological contact between the copper surface and the counter sphere results in the formation of a rough surface inside the wear tracks with trenches aligned in the direction of motion.

XPS measurements performed on the loaded sample revealed, besides the common surface contamination by oxgen and carbon, some amounts of iron, zinc, and chlorine impurities. Bombardment with Ar^+ ions of 3 keV energy for 60 min resulted in a contamination free copper surface. Measurements of the valence band using UPS with Ar (hν=11.6 eV) and He I (hν=21.2 eV) radiation are shown in Fig. 4a. The typical response from the Cu d-band appears in the range between 2 eV and 4 eV of binding energy and the Fermi edge is well pronounced indicating a clean copper surface [1]. Laterally resolved UPS measurements performed with Ar radiation are shown in Fig. 4b. Spectra were obtained with the μ-ESCA electron analyzer mounted to the PEEM collecting electrons from an area of approximately 300 μm². The comparison of the spectra measured inside the wear tracks and that of the surrounding unworn flat copper surface indicates differences in the composition of the material. The d-band emission located around 2 eV binding energy is weaker inside the wear track and additional structures are present at higher binding energies, especially apparent a feature at 5.7 eV. This change in the valence band can be related to the formation of copper oxide [2]. The presence of oxygen inside the wear marks after the sputter treatment indicates that the friction in the dynamic tribological contact between the copper surface and the counter sphere leads to the formation of an oxide layer under atmospheric conditions.

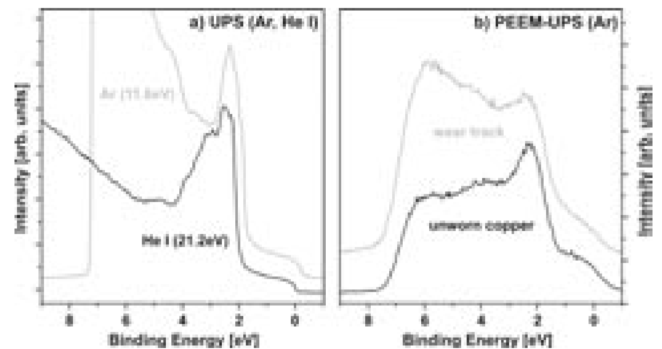

Fig. 4: UPS valence band spectra: a) lateral integrated UPS (Ar and He I) of the sputter cleaned surface, b) comparison of the lateral resolved UPS (Ar) measurements of the surface inside the wear track and the flat untreated copper area.

Composition of wear tracks: EDS studies

The scanning electron microscopy (SEM) image of a wear track developed at a copper surface after 2000 running cycles is presented in Fig. 5a. Large black patches were observed in the track. We analyzed the composition of the wear track, the black patches, and the unworn area by energy dispersive spectrometry (EDS), and present the results in Fig. 5b. Carbon was found to be the dominant adsorbate in the wear track. It segregated into black patches as shown by the highest carbon content in them, and distributed randomly. The oxygen content was also the highest in the black patches, indicating the accumulation of oxide particles in them.

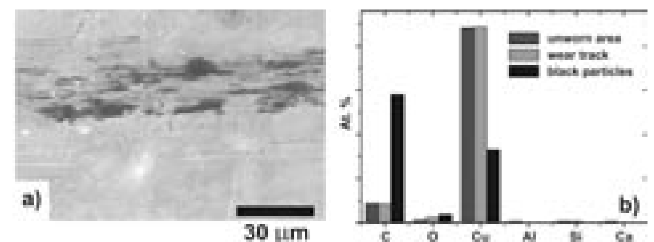

Fig. 5: Wear track (a) after 2000 running cycles, and its composition determined by EDS (b).

This work was supported by the Deutsche Forschungsgemeinschaft (SFB 622).

[1] F.L. Battye, A. Goldmann, L. Kasper, S. Hüfner, Z. Physik B 27 (1977), 209.
[2] L.F. Wagner, W.E. Spicer, Surf. Sci. 46 (1974), 301.

Plasma Deposited Fluorocarbon Films: Change of Surface Chemical Composition by X-ray Radiation

V. Yanev[1,*], M. Himmerlich[1], A. Opitz[2], R. Öttking[1], S. Krischok[1], and J.A. Schaefer[1]

[1] Department of Technical Physics

[2] Institute of Physics, University of Augsburg

Due to their outstanding properties, FC polymers are ideal materials for various chemical, biochemical, microelectronic, and MEMS applications [1 - 4]. In many applications these materials have to sustain X-ray radiation and to maintain their unique properties. Satellite and aerospace sensors and detectors, X-ray sensors in computer tomography, detectors in nuclear radiology and nuclear reactors are exposed to X-ray radiation. E-beams, UV and X-ray radiation are used for modification and treatment of masks, circuit boards and insulator materials.

In this context, we have investigated the influence of soft X-rays on the chemical composition of the surface of different plasma deposited FC films.

Deposition

Two types of FC films were produced in two different plasma systems. First, plasma deposition experiments were carried out in a conventional reactive ion etching system (RIE, radio-frequency 13.56 MHz, STS 320 PC). The FC plasma polymerisation was performed on Si(111) using trifluoromethane (CHF_3) as process gas at 35 W, 130 mTorr, and a flow rate of 25 sccm. Second, an inductively coupled RF plasma system (ICP, STS) was applied to deposit FC films on Si(111). Octafluorocyclobutane (C_4F_8) was used as process gas at a coil power of 600 W (platen power 0 W), a pressure of 19 mTorr, and a flow rate of 85 sccm. After deposition, the thickness of the RIE films was 65 nm and that of the ICP films 40 nm measured using an IR-ellipsometer (Plasmos SD 2302).

Method

The samples were implemented into an UHV system (base pressure 1.5×10^{-10} mbar) and exposed to Mg(Kα) radiation (1253.6 eV) using an X-ray source (OMICRON, DAR 400) operating at 170 W (13 kV, 13 mA). Simultaneously, XPS measurements were performed. The RIE films were exposed to X-rays for 288 min and the ICP films for 4320 min, respectively. C 1s, F 1s, O 1s and survey spectra were recorded in situ.

Results and discussion

The survey spectra for both, RIE and ICP films, show mainly fluorine and carbon with trace amounts of oxygen (below 2.5%). The recorded C 1s peaks are separated into 4 components assigned to CF_3 (at ≈ 294.2 eV BE), CF_2 (at ≈ 292 eV BE), CF (at ≈ 289.8 eV BE) bonds and C with no primary fluorine bonds (C–C, at ≈ 287.7 eV BE).

Changes in the chemical composition:

Fig. 1 shows the C 1s spectra (after 6 min. exposure to X-rays) of both, RIE and ICP films, and the final recorded C1s spectra (after 288 min. X-ray irradiation for the RIE samples and after 4320 min. X-ray irradiation for the ICP films). The binding energy (BE) axes are corrected to the surface charging by setting the binding energy of the F1s peak to 689.0 eV [5]. The C 1s spectrum taken during the first 6 min. (see Fig. 1a) revealed that in the RIE films 24.7 % of the detected carbon is bond as CF_2. Films with higher CF_2 content (40.7 %) were produced in the ICP system using C_4F_8 as process gas (see Fig. 1c). These results indicate that the ICP films are more PTFE-like compared to the RIE films.

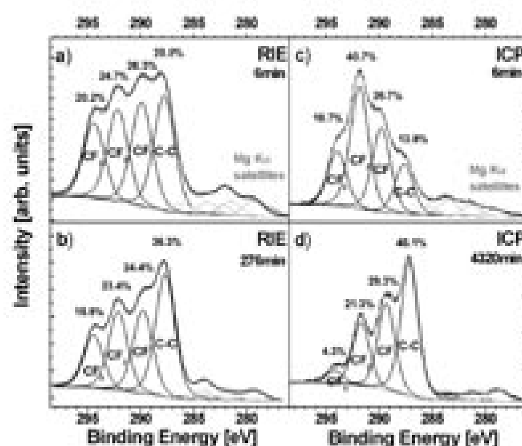

Fig. 1: C 1s XPS spectra (a) after 6 min. and (b) after 288 min. X-ray irradiation for the RIE films and (c) after 6 min. and (d) after 4320 min. for the ICP films. All spectra are corrected to surface charging.

It was also obvious that the chemical environment of the carbon and, therefore, the chemical composition of the FC films strongly depends on the X-ray irradiation time. In Fig. 2 the relative areas of the observed CF_x (x=0…3) components are shown as a function of the X-ray irradiation time for both, RIE and ICP samples.

* phone: +49-(0)3677-69-3406, email: vasil.yanev@tu-ilmenau.de

For the RIE films, the CF, CF_2, and CF_3 components all seem to decrease monotonously during the X-ray exposure. At the same time the concentration of C-C type bonds increases from 28.8 % to 36.3 %.
Similar to the RIE samples, the relative CF_3 and CF_2 peak areas of the ICP films decreased continuously with increasing irradiation time. During the first 300 min. of irradiation, the concentration of CF groups decreased as well. However, after 300 min. an increase of the CF bonds was observed. The relative amount of the C-C bonds increased continuously from 13.9% to 45.1% after 4320 min. irradiation.
The conversion of CF_x bonds to C-C type bonds indicate significant defluorination of the FC films.

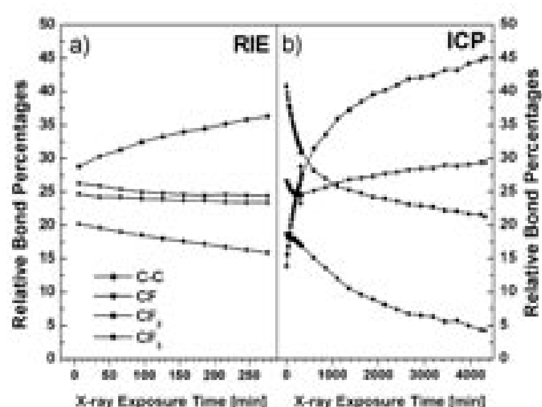

Fig. 2: Changes of the relative ratio of the four C1s components as a function of X-ray irradiation time for (a) RIE films and (b) ICP films.

The calculated fluorine to carbon (F/C) ratios and the evolution of F 1s spectra recorded during irradiation leads to the same conclusion (see Fig. 3). The analysis revealed that the F/C ratio of the RIE coatings decreased from 1.39 to 1.21 after 280 min. (exposure to X-ray radiation) and for the ICP films from 1.64 to 0.85 after 4320 min. irradiation.

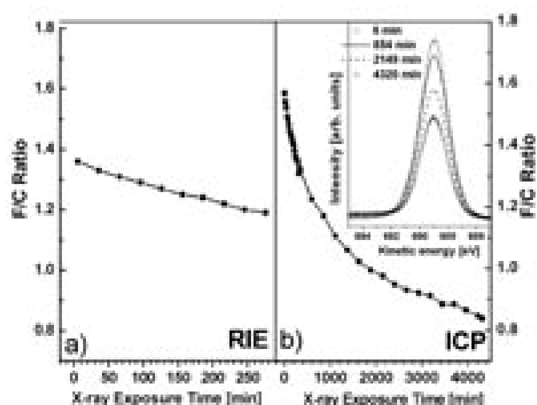

Fig. 3: Fluorine to carbon ratio as a function of X-ray irradiation time for (a) RIE films and (b) ICP films.

Surface charging effects:
Another fact indicating the change of the surface chemical composition of the FC films is the different BE shift of the C 1s peaks after various exposure times associated with surface charging effects. In Fig. 4, the F 1s peak shifts against the expected F 1s position (689.0 eV [5]) for both, RIE and ICP samples, and the recorded F 1s spectra (normalised but not corrected to the surface charging) of the ICP films during X-ray irradiation are shown.

The first spectra (after 6 min. of X-ray exposure) show a positive surface charging of 4.6 eV for the RIE films and 2.5 eV for the ICP films. The different shift for both samples can be explained by differences in the chemical structure and the film thickness. Obviously, the peak shift depends on the X-ray irradiation time (see Fig. 4). During the exposure the charging was reduced. For the RIE films the charging decreased to 2.7 eV (after 280 min. X-ray impact), and for ICP films to 0.1 eV (after 4320 min. irradiation). The FC surfaces become more conductive with increasing irradiation time.

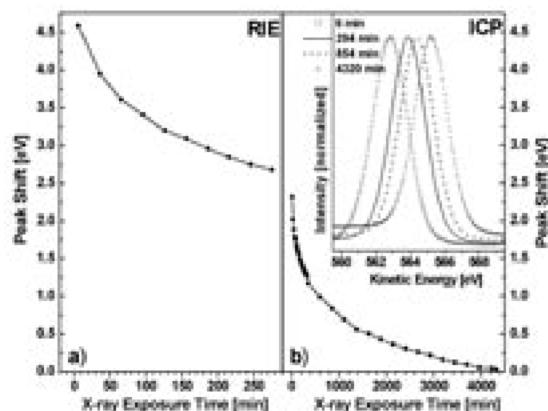

Fig. 4: Peak shift as function of X-ray irradiation time for (a) RIE films and (b) ICP films.

Conclusions
In conclusion, X-ray exposure leads to changes in the chemical composition, surface charging and variation of the conductivity of plasma deposited FC films indicating defluorination processes and chemical decomposition of the FC films. These are dependent on the exposure time of the FC films to X-ray radiation.

[1] A. Schober , G. Kittler, C. Buchheim, A. Majdeddin, V. Cimalla, M. Fischer, V. Yanev, M. Himmerlich, S. Krischok, J. A. Schäfer, H. Romanus, T. Sändig, J. Burgold, F. Weise, H. Wurmus, K. H. Drüe, M. Hintz, H. Thust, J. Gessner, M. Kittler, F. Schwierz, Th. Doll, E. Manske, R. Mastylo, G. Jäger, Ch. Knedlik, G. Winkler, H. Kern, R. Hoffmann, L. Spiess, A. Spitznas, E. Gottwald, K-F. Weibezahn, D. Wegener, A. Schwienhorst, O. Ambacher, Proc. 12. Heiligenstädter Kolloquium, Heiligenstadt (2004) 163.
[2] J. Burgold, F. Weise, M. Fischer, G. Schlingloff, Th. Henkel, J. Albert, G. Mayer, A. Schober, Macromolecular Rapid Communication 26, (2005) 265.
[3] V. Yanev, N. Schwesinger, H. Wurmus, Plasma Deposition and Patterning of Thin Fluorocarbon Polymer Films for Several Applications in Micromechanics and Microsystem Technology, Proc. 44th International Scientific Colloquium, Technical University of Ilmenau, Vol. 2, Ilmenau, Germany, (1999) 548.
[4] D. J. Balazs, C. Hollenstein and H. J. Mathieu, European Cells and Materials 3 (1), (2002) 7.
[5] J. F. Moulder, W. F. Stickle, P. E. Sobol, K. D. Bomben, Handbook of X-ray Photoelectron Spectroscopy, ed. J. Chastain and R. C. King, Jr., Physical Electronics, Inc. USA (1995).

Publications and Conference Contributions

Material Science

Departments of Materials for Electrical Engineering

Bias-magnetron sputtering of tungsten carbide coatings on steel
M. Gubisch, L. Spieß, H. Romanus, J. Schawohl, and Ch. Knedlik, Materialwissenschaft und Werkstofftechnik 35 (2004) 916.

Structure and composition of 3C-SiC:Ge alloys grown on Si (111) substrates by SSMBE
P. Weih, V. Cimalla, Th. Stauden, R. Kosiba, L. Spieß, H. Romanus, M. Gubisch, W. Bock, Th. Freitag, P. Fricke, O. Ambacher, and J. Pezoldt,
Mater. Sci. Forum 457 (2004) 293.

3C-SiC:Ge alloy grown on Si(111) substrates by SSMBE
P. Weih, V. Cimalla, Th. Stauden, R. Kosiba, G. Ecke, L. Spiess, H. Romanus, M. Gubisch, W. Bock, Th. Freitag, P. Fricke, O. Ambacher, and J. Pezoldt,
Phys. Stat. Sol. C 1 (2004) 347.

Investigation on preparation of multiwalled carbon nanotubes by DC arc discharge under N_2 atmosphere
S. Cui, P. Scharff, C. Siegmund, D. Schneider, K. Risch, S. Klötzer, L. Spiess, H. Romanus, and J. Schawohl,
Carbon 42 (2004) 931.

Synthesis of C_{60} intercalated graphite
V. Gupta, P. Scharff, K. Risch, H. Romanus, and R. Müller,
Sol. State Commun. 131 (2004) 153.

Insertion of C_{60} into multi-wall carbon nanotubes - a synthesis of C_{60}@MWCNT
T. Fröhlich, P. Scharff, W. Schliefke, H. Romanus, V. Gupta, C. Siegmund, O. Ambacher, and L. Spiess,
Carbon 42 (2004) 2759.

Characterization of sputtered NiO films using XRD and AFM
I. Hotovy, J. Huran, and L. Spiess,
J. Materials Sci 39 (2004) 2609.

Enhancement of H_2 sensing properties of NiO-based thin films with Pt surface modification
I. Hotovy, J. Huran, P. Siciliano, S. Capone, L. Spiess, and V. Rehacek,
Sensors and Actuators B 103 (2004) 300.

Sputter depth profiling of InN layers
R. Kosiba, G. Ecke, V. Cimalla, L. Spieß, S. Krischok, J. A. Schaefer, O. Ambacher, and W. J. Schaff,
Nucl. Instrum. Methods Phys. Res. B 215 (2004) 486.

Cubic InN on r-plane sapphire
V. Cimalla, U. Kaiser, I. Cimalla, G. Ecke, J. Pezoldt, L. Spiess, O. Ambacher, H. Lu, and W. Schaff,
Superlattices and Microstructures 36 (2004) 487.

Tribological characteristics of $WC_{(1-x)}$, W_2C, and WC tungsten carbide films
M. Gubisch, Y. Liu, S. Krischok, G. Ecke, L. Spieß, J. A. Schaefer, and Ch. Knedlik,
Proc. 31st Leeds-Lyon Symposium on Tribology 2004, Leeds, United Kingdom, in Tribology and Interface Engineering Series 48, Elsevier (2004).

NiO-based thin films with Pt surface modification for gas sensors
I. Hotovy, J. Huran, L. Spiess, and H. Romanus,
Proc. 10th Joint Vacuum Conference, Portoroz, (2004).

Thin film voltammetric microsensor for heavy metal analysis
V. Tvarozek, V. Rehacek, K. Shtereva, I. Novotny, V. Breternitz, Ch. Knedlik, and L. Spiess,
Proc. 24th Int. Conf. on Microelectronics (MIEL2004), Serbia and Montenegro (2004) 189.

NiO modified thin films for gas monitoring
I. Hotovy, J. Huran, L. Spiess, M. Gubisch, and J. Schawohl,
Proc. 5th International Conference on Advanced Semiconductor Devices and Microsystems, Smolenice, Slovakia (2004) 303.

Definierte Präparation von hexagonalem WSi_2 und Wolframsilizidmetallisierungen mit einstellbarem Temperaturkoeffizient der elektrischen Leitfähigkeit
H. Romanus, L. Spiess, Ch. Knedlik, and J. K. N. Lindner,
Proc. Thüringer Werkstofftag 2004, Ilmenau, in Schriftenreihe Werkstoffwissenschaften,
18 (2004) 119.

Untersuchungen zu Nickel-Zink-Ferrit-Schichten auf Kupferfolien für Leiterplatten
H. Romanus, K. Romankiewicz, B. Schwenke, V. Breternitz, Ch. Knedlik, and G. Teichert,
Proc. Thüringer Werkstofftag 2004, Ilmenau, in Schriftenreihe Werkstoffwissenschaften,
18 (2004) 125.

Nanoschichten für die Nanopositionierung
M. Gubisch, Y. Liu, L. Spiess, H. Romanus, and Ch. Knedlik,
Proc. Thüringer Werkstofftag 2004, Ilmenau, in Schriftenreihe Werkstoffwissenschaften,
18 (2004) 131.

Analyse nanokristalliner Schichten auf rauen Substraten
V. Cimalla, L. Spiess, M. Gubisch, I. Hotovy, H. Romanus, and O. Ambacher,
Proc. Thüringer Werkstofftag 2004, Ilmenau, in Schriftenreihe Werkstoffwissenschaften,
18 (2004) 177.

Lateralkraftmikroskopie an elektrischen Kontakten
V. Cimalla, L. Spiess, H. Romanus, and O. Ambacher,
Proc. Thüringer Werkstofftag 2004, Ilmenau, in Schriftenreihe Werkstoffwissenschaften,
18 (2004) 203.

Department of Metallic Materials and Composite Materials

Untersuchung von Einflussfaktoren auf das tribologische Verhalten von Werkstoffen gegen Eis
F. Albracht, S. Reichel, V. Winkler, and H. Kern,
Materialwissenschaft und Werkstofftechnik,
35 (2004) 620.

Composite ceramic-metal coatings by means of combined electrophoretic deposition and galvanic methods
H. G. Krüger, A. Knote, U. Schindler, H. Kern, and A. R. Boccaccini,
Journal of materials science 39 (2004) 839.

Festkörper mit negativer thermischer Ausdehnung
Ch. Georgi and H. Kern,
Proc. Thüringer Werkstofftag 2004, Ilmenau, in Schriftenreihe Werkstoffwissenschaften,
18 (2004) 63.

Ekektrophoretische Beschichtung zur Realisierung niedrig emittierender keramischer Schichten
A. Knote, H. G. Krüger, H. Kern, and J. Manara,
Proc. Thüringer Werkstofftag 2004, Ilmenau, in Schriftenreihe Werkstoffwissenschaften,
18 (2004) 97.

Über die Einflussfaktoren der Reibung auf Eis
F. Albracht, H. Kern, S. Reichel, and V. Winkler,
Tribologie-Fachtagung mit internationaler Beteiligung, Göttingen (2004).

Technology

Department of Nanotechnology

Efficient large area polymer solar cells on flexible substrates
M. Al-Ibrahim, H.-K. Roth, and S. Sensfuss,
Applied Physics Letters 85 (2004) 1481.

Arylene-Vinylene/Arylene-EthynyleneCopolymers: Synthesis, Characterization and Photovoltaic Applications
D. A. M. Egbe, E. Klemm, B. Carbonnier, T. Pakula, S. Sensfuss, M. Al-Ibrahim, A. Konkin, H. Hoppe, and N. S. Sariciftci,
Macromol. Rapid Commun. 25 (2004) 49.

Determination of polaron lifetime and mobility in a polymer/fullerene solar cell by means of photoinduced absorption
C. Arndt, U. Zhokhavets, M. Mohr, G. Gobsch, M. Al-Ibrahim, and S. Sensfuss,
Synthetic Metals 147 (2004) 257.

Auger Electron Spectroscopy of Silicon Carbide
R. Kosiba, J. Liday, G. Ecke, O. Ambacher, and J. Breza,
J. Electrical Engineering 55 (2004) 269.

Untersuchung der Anfangsstadien des Wachstums von SiC Nanoclustern auf Siliziumsubstraten
Yu. V. Trushin, E. E. Zhurkin, K. L. Safonov, A. A. Schmidt, V. S. Kharlamov, S. A. Korolyov, M. N. Lubov, and J. Pezoldt,
Pizma v Zh. Techn. Fiz., 30 (2004) (15) 48. (russ.).
Initial stages of the MBE growth of silicon carbide nanoclusters on a silicon substrate
Tech. Phys. Lett. 30 (2004) 641. (engl.).

SIMS investigations of the influence of Ge pre-deposition on the interface quality between SiC and Si
J. Pezoldt, Ch. Zgheib, P. Masri, M. Averous, F. M. Morales, R. Kosiba, G. Ecke, P. Weih, and O. Ambacher,
Surf. Interface Anal. 36 (2004) 969.

Photoreflectance studies of (Al)Ga- and N-face AlGaN/GaN heterostructures
C. Buchheim, A. T. Winzer, R. Goldhahn, G. Gobsch, O. Ambacher, A. Link, M. Eickhoff, and M. Stutzmann,
Thin Solid Films 450 (2004) 155.

Structural and optical properties of both pure poly (3-octylthiophene) (P3OT) and P3OT/ fullerene films
T. Erb, S. Raleva, U. Zhokhavets, G. Gobsch, B. Stühn, M. Spode, and O. Ambacher,
Thin Solid Films 450 (2004) 97.

Temperature dependent electric fields in GaN Schottky diodes studied by electroreflectance
S. Shokhovets, D. Fuhrmann, R. Goldhahn, G. Gobsch, O. Ambacher, M. Hermann, and M. Eickhoff,
Thin Solid Films 450 (2004) 163.

Two dimensional electron gas recombination in undoped AlGaN/GaN heterostructures
G. Martinez-Criado, C. Miskys, U. Karrer, O. Ambacher, and M. Stutzmann,
Jap. J. Appl. Phys. 43 (2004) 3360.

Vertical transport in group III-nitride heterostructures and application in AlN/GaN resonant tunneling diodes
M. Hermann, E. Monroy, A. Helman, B. Baur, M. Albrecht, B. Daudin, O. Ambacher, M. Stutzmann, and M. Eickhoff,
phys. stat. sol. c1 (2004) 2210.

High-resolution diffuse x-ray scattering from threading dislocation in heteroepitaxial layers
S. Danis, V. Holy, Z. Zhong, G. Bauer, and O. Ambacher,
Appl. Phys. Lett. 85 (2004) 3065.

Comment on „Mie resonances, Infrared Emission, and the Band Gap of InN“
F. Bechstedt, J. Furthmüller, O. Ambacher, and R. Goldhahn,
Phys. Rev. B 93 (2004) 269701.

Linear alignement of SiC dots on silicon substrates
V. Cimalla, A. A. Schmidt, Th. Stauden, K. Zekentes, O. Ambacher, and J. Pezoldt,
J. Vac. Sci. Technol. B22 (2004) L20.

Self organized SiC nanostructures on silicon
V. Cimalla, A. A. Schmidt, Ch. Förster, O. Ambacher, K. Zekentes, and J. Pezoldt,
Superlattices and Microstructures 36 (2004) 345.

Cubic InN on r-plane sapphire
V. Cimalla, U. Kaiser, I. Cimalla, G. Ecke, J. Pezoldt, L. Spiess, and O. Ambacher,
Superlattices and Microstructures 36 (2004) 487.

Growth of $Al_xGa_{1-x}N$-layers on planar and patterned substrates
U. Rossow, D. Fuhrmann, M. Greve, J. Bläsing, A. Krost, G. Ecke, N. Riedel, and A. Hangleiter,
J. Cryst. Growth 272 (2004) 506.

Sputter depth profiling of InN layers
R. Kosiba, G. Ecke, V. Cimalla, L. Spieß, and O. Ambacher,
Nucl. Instr. and Meth. B 215 (2004) 486.

Investigations of MBE grown InN and the influence of sputtering on the surface composition
R. Krischok, V. Yanev, O. Balykov, M. Himmerlich, J.A. Schäfer, R. Kosiba, G. Ecke, I. Cimalla, V. Cimalla, O. Ambacher, H. Lu, W. J. Schaff, and L. F. Eastman,
Surface Science 566 (2004) 849.

Study of pinholes and nanotubes in AlInGaN films by cathodoluminescence and atomic force microscopy
H. Herrera, A. Cremades, J. Piqueras, M. Stutzmann, and O. Ambacher,
J. Appl. Phys. 95 (2004) 5305.

Lateral alignment of SiC dots on silicon substrates
V. Cimalla, J. Pezoldt, Th. Stauden, Ch. Förster, and O. Ambacher,
phys. stat. sol. c1 (2004) 337.

The role of Ge predeposition temperature in the epitaxy of SiC on Silicon
F. M. Morales, Ch. Zgheib, S. I. Molina, D. Araujo, R. Garcia, C. Fernandez, A. Sanz-Hervas, P. Masri, P. Weih, Th. Stauden, V. Cimalla, O. Ambacher, and J. Pezoldt,
phys. stat. sol. c1 (2004) 314.

3C-SiC: Ge alloy grown on Si(111) substrates by SSMBE
P. Weih, V. Cimalla, Th. Stauden, R. Kosiba, G. Ecke, L. Spiess, H. Romanus, M. Gubisch, W. Bock, Th. Freitag, P. Fricke, O. Ambacher, and J. Pezoldt,
phys. stat. sol. c1 (2004) 347.

Kinetic Monte Carlo simulations of SiC nucleation on Si(111)
A. A. Schmidt, K. L. Safonov, Yu. V. Trushin, V. Cimalla, O. Ambacher, and J. Pezoldt,
phys. stat. sol. (a) 201 (2004) 333.

Infrared ellipsometry of SiC/Si heterostructures with Ge modified interfaces
Ch. Zgheib, Ch. Förster, P. Weih, V. Cimalla, M. Kazan, P. Masri, O. Ambacher, and J. Pezoldt,
Thin Solid Films 455 (2004) 183.

In situ spectroscopic ellipsometry of hydrogen-argon plasma cleaned silicon surfaces
Ch. Förster, F. Schnabel, P. Weih, Th. Stauden, O. Ambacher, and J. Pezoldt,
Thin Solid Films 455- (2004) 695.

Initial stages of the MBE growth of silicon carbide nanoclusters on a silicon substrate
Yu.V. Trushin, E. E. Zhurkin, K.L. Safonov, A. A. Schmidt, V .S. Kharlamov, S. A. Korolyov, M. N. Lubov, and J. Pezoldt,
Technical Physics Letters, 30 (2004) 641.

Flash lamp supported deposition of 3C-SiC (FLASiC) – a promising technique to produce high quality cubic SiC layers
W. Skorupa, D. Panknin, W. Anwand, M. Voelskow, G. Ferro, Y. Monteil, A. Leycuras, J. Pezoldt, R. McMahon, M. Smith, J. Camassel, J. Stoemenos, E. Polychroniadis, P. Godignon, N. Mestres, D. Turover, S. Rushworth, and A. Friedberger,
Proc. Mater. Sci. Forum, Silicon Carbide and Related Materials, Bologna, Italy (2003), (ICSCRM 2003), 457 (2004) 175.

Diffusion from platinum silicide for the local lifetime control in Silicon
J. Vobecky, P. Hazdra, G. Ecke, and D. Kolesnikov,
Proc. International Seminar on Power Semiconductors, Prague, Czech Republic (2004) 187.

Structure and composition of 3C-SiC:Ge alloys grown on Si (111) substrates by SSMBE
P. Weih, V. Cimalla, Th. Stauden, R. Kosiba, L. Spieß, H. Romanus, M. Gubisch, W. Bock, Th. Freitag, P. Fricke, O. Ambacher, and J. Pezoldt,
Proc. Mater. Sci. Forum, Silicon Carbide and Related Materials, Bologna, Italy (2003), (ICSCRM 2003), 457 (2004) 293.

Influence of the Ge coverage prior to carbonization on the structure of SiC grown on Si(111)
F. M. Morales, Ch. Zgheib, S. I. Molina, D. Araújo, R. García, C. Fernández, A.Sanz-Hervás, P. Masri , P. Weih, Th. Stauden, O. Ambacher, and J. Pezoldt,
Proc. Mater. Sci. Forum, Silicon Carbide and Related Materials, Bologna, Italy (2003), (ICSCRM 2003), 457 (2004) 297.

Stress control in 3C-SiC films grown on Si(111)
Ch. Zgheib, P. Masri, P. Weih, O. Ambacher, and J. Pezoldt,
Proc. Mater. Sci. Forum, Silicon Carbide and Related Materials, Bologna, Italy (2003), (ICSCRM 2003), 457 (2004) 301.

Etching of SiC with fluorine ECR plasma
Ch. Förster, V. Cimalla, R. Kosiba, G. Ecke, P. Weih, O. Ambacher, and J. Pezoldt,
Proc. Mater. Sci. Forum, Silicon Carbide and Related Materials, Bologna, Italy (2003), (ICSCRM 2003), 457 (2004) 821.

Formation of 3C-SiC films embedded in SiO_2 by sacrificial oxidation
D. Panknin, P. Godignon, N. Mestres,
E. Polychroniadis, J. Stoemenos, G. Ferro, J. Pezoldt, and W. Skorupa,
Proc. Mater. Sci. Forum, Silicon Carbide and Related Materials, Bologna, Italy (2003), (ICSCRM 2003), 457 (2004) 1515.

Growth of non-polar a-plne and cubic InN on r-plane sapphire by molecular beam epitaxy
H. Lu, W. J. Schaff, L. F. Eastman, V. Cimalla,
J. Pezoldt, O. Ambacher, J. Wu, W. Walukewicz,
Proc. Materials Research Society Symposium, GaN and Related Alloys, Boston (2003), 798 (2004) Y12.6.1.

Infrarotellipsometrie - ein Verfahren für die Materialcharakterisierung
J. Pezoldt and Ch. Wang,
Proc. Thüringer Werkstofftag 2004, Ilmenau, in Schriftenreihe Werkstoffwissenschaften,
18 (2004) 159.

Strukturselektion in multivariablen Kristallen
J. Pezoldt and A. A. Kalnin,
Proc. Thüringer Werkstofftag 2004, Ilmenau, in Schriftenreihe Werkstoffwissenschaften,
18 (2004) 167.

Trockenätzen von Siliziumkarbid
Ch. Förster, V. Cimalla, J. Pezoldt, G. Ecke,
and O. Ambacher,
Proc. Thüringer Werkstofftag 2004, Ilmenau, in Schriftenreihe Werkstoffwissenschaften,
18 (2004) 185.

Department of Microsystems Technology

Non-contact characterization of vertical regions of microstructures based on monochromatic speckle techniques
B. Horvath and A. Herztsch,
Measurement Science and Technology
15 (2004) 923.

Inductive structures in LTCC based on hot embossig techniques
J. Botiov, A. Albrecht, M. Fischer, K.H. Drue,
M. Hintz, and H. Wurmus,
Proc. MID 2004, Erlangen (2004).

Silicon based hybrid printing systems
J. Burgold, F. Weise, M. Fischer, L. Dressler,
and H. Wurmus,
Proc. DPI-Workshop: Inkjet Printing of functional Polymers and Materials, Eindhoven, Netherlands (2004).

Advanced LTCC Processes using Pressure Assisted Sintering
M. Hintz, H. Thust, A. Albrecht, and R. Tschernev,
Proc. SMTA Pan Pacific, Hawaii, USA (2004).

Ein chip-basiertes Tool zur kombinatorischen Synthese und biologischem Screening
A. Schober, Th. Henkel, A. Gross, and A. Albrecht,
Proc. Chemische und biologische Mikrolabortechnik, Ilmenau (2004).

Realisation of a Microdevice for Gas Combustion
M. Stubenrauch and N. Schwesinger,
Proc. 15th Micro Mechanics Europe Workshop 2004, Leuven, Belgium (2004).

Microcombustion system in MEMS technology
M. Stubenrauch and N. Schwesinger,
Proc. 18th Eurosensors Conference 2004, Rome, Italy (2004) 588.

Microfluidic Devices as Life Support Systems for Cells and Motor Proteins
M. Stubenrauch, D. Voges, K. Mandisloh,
and C. Schilling,
Proc. 3rd Symposium on Micro- and Nanostructures of Biological Systems, Halle/Saale (2004).

Design

Department of Design and Technology of Electronic Components

Polymeta – A Novel Technology for Printed Circuit Boards on Basis of Physical Vapor Deposition
Gert Winkler, Gernot Bischoff, Aneta Sutor,
Steffen Griehl, Tobias Müller,
Proc. 28th International Conference and Exhibition IMAPS-Poland, Wroclaw, Poland (2004) 405.

Devices

Department of Solid-State Electronics

Evolution and Recent Advances in RF/Microwave Transistors
J. J. Liou and F. Schwierz,
J. Telecomm. and Information Technology
4 (2004) 99.

Excessive Noise in Nanoscaled Double-Gate MOSFETs: A Monte Carlo Study
V. Polyakov and F. Schwierz,
Semiconductor Science and Technology
19 (2004) 145.

Subthreshold Behavior of Triple-Gate MOSFETs on SOI Material
M. C. Lemme, T. Mollenhauer, W. Henschel,
T. Wahlbrink, M. Baus, O. Winkler, R. Granzner,
F. Schwierz, B. Spangenberg, and H. Kurz,
Solid-State Electronics 48 (2004) 529.

Electrical Characterization of 12 nm EJ-MOSFETs on SOI Substrates
W. Henschel, T. Wahlbrink, Y. M. Georgiev,
M. Lemme, T. Mollenhauer, B. Vratzov, A. Fuchs,
H. Kurz, M. Kittler, and F. Schwierz,
Solid-State Electron. 48 (2004) 739.

Fabrication and analysis of polymer field-effect transistors
S. Scheinert and G. Paasch,
phys. stat. sol. (a) 201 (2004) 1263.

Organic field-effect transistors with nonlithographically defined submicrometer channel length
S. Scheinert, T. Doll, A. Scherer, G. Paasch,
and I. Hörselmann,
Appl. Phys. Lett. 84 (2004) 4427.

The influence of distributed trap states on the characteristics of top and bottom contact organic field-effect transistors
T. Lindner, G. Paasch, and S. Scheinert,
J. Mat. Res. 19 (2004) 2014.

Simulation of Base Boron Out-Diffusion in SiGe HBTs
R. Kinder, P. Beno, L. Hulenyi, J. Gessner, F. Schwierz,
J. Breza, and A. Grmanova,
Proc. 5th Int. Conf. on Advanced Semiconductor
Devices and Microsystems ASDAM (2004) 43.

SiGe HBTs for Ultra-High Speed Applications
F. Schwierz,
Invited Paper, Proc. 7th ICSICT, Beijing,
China (2004) 2114.

A Mobility Model for AlGaN/GaN 2DEGs
F. Schwierz,
Advanced Heterostructure Workshop, Big Island
Hawaii, USA (2004).

State of the Art Performance of Wide Bandgap RF Power Transistors: GaN vs. SiC
F. Schwierz and V. Polyakov,
Advanced Heterostructure Workshop, Big Island
Hawaii, USA (2004).

Scaling organic transistors: Materials and Design
G. Paasch and S. Scheinert,
Proc. Materials Science – Poland, Srem,
Poland 22 (2004) 423.

Modules

Department of Microperipherics

Photostrukturierte Elemente und Leitungen in LTCC
R. Perrone, M. Hintz, K.-H. Drüe, R. Münnich,
and H. Thust,
PLUS, 6 (2004) 126.

Progress in Passive Integration of Coils by Using Photoimageable Inks on and into LTCC
R. Perrone, K.H. Drüe, and H. Thust,
Proc. International Student Seminar on Microwave
Applications of Novel Physical Phenomena,
St. Petersburg, Russia (2004) 42.

20 GHz LTCC applications for satellite communications - challenges for design and technology
J. Trabert, R. Perrone, R. Münnich, R. Stephan,
M.A. Hein, and H. Thust,
Proc. International Student Seminar on Microwave
Applications of Novel Physical. Phenomena,
St. Petersburg, Russia (2004) 45.

LTCC Technologies for advanced RF/Microwave Applications
H. Thust, R. Perrone, K.-H. Drüe, and M. Hintz,
Proc. 28th IMAPS-Polen Conf., Wroclaw,
Polen (2004) 119.

Progress in Integration of Planar and 3D Coils on LTCC by Using Photoimageable Inks
R. Perrone, H. Thust, and K.-H. Drüe,
Proc. 37th IMAPS-Long Beach Conf.,
Long Beach, USA (2004).

Feinstrukturierung durch photodefinierbare Materialien – Übersicht und Anwendung
H. Thust, R. Perrone, K.-H. Drüe, and A. Albrecht,
Proc. DKG-Symposium Verfahren der keramischen Mehrlagentechnik: Stand und Zukunftsperspektiven, Erlangen (2004), in Verfahrenstechnik, 18 (2004) 22.

Neue Technologievarianten von LTCC durch druckunterstütztes Sintern
M. Hintz, H. Thust, T. Rabe, and B. Schulz,
Proc. DKG-Symposium Verfahren der keramischen Mehrlagentechnik: Stand und Zukunftsperspektiven, Erlangen (2004), in Verfahrenstechnik,
18 (2004) 174.

Sintern von LTCC (Low Temperature Co-fired Ceramics)-Substraten ohne laterale Schwindung
T. Rabe, W. A. Schiller, M. Hintz, and H. Thust,
Proc. DKG-Jahrestagung, Karlsruhe (2004).

Systems

Department of Process Measurement

Development of a Focus Sensor and its Integration into the Nanopositioning and Nanomeasuring Machine
R. Mastylo, E. Manske, and G. Jäger,
Proc. OPTO-Conference "Optical Technologies, Optical Sensors and Measuring Techniques",
Nürnberg (2004) 123.

Advances in Traceable Nanometrology with the Nanopositioning and Nanomeasuring Machine
E. Manske, R. Mastylo, T. Hausotte, N. Hofmann, and G. Jäger,
Proc. Nanoscale 2004, Braunschweig (2004).

Analytics

Department of Technical Physics

Understanding chemisorption and epitaxy of large aromatic adsorbates
F.S. Tautz, M. Eremtchenko, and J. A. Schaefer,
Pico 8 (2004) 4.

Investigations of MBE grown InN and the influence of sputtering on the surface composition
S. Krischok, V. Yanev, O. Balykov, M. Himmerlich, J.A. Schaefer, R. Kosiba, G. Ecke, I. Cimalla, V. Cimalla, O. Ambacher, H. Lu, W.J. Schaff, and L.F. Eastman,
Surface Science 566 (2004) 849.

Influence of the RF power on the deposition rate and the chemical surface composition of fuorocarbon films prepared in dry etching gas plasma
V. Yanev, S. Krischok, A. Opitz, H. Wurmus, J.A. Schaefer, N. Schwesinger, and S.-I.-U. Ahmed,
Surface Science 566 (2004) 1229.

Surface Science Tools and their application to nanostystems like C_{60} on indium phosphide
J.A. Schaefer, G. Cherkashinin, S. Döring, M. Eremtchenko, S. Krischok, D. Malsch, A. Opitz, T. Stolz, and R. Temirov,
in Frontiers of Multifunctional Integrated Nanosystems, Kluwer Academic Publishers (2004) 131.

Viscosity effect on GaInSn studied by XPS
F. Scharmann, G. Cherkashinin, V. Breternitz, Ch. Knedlik, G. Hartung, Th. Weber, and J. A. Schaefer,
Surface and Interface Analysis 36 (2004) 981.

Structure, bonding and growth at a metal-organic interface in the weak chemisorption regime: perylene/Ag(111)
M. Eremtchenko, D. Bauer, J.A. Schaefer, and F. S. Tautz,
Journal of Materials Research 19 (2004) 2028.

Polycyclic aromates on close-packed metal surfaces: functionalisation, molecular chemisorption and organic epitaxy
M. Eremtchenko, D. Bauer, J.A. Schaefer, and F. S. Tautz,
New Journal of Physics 6 (2004) 4.

The interface between benzenes (C_6H_6 ; C_6H_5Cl ; 2-C_6H_4OHCl) and amorphous solid water studied with metastable impact electron spectroscopy and ultraviolet photoelectron spectroscopy (He I and II)
A. Borodin, O. Höfft, U. Kahnert, V. Kempter, S. Krischok, and M.O. Abou-Helal,
Journal of Chemical Physics, 120 (2004) 5407.

Die tribologischen Eigenschaften von hydrophoben selbstorganisierten organischen Monoschichten: Einfluss der Gleitgeschwindigkeit und Messungen der Lebensdauer
W. Hild, G. Hungenbach, S.I.-U. Ahmed, M. Scherge, and J.A. Schaefer,
Tribologie und Schmierungstechnik 1 (2004) 5.

Sputter depth profiling of InN layers
R. Kosiba, G. Ecke, V. Cimalla, L. Spieß, S. Krischok, J.A. Schaefer, O. Ambacher, and W.J. Schaff,
Nuclear Instruments and Methods in Physics Research B 215 (2004) 486.

Highly efficient electron field emission from decorated multiwalled carbon nanotube films
M. Sveningsson, R.E. Morjan, O.A. Nerushev, E.E.B. Campbell, D. Malsch, and J.A. Schaefer,
Journal of Appl. Phys. Lett. 85 (2004) 4487.

Einfluss der Rauheit auf die mikrotribologischen Eigenschaften von unterschiedlich strukturierten Siliziumoberflächen bedeckt mit selbstorganisierten Monoschichten
W. Hild, G. Hungenbach, J. A. Schaefer, M. Fischer, S.I.-U. Ahmed, and M. Scherge,
Materialwissenschaft und Werkstofftechnik 35 (2004) 711.

Nanotribologische Untersuchungen von ultradünnen Wasserfilmen auf hydrophilem Siliziumoxid
A. Opitz, S. I.-U. Ahmed, M. Scherge, and J. A. Schaefer,
Tribologie und Schmierungstechnik 5 (2004) 7.

Grundlagenuntersuchungen an herkömmlichen Hochspannungsleuchtröhren
C. Blankenhagen, W. Boehm, D. Gall, G. Hartung, J. A. Schaefer, and J. Sommer,
Licht 3 (2004) 208.

Heiße Wendelkathoden in modifizierten Entladungslampen
C. Blankenhagen, W. Boehm, D. Gall, G. Hartung, J. A. Schaefer, and J. Sommer,
Licht 5 (2004) 37.

Silicide contacts for Si/Ge devices
J.E. Burnette, M. Himmerlich, and R.J. Nemanich,
in Silicide Technology for Integrated Circuits, The Institution of Electrical Engineers, London, ISBN 0-86341-352-8.

Monitoring the motion of linear bearings with a resolution down to nanometers
Y. Liu, W. Hild, M. Kitsche, S. Doering, G. Hungenbach, M. Scherge, and J.A. Schaefer,
in Smart Materials & Structures, Cansmart 2004, Montreal, Canada, (2004) 105.

Nanoschichten für die Nanopositionierung
M. Gubisch, Y. Liu, L. Spiess, and C. Knedlik,
Proc. Thüringer Werkstofftag 2004, Ilmenau, in Schriftenreihe Werkstoffwissenschaften, 18 (2004) 131.

Bearings and bearing materials tested for Nanopositioning
Y. Liu, W. Hild, M. Kitsche, S. Doering, S. Lasse, G. Hungenbach, M. Scherge, and J.A. Schaefer,
31st Leeds-Lyon Symposium on Tribology, Leeds, United Kingdom, in Tribology and Interface Engineering Series 48, Elsevier (2004).

Tribological characteristics of WC_{1-x}, W_2C, and WC tungsten carbide films
M. Gubisch, Y. Liu, S. Krischok, G. Ecke, L. Spieß, J. A. Schaefer, and Ch. Knedlik,
31st Leeds-Lyon Symposium on Tribology, Leeds, United Kingdom, in Tribology and Interface Engineering Series 48, Elsevier (2004).

Theses

PhD-Theses

Henry Romanus (1.06.2004)
Department of Materials for Electrical Engineering
„Siliziumkarbidelektronik: technologische und werkstoffwissenschaftliche Untersuchungen zur Metallisierung/Kontaktierung“

Arne Albrecht (24.08.2004)
Department of Microsystems Technology
“Grundlagen einer magnetischen Manipulation von Partikeln für Anwendungen in der miniaturisierten kombinatorischen chemischen Reaktionstechnik“

Waleed Ehrhardt (24.08.2004)
Department of Microperipherics
“Einfluss von Hochspannungsimpulsen auf Schichtwiderstände und Entwicklung eines Abgleichverfahrens“

Diploma-Theses

Gabriel Kittler (9.02.2004)
Department of Nanotechnology
“Surface modification of sensors for nano- and picofluidic systems”

Marian Keck (7.04.2004)
Department of Microsystems Technology
„Entwicklung und Untersuchung eines spektroskopischen Sensors für die Flüssigkeitscharakterisierung“

Jörg Paschke (13.04.2004)
Department of Microsystems Technology
„Elektrostatischer Antrieb“

Ronny Wagner (3.05.2004)
Department of Nanotechnology
„AlGaN-based hetero- and nanostructures for detection of UV-light“

Oliver Schulz (19.05.2004)
Department of Nanotechnology
“Degardation of polymer solar cells, polymer layers and polymer/fulleren-composite layers”

Stefan Döring (16.06.2004)
Department of Technical Physics
“Vibronische, elektronische und strukturelle Untersuchungen von C_{60}-Fullerenen auf InP(001)“

Kristin Mandisloh (2.08.2004)
Department of Microsystems Technology
„Handling von biologischen Elementen in mikrofluidischen Systemen“

Jeanette Körner (13.08.2004)
Department of Materials for Electrical Engineering
„Querschnittspräparation und Untersuchung von Schichtsystemen“

Björn Schwenke (13.08.2004)
Department of Materials for Electrical Engineering
„Entwicklung von Nanokomposit- bzw. Multilayerschichten auf der Basis von Wolframkarbid und Molybdändisulfid mit Hilfe der Magnetronsputtertechnik“

Ralf Brunner (26.08.2004)
Department of Technical Physics
“Structural and Electronic Analysis of Catalytically Grown Carbon Nanotubes on Quartz Using Spray Pyrolysis of Ferrozene/Benzene Solutions”

Martin Rebhahn (27.08.2004)
Department of Technical Physics
“Untersuchungen zum Einfluss der Endbearbeitung auf tribologische Eigenschaften von kupferbasierten Legierungen“

Thomas Stolz (30.09.2004)
Department of Technical Physics
“Investigation of nanoscale indium segregation on InP(001)-(2x4) with surface sensitive techniques”

Rene Bergmann (4.10.2004)
Department of Microsystems Technology
„Einsatz elektrisch leitfähiger Glaslote für Waferbondverbindungen“

Björn Schröter (25.10.2004)
Department of Microsystems Technology
„Entwurf und Umsetzung eines Mikroventils mit magnetischem Antrieb“

Daniéll Malsch (30.11.2004)
Department of Technical Physics
“Chemical vapour deposition and characterization of carbon nanotubes”

Sven Rentsch (08.12.2004)
Department of Microperipherics
“Breitbandige HF-Anschlüsse an LTCC Gehäuse”

Martin Kitsche (17.12.2004)
Department of Technical Physics
"Einfluss verschiedener Faktoren auf die Adhäsion von Elastomeren"

Sascha Perlitz (17.12.2004)
Department of Technical Physics
„Phaseretrieval zur Evaluation der Abbildungseigenschaften eines optischen Systems"

Student research project reports

Björn Schröder (Januar 2004)
Department of Microsystems Technology
"Kapazitiver Drucksensor"

Hagen Luckner (31. 01.2004)
Department of Microsystems Technology
"Elektrochemisches Ätzen"

Dorothea Förster (19.03.2004)
Department of Microperipherics
"Spulen in LTCC mit Fodel-Technologie"

Sven Rentsch (22.03.2004)
Department of Microperipherics
"Ermittlung von Flipchip-Parametern auf fotostrukturierten (Fodel) Dickschichtpasten"

Michael Sachs (29.03.2004)
Department of Process Meassurement
"Konstruktion, Montage und Erprobung eines Fixfokussensors mit Lichtleitkabeleinkopplung"

Steffen Herrmann (31.05.2004)
Department of Microsystems Technology
"Thermische Untersuchung von Mikrospulen durch Simulation"

Sebastian Stoebenau (Juni 2004)
Department of Microsystems Technology
"Leiterbahnen aus Poly-Silizium"

Merten Niebelschütz (12.06.2004)
Department of Nanotechnology
"In situ – resistance measurement of layers during ion beam sputtering"

Florentina Will (12.06.2004)
Department of Nanotechnology
"Construction of a sample heating system for Augerelectronspectroscopy"

Ole Jens Otto Nagel (Juli 2004)
Department of Microsystems Technology
"Technologische Realisierung eines Mikroschwingers"

Meike Hoffmann (31.08.2004)
Department of Microsystems Technology
"Integration eines hochauflösenden Temperatursensors"

Ming-Jian Tok (31.08.2004)
Department of Microsystems Technology
"Mikro-Makro Schnittstellen für Dosiersysteme"

Martin Correns (9.11.2004)
Department of Microsystems Technology
"Strobuskopanordnung zur Beobachtung von dynamischen Vorgängen"

Christoph Kluge (26.11.2004)
Department of Microperipherics
"Schrumpfungen und Wärmeverteilung in LTCC"

Maria Elisa Morillas Jimenez (6.12.2004)
Department of Microperipherics
"Wärmetransportmechanismen und Herstellungsverfahren von LTCC Multilayer und konkurrierenden Technologien"

Invited Talks, Colloquia, and Workshops

Dr. Stefan Kunze
„Messung von Schaltzuständen an miniaturisierten Elektrodenstrukturen mit Hilfe der elektrostatischen Kraftmikroskopie"
Institut für Bioprozess- und Analysenmesstechnik, Heilbad Heiligenstadt, 7.01.2004

Dr. Henkel und Prof. Köhler
„Erzeugung, Manipulation und Analyse von Reaktionsräumen in mikrofluidischen Bauelementen"
Institut für Physikalische Hochtechnologie, Jena und TU Ilmenau, 21.01.2004

Dr. Rüdiger Goldhahn
„Ellipsometrie an Gruppe-III-Nitriden"
FG Experimentaphysik I, TU Ilmenau, 4.02.2004

Dipl.-Ing. Marko Pudas
„Gravure-offset Printing of Ultra-fine-line Thick-film for Electronics"
University Oulu, Finland, 6.02.2004

Dr. Steffen Oswald
„Tiefenprofil und Grenzflächenanalytik im nm-Bereich"
Leibniz-Institut für Festkörper- und Werkstoffforschung, Dresden, 3.03.2004

Prof. Thomas Leisner
„Berührungslose Speicherung, Manipulation und Charakterisierung von Mikrotröpfchen in elektrodynamischen Speichern"
Fachgebiet Umweltphysik, TU Ilmenau, 17.03.2004

Dr. Mathias Procop
„Stand und Perspektiven der Materialanalyse mittels Röntgenspektroskopie am Rasterelektronenmikroskop"
Bundesanstalt für Materialforschung und -prüfung, Berlin, 31.03.2004

Dr. Jens Müller
„Multilayer-Schaltkreise für biomedizinische Anwendungen"
Micro Systems Engineering GmbH, Berg, 12.05.2004

Dr. Chris Smith
„Material with negative Poison ratio"
University of Exeter, Great Britain, 13.05.2004

Dr. Gertrud Klauer
„Funktion tierischer Mechano-Sensoren"
Universität Frankfurt/ Main, 14.05.2004

Prof. Joachim Meyer
„Hochauflösende analytische Transmissionselektronenmikroskopie und ihre Anwendungen in der Nanotechnologie"
Gemeinschaftslabor für Elektronenmikroskopie, RWTH Aachen, 26.05.2004

Dr. Aimo Winkelmann
„Elektronenbeugungsmethoden zur Strukturbestimmung ultradünner Filme aus SiC und AlN"
Max-Plank-Institut für Mikrostrukturphysik, Halle, 9.06.2004

Dr. Torsten Zech
„Einsatz von Mikroreaktoren für die kombinatorische Katalysatorforschung"
HTE AG, Heidelberg, 17.06.2004

Dr. Karen Lemke
„Kultivierung von Mikroorganismen und tierischen Zellen – Voraussetzung für die online Sensorik"
Institut für Bioprozess- und Analysenmesstechnik, Heiligenstadt, 23.06.2004

Prof. Wolfgang J. Choyke
„SiC in the Grand Scheme"
University of Pittsburgh, PA, USA, 7.07.2004

Dr. V. Rehacek und Dr. I. Hotovy
„Thin film mercury microelectrodes for heavy metal determination" und
„Gas sensor based on Pt-modified NiO sputtered thin films for the detection of hydrogen"
TU Bratislava, Slovac Republic, 14.07.2004

Dr. Petra Meier
„Technologische Realisierung eines künstlichen Wurms für die Wirbelsäulen-Chirurgie"
Nachwuchsgruppe „Peristaltische Sonde",
TU Ilmenau, 21.07.2004

Prof. Tadeusz Pisarkiewicz
„Microfabrication and microcomponents for gas sensing"
AGH University of Science and Technology, Krakow, Poland, 28.07.2004

Dr. Frank Machalett
„Nanostrukturierung von Festkörpern durch fokussierte Ionenstrahlen und ausgewählte Anwendungen der Ionenmikroskopie"
Institut für Festkörperphysik, Friedrich-Schiller-Universität, Jena, 13.10.2004

Prof. Yurii V. Trushin
„Simulation der Keimbildung von SiC-Nanoclustern"
Ioffe Physico-Technical Institute, Russian Academy of Sciences, St. Petersburg, Russian Federation, 3.11.2004

Prof. Peter Kordoš
„Material and device issues of AlGaN/GaN HEMTs"
Department of Microelectronics, Slovak Technical University, Bratislava, Slovac Republic, 29.11.2004

Dr. Michael Haschke
„Mikro- und Nanostrukturiertes Glas – Anwendungen im Röntgenbereich und als photonische Kristalle"
Institut für Gerätebau GmbH, Berlin, 8.12.2004

Workshops

Thüringer Werkstofftag 2004 (21.04.2004)
Proc.: L. Spieß,H. Kern,Ch. Knedlik, (ed.)
Thüringer Werkstofftag 2004
Köster Verlag Berlin, ISBN 3-89574-519-7, 219 p.

Jobmaschine Mikrosystemtechnik (18. - 19.05.2004)
Innovationspotential und Fachkräftebedarf in Thüringen,
Federal Ministry of Education and Research,
Thuringian Ministry for Science, Research, and Art.

Fachtagung Mikrosystemtechnik stärken - Fachkräfte sichern - Kräfte bündeln (24.11.2004)
Federal Ministry of Education and Research,
Technical University of Ilmenau,
Center for Micro- and Nanotechnologies,
FasiMiT - Aus- und Weiterbildungsnetzwerk Mikrosystemtechnik in Thüringen.

International Workshop on Convergent Beam Electron Diffraction II (21. - 23.06.2004)
U. Kaiser, M. Tanaka (JPN)
FEI-Company (G, NL, USA),
JEOL (G, JPN),
LEO Electron Microscopy Group (G)

Scientific Projects

Federal Ministry of Education and Research (Bundesministerium für Bildung und Forschung, BMBF)

Aufbau eines Aus- und Weiterbildungsnetzwerks innerhalb der Mikrosystemtechnik in Thüringen
(FASIMIT), Project manager: Prof. Wurmus
Mike Stubenrauch, Verein MicroComp e.V.

Nanobiotechnologie-Verbundprojekt: Kristalloides P-Protein – Prototyp bioanaloger Nanoaktuatoren; Teilprojekt 3: Prototypische Anwendungen
(P-Protein), Project manager: Prof. Wurmus
Jörg Burgold, Karin Friedel, Mike Stubenrauch, Danja Voges

InnoRegio Inprosys - Verbundprojekt: Hochpräzise optoelektronische Messsysteme für die Präzisionsfertigung
(HOMS), Project manager: Prof. Jäger
Nataliya Dorozhovets, Uwe Gerhardt, Victor Mandryka

German Science Foundation (Deutsche Forschungsgemeinschaft, DFG)

Heteroepitaxie von Gruppe III-Nitriden auf Diamantsubstraten für optoelektronische und elektronische Anwendungen
(Diamant), Project manager: Prof. Ambacher
Dorin Cornel Cengher, Rastislav Kosiba, Markus Mehnert

Entwicklung piezoelektrischer, mit Halbleiterbauelementen integrierbarer AlGaN/Si-Nanoresonatoren für elektrokeramische Hochfrequenzsensoren
(Pi-NEMS), Project manager: Prof. Ambacher
Klemens Brückner, Christian Förster, Matthias Hein, Ralf Stephan

Bauelementeverhalten und Transporteigenschaften organischer Feldeffekt-Transistoren: Experiment-Simulation-Theorie
Project manager: Dr. Scheinert
Andrej Herasimovich, Ingo Hörselmann, Silvia Klaube

Analytische Transmissionselektronenmikroskopie und Bildsimulation zur Untersuchung der Gitterplatzbesetzung und Clusterbildung in p- und n-dotiertem SiC nach Ionenimplantation,
Project manager: Dr. Kaiser
Andrey Chuvilin

Thuringian Ministry of Culture (Thüringer Kultusministerium)

Zell- und Biomolekül-Sensoren in Piko- und Nanofluidischen Systemen
(Pikofluidik), Project manager: Prof. Ambacher
Majdeddin Ali, Arne Albrecht, Falko Baier, Volkmar Breternitz, Carsten Buchheim, Jörg Burgold, Volker Cimalla, Lothar Dressler, Karl-Heinz Drüe, Michael Fischer, Karin Friedel, Uwe Genatis, Jörg Geßner, Maik Gubisch, Gabriele Harnisch, Birgitt Hartmann, Michael Hintz, Rene Hoffmann, Matthias Kallenbach, Jaroslaw Kita, Gabriel Kittler, Mario Kittler, Ina Koch, Stefan Krischok, Annette Läffert, Regina Lenk, Rostyslav Mastylo, Christian Müller, Andreas Opitz, Rolf Öttking, Elvira Remdt, Henry Romanus, Jens Schawohl, Andreas Schober, Björn Schwenke, Frank Schwierz, Martina Sieler, Lothar Spieß, Mike Stubenrauch, Aneta Sutor, Frank Weise

Entwicklung und Charakterisierung von nanoskaligen Verschleißschutzschichten
(NANOVSS), Project manager: Prof. Knedlik
Elvira Remdt, Henry Romanus, Jens Schawohl, Lothar Spieß

Entwicklung von LTCC-Schaltungen für Anwendungen bis 20GHz
(LTCC für 20GHz), Project manager: Prof. Thust
Waleed Erhardt, Uwe Genatis, Michael Hintz, Ina Koch, Regina Lenk, Ashraf Mokayyes, Ralph Münnich, Ruben Perrone, Martina Sieler

Herstellung von organischen Mischschichten mit nanoskaligen Domänen für Solarzellen aus konjugierten Polymeren
(ORSOL), Project manager: Prof. Ambacher
Maher Al-Ibrahim, Irina Cimalla, Volker Cimalla, Gernot Ecke, Rastislav Kosiba, Sylvia Probst, Willy Schliefke, Matthias Spode, Jutta Uziel

Realisierung, Charakterisierung und Optimierung von AlGaN-basierenden UV-Detektoren mit integrierten Bandpassfiltern auf Siliziumsubstraten
(UVSENS), Project manager: Prof. Ambacher
Carsten Buchheim, Irina Cimalla, Volker Cimalla, Gernot Ecke, Christian Förster, Rastislav Kosiba, Vadim Lebedev, Ilona Marquardt, Sylvia Probst, Thomas Stauden, Andreas Winzer

Inbetriebnahme der neuen technologischen Ausrüstungen, Charakterisierung der Prozesse, Kostenanalyse zur Einführung einer Kostenrechnung (ZMN-Anlaufphase), Project manager:
Prof. Ambacher (Direktor)
Oleg Balykov, Gernot Bischoff, Manuela Breiter, Volkmar Breternitz, Carsten Buchheim, Jörg Burgold, Genady Cherkachinin, Volker Cimalla, Lothar Dressler, Karl-Heinz Drüe, Michael Fischer, Karin Friedel, Uwe Genatis, Maik Gubisch, Jin Guo, Gabriele Harnisch, Birgitt Hartmann, Rene Hoffmann, Andrej Jancura, Ute Kaiser, Matthias Kallenbach, Ina Koch, Stefan Krischok, Regina Lenk, Markus Mehnert, Feng Qiao, Elvira Remdt, Henry Romanus, Jens Schawohl, Martina Sieler, Lothar Spieß, Anata Sutor, Gerd Teichert, Frank Weise

SiC-Hochfrequenztransistor mit neuen Materialien (NEMASIC), Project manager: Prof. Doll
Gernot Ecke, Christian Fachmann, Christian Förster, Jörg Geßner, Mario Kittler, Rastislav Kosiba, Ilona Marquardt, Thorsten Mülln, Jörg Pezoldt, Henry Romanus, Frank Schwierz, Lothar Spieß, Thomas Stauden, Petia Weih

Wachstumskinetik und elektrische Eigenschaften niedermolekularer organischer Funktionsschichten für die Anwendung in Feldeffekttransistoren (Organische Funktionsschichten),
Project manager: Prof. Schäfer
Falko Baier, Oleg Balykov, Jin Guo, Gudrun Hungenbach, Stefan Krischok, Annette Läffert, Thomas Stolz, Doreen Thiele, Vasil Yanev

Organische Schichten und ihre Grenzflächen zur Anwendung in Feldeffekt-Transistoren,
Project manager: Prof. Doll
Andrej Herasimovich, Ingo Hörselmann, Maxi Scheinert, Rüdiger Traute

Anisotrope Nanostrukturen aus Funktionspolymerkompositen für optische und elektronische Bauelemente
(NANORG 1), Project manager: Prof. Gobsch
Maher Al-Ibrahim, Andrej Herasimovich, Thomas Kups, Elke Langhammer, Uladzimir Zhokhavets

European Union (Europäische Union)

Herstellung und Optimierung von 3C-SiC-Schichten auf Siliziumsubstraten durch eine Kombination der Molekularstrahlepitaxie und des lichtinduzierten Ausheilens von Defekten
(FLASIC), Project manager: Dr. Pezoldt
Genady Cherkachinin, Volker Cimalla, Gernot Ecke, Christian Förster, Rastislav Kosiba, Ilona Marquardt, Markus Mehnert, Thomas Stauden, Petia Weih, Charbel Zgheib

New Generation of GaN-based sensor arrays for nano- and pico-fluidic systems for fast and reliable biomedical testing
(GANANO), Project manager: Prof. Ambacher (Project coordinator)
Dorin Cornel Cengher, Simone Gutsche, Gabriel Kittler, Ulrich Liebold

New Process for Realisation of Electrical Connections between Layers of printed Circuit Boards and a Method to implant Micro Components using the Embedded Micro Connector
(EMCI), Project manager: Prof. Winkler
Gernot Bischoff, Ashraf Mokayyes, Aneta Sutor

Office of Naval Research (ONR)

Pyroelectric AlGaN/GaN HEMTs for ion, gas & Polar liquid sensors
(NICOP), Project manager: Prof. Ambacher
Volker Cimalla, Gernot Ecke, Christian Förster, Rastislav Kosiba, Vadim Lebedev, Ilona Marquardt, Jörg Pezoldt, Thomas Stauden, Petia Weih

Arbeitsgemeinschaft industrieller Forschungsvereinigungen „Otto von Guericke“ e. V. (AiF)

Untersuchung und Entwicklung der hard- und softwaretechnischen Grundlagen für eine automatisch gesteuerte Vorrichtung mit Inline Messung zum strukturbewahrenden Präzisionsabgleich,
Project manager: Prof. Thust
Waleed Y. Ehrhardt, Torsten Thelemann

Deutsche Bundesstiftung Umwelt (DBU)

’Syn and Sort’ ressourcensparendes kombinatorisches Synthesesystem
Project manager: Prof. Ambacher,
Lothar Dressler, Michael Gebinoga, Gabriele Harnisch, Siegmar Hecht

German Aerospace Society (Deutsches Zentrum für Luft- und Raumfahrt, DLR)

Keramische Mikrowellenschaltkreise für die Satellitentechnik
(KERAMIS), Project manager: Prof. Thust
Karl-Heinz Drüe, Uwe Genatis, Matthias Hein, Ralph Münnich, Ruben Perrone, Martina Sieler, Ralf Stephan, Johannes Trabert

Niedrigdimensional Strukturen für effektive Intraband- und Interbandoptiken,
Project manager: Dr. Kaiser
WTZ with Russian Federation

Industry

Matsushita Electric Works, Ltd.
Liquid Metal Micro Relay (LMMR),
Project manager: Prof. Knedlik, Prof. Wurmus
Mathias Bründel, Friedhelm Scharmann

Roth & Rau AG
Entwicklung eines Chlorgas basierenden Plasma-Ätzprozesses,
Project manager: Prof. Ambacher

Fraunhofer-Institut für Angewandte Optik und Feinmechanik (IOF), Jena
Transmissionselektronenmikroskopie – Strukturuntersuchungen an oxidischen fluoridischen und metallischen Aufdampfschichten,
Project manager: Dr. Kaiser
Johannes Biskupek, Andrey Chuvilin, Thomas Kups

Fraunhofer-Institut für Angewandte Optik und Feinmechanik (IOF), Jena
XTEM Analyse ultradünner Schichtsysteme,
Project manager: Dr. Kaiser
Thomas Kups

Fraunhofer-Institut für Angewandte Optik und Feinmechanik (IOF), Jena
TEM-Untersuchungen an metallischen Inseln,
Project manager: Dr. Kaiser
Andrey Chuvilin, Thomas Kups

Thüringer Institut für Textil- und Kunststoff-Forschung e.V. (TITK) Rudolstadt/Schwarza:
Polymere Feldeffekttransistoren,
Project manager: Dr. Scheinert
Andrej Herasimovich

Degussa AG
Entwicklung von Mikrofluidischen Komponenten,
Project manager: Prof. Wurmus
Heike Bartsch de Torres, Mike Stubenrauch

VIA electronic GmbH
Design und Simulation von HF-Strukturen in LTCC,
Project manager: Prof. Thust

Robert Bosch GmbH
Design und Aufbau eines LTCC-basierenden 24 GHz Demonstrators,
Project manager: Prof. Thust
Marcus Norén

Adresses

ZMN
Center for Micro- and Nanotechnologies
Gustav-Kirchhoff-Str. 7
98693 Ilmenau
Germany

phone: +49-(0)3677-69-3401
fax: +49-(0)3677-69-3499

e-mail: zmn@tu-ilmenau.de
URL: http://www.tu-ilmenau.de/zmn

Prof. Oliver Ambacher:
oliver.ambacher@tu-ilmenau.de
phone: +49-(0)3677-69-3723

Dr. Thomas Friedrich:
thomas.friedrich@tu-ilmenau.de
phone: +49-(0)3677-69-3380

Prof. Gerd Jäger:
jaeger@mb.tu-ilmenau.de
phone: +49-(0)3677-69-2822

Prof. Heinrich Kern:
kern@tu-ilmenau.de
phone: +49-(0)3677-69-2533

Prof. Christian Knedlik:
christian.knedlik@tu-ilmenau.de
phone: +49-(0)3677-69-3611

Dr. Jens Müller:
jens.mueller@tu-ilmenau.de
phone: +49-(0)3677-69-3381

Prof. Jürgen A. Schäfer:
juergen.schaefer@tu-ilmenau.de
phone: +49-(0)3677-69-3609

Dr. Susanne Scheinert:
susanne.scheinert@tu-ilmenau.de
phone: +49-(0)3677-69-3222

Prof. Heiko Thust:
heiko.thust@tu-ilmenau.de
phone: +49-(0)3677-69-2605

Prof. Gert Winkler:
gert.winkler@tu-ilmenau.de
phone: +49-(0)3677-69-2606

Prof. Helmut Wurmus:
helmut.wurmus@tu-ilmenau.de
phone: +49-(0)3677-69-2487

ZMN, Center for Micro- and Nanotechnologies

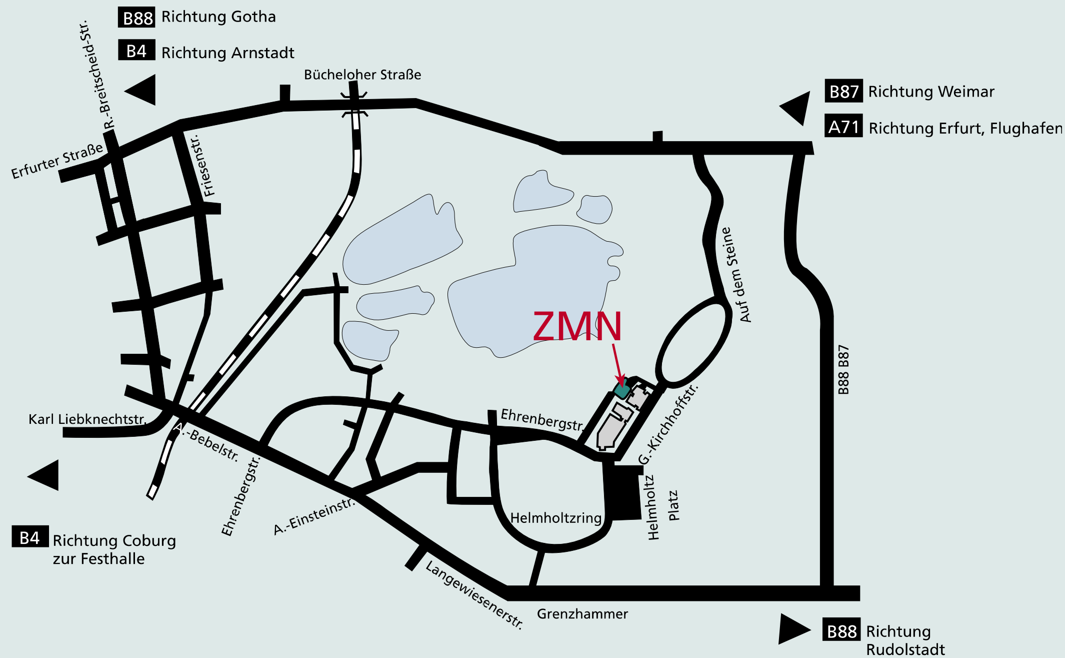

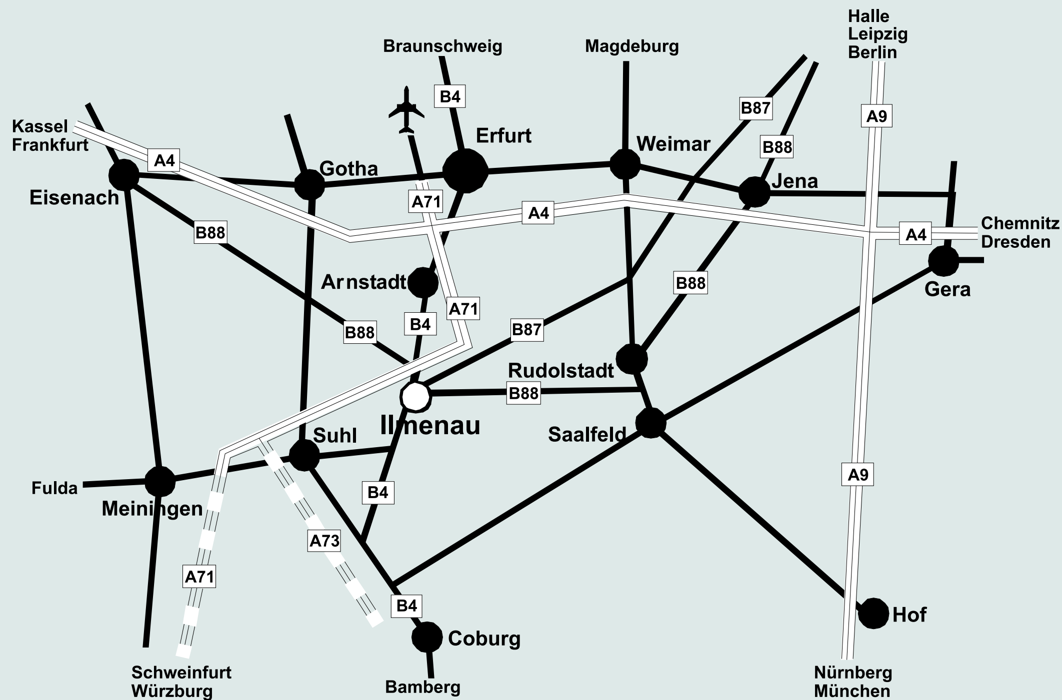

ZMN, Center for Micro- and Nanotechnologies
Gustav Kirchhoff-Str. 7
98693 Ilmenau, Germany
phone: +49-(0)3677-69-3400
fax: +49-(0)3677-69-3499
email: zmn@tu-ilmenau.de
URL : http://www.tu-ilmenau.de/zmn

Director: Prof. Oliver Ambacher
Contact: Dr. Herwig Döllefeld